CENTRAL RESEARCH LIBRARY
DOCUMENT COLLECTION

4

MARTIN MARIETTA ENERGY SYSTEMS LIBRARIES

3 4456 0251415 2

ORNL-2609
Physics and Mathematics
TID-4500 (14th ed.)
February 15, 1958

NEUTRON PHYSICS DIVISION

ANNUAL PROGRESS REPORT

FOR PERIOD ENDING SEPTEMBER 1, 1958

OAK RIDGE NATIONAL LABORATORY
CENTRAL RESEARCH LIBRARY
CIRCULATION SECTION
4500N ROOM 175
LIBRARY LOAN COPY
DO NOT TRANSFER TO ANOTHER PERSON
If you wish someone else to see this report, send in name with report and the library will arrange a loan.
UCN-7969 (3 9-77)

OAK RIDGE NATIONAL LABORATORY
operated by
UNION CARBIDE CORPORATION
for the
U.S. ATOMIC ENERGY COMMISSION

Printed in USA. Price 300 cents. Available from the

Office of Technical Services
U. S. Department of Commerce
Washington 25, D. C.

LEGAL NOTICE

This report was prepared as an account of Government sponsored work. Neither the United States, nor the Commission, nor any person acting on behalf of the Commission:

A. Makes any warranty or representation, express or implied, with respect to the accuracy, completeness, or usefulness of the information contained in this report, or that the use of any information, apparatus, method, or process disclosed in this report may not infringe privately owned rights; or

B. Assumes any liabilities with respect to the use of, or for damages resulting from the use of any information, apparatus, method, or process disclosed in this report.

As used in the above, "person acting on behalf of the Commission" includes any employee or contractor of the Commission to the extent that such employee or contractor prepares, handles or distributes, or provides access to, any information pursuant to his employment or contract with the Commission.

ORNL-2609 ERRATA

page 28

The denominator of the equation should read:

$$\left[\int_0^{0.2} \phi_M \Sigma dE + \lambda \int_{0.2}^{10^6} (\Sigma/E)\, dE\right.$$

page 48

The figure caption should read:

.....Fission. The top curve represents the prompt radiation on an arbitrary scale. Random backgrounds.....

page 51

The righthand scale (for the continuous belt spectrum) should be in units of:

$$\text{Photons} \cdot \text{Mev}^{-1} \cdot \text{fission}^{-1}$$

page 61

The third number in the second column of the table should be:

288 ± 60 <u>not</u> 288 ± 6

The third number in the fourth column of the table should be:

3.15 ± 0.65 <u>not</u> 3.05 ± 0.65

Footnote c for the table should read:

.....Beryllium and Graphite, Transactions of American Nuclear Society, June, 1958, Vol. 1, No. 1, paper 11-1, p. 94.

page 136

The resistance between Pin 6 of V_{3A} and Pin 2 of V_{3B} should be changed from 2.2 K to 2.2 Meg.

ORNL-2609
Physics and Mathematics
TID-4500 (14th ed.)
February 15, 1958

Contract No. W-7405-eng-26

NEUTRON PHYSICS DIVISION ANNUAL PROGRESS REPORT

for Period Ending September 1, 1958

E. P. Blizard, Director
A. Simon, Associate Director

A. D. Callihan, Leader, Critical Experiments Facility
C. E. Clifford, Leader, Tower Shielding Facility
F. C. Maienschein, Leader, Bulk Shielding Facility
W. Zobel, Leader, Lid Tank Shielding Facility

DATE ISSUED

OCT 16 1958

OAK RIDGE NATIONAL LABORATORY
Operated by
UNION CARBIDE NUCLEAR COMPANY
A Division of Union Carbide and Carbon Corporation
Post Office Box X
Oak Ridge, Tennessee

MARTIN MARIETTA ENERGY SYSTEMS LIBRARIES

3 4456 0251415 2

TABLE OF CONTENTS AND SUMMARY

1. RESEARCH FOR LIGHT-WATER-MODERATED REACTORS

1.1. *THE POOL CRITICAL ASSEMBLY: A DESCRIPTION OF THE FACILITY AND THE INITIAL CRITICAL EXPERIMENTS*

E. B. Johnson and K. M. Henry 3

A relatively low-power reactor research facility, identified as the Pool Critical Assembly (PCA), has been installed in one end of the pool at the Bulk Shielding Facility. It consists of a pool-type reactor which can use either BSR or ORR fuel elements along with BSR-type control rods. The initial critical experiments were with arrays of ORR elements (93.2% U^{235}-enriched), some containing 168 g of U^{235} per element and others containing 140 g of U^{235} per element. The critical masses for the various assemblies are presented.

1.2. *EFFECT OF LARGE VOIDS IN THE REFLECTOR OF THE POOL CRITICAL ASSEMBLY ON REACTIVITY*

A. B. Reynolds 7

Preparations are nearly complete for a series of experiments with the PCA to measure the effect of large voids in the reflector of a reactor. Voids of various sizes will be simulated by the separation of water-filled Plexiglas boxes which will be contained in an aluminum tank placed against one face of the reactor core. A method for calculating the reactivity effect of a void in a reflector is being developed.

1.3. *A CALCULATION OF THE ENERGY SPECTRUM AND ANGULAR DISTRIBUTION OF GAMMA RAYS AT THE SURFACE OF THE BSF REACTOR*

L. A. Bowman, W. W. Dunn, R. H. Lessig, and D. K. Trubey 11

A new attempt has been made to calculate the energy spectrum of the gamma rays leaking from the BSF reactor by integrating the sources over the entire reactor and applying an attenuation kernel. The primary gamma-ray spectrum was grouped into six initial energy groups, E_0, of 0.5, 1, 2, 4, 6, and 8 Mev, and the collided and uncollided fluxes were calculated separately. NDA moments method results were then used to convert the fluxes to an energy spectrum, which compared favorably with a previously calculated spectrum, but was in the usual disagreement with experimental results. The angular distribution was estimated by computing the angular distribution of the uncollided flux and making the assumption that the collided flux was scattered straight ahead.

2. NEW REACTORS FOR THE BULK SHIELDING AND TOWER SHIELDING FACILITIES

2.1. *A UO_2–STAINLESS STEEL BULK SHIELDING REACTOR CORE (BSR-II)*

E. G. Silver 15

Some recent calculations pertaining to the UO_2–stainless steel Bulk Shielding Reactor II are presented, as well as a status summary on the project.

2.2. *A SPHERICAL TOWER SHIELDING REACTOR (TSR-II)*

C. E. Clifford and L. B. Holland 16

The latest design of the TSR-II, with its associated controls and 5-Mw water cooling system, and several studies supporting the design are presented. The critical mass has been set at 8.1 kg with 1.6% excess reactivity. Control will be achieved by moving six umbrella-shaped grids of Inconel-clad cadmium in the internal water reflector. A description of the first shield is also presented.

3. CRITICAL EXPERIMENTS

3.1. *DETERMINATION OF η OF U^{233} AND Pu^{239} BY COMPARISON OF REACTIVITY EFFECTS IN A FLUX TRAP CRITICAL ASSEMBLY*

D. W. Magnuson and R. Gwin 27

The values of η of U^{233} and η of Pu^{239} relative to the value of η of U^{235} were determined by a method in which reactivity contributions made by small samples of the fissionable isotopes and purely absorbing materials to a critical assembly were compared. The experimental assembly consisted of a water column located axially within a critical cylindrical annulus of uranyl fluoride solution. The samples were aqueous solutions and were inserted along the axis of the water column. The value of η of U^{233} determined by this method is 2.31 ± 0.06; the value of η of Pu^{239} is 2.03 ± 0.08.

3.2. *DETERMINATION OF η OF U^{233} BY COMPARISON OF CRITICAL EXPERIMENTS IN A 69.2-cm-dia SPHERE*

D. W. Magnuson 29

Critical assemblies of uranyl nitrate solutions of U^{233} and U^{235} in identical spherical geometry were compared to determine the value of η of U^{233} relative to the value of η of U^{235}. The resulting value for U^{233} was 2.268 ± 0.042.

3.3. *CRITICAL PARAMETERS FOR POISONED ANNULAR CYLINDERS CONTAINING AQUEOUS SOLUTIONS OF U^{235}*

J. K. Fox and L. W. Gilley 31

Experiments were performed to determine the critical parameters of aqueous solutions of 93.2% U^{235}-enriched uranyl fluoride contained in cylindrical annuli formed by various combinations of aluminum cylinders varying in diameter from 2 to 30 in. In all the experiments the inside cylinder was lined with a 20-mil-thick cadmium sheet and filled with water to a height of 48 in., and in some experiments a water reflector was used on the sides and bottom of the outside cylinder. The data indicate that for a solution having an $H:U^{235}$ atomic ratio of 50.4 the critical, infinitely high, reflected annulus would have a minimum thickness between 2.5 and 3 in., while the unreflected annulus would have a thickness between 3.75 and 4.5 in. The corresponding thicknesses for a solution having an $H:U^{235}$ atomic ratio of 309 would be between 3.5 and 4 in. for the reflected annulus and between 4.5 and 5.5 in. for the unreflected annulus.

3.4. *CRITICAL EXPERIMENTS WITH ARRAYS OF ORR AND BSR FUEL ELEMENTS*

J. K. Fox and L. W. Gilley 34

Critical experiments were performed with ORR and BSR fuel elements to determine safe arrays in which the elements could be handled and stored. The data indicate that the optimum spacing for criticality of 168-g ORR elements in water is 0.2 in. between locating bosses and that an infinite array of vertically placed elements one element high would probably be subcritical with a $1\frac{1}{2}$-in. spacing between locating bosses. For uniform arrays of adjacent elements in water, variation in the fuel loading per element between 140 and 200 g made very little difference in the critical mass. When 132 elements with an average loading of 160 g per element were closely packed in water in an 11 by 12 element array in which the rows were separated with 20-mil-thick cadmium sheets, no appreciable source neutron multiplication was observed; nor was there any appreciable multiplication when both the cadmium sheets and the water moderator were removed and the array was surrounded with a 12-in.-thick paraffin reflector. A two-row slab-shaped array with twenty-four 200-g center elements and fourteen 168-g elements on each end, all spaced 0.2 in. between locating bosses, was subcritical, and it appears that two infinitely long rows of 168-g elements would be subcritical.

3.5. *CRITICAL EXPERIMENTS WITH 2.09% U^{235}-ENRICHED URANIUM METAL PLATES IN WATER*

J. K. Fox, J. T. Mihalczo, and L. W. Gilley 37

Experiments were performed with 2.09% U^{235}-enriched uranium metal plates in a light-water-moderated and -reflected assembly. Each plate was 30 in. long, $3\frac{1}{8}$ in. wide, and $\frac{1}{4}$ in. thick and contained 7.09 kg of uranium. In the first assemblies the plates were arranged in rows with edges adjacent, and the

spacing between rows was varied from $\frac{5}{8}$ to $1\frac{1}{8}$ in. The optimum spacing was about $\frac{7}{8}$ in. With the spacing between rows maintained at $\frac{7}{8}$ in., the spacing between the edges of the plates was varied from 0 to $\frac{5}{8}$ in. The optimum spacing between edges was $\frac{5}{16}$ in. The minimum critical mass in these assemblies was 6.74 kg of U^{235}.

3.6. *SOME STUDIES OF WATER, STYROFOAM, AND PLEXIGLAS REFLECTORS*

J. K. Fox and L. W. Gilley 38

The reflecting properties of water, Styrofoam, and Plexiglas were studied in critical experiments with 6-in.-thick slabs of aqueous solutions of UO_2F_2 enriched to 93% in U^{235}. It was found that Styrofoam is significantly less effective than water as a neutron reflector, since the height of a slab with an effectively infinite Styrofoam reflector (except on top) was reduced by only about 20% from that of the unreflected slab, while the height of a slab with an effectively infinite water reflector was reduced by more than a factor of 3. The effects of placing water, Styrofoam, and Plexiglas between two-slab assemblies, both unreflected and water-reflected, were also investigated.

3.7. *HOMOGENEOUS HYDROGEN-MODERATED CRITICAL ASSEMBLIES WITH 2% U^{235}-ENRICHED URANIUM*

J. J. Lynn, J. T. Mihalczo, and W. C. Connelly 40

A series of experiments with blocks of 2% U^{235}-enriched mixtures of uranium tetrafluoride (UF_4) and paraffin ($C_{25}H_{52}$) is in progress. Thus far experiments have been performed with two mixtures, one containing 92.1 wt % UF_4 and the other containing 88.6 wt % UF_4, corresponding to $H:U^{235}$ atomic ratios of 195 and 294, respectively. Both cylindrical and parallelepipedal geometries were assembled, some of which were surrounded with an effectively infinite reflector of paraffin and Plexiglas. In two additional experiments assemblies with effective $H:U^{235}$ atomic ratios of 245 and 400 were investigated.

3.8. *CRITICAL PARAMETERS OF URANIUM SOLUTIONS IN SIMPLE GEOMETRY*

J. K. Fox, L. W. Gilley, R. Gwin, and J. T. Thomas 42

Some data are presented describing the critical conditions of spherical volumes of aqueous solutions of U^{233} and U^{235}.

4. FISSION PHYSICS

4.1. *THE ENERGY SPECTRUM OF PROMPT GAMMA RAYS ACCOMPANYING THE THERMAL FISSION OF U^{235}*

R. W. Peelle, F. C. Maienschein, and T. A. Love 45

A preliminary energy spectrum of prompt gamma rays emitted in the thermal-neutron fission of U^{235} has been obtained for the region from 0.3 to 10 Mev. Gamma rays in this interval are summed to indicate a total energy release of 7.2 ± 0.8 Mev per fission.

4.2. *CHARACTERISTICS OF FISSION-PRODUCT GAMMA RAYS EMITTED BETWEEN 5×10^{-8} AND 10^{-6} sec AFTER THERMAL FISSION OF U^{235}*

F. C. Maienschein, R. W. Peelle, and T. A. Love 47

Gamma rays have been observed in the time interval from 5×10^{-8} to 10^{-6} sec after fission. The number observed with a single-crystal spectrometer was about 6% of the number of prompt fission gamma rays. Pulse-height spectra for various times after fission and time distributions for selected energy groups are presented. The gamma rays are assumed to arise from isomeric transitions in fission products since beta decay with such short half lives would be energetically forbidden.

4.3. *CHARACTERISTICS OF FISSION-PRODUCT GAMMA RAYS EMITTED FROM 1 TO 1800 sec AFTER THERMAL FISSION OF U^{235}*

W. Zobel, T. A. Love, G. M. Estabrook, and R. W. Peelle 50

A new matrix has been constructed to aid in the analysis of the data collected during the fission-product gamma-ray experiment. The results of an analysis in which this matrix was used are presented.

5. EXPERIMENTAL REACTOR PHYSICS

5.1. AN INVESTIGATION OF THE SLOWING DOWN OF FISSION NEUTRONS IN WATER

T. V. Blosser, D. K. Trubey, and E. P. Blizard 55

In an attempt to resolve the discrepancy between the experimentally determined age of fission neutrons to indium resonance energy in water and the computed age, an experiment is being performed in the water tank at the ORNL Graphite Reactor thermal column to investigate various effects inherent in the experiments. These include the effect of the water-graphite boundary, the effect of the detector on the flux detected, the effect of the size of the fission source, and the effect of the detector on the flux impinging on the source. It has already been established that the effect of the cadmium covers on the indium foil detectors varies with the source-detector separation distance.

5.2. TIME-DEPENDENT NEUTRON DIFFUSION MEASUREMENTS

G. deSaussure and E. G. Silver 59

The pulsed-neutron method is being used to determine the diffusion parameters of thermal neutrons in crystalline moderators as a function of the temperature of the material. Precise results have been obtained for room-temperature beryllium. Preliminary results have also been obtained for beryllium at liquid-nitrogen temperature.

5.3. A 300-kv PARTICLE ACCELERATOR

J. D. Kington 61

A 300-kv particle accelerator has been constructed for the BSF, and initial operation has been surprisingly free of difficulties. The accelerator will be used to supply neutrons for the time-dependent neutron diffusion experiment and to supply neutrons and gamma rays for spectrometer calibrations.

6. REACTOR THEORY

6.1. RESONANCE ABSORPTION OF NEUTRONS IN NUCLEAR REACTIONS

L. Dresner 65

A detailed theoretical study has been made of resonance absorption of neutrons in homogeneous media for the "narrow resonance" approximation and in heterogeneous media for both the "narrow resonance" and "infinite mass absorber" approximations. The study included a statistical treatment of unresolved resonances and an investigation of the effect of fluctuations in the widths on resonance absorption cross sections.

6.2. ON THE CONNECTION BETWEEN NEUTRON FLUX AND SLOWING-DOWN DENSITY

L. Dresner 66

Various approximate connections between neutron flux and slowing-down density have been suggested. The validity of these approximations is investigated by comparison with a particular class of slowing-down problems in which the resonance escape probability can be calculated exactly.

6.3. COMPARISON OF THEORETICAL STUDIES OF UNREFLECTED AQUEOUS U^{235} CRITICAL ASSEMBLIES WITH EXPERIMENTS

R. Gwin, R. H. Lessig, D. K. Trubey, and A. M. Weinberg 68

The empirical kernel method for treating bare critical systems is discussed and is utilized to predict the material buckling of aqueous U^{235} bare reactors in an effort to clarify the age discrepancy. These results are compared with the critical geometric buckling as derived from experiment. In the comparison it is found that an uncertainty regarding the proper experimental extrapolation distance arises and prevents an unambiguous comparison.

6.4. *A CALCULATION OF THE INFINITE MEDIUM NEUTRON MULTIPLICATION FACTOR IN A U^{235}-H_2O SOLUTION*

D. K. Trubey and R. H. Lessig 73

The infinite medium multiplication factor has been computed for $U^{235}O_2$-H_2O solutions (up to 480 g of U^{235} per liter) as a function of neutron energy.

6.5. *THE EFFECT OF EPITHERMAL FISSION ON AQUEOUS HOMOGENEOUS REACTORS*

S. Terasawa 78

In light-water-moderated reactors epithermal fissions become important as the concentration of fissionable material increases. The magnitude of the effect for U^{235} and U^{233} light-water-moderated reactors is estimated by use of a very simple model and values of numerical integrations of BNL-325 cross sections.

6.6. *CALCULATIONS OF NEUTRON AGES IN VARIOUS MEDIA*

R. R. Coveyou and J. G. Sullivan 82

The Oracle Monte Carlo neutron age code, Chrones, has been used to compute the ages of neutrons from monoenergetic sources to indium resonance, as a function of source energy, in infinite media of Be, BeO, H, O, C, C + H_2O, CH_2 (oil), $C_{12}H_{10}$ (diphenyl), D_2O, and H_2O. A typical plot for water is presented. The ages of neutrons from fission spectrum sources in these media and in various H_2O-D_2O mixtures have also been calculated. The application of the Corn Pone and the O5R codes to age calculations is discussed.

6.7. *CORN PONE: A MULTIGROUP, MULTIREGION REACTOR CODE*

W. E. Kinney, R. R. Coveyou, and J. G. Sullivan 84

The Edit Routine of Corn Pone, which is nearly complete, reports the multiplication constant and input data for each case. Events, sources, cross sections, flux integrals, neutron balance, fluxes, and currents may be edited if desired. New formulas for the end-point fluxes at region interfaces are being used in the Integration Routine to eliminate group-to-group oscillations of the flux. A version of Corn Pone has been written which solves the second-order approximation difference equations. Corn Pone has been used to estimate the effect of source plate absorption on the age of fission neutrons in light water. The calculations indicated an increase of 0.12 cm^2 in the age due to absorption in an infinite slab source whose thickness and composition were the same as those of the source plate of the Hill, Roberts, and Fitch age experiment.

6.8. *THE OAK RIDGE RANDOM RESEARCH REACTOR ROUTINE (O5R): A GENERAL-PURPOSE MONTE CARLO CODE FOR THE IBM-704*

R. R. Coveyou, J. G. Sullivan, H. P. Carter 87

A general-purpose Monte Carlo reactor code is being developed for the IBM-704. The immediate purpose of the code will be to facilitate the analysis of the problems which arise in the calculations and measurements of the age of neutrons in water.

6.9. *CROSS-SECTION TAPES FOR IBM-704*

J. G. Sullivan 87

The Oracle master cross-section tape has been transcribed for use on the IBM-704. The routines producing the Oracle Monte Carlo cross-section tape from the master cross-section tape have been translated into the IBM-704 language so that the Monte Carlo tape for the IBM-704 can be prepared for use at any time.

7. SHIELDING RESEARCH

7.1. *MONTE CARLO CALCULATION OF GAMMA-RAY DOSE RATES RESULTING FROM NEUTRON CAPTURES IN AIR*

F. L. Keller, C. D. Zerby, and W. W. Dunn 91

A Monte Carlo calculation of the gamma-ray fluxes and dose rates resulting from neutron captures in air was performed, in which the source was assumed to be monoenergetic and both the source and detector were assumed to be suspended in an infinite body of air. The neutron source was taken to be either a point isotropic or a line-beam source, and the problem was idealized to that of determining the dose rate and angular distribution of capture gamma rays at the detector. For the point isotropic source and a 50-ft separation distance it was found that the dose rate varied with the neutron source energy approximately as $E^{-1/3}$. Curves for the various monoenergetic line-beam sources and a 65-ft separation distance plotted as a function of the beam angle were relatively flat over the region from 30 to 180 deg, becoming flatter as the source energy increased.

7.2. *STUDY OF GAMMA RAYS PRODUCED BY NEUTRON INTERACTIONS IN AIR*

C. E. Clifford, V. R. Cain, and F. J. Muckenthaler 94

An experiment was performed at the Tower Shielding Facility to study the production of secondary gamma rays in air by thermal-neutron capture in nitrogen and by the inelastic scattering of fast neutrons. A beam of neutrons from the TSF reactor irradiated a cone of air, and the gamma rays resulting from neutron interactions within the cone were observed by a gamma-ray spectrometer 52 ft from the reactor. The ratio of the nitrogen capture gamma rays observed to the other gamma rays observed was varied in some experiments by covering the reactor beam with boron-impregnated Plexiglas, which reduced the number of low-energy neutrons emitted by the beam. The difference between the measurements was then used to separate the pulse-height spectrum associated with nitrogen capture gamma rays from the spectrum associated with other sources. The spectrum remaining after the subtraction of the capture gamma-ray spectrum was presumed to be due to inelastically scattered fast neutrons.

7.3. *ANALYSIS OF THE RECENT TSF SECONDARY GAMMA-RAY EXPERIMENT*

F. L. Keller and O. S. Merrill 99

A calculation was performed to obtain predicted pulse-height spectra of capture and inelastic scattering gamma rays which could be compared with the experimental spectra presented in Sec. 7.2. While experimental cross sections were available for the calculation of the nitrogen capture gamma-ray spectrum, many of the cross sections used to predict the spectrum of inelastic scattering gamma rays were theoretical. In spite of this the calculated and experimental pulse-height spectra were in agreement.

7.4. *LTSF STUDY OF SECONDARY GAMMA-RAY PRODUCTION IN LEAD*

J. M. Miller 104

A study of the production of secondary gamma rays in lead was made with lead thicknesses that varied from 1 to 9 in. The lead was followed by either an oil medium or a borated water medium in which gamma-ray dose-rate measurements were made. From these tests it appears that the first 3 in. of lead attenuated most of the primary gamma rays from the LTSF source plate; further, the total dose rates at fixed distances from the source were not affected when the lead thickness was increased beyond 3 in. The measurements in the borated water were a factor of 3 lower than the dose rates in the oil in the region close to the lead and were a factor of 13 lower approximately 120 cm beyond the lead.

7.5. *THERMAL-NEUTRON FLUXES MEASURED IN OIL AT THE LTSF: AN ERRATUM*

L. Jung 109

A corrected curve of thermal-neutron flux measurements in oil at the LTSF is presented. It is 16% higher than the curve presented in the previous annual report (ORNL-2389).

7.6. MONTE CARLO CALCULATION OF GAMMA-RAY DOSE-RATE BUILDUP FACTORS FOR LEAD AND WATER SHIELDS

L. A. Bowman and D. K. Trubey 110

The analysis of calculations of the penetration of monoenergetic, monodirectional gamma rays through stratified slabs has proceeded to the extent that the dose-rate buildup factors for normal incidence can be compared with a formula proposed by Kalos. These calculations involve 512 problems resulting from all combinations of eight different lead and water configurations, four total slab thicknesses (1, 2, 4, and 6 mfp), four energies for the incident gamma rays (1, 3, 6, and 10 Mev), and four angles of incidence (0, 60, 70.5, and 75.5 deg).

7.7. MONTE CARLO CALCULATION OF THE DEPOSITION OF GAMMA-RAY HEATING IN STRATIFIED LEAD AND WATER SLABS

L. A. Bowman and D. K. Trubey 115

Some typical plots of the heating results from the calculations discussed in Sec. 7.6 are presented as the per cent of the total energy incident upon the slab absorbed in a specified region. The results are compared with an empirical formula.

7.8. A MONTE CARLO CODE FOR THE CALCULATION OF DEEP PENETRATIONS OF GAMMA RAYS

S. K. Penny 118

A Monte Carlo code is being developed for the IBM-704 machine to calculate the angular and energy distributions of gamma rays at a point detector emitted from a monoenergetic, point isotropic or point monodirectional source embedded in an infinite homogeneous isotropic medium. The code is now in the debugging stage.

7.9. THE EFFECT OF ANISOTROPIC SCATTERING ON THE NEUTRON FLUX IN AIR

C. D. Zerby 119

For most calculations of neutron scattering in air, isotropic scattering in the center-of-mass system is assumed, although it does not represent the actual case. For purposes of comparison a calculation was performed in which anisotropic scattering was assumed. The results from the calculations indicate that the isotropic scattering method of calculation is conservative.

7.10. BREMSSTRAHLUNG SPECTRA IN SODIUM IODIDE AND IN AIR

C. D. Zerby and H. S. Moran 121

A calculation was performed to determine the spectra of bremsstrahlung radiation resulting from the degradation of electrons in sodium iodide and in air. The assumptions made, the equations used, and the results obtained are presented.

7.11. RADIATION TRANSMISSION THROUGH BORAL AND SIMILAR HETEROGENEOUS MATERIALS CONSISTING OF RANDOMLY DISTRIBUTED ABSORBING CHUNKS

W. R. Burrus 125

Shields consisting of randomly distributed absorbing chunks in a relatively transparent matrix must be from a few per cent to several hundred per cent greater in mass than homogeneous shields which give the same amount of attenuation. This is the result of radiation "channeling" in the spaces between the absorbing chunks. A method for calculating the transmission of radiation through heterogeneous shields has been developed, and a typical calculation for boral has been performed. The computed results are compared with experimental results.

7.12. A MONTE CARLO CALCULATION OF THE NEUTRON PENETRATION OF FINITE WATER SLABS

J. Hilgeman, F. L. Keller, and C. D. Zerby 127

Neutron dose-rate distributions beyond water slabs 1, 3, 4, and 6 mfp thick were calculated for plane monodirectional, monoenergetic sources incident on the slabs at angles of 0, 30, 60, and 75 deg. The source energies considered were 0.55, 1.2, 2, 4, 6, and 8 Mev. Typical dose-rate buildup factors are presented for all calculations for the 2-Mev source. The dose rates at the rear of the slabs resulting

from neutrons multiply scattered within the slabs were also calculated, and typical results for a 2-Mev source are presented.

7.13. A HIGH-ENERGY ACCELERATOR SHIELDING PROGRAM

C. D. Zerby 130

A high-energy accelerator shielding program has been initiated to perform calculations of the spatial and energy distributions of high-energy particles penetrating an idealized shield. The program will consist of two parts: the development of an IBM-704 machine code and a determination of the best differential cross-section data to be used in the calculations.

8. RADIATION DETECTOR STUDIES

8.1. THE MODEL IV GAMMA-RAY SPECTROMETER

G. T. Chapman and T. A. Love 133

A new gamma-ray spectrometer system is currently being fabricated for use at the Bulk Shielding Facility. The system will include a $9\frac{3}{8}$-in.-dia total absorption NaI(Tl) crystal detector, a lead-lithium alloy shield for the crystal, and a positioning device consisting of a bridge-type crane to support the shield and a small analog computer for indicating the detector position in the BSF pool. The development of the spectrometer has included considerable work to improve the response of the NaI(Tl) crystal. The use of an array of seven 3-in.-dia photomultiplier tubes has resulted in an improvement in the energy resolution of the crystal as compared with the previously used photomultiplier tube arrangements. The resolution obtained with photons entering the side of the crystal is consistently better than that obtained with the photons entering the conical end of the crystal.

8.2. A PULSE PREAMPLIFIER WITH CASCODE INPUT

T. A. Love, R. W. Peelle, and W. R. Burrus 135

A design is presented for a pulse preamplifier suited for application with certain nuclear detectors. A "cascode" input stage is used to reduce noise significantly, and a low-impedance output is provided by a "bootstrap" final stage. The resulting amplifier is more satisfactory than some designs in common use.

8.3. ENERGY RESPONSE OF THE HORNYAK SCINTILLATION NEUTRON DETECTOR

W. J. Fader 137

An investigation of the energy response of the Hornyak scintillation detector has been carried out. Predicted results have been compared with experimental results.

8.4. LUMINESCENCE EMISSION SPECTRA OF LITHIUM IODIDE SCINTILLATION CRYSTALS

H. G. Hanson, J. J. Manning, and R. B. Murray 138

A program for investigating the scintillation response of lithium iodide crystals to various charged particles has been initiated. As a first step the luminescence emission spectra of both unactivated and activated crystals excited by alpha particles, gamma rays, or the alpha-triton pair resulting from slow-neutron capture have been investigated as a function of temperature in the region between room temperature and liquid-nitrogen temperature. The luminescence spectrum was observed to be more dependent on the activator content and the temperature of the crystal than on the type of exciting charged particle.

8.5. THE $Li^6(n,\alpha)T$ CROSS SECTION AS A FUNCTION OF NEUTRON ENERGY FROM 1.2 TO 8 Mev

R. B. Murray, H. W. Schmitt, J. J. Manning 145

The cross section for the reaction $Li^6(n,\alpha)T$ has been measured as a function of neutron energy in the region $1.2 \leq E_n \leq 8$ Mev. The magnitude of $\sigma_{n,\alpha}$, as measured in this experiment, depends on the absolute value of $\sigma_{fiss}(U^{238})$, while the shape of the cross section vs energy curve depends on the known energy dependence of $\sigma_{fiss}(U^{238}$ or $Np^{237})$. Statistical and other point-to-point uncertainties range from ±5 to ±9%, while the over-all uncertainty in the absolute value of the cross section is ±7%. The cross section obtained from these measurements is consistent with that determined at other laboratories. The data presented here can be smoothly joined to the measured cross section above 12.5 Mev.

Part 1

RESEARCH FOR LIGHT-WATER-MODERATED REACTORS

1.1. THE POOL CRITICAL ASSEMBLY: A DESCRIPTION OF THE FACILITY AND THE INITIAL CRITICAL EXPERIMENTS

E. B. Johnson K. M. Henry

During the past year a relatively low-power reactor research facility, identified as the Pool Critical Assembly (PCA), was designed, fabricated, and installed by ORNL personnel. It consists of a light-water-moderated and -reflected pool-type reactor and is intended to augment the Bulk Shielding Reactor and the Oak Ridge Research Reactor programs by handling most of the low-power (up to 10 kw) experiments for these two reactors. Examples of such experiments are those for the ORSORT training classes, reactor safety studies, and other general determinations of reactivity effects. The PCA should approximate the nuclear characteristics of the BSR except that the fuel elements will be rotated 90 deg from those in the BSR.

Description of the PCA

The PCA, pictured in Fig. 1.1.1, is located in the north end of the pool of the Bulk Shielding Facility. The support structure for the core and control chambers is mounted on a plate anchored to the floor of the pool, and the support structure for the tops of the rod drives, the chamber lift tubes, and the trough for the power and signal cables is attached to the pool wall at the surface of the pool. The loading platform is located above the pool rail over the cable trough and the core. The control system, which is basically similar to that of the BSR, is located off the northwest side of the pool room.

The PCA was designed to receive fuel elements with either round (BSR-type) or square (ORR-type) end boxes. This is accomplished by means of "stacked" grid plates, the BSR grid plate (round holes) resting on top of the ORR grid plate (square holes). When a core consisting of ORR fuel elements is to be installed, the BSR grid plate is lifted off, making the ORR grid plate available.

Control of a core consisting of either BSR or ORR fuel elements is accomplished by means of four BSR-type control rods and associated drive mechanisms. The rods are moved within special control-rod elements. Three of the control rods contain boron carbide as the neutron-absorbing material and are designated as shim-safety rods. The fourth rod is a shell of type 347 stainless steel and is called the regulating rod. The shim-safety rods are supported and positioned by electromagnets. The regulating rod is attached directly to its drive mechanism and may be positioned either manually or by the servomechanism. The fuel elements through which these rods travel are identical, each containing about 70 g of U^{235} in nine fuel-bearing plates. When a control rod is completely withdrawn from a control-rod element, a 1 by 2.6 in. water space remains in the element and extends over the entire height of the fuel section. These special elements may be positioned in the ORR grid plate by the use of adapters which support the rod elements at the correct height for the ORR fuel elements. These same rod elements are used without adapters in the BSR grid plate.

Critical Experiments

The first series of critical experiments in the PCA was performed with ORR fuel elements, following preliminary nonnuclear testing of the control system both by members of the Reactor Controls Department and of the Neutron Physics Division. These tests were motivated by the desire for a critical assembly of the ORR fuel elements prior to their use in the ORR.

The PCA was taken to criticality for the first time on March 12, 1958. The initial critical loading consisted of the 4 BSR-type control rod elements and 18 ORR fuel elements, each containing about 168 g of U^{235} in 19 fuel-bearing plates. This loading represented an attempt to approximate a water-reflected 4 by 6 element array that was similar to an array contemplated as the initial loading of the ORR. The loading was two fuel elements short of a full 4 by 6 core and contained a total of 3307 g of U^{235} with an excess reactivity of about 1%. The extrapolated critical mass was 3200 g of U^{235}. Three other arrangements of the ORR 168-g elements were also assembled. Figure 1.1.2 shows these in outline, together with other pertinent information.

Figure 1.1.3 shows five core arrangements using ORR 140-g fuel elements and one arrangement using BSR 140-g elements. The observed difference in critical mass between the core using

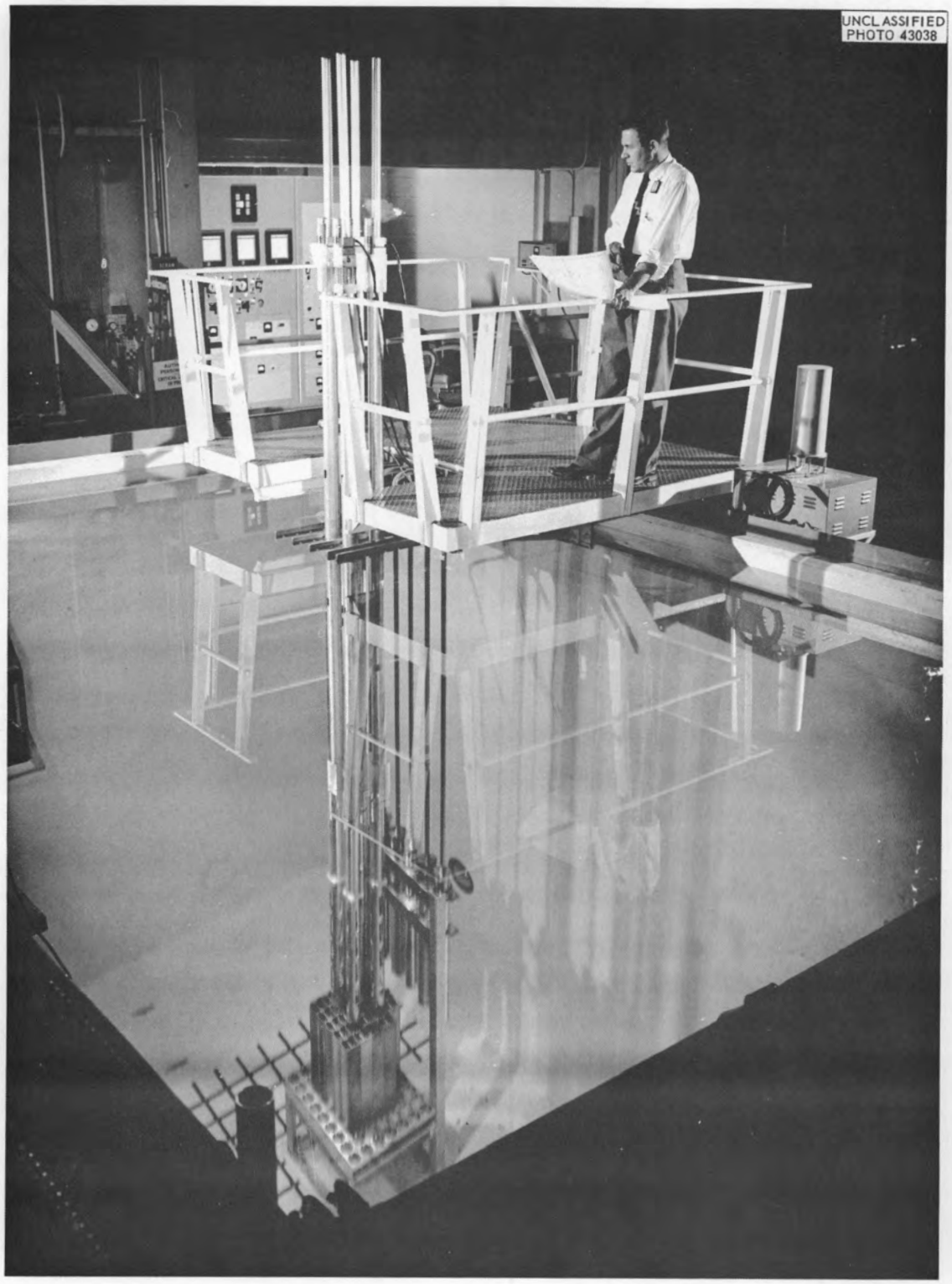

Fig. 1.1.1. The Pool Critical Assembly.

BSR elements (loading 10) and a similar core using ORR elements (loading 9) was 260 g of U^{235}. This difference may be predicted by assuming that the difference in critical mass is caused simply by the difference in the metal-to-water ratios of the two types of elements. The predicted result based on a calculated curve of age vs metal-to-water ratio[1] is 211 g. When an experimental curve[1] of age vs metal-to-water ratio is used, the result is 311 g. Both values are in reasonable agreement with the observed quantity.

[1] L. D. Roberts and T. E. Fitch, *The Slowing Down Distribution to Indium Resonance of Fission Neutrons from a Point Fission Source in Two Mixtures of Aluminum and Light Water, 1:1 and 1:2 by Volume*, ORNL-294 (Feb. 23, 1949).

UNCLASSIFIED
2-01-058-0-427

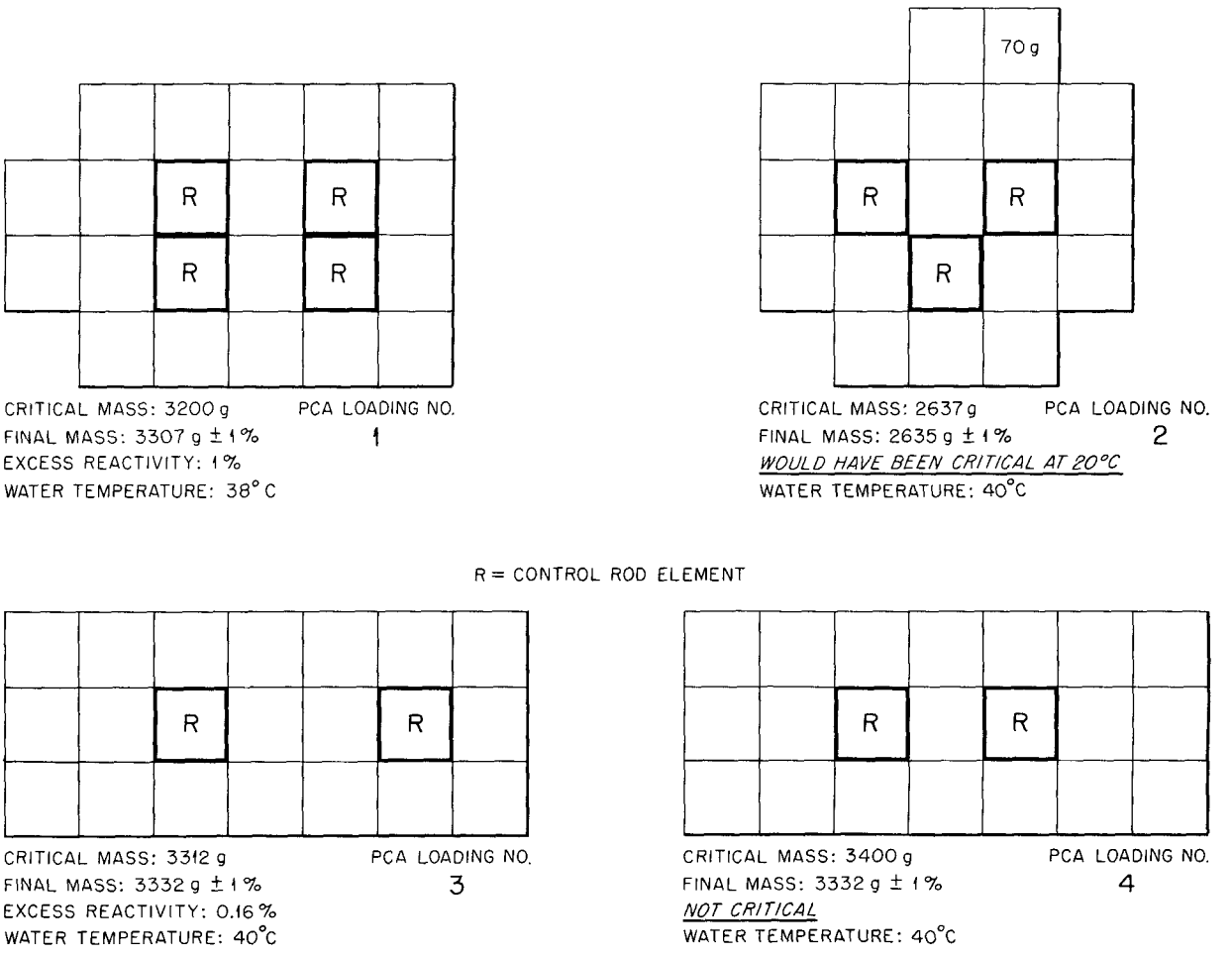

Fig. 1.1.2. PCA Loadings Using ORR 168-g Fuel Elements and BSR-Type Control Rod Elements.

UNCLASSIFIED
2-01-058-0-428

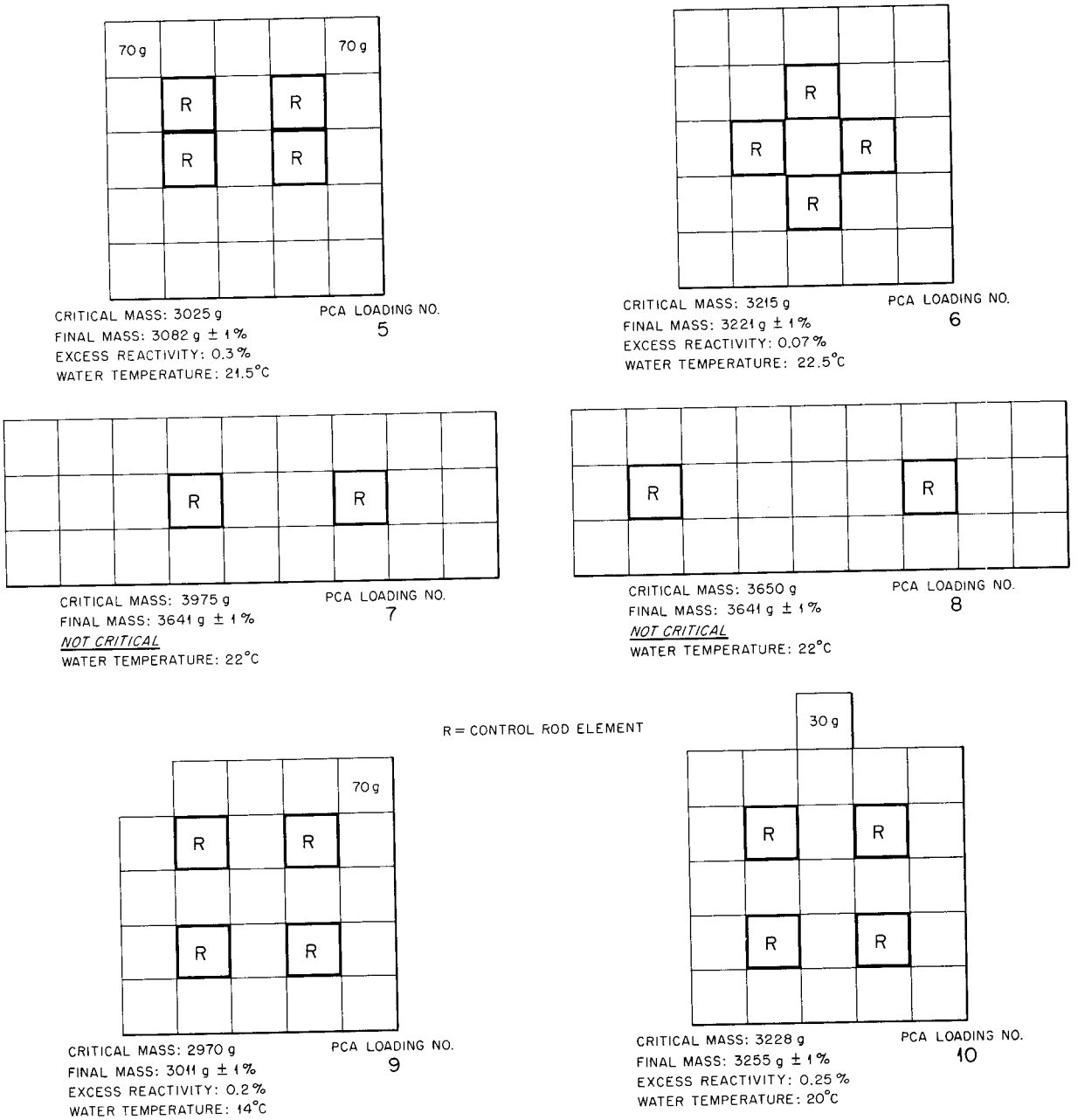

Fig. 1.1.3. PCA Loadings Using ORR 140-g Fuel Elements and BSR-Type Control Rod Elements. Loading 10 used BSR 140-g elements.

1.2. EFFECT OF LARGE VOIDS IN THE REFLECTOR OF THE POOL CRITICAL ASSEMBLY ON REACTIVITY

A. B. Reynolds[1]

Preparations are nearly complete for a series of experiments which will be performed at the Pool Critical Assembly (described in Sec. 1.1) to measure the effect of large voids in the reflector of a reactor. The experiments will consist of measurements of reactivity changes effected by the introduction of voids of various sizes in the reflector on one face of the reactor.

Methods for Simulating Voids

The simulated voids will be formed inside a large aluminum tank placed adjacent to one face of the PCA core. The dimensions of the tank, which is shown in Fig. 1.2.1, are approximately 6½ by 4 by 3 ft. The large flat surface of the tank shown in the foreground will be located adjacent to the PCA core in a position such that the horizontal mid-planes of the core and the tank are approximately coplanar.

Water-filled boxes made of ¼-in.-thick Plexiglas will be placed inside the tank. These boxes, which are shown in the background in Fig. 1.2.1 and in more detail in Fig. 1.2.2, have inside dimensions of 48 by 18 by 2 in. and are watertight except for holes located in the top so that the boxes can be filled with water. Initially they will be arranged in the tank in two 17-box layers, and when the two layers are together, the horizontal plane between them and the mid-plane of the reactor core will be coplanar. In the first experiment the entire tank, including the Plexiglas boxes, will be filled with water so that the core will be essentially water-reflected. The water will then be expelled from the tank by means of compressed air, leaving a void everywhere except at the positions of the water-filled boxes. Adjacent boxes in the two layers can then be separated so that voids will extend through the reflector to the reactor face.[2] An example of one arrangement of the boxes for a 10 by 10 by 48 in. void whose long center axis is an extension of the horizontal axis of the reactor core is shown in Fig. 1.2.2.

Planned Experiments

For the series of experiments presently planned, the problems to be studied can be divided into the following three general groups: a study of the effect of centrally located voids, a study of the effect of varying the location of a void of a fixed size, and a study of superposition of reactivity effects of several voids present on the same face. It is further planned to measure the reactivity effect of placing cadmium between several of the voids and the core.

Approximate Method for Calculating the Reactivity Effect of Voiding an Entire Face of a Core

The accurate calculation of the reactivity effect of a large void in the reflector of a reactor is very difficult. An approximate method for calculating the effect of voiding an entire face of a core has been developed, however. This approximate method, together with the major assumptions, is briefly outlined below.

The essential problem is the determination of the return-current boundary conditions at the void-core interface. Two-group diffusion theory was used to determine the critical eigenvalues for a reactor both completely water-reflected and with a void on one face represented by one of several possible return-current boundary conditions. The reactivity effect of the void was then determined from the critical eigenvalues, which were determined analytically by reducing the three-dimensional problem to a one-dimensional problem. Hence, the error introduced by neglecting corner effects was present.

The boundary condition of zero-return fast and thermal currents would correspond to an infinite void. A zero-return thermal current boundary condition could be obtained in practice by placing a cadmium slab adjacent to the core. The problem of more pertinent interest, however, is the problem for which return fast and thermal currents are present due to reflection from the walls of a void

[1]Massachusetts Institute of Technology.

[2]The original suggestion to simulate voids by the vertical movement of the water-filled boxes was made by P. E. Oliver of the ORNL Engineering and Maintenance Division.

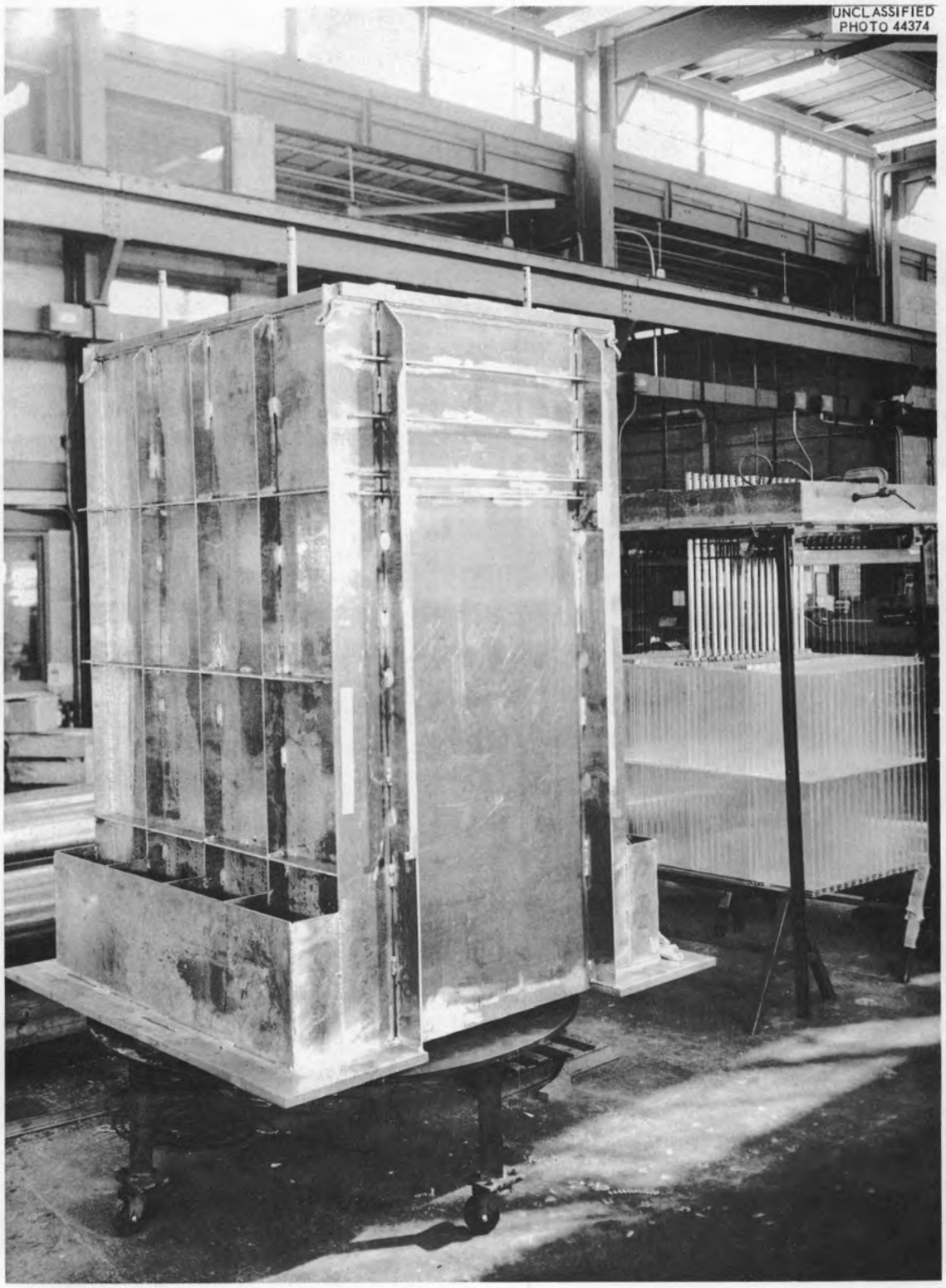

Fig. 1.2.1. Aluminum Tank for Experiments Investigating the Effects of Voids in the PCA Reflector.

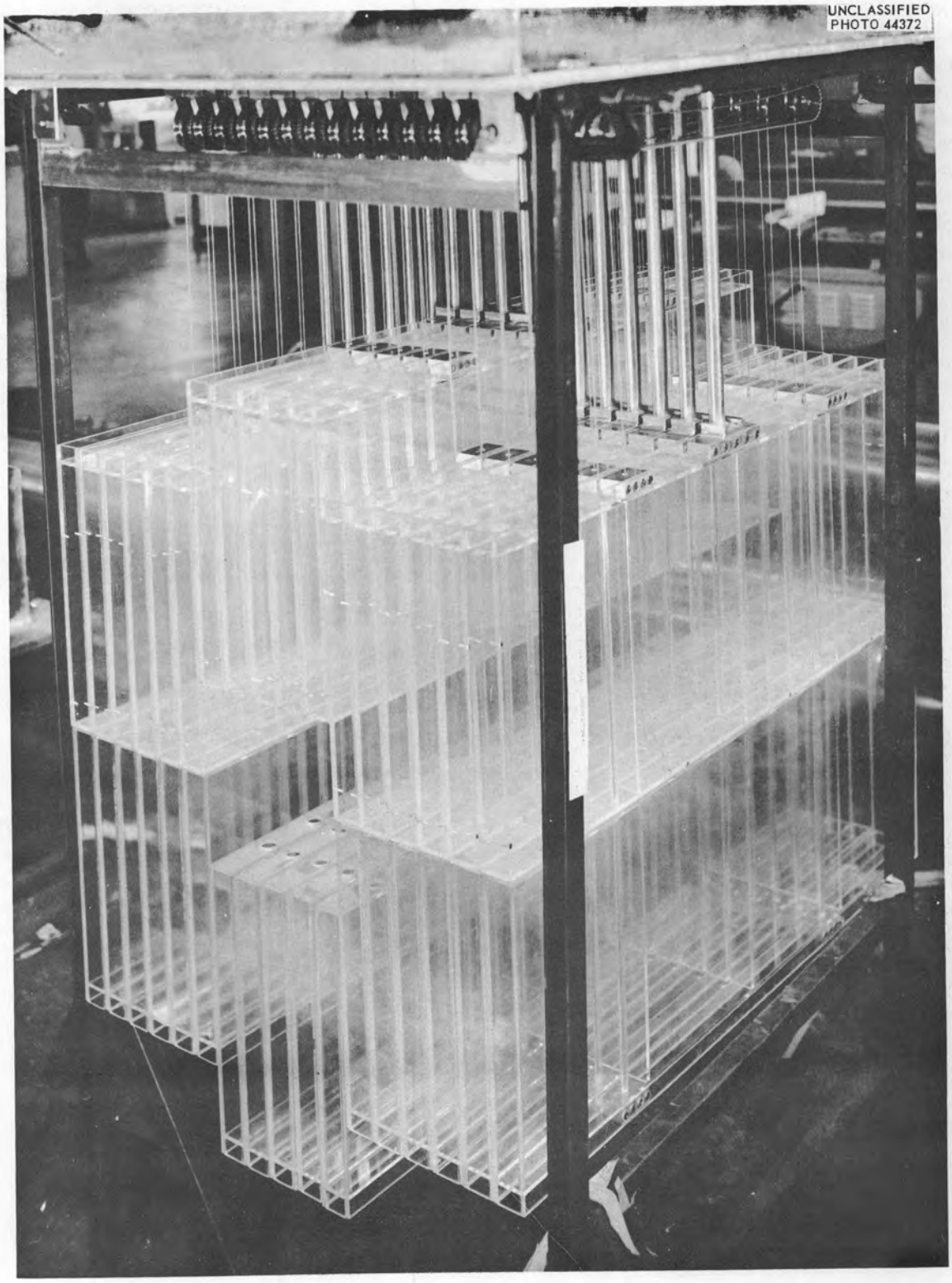

Fig. 1.2.2. Plexiglas Boxes for Experiments Investigating the Effects of Voids in the PCA Reflector. The boxes will be contained in an aluminum tank, and voids will be formed by the separation of adjacent water-filled boxes.

of finite size which covers an entire face of the core.

An attempt has been made to obtain the return fast and thermal currents from each surface of such a void by setting up neutron balances around each surface and employing the albedo concept. The neutron balances take into account multiple reflections in much the same way that heat balances handle multiple reflections from irradiating surfaces of enclosures in radiant heat transfer problems. Instead of the single albedo generally used in radiant heat transfer, a 2 by 2 matrix albedo was necessary to account for fast-neutron reflection, thermal-neutron reflection, and slowing down of fast neutrons to thermal before returning back across a surface. In order to obtain analytical solutions, several major assumptions, the effects of which are not known and are difficult to determine, were made. It was assumed that all radiation from each surface was isotropic. It was also assumed that the neutron source at each surface was constant over that surface even though the source at the void-core interface more nearly approaches a cosine distribution.

Preliminary results calculated with the method outlined above seem reasonable when compared with existing experimental measurements. For example, for a BSR 5 by 7 fuel element loading the measured reactivity effect of voiding the entire seven-element face was 2.6%.[3] With a cadmium slab between the core and the void the effect was increased to 2.9%. Preliminary values for a slightly different reactor calculated by the method outlined above were 4.2% for zero-return fast and thermal currents, 3.9% for a zero-return thermal current and a nonzero fast current, and 3.5% for nonzero fast and thermal currents. A conclusive test of the applicability of the method is not yet possible because of insufficient experimental results and the uncertainty of the effects of the major assumptions involved in the calculation.

[3]E. B. Johnson, K. M. Henry, and J. D. Flynn, *The Reactivity Effect of an Air Tank Against One Face of the Bulk Shielding Reactor*, ORNL-2179 (March 4, 1957).

1.3. A CALCULATION OF THE ENERGY SPECTRUM AND ANGULAR DISTRIBUTION OF GAMMA RAYS AT THE SURFACE OF THE BSF REACTOR

L. A. Bowman[1] W. W. Dunn[2] R. H. Lessig[2] D. K. Trubey

In the past it has not been possible to use directly the Monte Carlo shielding codes to check or predict the experimental results of shielding experiments performed with the BSF reactor. While theoretical calculations of the energy spectrum have been performed[3,4] for comparison with the experimentally measured gamma-ray spectrum,[5] there is only limited information on the angular distribution at the reactor surface.[6] A new attempt has been made to calculate the energy spectrum from primary gamma-ray sources and, in addition, to estimate the angular distribution of the gamma rays at the reactor surface.

The primary gamma-ray sources considered in this calculation were (1) prompt fission and capture gamma rays from uranium, (2) fission-product-decay gamma rays, (3) capture and decay gamma rays from aluminum, and (4) capture gamma rays from water. These sources were grouped into initial energy groups of 0.5, 1, 2, 4, 6, and 8 Mev. The uncollided flux in each energy group at a point on the center of the north face of the reactor was then computed as a function of the angles ϕ and θ, which describe the point with respect to the vertical and horizontal axes, respectively. The collided flux was determined for each energy group by multiplying the uncollided flux by the factor $[B(\mu R) - 1]$, where $B(\mu R)$ is the energy buildup factor. The energy distribution was then estimated by dividing the collided flux into contributions to that particular energy group and each lower energy group and by making the assumption that the collided flux had a differential energy spectrum of the type computed by NDA[7] for a point source through 1 mfp of water. It was further assumed that the collided photons were not changed in direction by collisions. Thus, the total flux in a particular direction, $\phi(\theta,\phi,E)$, was the sum of the uncollided flux for that energy group and that direction plus the collided contributions from each higher energy group. The total and uncollided fluxes for $\theta = 0$ were converted to an energy spectrum and plotted in Fig. 1.3.1 as a histogram. Also shown are the results of calculations by deSaussure[3,4] and the experimental results.[5]

The gamma-ray energy spectrum normal to the reactor surface, as calculated in this study, is in good agreement with previous calculations by deSaussure.[3,4] However, the present calculation is admittedly an overestimation, particularly in the low-energy range, since it was assumed that the collided flux, as calculated by the energy buildup factors, is all traveling in the outward direction.

The method of calculation is given in more detail in another paper,[8] along with the energy fluxes from all angles. Typical plots of the angular distribution are also included.

---

[1]On assignment from Wright Air Development Center.

[2]On assignment from U.S. Air Force.

[3]G. deSaussure, ORNL-2221, p 347 (1956) (classified).

[4]G. deSaussure, *Appl. Nuclear Phys. Ann. Prog. Rep. Sept. 1, 1957*, ORNL-2389, p 29; *A Calculation of the Gamma-Ray Spectrum of the Bulk Shielding Reactor*, ORNL CF-57-7-105 (July 31, 1957).

[5]F. Maienschein and T. Love, *Nucleonics* 12(5), 6–8 (1954).

[6]F. C. Maienschein, F. T. Bly, and T. A. Love, ORNL-1714, Parts I and II (Aug. 20, 1954) (classified).

[7]H. Goldstein and J. E. Wilkins, Jr., *Calculations of the Penetrations of Gamma Rays. Final Report*, NYO-3075 (June 30, 1954).

[8]L. A. Bowman *et al.*, *A Calculation of the Energy Spectrum and Angular Distribution of Gamma Rays at the Surface of the BSF Reactor*, ORNL CF-58-4-75 (April 15, 1958).

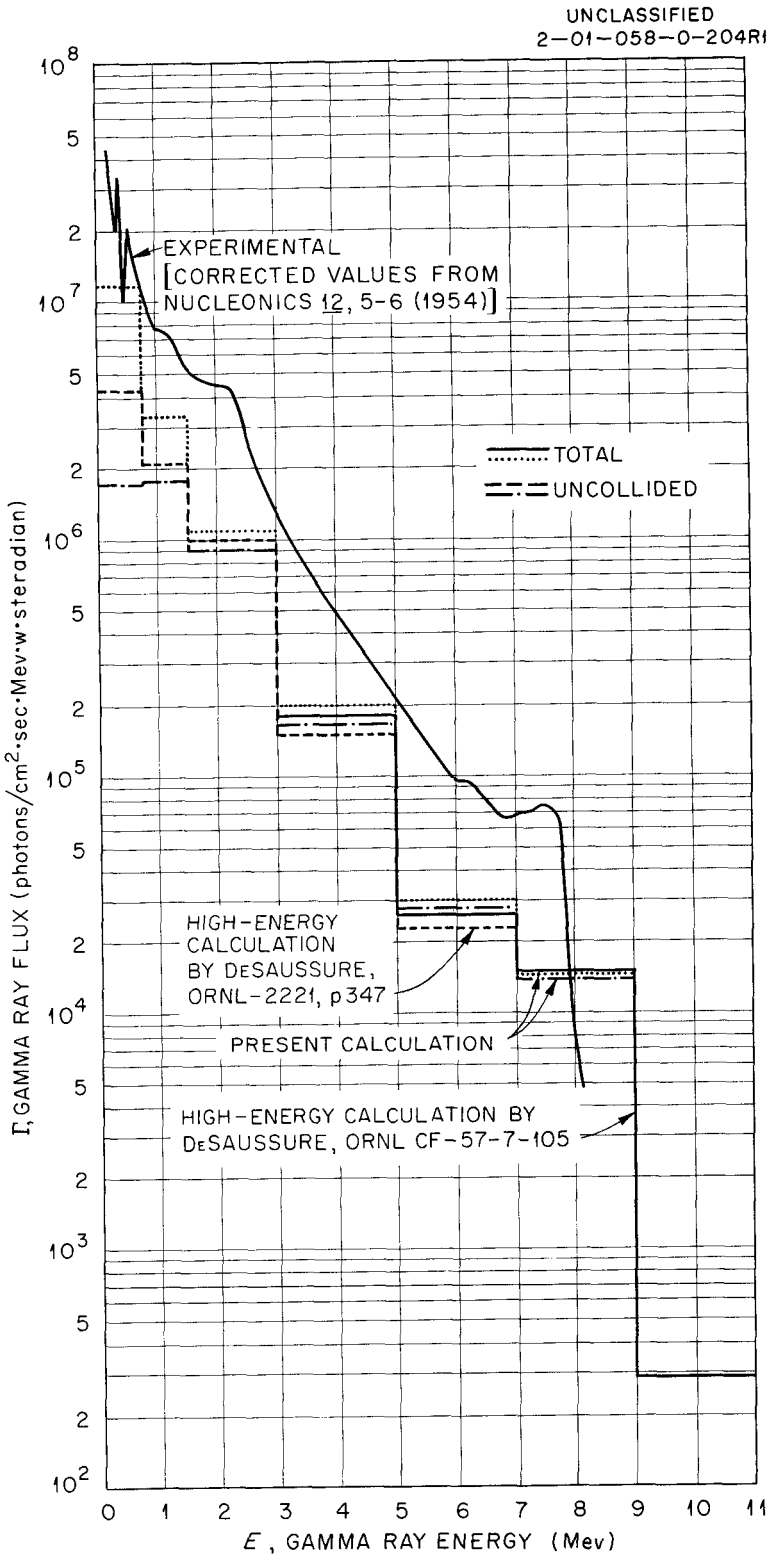

Fig. 1.3.1. Comparison of Calculated and Experimental Spectra of Gamma Rays at the Surface of the Bulk Shielding Facility Reactor ($\theta = 0$ deg).

Part 2

NEW REACTORS FOR THE BULK SHIELDING AND TOWER SHIELDING FACILITIES

2.1. A UO_2–STAINLESS STEEL BULK SHIELDING REACTOR CORE (BSR-II)

E. G. Silver

It was reported previously[1] that a UO_2–stainless steel core had been designed for the Bulk Shielding Reactor. This new core, which has been approved by the Advisory Committee on Reactor Safeguards and is now being fabricated, will be called the Bulk Shielding Reactor II (BSR-II). It will be used to ascertain the possible advantages of such a core for pool-type, low-power, research reactors.

The BSR-II has been described in detail in a report which was submitted to the Advisory Committee on Reactor Safeguards.[2] It will consist of a 15-in. cubical core of 25 plate-type fuel elements, four of which will be modified to accommodate four pairs of control plates. In order to cope with the short neutron lifetimes occurring in the reactor, the control plates will be spring-accelerated over the first portion of their travel, rather than being dropped by gravity only.

Most of the calculations required for the design of the BSR-II were included in the last report;[1] however, a few additional investigations have been carried out as described below.

The temperature rise in the BSR-II central fuel element caused by water loss from the core after shutdown was calculated on the basis of an extrapolation from an experiment performed with a BSR-I element. The result indicates that the temperature increase caused by fission-product heat generation is less than 500°C under the most severe conditions anticipated.

The hazard to areas away from the Laboratory after maximum irradiation due to a total dispersal of the fission products from the BSR-II was calculated for average day and night meteorological conditions. The contamination of water in nearby areas due to water dispersal of all the fission products was also calculated. However, the contingencies described were judged as not credible and therefore were not included in the safeguard report.[2]

The mechanical strength of the fuel elements and control-plate fuel elements against deformation or control-plate binding was calculated. The conclusions reached are summarized in Tables 2.1.1 and 2.1.2. These forces were calculated by assuming the minimum clearances permitted by the design tolerances and dimensions.

It is planned that a series of tests will be carried out with the entire reactor and control system at the SPERT-I Facility at Arco, Idaho, in order to determine the actual characteristics of the integral system with respect to the control of short positive-period excursions. The reactivity insertion to initiate such short periods will be accomplished by insertion of fuel by means of a modified control-plate drive which will insert either four or six fuel plates into the core.

Table 2.1.1. Forces Which Will Cause the BSR-II Elements To Yield at the Lower End Box

Type of Element	Force Applied Laterally at Top of Element (lb)	
	Force Applied Parallel to Fuel Plates	Force Applied Perpendicular to Fuel Plates
Standard element	820	284
Control plate element	1030	529

Table 2.1.2. Forces Which Will Cause Binding of BSR-II Control Plates

Type of Support	Force Applied Against Control Plate Channel Cover (lb)	
	Force Applied at Center Point	Force Applied Along Centerline
Simply supported	14	54
Rigidly Clamped	53	210

[1] E. G. Silver and J. Lewin, *Appl. Nuclear Phys. Ann. Prog. Rep. Sept. 1, 1957*, ORNL-2389, p 33–50.

[2] E. G. Silver and J. Lewin, *Safeguard Report for a Stainless Steel Research Reactor for the BSF (BSR-II)*, ORNL-2470 (July 16, 1958).

2.2. A SPHERICAL TOWER SHIELDING REACTOR (TSR-II)

C. E. Clifford L. B. Holland

The advantages of using a spherically symmetric reactor at the Tower Shielding Facility were discussed previously.[1] At the same time a description of a preliminary design of such a reactor was presented. Final design of the reactor, which will be identified as the Tower Shielding Reactor II (TSR-II), is now essentially complete. The several design changes which have been incorporated since the last report and other studies which have been carried out for the TSR-II are described below.

Mechanical Design[2]

The latest design for the TSR-II is shown in Fig. 2.2.1. The core has been modified slightly to provide more clearance for the thermal expansion that will occur when the reactor is operating at a power of 5 Mw. In the earlier layouts it was planned to place the lead-boral shield adjacent to the aluminum pressure tank. In order to ensure that the tank is not heated above a safe level by gamma-ray heating in the lead and neutron heating in the boral, it will be separated from the shield by a $\frac{1}{4}$-in.-thick layer of water. The lower portion of the lead-boral shield, which is hemispherical, will be supported by four lugs which engage slots in a ring on the tank wall at the horizontal mid-plane of the core. With this arrangement there will be sufficient room for the shield to expand downward or radially at the mid-plane with heating.

A 2-ft-thick shield of lead shot and water has been added above the central fuel elements to reduce the gamma-ray radiation leakage through the central cylinder. This will be especially important when the reactor is enclosed in a shield mockup. This lead-water shield, which can be seen in Fig. 2.2.1, will be penetrated by approximately 120 helical ducts through which the cooling water will flow. The gamma-ray leakage through this shield will never exceed the leakage through any shield used with the TSR-II. The shield shown above the core in the region between the reactor tank and the inner cylinder will be removable.

In order to facilitate removal and insertion of the fuel elements and the upper shielding, the inside diameter of the upper portion of the reactor tank has been increased from 36.75 in. to 39.75 in. In addition, the fission chambers have been moved outward in the upper region of the inner cylinder to provide more room for the control mechanism positioning and actuating devices, which will be housed in a turret atop the central cylinder region.

The design of the TSR-II is such that it can be encased in various shields. The first shield with which the reactor will be used will be a spherical shield having a beam hole both fore and aft. The entire assembly will be suspended from a platform, as shown in Fig. 2.2.2, and it can be rotated around the vertical axis so that the beam holes can sweep a horizontal plane. When the reactor is suspended in this manner, the cooling water will pass through a coaxial swivel joint before it enters and after it leaves the reactor tank.

The reactor and beam shield may also be suspended so that the beam holes will sweep a vertical plane. For this case, two 12-ft girder-like members will be attached to the side of the shield through an axle and bearings, and the cooling water will enter through a swivel fitting and the hollow axle of one support member and leave through a similar arrangement on the other support member. By alternately using the two beam holes, a beam can sweep the whole 360 deg in the vertical plane without tilting the reactor more than 90 deg from the vertical position.

Calculations have indicated that, with a 30-deg conical section removed from the shield, a 6775 ft-lb torque will be required to rotate the reactor and shield so that the removed section will sweep a vertical arc. A much smaller torque will be required to sweep the horizontal arc. A Char-Lynn torque booster working through a worm and 180-tooth gear will be used to rotate the reactor assembly. A torque booster under full load has performed satisfactorily in laboratory tests.

Control Mechanism[3]

The design of the control mechanism for the TSR-II has been completed, and a model has been successfully tested. The design is shown in

[1] C. E. Clifford and L. B. Holland, *Appl. Nuclear Phys. Ann. Prog. Rep. Sept. 1, 1957*, ORNL-2389, p 53.

[2] The mechanical design of the TSR-II is being done by the Engineering Department.

[3] The controls system for the TSR-II is being developed by the Reactor Controls Group.

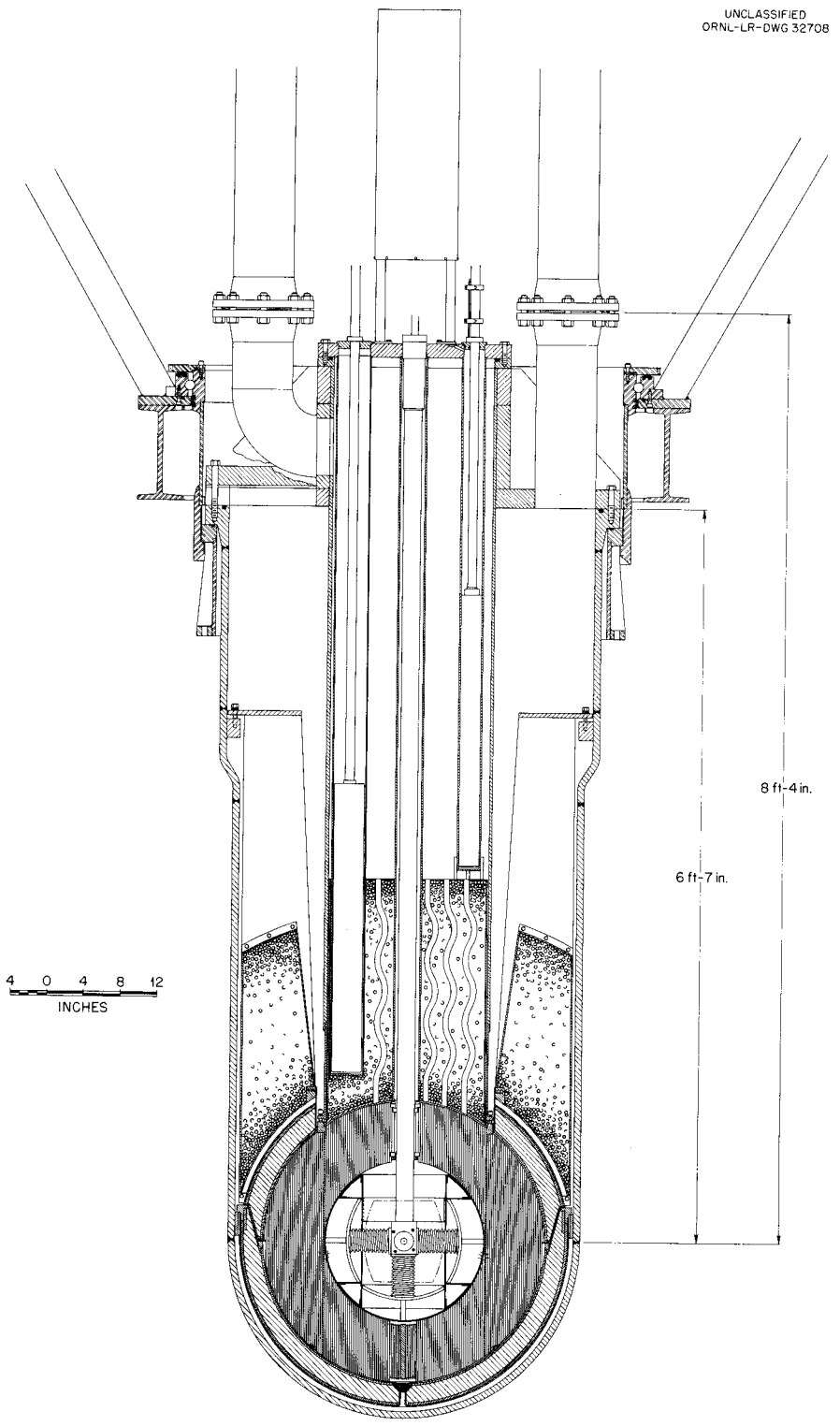

Fig. 2.2.1. TSR-II Design (Vertical Section).

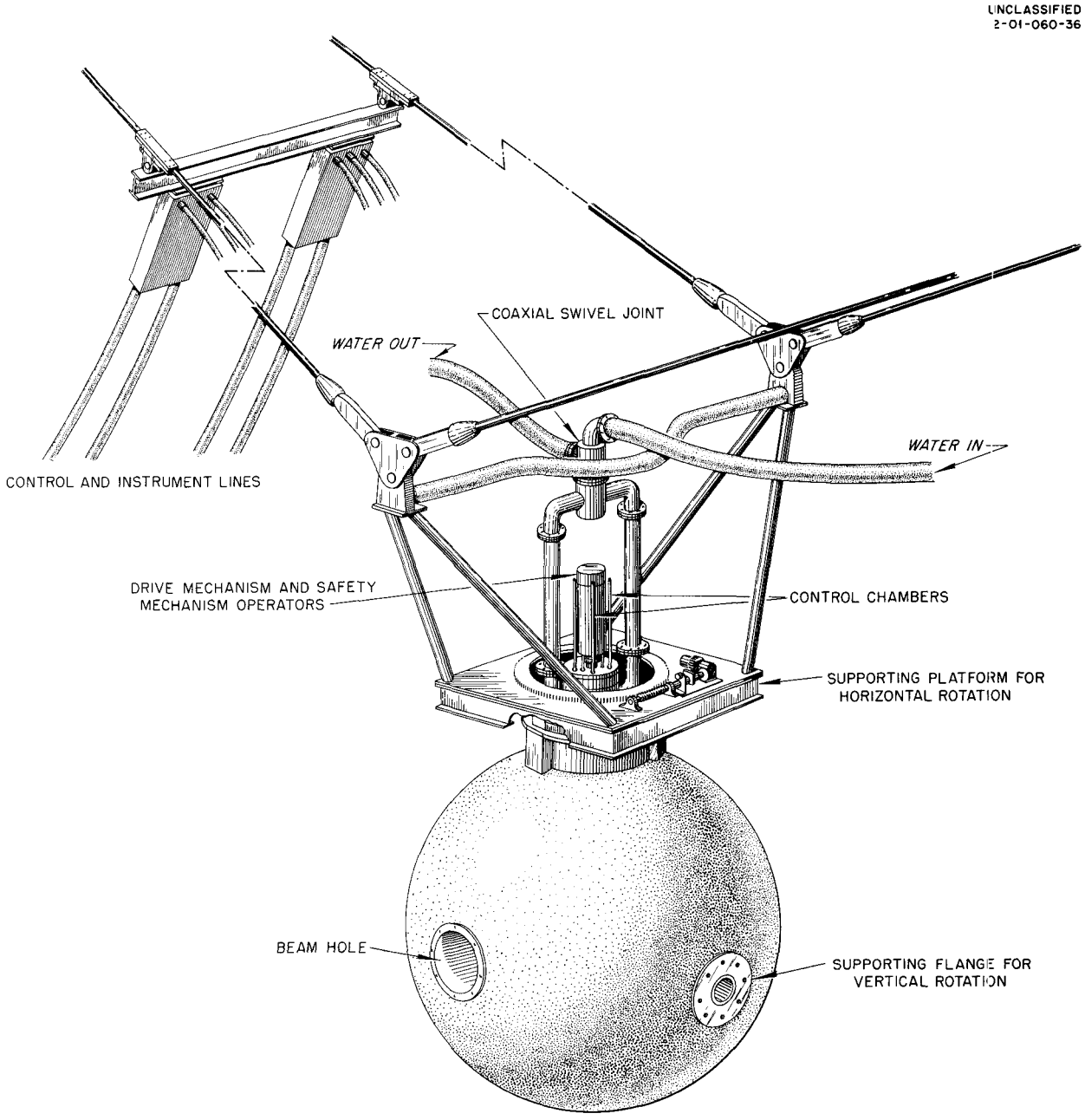

Fig. 2.2.2. TSR-II in Beam Shield.

Fig. 2.2.3. Normally the spring will hold the control grid against the fuel. Water will flow through the mechanism until the flow area through the piston is closed by the drive nut. The pressure will build up in the cylinder, and the control grid can then follow the drive nut to control the reactor. Interrupting or bypassing the water flow will scram the mechanism. Five control mechanisms will operate control grids for shim-safety purposes. A sixth grid for fine control will not scram. Each umbrella-shaped grid will consist of Inconel-clad cadmium ribbons.

An electrohydraulic transducer will be used to actuate the control mechanism. The purpose of the electrohydraulic transducer is to allow electrical control of the water pressure in the control mechanism with the standard ORNL magnet amplifier circuitry. As the reactor power level increases

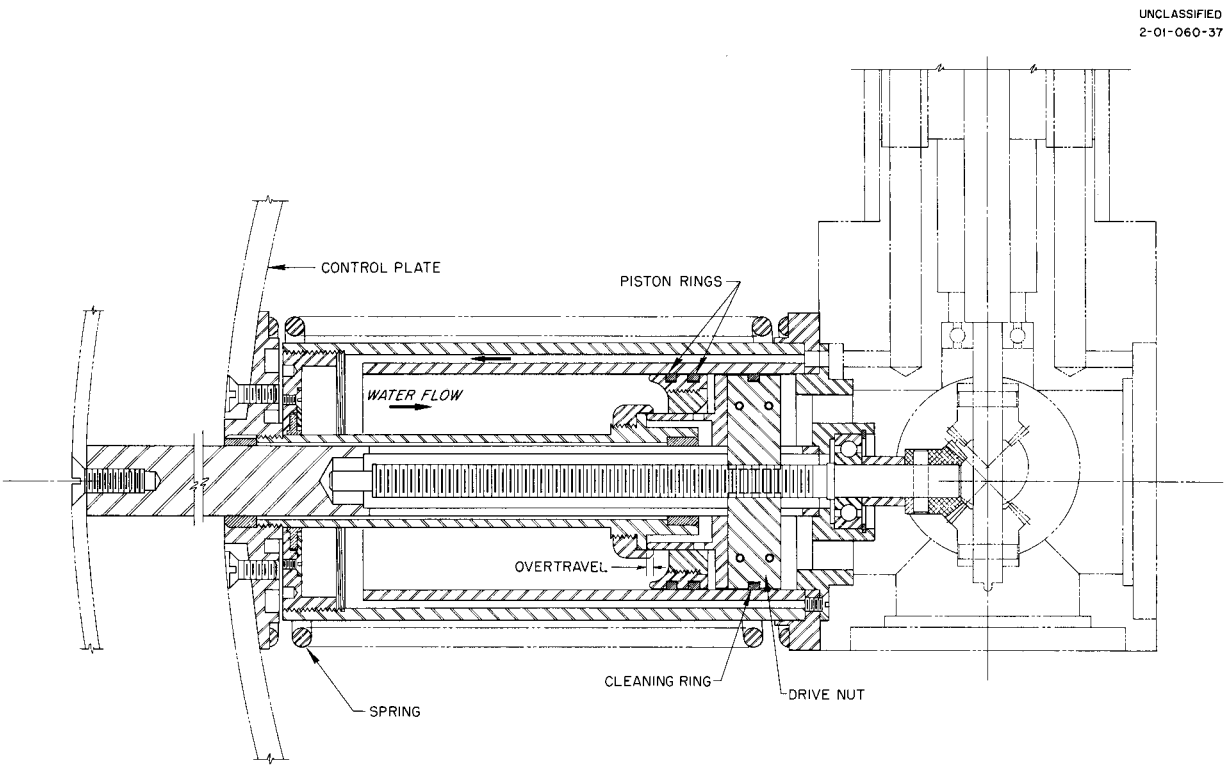

Fig. 2.2.3. TSR-II Control Mechanism.

above the maximum operating level, the transducer bypasses more water. It is so adjusted that at 150% of maximum power the control mechanism pressure is reduced to the scram level.

TSR-II Block Diagram[3]

The block diagram of the TSR-II is shown in Fig. 2.2.4. To permit the operation indicated in the circles on the diagram, all the conditions indicated in the blocks along a line from the control power to the circle must be satisfied. The conditions in the double line blocks are met by manual operation; all other conditions are automatic. The logic of the system falls into the general pattern of other ORNL reactors; however, many small differences were necessitated by the special nature of the TSR-II.

Nuclear Calculations[4]

Since the previous report,[1] a multigroup, multiregion reactor code (see Sec. 6.7) has become available. An adaptation of this code to a Goertzel-Selengut type has been used to make a number of further calculations for the TSR-II. The control plate effectiveness was recalculated, treating the control grids simply as thin regions or shells, as a function of separation distance from the fuel. The shape of the curve was in good agreement with the earlier Oracle calculations using the 3G3R code,[1] although it was a factor of 5.2 higher. The apparent discrepancy is due primarily to the difference in absorption cross section used for the shells.

In order to confirm the validity of the method used for this and other nuclear calculations, calculations were also performed for three critical experiments which were set up in finite slab geometry as shown in Fig. 2.2.5 (the figure shows only one-half of each configuration). Each fuel region consisted of a 4 by 6 array of standard BSR fuel elements, and boral sheets simulated the control plates. Clean, or nearly clean, experiments[5] were obtained for configurations A and B

[4]The nuclear calculations for the TSR-II were performed by M. E. LaVerne.

[5]These critical experiments were performed by D. F. Cronin, J. K. Fox, and L. W. Gilley.

UNCLASSIFIED
ORNL-LR-DWG 32707

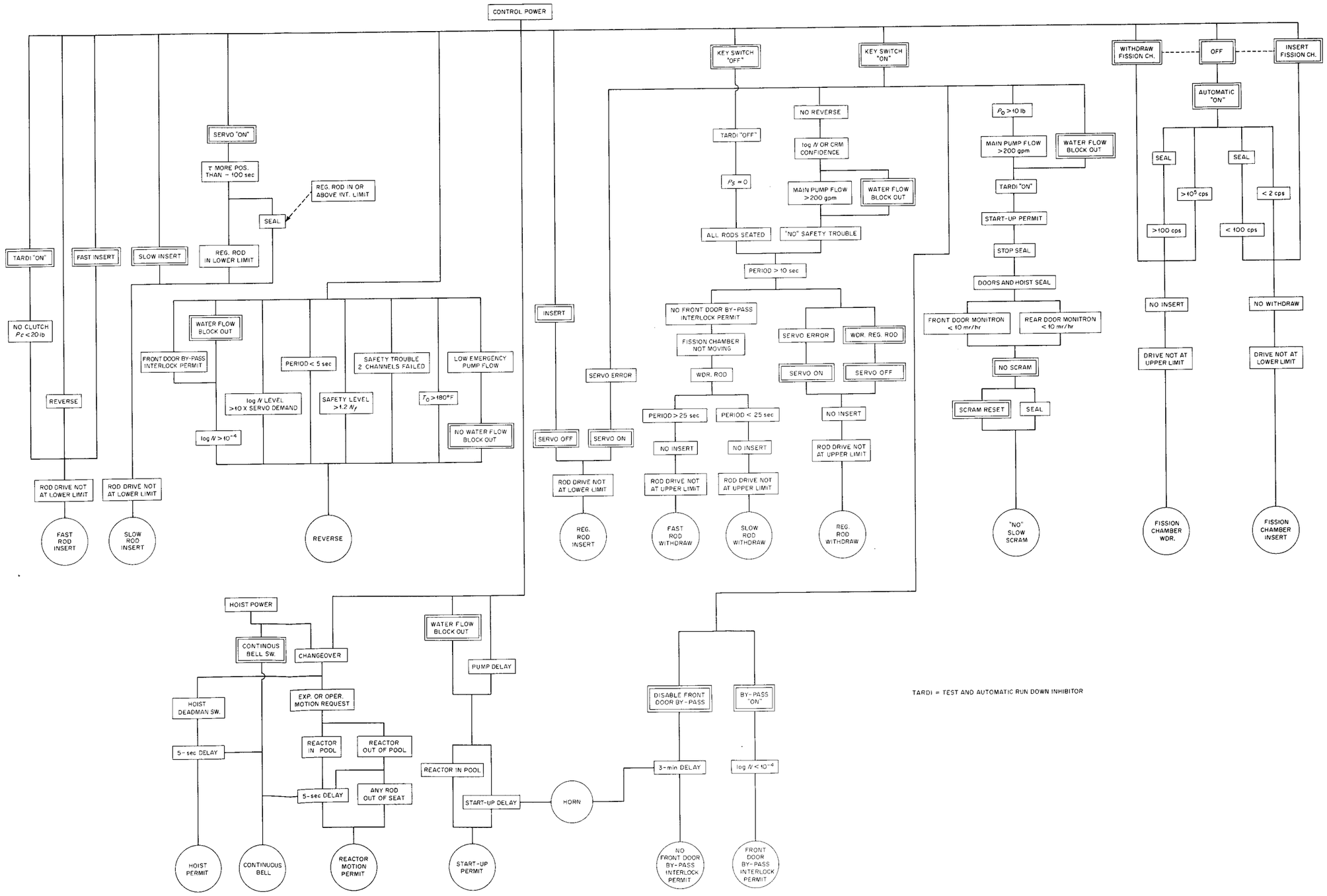

Fig. 2.2.4. Block Diagram of the TSR-II.

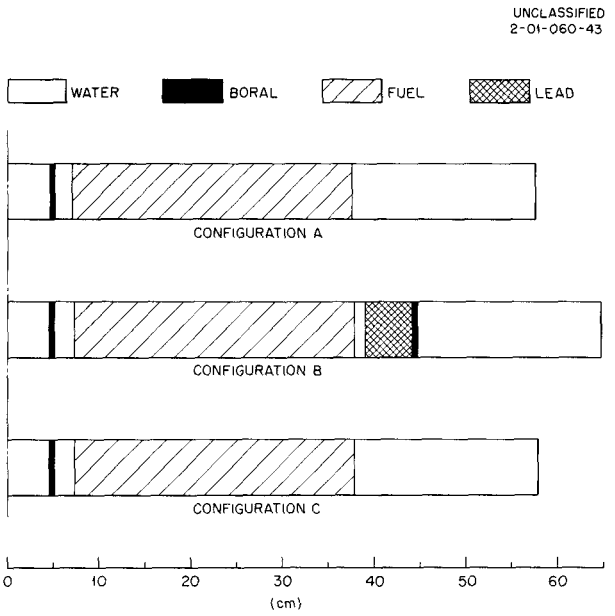

Fig. 2.2.5. Configuration for Critical Experiments.

by heating the water in the assembly tank and simultaneously withdrawing a cadmium rod to maintain the assembly critical. In configuration B, a portion of the rod (2.75¢ worth) was still inserted when the rod travel was used up.

Configuration C was set up to evaluate the effect on reactivity of removing the lead and boral layers. Because estimates of excess reactivity at room temperature for both configurations B and C were available from rod calibrations, configuration C was not heated to attain the "clean" state.

A comparison between experiment and calculation is presented in Table 2.2.1. The error for the three cases averages about 1%. The experimental k is the multiplication constant that would have been observed with the rod completely withdrawn, i.e., in the "clean" condition. Previously computed temperature coefficients were used to correct the calculated k for differences between experimental and calculational thermal base and density.

Core-void coefficients were computed for the change in the multiplication constant produced by deleting the water (but not the aluminum or uranium) from thin spherical annuli in the core. Temperature coefficients were also calculated for both density only and thermal base only changes. A summary of the reactivity coefficients is given below.

Average void coefficient for core	-2.15×10^{-4}% per cubic centimeter of void
Temperature coefficients	
Density coefficient	-1.39×10^{-2}%/°C
Thermal-base coefficient	$+0.62 \times 10^{-2}$%/°C
Net coefficient	-0.77×10^{-2}%/°C

Critical Mass[4]

Calculations and critical experiments have indicated that the TSR-II lead-boral shield does not measurably change the critical mass. Therefore, to obtain the critical mass of U^{235} for the TSR-II, a calculation was made for a clean, cold, water-reflected, spherical annulus with the TSR-II core dimensions and volume fractions. Sufficient U^{235} was added to increase the reactivity by 6.8%, which resulted in a U^{235} loading for the core of 8.1 kg.

Of the 6.8% increase in the reactivity, 1.5% is to cover the worth of the control plates in the fully withdrawn position, 0.3% is allowed for structural material in the core region, 1.4% is to cover the worth of fixed neutron absorber plates in the internal reflector region, 2.0% is to allow for error

Table 2.2.1. Comparison Between Calculated and Experimental Values of k

Configuration	Water Temperature (°F)	k		Corrections to Calculated k		Corrected k Calculated	Error (%)
		Experimental	Calculated	Density	Thermal Base		
A	108	1.0000	0.9897		0.0014	0.9911	0.9
B	118.9	1.0002	0.9872		0.0018	0.9890	1.1
C	73.4	1.0081	0.9921	0.0035	0.0002	0.9958	1.2

in the calculations, and 1.6% is the amount that can be controlled by the control plates. The 1.6% covers the following: 0.6% to counteract the negative temperature coefficient of reactivity from 40 to 180°F, 0.3% excess reactivity necessary to permit servo control, 0.6% to counteract xenon buildup for 8 hr of operation at 5 Mw, and 0.1% for short-time burnup of U^{235}. The 1.6% $\Delta k/k$ is approximately one-half of the reactivity worth of the safety plates.

Control Plate Effectiveness

The mechanical construction of the control grids does not duplicate the model used in the nuclear calculations, which was assumed to be a complete spherical shell that moved uniformly away from the fuel region. In order to determine the worth of the actual control device, each grid area was divided into rings with their common center at the center of the plate. The worth of each ring was then determined as a function of its normal position from the core. The total worth of the plate was determined by summing the worth of all areas of each plate for a given separation distance between the core and the center of the plate. After the control plate worth was established, the thermal-neutron flux distribution throughout the reactor (see Fig. 2.2.6) and the source distribution in the core (see Fig. 2.2.7) were determined from the multigroup calculations with the control shell positioned for operation at 5 Mw.

Hydrodynamics Studies[6]

A full-scale, quarter-sphere model has been constructed for a study of the flow features of the

[6]These studies are being made by H. W. Hoffman and W. R. Gambill.

UNCLASSIFIED
2-01-060-45

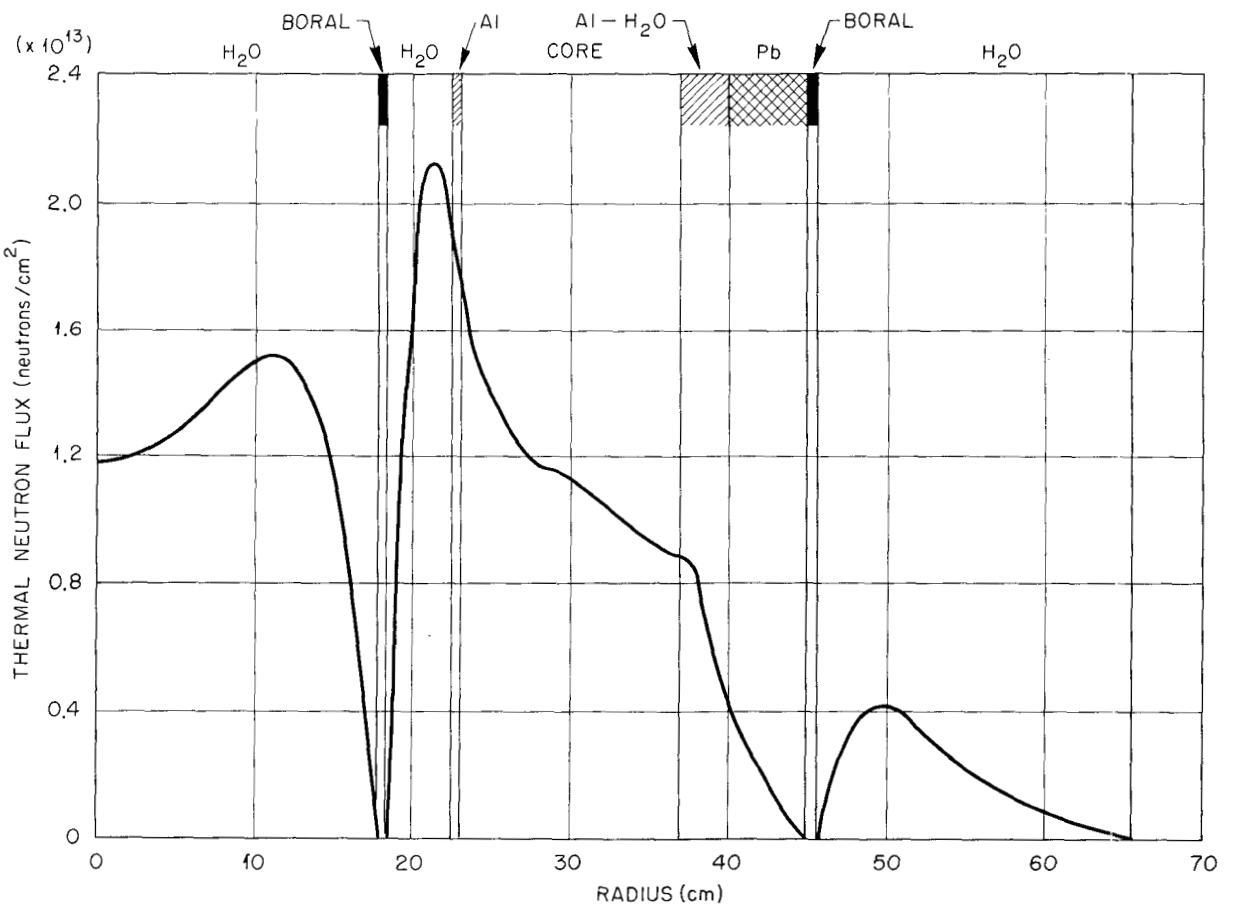

Fig. 2.2.6. Thermal-Neutron Flux in the TSR-II at 5 Mw Power Level as a Function of Radius.

TSR-II core. Flow rates are being measured with the model in both a vertical and a horizontal position and with the water temperature varied from 58 to 102°F. Preliminary data indicate that the core hydrodynamics will be more of a problem than heat transfer. The tests are being continued to determine the proper orificing to correctly distribute the flow in the various channels.

Heat Removal Equipment[7]

A 5-Mw air cooler will be used to remove the heat from the reactor cooling water. A flow diagram of the complete water system, along with tentative locations of the pressure- and temperature-measuring elements, is shown in Fig. 2.2.8. The main components of this system will be: (1) a 60-hp circulating pump capable of delivering 1000 gpm when the reactor is operating at a 200-ft altitude; (2) a venturi nozzle for measuring water flow; (3) the reactor, which will operate up to a 5-Mw heat output; (4) a two-cell, air-cooled heat exchanger capable of removing 17,065,000 Btu/hr from water entering at 160°F and leaving at 125.8°F when the ambient air temperature is 75°F; and (5) a 1500-gal detention tank.

There will also be the following auxiliary units of the flow system: (1) a main bypass valve for reduced flow when the reactor is operating in the power range from 5 kw to 5 Mw; (2) a 5-hp d-c emergency circulating pump which will operate continuously and which is required for removing afterheat following any emergency shutdown that may occur while the radiator is operating at 5 Mw and for circulating the water while the reactor is operating at a power below 5 kw; (3) a water-level control system which will consist of a 250-gal level tank, compressed gas to remove water from the system, and a fill pump which will take water from the pool and put it into the system; (4) a 40-kw heater to prevent water lines from freezing when the reactor is not operating (the air cooler will be supplied with louvers and additional heaters); (5) a mixed-bed demineralizer which will bypass the detention tank with a flow of 40 gpm and which can also be used to keep the reactor pool water clean; and (6) a Tracerlab fission break monitor which will give an alarm if iodine activation, which would indicate a rupture in a fuel element, is noted in the reactor outlet water.

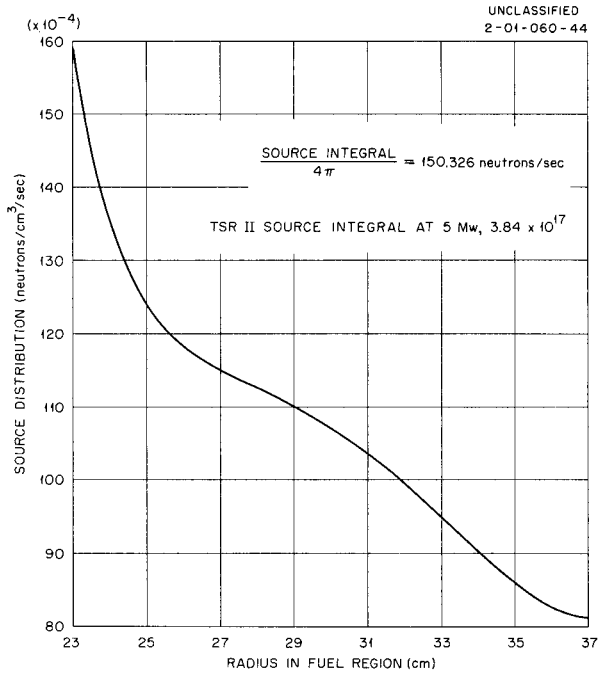

Fig. 2.2.7. Source Distribution in the TSR-II with Boral Shell 4 cm from Fuel Elements as a Function of Radial Position in the Fuel Region.

[7]The water cooling system design is being done by the Engineering Department.

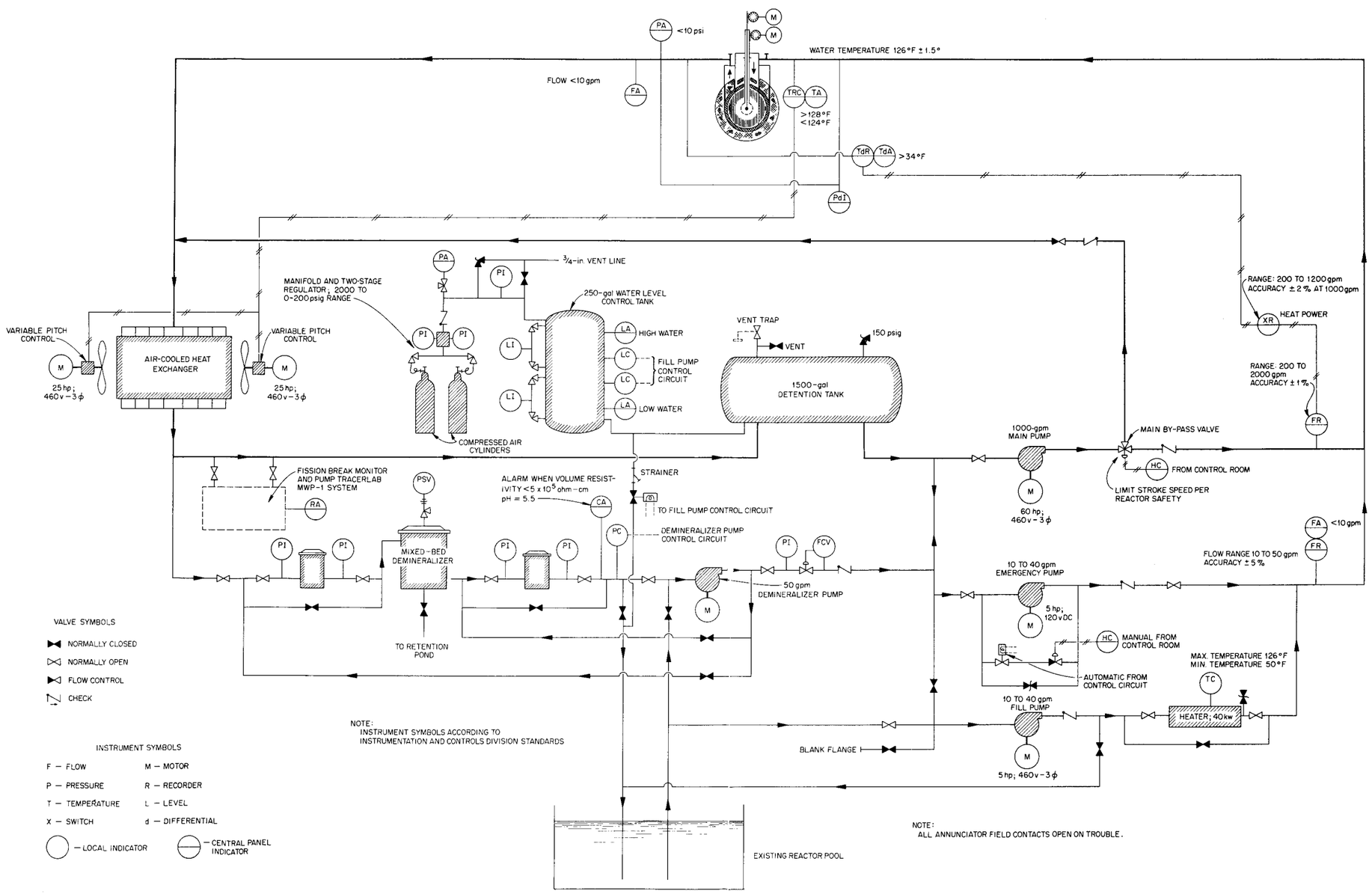

Fig. 2.2.8. Cooling Water Flow Sheet for the TSR-II.

Part 3

CRITICAL EXPERIMENTS

3.1. DETERMINATION OF η OF U^{233} AND Pu^{239} BY COMPARISON OF REACTIVITY EFFECTS IN A FLUX TRAP CRITICAL ASSEMBLY

D. W. Magnuson R. Gwin

The values of η, the number of neutrons produced in fissionable isotopes per neutron absorbed, are of great importance to the design and calculation of reactors. The value of η of U^{233} is of primary importance for the development of breeder reactors. Although the value of η of U^{235} is well established, those of Pu^{239} and U^{233} are less precisely known. Two methods for determining the value of η of U^{233} relative to the value of η of U^{235} have been used at ORNL. The first method, which is described in this section, was also used to obtain a value of η of Pu^{239}. The second method involves a direct comparison of critical assemblies in identical geometry and is described in Sec. 3.2.

Experiments were performed to compare the reactivity contributions to a critical assembly by small amounts of fissionable and purely absorbing materials. The assembly consisted of a 15-cm-dia water column located axially within a critical cylindrical annulus of uranyl fluoride solution enriched to 93.2% in the U^{235} isotope. The outside diameter of the annulus was 38.1 cm. The height was nominally 51 cm but was varied ±1 cm in order to control the assembly. Samples of aqueous solutions of the fissionable and absorbing materials were inserted axially into the water column after a stable critical system had been achieved, and the resulting reactivities were measured by means of period determinations and the latest delayed-neutron data.[1] This arrangement, which is illustrated in Fig. 3.1.1, had two important features: (1) the neutron flux in the sample region was essentially Maxwellian; and (2) the sensitivity of the system was sufficiently high to use samples which were essentially infinitely dilute. (The maximum density of the fissionable isotopes was 3.2 g/liter in a sample having a volume of 136 ml.)

The equation giving the reactivity contributions from the production of fission neutrons and the absorption of neutrons in the sample is

$$\rho = C_1 \int \eta(E)\, \Sigma_{af}(E)\, \phi(E)\, dE - C_2 \int \Sigma_{at}(E)\, \phi(E)\, dE \ ,$$

where Σ_{af} is the macroscopic absorption cross section of the fissionable isotope, Σ_{at} is the total absorption cross section, and the neutron flux energy dependence is given by

$$\phi(E) = \phi_M \text{ (Maxwellian)} \qquad \text{for } 0 \leqq E \leqq 0.2 \text{ ev} \ ,$$

$$\phi(E) = \lambda/E \qquad \text{for } 0.2 \leqq E \leqq 10^6 \text{ ev} \ .$$

The constant C_2 is a measure of the importance of thermal neutrons and is determined by the reactivity measurements with purely absorbing isotopes. The constant C_1 is a measure of the importance of fission neutrons and is determined by the reactivity measurements with U^{235}.

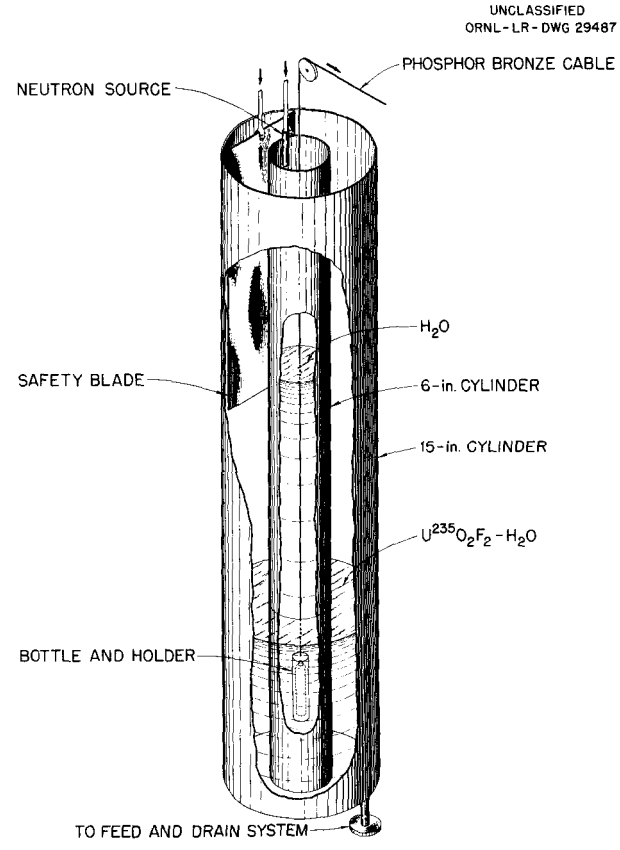

Fig. 3.1.1. Experimental Configuration for Determinations of η with a Flux Trap Critical Assembly.

[1] G. R. Keepin, T. F. Wimett, and R. K. Zeigler, *Phys. Rev.* 107, 1044 (1957).

The proportionality constant, λ, between the parts of the neutron energy spectrum was evaluated by using the gamma-ray activities induced in both bare and cadmium-covered gold and U^{235} foils after irradiation in the flux of the water column when the critical assembly was operating at approximately 1 w. The radial distributions of the activities of bare and cadmium-covered gold foils exposed both in the water column and in the fuel annulus are shown in Fig. 3.1.2, and the fraction

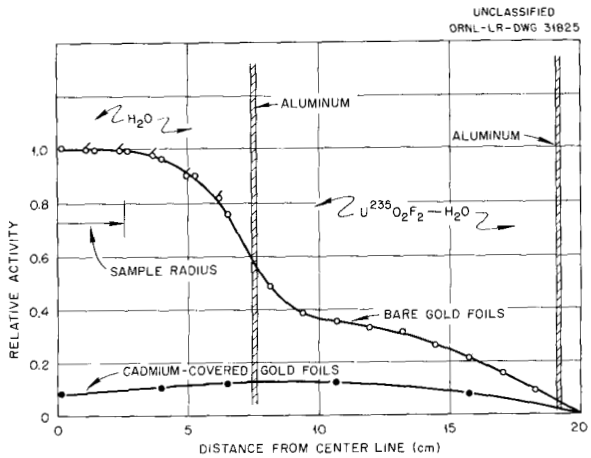

Fig. 3.1.2. Activities of Gold Foils Exposed Along a Radius in the Cylindrical Annular Assembly.

of fissions above the cadmium cutoff is given in Fig. 3.1.3. These figures show that the thermal and epithermal fluxes were constant in the region occupied by the samples. At the center of the water column the cadmium ratio of the gold activity was 12.0; this ratio was 82 for the U^{235} foils. The following relation was used to evaluate λ:

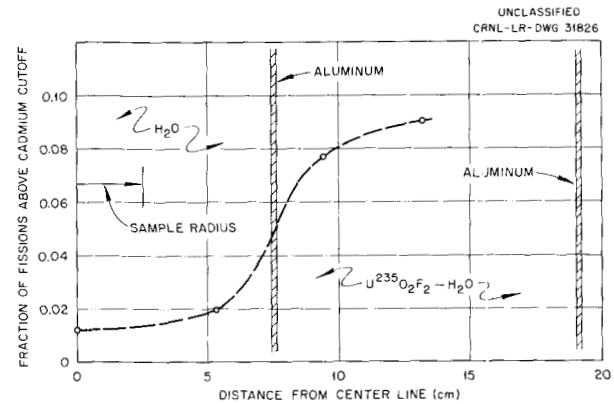

Fig. 3.1.3. Radial Distribution of the Fraction of Fissions Above the Cadmium Cutoff in the Cylindrical Annular Assembly.

$$\frac{\text{Activity of cadmium-covered foils}}{\text{Activity of bare foils}} = \frac{\lambda \int_{0.4}^{10^6} (\Sigma/E)\, dE}{\left[\int_0^{0.2} \phi_M \Sigma dE + \int_{0.2}^{10^6} (\Sigma/E)\, dE\right]}.$$

For the gold foils Σ is the macroscopic activation cross section and for the U^{235} foils Σ is the fission cross section. The reactivity contributions of several indium samples[2] were compared with those of $1/v$ absorbers as an additional method of evaluating the proportionality constant, λ. The value of λ varied from 0.019 to 0.022 when normalized to $\int \phi_M dE = 1$; the value used in the calculations was 0.021.

A value of 2.31 ± 0.06 was obtained for η of U^{233} and a value of 2.03 ± 0.08 for η of Pu^{239}, when world-consistent values for the cross sections and for η of U^{235} and values of resonance integrals for the fissionable isotopes calculated by Kinney[3] were used.

* See errata.

[2]The resonance integrals for the samples were calculated by L. Dresner.

[3]W. E. Kinney, unpublished Oracle calculations.

3.2. DETERMINATION OF η OF U^{233} BY COMPARISON OF CRITICAL EXPERIMENTS IN A 69.2-cm-dia SPHERE

D. W. Magnuson

One method recently used at ORNL for the determination of values of η of U^{233} and Pu^{239} relative to the value of η of U^{235} was described in Sec. 3.1. A second method, in which a direct comparison of critical assemblies of U^{233} and U^{235} in identical geometry was made, was used for the determination of η for U^{233}.

The critical experiments were performed with uranyl nitrate solutions of U^{233} and U^{235} in a 69.2-cm-dia sphere. This sphere was considerably larger than the spheres used in previous experiments at this Laboratory,[1] and the fraction of epithermal neutron absorptions and fissions was greatly reduced. The corrections for the epithermal effects are based on the usual neutron energy spectrum, a Maxwellian plus a $1/E$ tail. The proportionality factor, λ, between these parts of the neutron spectrum was evaluated by counting the gamma-ray activity from fission products in bare and cadmium-covered U^{235} metal foils, 0.002 in. thick and 0.3125 in. in diameter, which were irradiated in the centers of the critical spheres. This relation is

$$\frac{\text{Activity of cadmium-covered } U^{235} \text{ foils}}{\text{Activity of bare } U^{235} \text{ foils}} = \frac{\lambda \int_{0.4}^{10^6} (\Sigma_f/E)\, dE}{\left[\int_0^{0.2} \phi_M \Sigma_f\, dE + \lambda \int_{0.2}^{10^6} (\Sigma_f/E)\, dE\right]} ,$$

where Σ_f is the macroscopic fission cross section, ϕ_M is the Maxwellian flux, and λ/E is the epithermal flux.

The critical equation for the η comparisons was used in the following form:

$$k_{\text{eff}} = \frac{K(B)\left[\eta/(1 + L^2B^2) \int_0^{\infty} \phi_M \Sigma_{af}\, dE + \lambda\nu \int_{0.2}^{10^6} (\Sigma_f/E)\, dE\right]}{\left[\int_0^{\infty} \phi_M \Sigma_{at}\, dE + \lambda \int_{0.2}^{10^6} (\Sigma_{at}/E)\, dE\right]} ,$$

in which B^2 is the buckling, Σ_{af} is the macroscopic absorption cross section of the fissionable isotope, Σ_{at} is the total macroscopic absorption cross section, $K(B)$ is the nonleakage probability of fission neutrons to thermal energies, and ν is the number of neutrons produced per fission. The diffusion length, L, is calculated from

$$L^2 = L_0^2 \frac{\Sigma_{ah}}{\Sigma_{at}} ,$$

in which L_0 is the diffusion length in water and Σ_{ah} is the absorption cross section for water. The

[1] J. T. Thomas, J. K. Fox, and D. Callihan, *A Direct Comparison of Some Nuclear Properties of U-233 and U-235*, ORNL-1992 (Nov. 28, 1955).

assumption is made that $K(B)$ is the same for the two critical systems. Table 3.2.1 summarizes the critical conditions for the two solutions.

Using the values of the appropriate resonance integrals as determined by Kinney[2] yields a value for η of U^{233} of 2.268 ± 0.042. This value is independent of an extrapolation distance, δ, of 3.7 or 2.5 cm, both of which are reported in Sec. 6.3. The nonleakage probability of fission neutrons determined from the critical equation is $K(B) = 0.8362$ for $\delta = 3.7$ cm and $K(B) = 0.8375$ for $\delta = 2.5$ cm. If this nonleakage probability is expressed as a function of the moments and the buckling, B^2, and if it is assumed that the slowing-down distributions in water give correct higher moments, then the experimental value of $K(B)$ can be used to evaluate the second moment.[3] This equation is

$$K(B) = \sum_{i=0}^{\infty} \frac{(-1)^i}{(2i+1)!} B^{2i} \overline{r^{2i}} ,$$

and the age $\tau = \overline{r^2}/6 = 30.07$ and 28.73 cm^2 for $\delta = 3.7$ and 2.5 cm, respectively.

[2]W. E. Kinney, unpublished Oracle calculations.

[3]D. K. Trubey, H. S. Moran, and A. M. Weinberg, *Appl. Nuclear Phys. Ann. Prog. Rep. Sept. 1, 1957*, ORNL-2389, p 158.

Table 3.2.1. Properties of Critical Uranyl Nitrate Solutions of U^{233} and U^{235} in a 69.2-cm-dia Sphere

	U^{233} Solution	U^{235} Solution
Total uranium concentration at 25°C:	17.24 mg/ml	20.15 mg/ml
Uranium loading:	2.93 kg of U^{233}	3.27 kg of U^{235}
k_{eff} at 20°C:	1.00065	1.00118
Cadmium ratio of U^{235} foils:	37.9	36.5
λ:	0.0416	0.0433

Constituent	Microscopic Cross Section, σ_a (cm^2)	U^{233} Solution		U^{235} Solution	
		Isotopic Density (atoms/ml)	Macroscopic Cross Section, Σ_a (cm^{-1})	Isotopic Density (atoms/ml)	Macroscopic Cross Section, Σ_a (cm^{-1})
	$\times 10^{-24}$	$\times 10^{20}$		$\times 10^{20}$	
U^{233}	578.7	0.4355	0.02520		
U^{235}	676.0			0.4811	0.03252
U^{234}	92	0.0073	0.00007	0.0054	0.00005
U^{236}	6			0.0014	0.00000
U^{238}	2.75	0.0029	0.00000	0.0284	0.00001
Th	7.0	0.0020	0.00000		
Al	0.23	0.048	0.00000		
N	1.88	1.275	0.00024	1.869	0.00035
H	0.33	667.4	0.02203	667.4	0.02203
			$\Sigma_{at} = 0.04754$		$\Sigma_{at} = 0.05496$

3.3. CRITICAL PARAMETERS FOR POISONED ANNULAR CYLINDERS CONTAINING AQUEOUS SOLUTIONS OF U^{235}

J. K. Fox L. W. Gilley

Information concerning the critical parameters of U^{235}-enriched uranium solutions contained in cylindrical annuli is valuable in nuclear safety considerations in uranium processing plant design and operations. In a few experiments reported previously[1] the critical parameters of aqueous solutions of 93.2% U^{235}-enriched uranyl fluoride (UO_2F_2) solutions contained in vessels of annular cylindrical geometry were investigated at a chemical concentration corresponding to an $H:U^{235}$ atomic ratio of about 73. These data have now been extended with experiments performed with solutions having $H:U^{235}$ atomic ratios of 50.4 and 309. The annuli were formed by various combinations of cylinders varying in diameter from 2 to 30 in. The cylinders were fabricated from type 2S aluminum and had wall thicknesses of $\frac{1}{16}$ in. and bottom plate thicknesses of $\frac{1}{2}$ in. In all the experiments the inside cylinder was lined with a 20-mil-thick cadmium sheet and filled with water to a height of 48 in. Experiments were performed both with and without a water reflector on the sides and bottom of the outer cylinder but with no top reflector in any case.

The results of these experiments are summarized in Table 3.3.1, and the critical solution height as a function of the thickness of the annulus is shown in Fig. 3.3.1 for both the water-reflected and the unreflected annuli having outside diameters of 10, 12, 15, 20, and 30 in. and a solution concentration corresponding to an $H:U^{235}$ atomic ratio of 50.4. Figure 3.3.2 is a plot of the corresponding data for an $H:U^{235}$ ratio of 309.

[1] J. K. Fox, L. W. Gilley, and D. Callihan, *Critical Mass Studies, Part IX. Aqueous U^{235} Solution*, ORNL-2367, p 33 (Feb. 5, 1958).

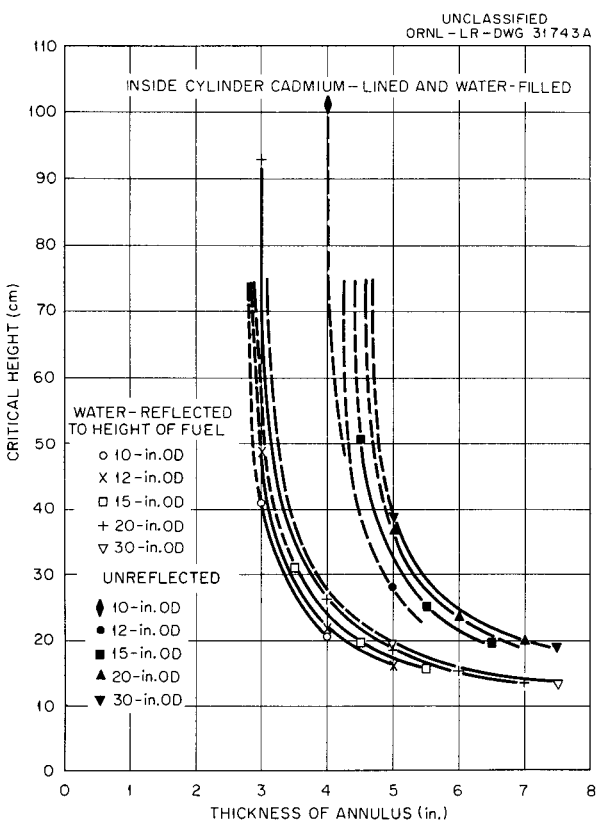

Fig. 3.3.1. Critical Heights of Cylindrical Annuli Containing Aqueous Solutions of 93.2% U^{235}-Enriched Uranyl Fluoride as a Function of the Thicknesses of the Annuli: $H:U^{235}$ Atomic Ratio = 50.4.

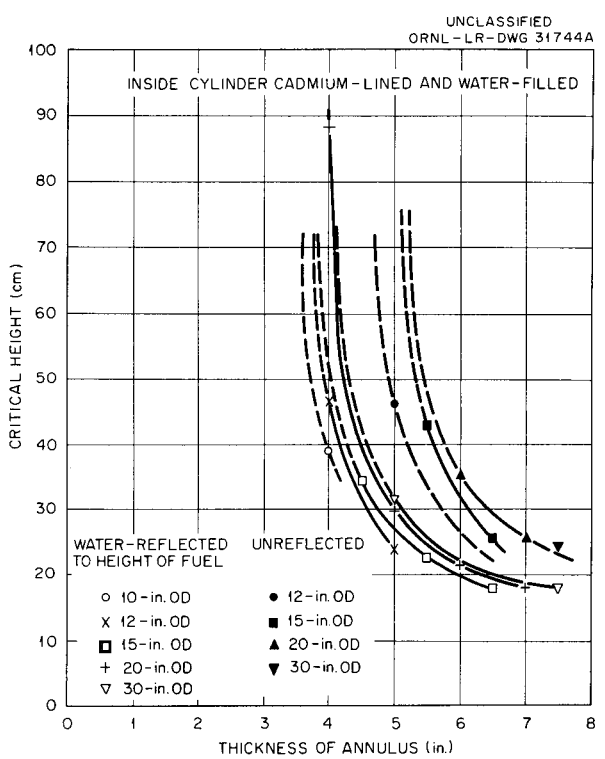

Fig. 3.3.2. Critical Heights of Cylindrical Annuli Containing Aqueous Solutions of 93.2% U^{235}-Enriched Uranyl Fluoride as a Function of the Thicknesses of the Annuli: $H:U^{235}$ Atomic Ratio = 309.

The earlier experiments[1] indicated that the 0.5-in.-thick bottom plate of these annuli introduces an error in the measured critical heights of about 0.5 cm, increasing the measured heights for the reflected annuli and decreasing it for the unreflected annuli. The data reported here have not been corrected for this error. Furthermore, the absence of a reflector above the surfaces of the otherwise reflected annuli makes the critical heights reported here too large by the reflector savings. This corresponds to a difference in critical heights of about 3.5 cm for the water-reflected annuli.

For all the annuli tested with solutions having an $H:U^{235}$ atomic ratio of 50.4 the critical infinitely high, reflected annulus would have a minimum thickness between 2.5 and 3 in. The corresponding infinitely high, unreflected annulus for this solution would be between 3.75 and 4.5 in. thick. The thicknesses of the critical annuli were increased by about 1 in. when the $H:U^{235}$ atomic ratio was increased to 309. Thus, for this solution the minimum thickness of the infinitely high, reflected annulus would be between 3.5 and 4 in., while the minimum thickness for the infinitely high, unreflected annulus would be between 4.5 and 5.5 in. The data indicate that the thickness of the infinitely high annulus increases with the diameter of the outer cylinder.

This paper has been issued as a separate report.[2]

[2] J. K. Fox and L. W. Gilley, *Critical Parameters for Poisoned Annular Cylinders Containing Aqueous Solutions of U^{235}*, ORNL CF-58-8-5.

Table 3.3.1. Critical Parameters of Enriched U^{235} Solutions in Cylindrical Annular Geometry

Solution concentration:		
g of U per g of solution	0.0812	0.3230
g of U^{235} per cc of solution	0.0836	0.4813
$H:U^{235}$ atomic ratio	309	50.4
Specific gravity	1.1051	1.599

Diameter of Assembly		Annulus Thickness (in.)	$H:U^{235}$ Atomic Ratio	Critical Values		
Outside (in.)	Inside (in.)			Height (cm)	Volume (liters)	Mass (kg of U^{235})
Effectively Infinite Outside Water Reflector to Height of Fuel						
10	2	4	50.4	20.2	9.8	4.7
	4	3	50.4	40.9	17.4	8.4
	2	4	309	39.1	19.0	1.59
12	2	5	50.4	16.0	11.3	5.4
	4	4	50.4	21.8	14.2	6.8
	6	3	50.4	48.7	26.6	12.8
	2	5	309	24.0	17.0	1.42
	4	4	309	46.6	30.2	2.53
15	4	5.5	50.4	15.4	16.3	7.9
	6	4.5	50.4	19.5	18.7	9.0
	8	3.5	50.4	31.1	25.4	12.2
	10	2.5	50.4	*		
	2	6.5	309	18.3	20.5	1.71
	4	5.5	309	22.7	24.0	2.01
	6	4.5	309	34.6	33.1	2.77
	8	3.5	309	*		

Table 3.3.1 (continued)

Diameter of Assembly		Annulus Thickness (in.)	$H:U^{235}$ Atomic Ratio	Critical Values		
Outside (in.)	Inside (in.)			Height (cm)	Volume (liters)	Mass (kg of U^{235})
		Effectively Infinite Outside Water Reflector to Height of Fuel				
20	6	7	50.4	13.3	24.5	11.8
	8	6	50.4	15.0	25.5	12.3
	10	5	50.4	18.4	28.0	13.5
	12	4	50.4	26.0	33.7	16.2
	14	3	50.4	93.3	96.4	46.4
	6	7	309	18.5	34.1	2.85
	8	6	309	21.4	36.4	3.04
	10	5	309	30.4	46.2	3.86
	12	4	309	88.3	114.5	9.57
30	15	7.5	50.4	13.4	45.8	22.0
	20	5	50.4	19.0	48.2	23.2
	24	3	50.4	91**		
	15	7.5	309	18.1	61.9	5.17
	20	5	309	31.6	80.1	6.70
		No Outside Reflector				
10	2	4	50.4	101.5	49.4	23.7
12	2	5	50.4	27.8	19.7	9.5
	4	4	50.4	*		
	2	5	309	46.2	32.8	2.74
15	4	5.5	50.4	24.9	26.4	12.7
	6	4.5	50.4	50.5	48.4	23.3
	8	3.5	50.4	*		
	2	6.5	50.4	19.2	21.5	10.4
	2	6.5	309	25.8	28.9	2.42
	4	5.5	309	42.9	45.4	3.80
	6	4.5	309	*		
20	6	7	50.4	19.2	35.4	17.0
	8	6	50.4	23.1	39.3	18.9
	10	5	50.4	36.3	55.2	26.6
	12	4	50.4	*		
	6	7	309	25.5	47.0	3.93
	8	6	309	35.0	59.6	4.98
	10	5	309	*		
30	15	7.5	50.4	18.8	64.3	31.0
	20	5	50.4	38.8	98.3	47.3
	15	7.5	309	24.2	82.8	6.92

*Extrapolation of the reciprocal source neutron multiplication curve from a solution height of at least 91 cm indicates that these assemblies could not be made critical at any height.

**Extrapolation of the reciprocal source neutron multiplication curve from a solution height of 77.4 cm indicates that this assembly could not be made critical at a height less than 91 cm, if it could be made critical at all.

3.4. CRITICAL EXPERIMENTS WITH ARRAYS OF ORR AND BSR FUEL ELEMENTS

J. K. Fox L. W. Gilley

The increasing number of pool-type reactors being constructed throughout this and other countries has emphasized the need for defining the nuclear parameters which will assure the safe handling and storage of the fuel elements for these reactors. The important parameter to establish is the maximum number of fuel elements which will remain subcritical when arranged in patterns appropriate to the specific requirements. Although some data on square arrays are available from experiments performed with the Bulk Shielding Reactor, they are too limited in scope for general application. A number of experiments were therefore performed at the Critical Experiments Facility to determine critical lattices of this type of element.

Elements were available for these experiments from the inventories of the Oak Ridge Research Reactor and the Bulk Shielding Reactor. They contained uranium enriched to 93.2% in U^{235} and varied in total U^{235} content as follows:

1. 24 ORR elements, each containing 200 g of U^{235} (18 of these elements were received near the end of the experiments),
2. 28 ORR elements, each containing 168 g of U^{235},
3. 28 ORR elements, each containing 140 g of U^{235},
4. 70 BSF elements, each containing 135–140 g of U^{235},
5. 8 BSF elements, each containing 31–109 g of U^{235}.

The heavier loaded elements are always of the most interest for experiments of this type, but unfortunately only a few 200-g elements were available at the beginning of this series. As a result, the experiments largely consisted of various arrangements of 168-g elements. They were first arranged vertically in approximately square arrays, one element high, in water, and the spacing between elements was varied. The results are shown in Table 3.4.1 and Fig. 3.4.1 in terms of the critical number of fuel elements as a function of the distance between locating bosses. (The locating bosses are mounted on the end boxes of the elements and extend laterally on all four sides.) These distances can be converted to fuel-to-fuel spacings by adding 0.44 in. to the distances between bosses parallel to the fuel plates and 0.164 in. to the distances between bosses perpendicular to the plates.

Because of the limited inventory of 168-g elements it became necessary to combine them with elements having other loadings for the larger spacings between elements. For the 1-in. spacing, for example, three 140-g elements were added on the edge of an array of twenty-eight 168-g elements. For the $1\frac{1}{4}$-in. spacing, twenty-eight 168-g elements were placed in a ring around six 200-g

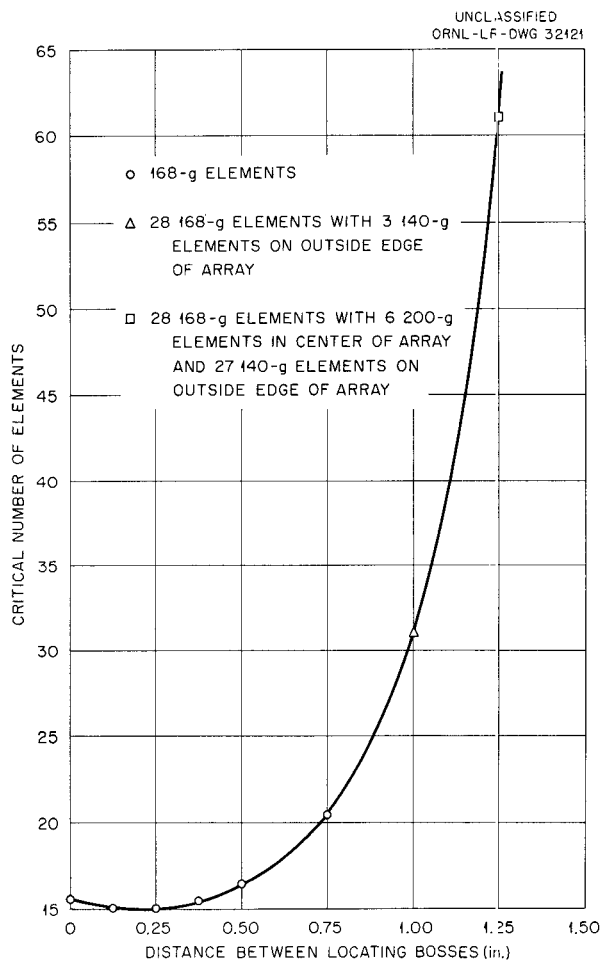

Fig. 3.4.1. Critical Number of ORR Fuel Elements in Approximately Square Arrays in Water as a Function of the Distance Between Locating Bosses.

center elements, and twenty-seven 140-g elements were positioned in an outer ring. Placing the heavier loaded elements in the center gave the maximum reactivity for the elements available at the time. This assumption can be substantiated by comparing the difference in the critical masses of two arrays shown in Table 3.4.1 which used approximately the same number of 168-g elements in combination with 140-g elements. The reactivity was lower in the array in which the 140-g elements were grouped in the center of the array rather than being dispersed throughout the array.

The curve in Fig. 3.4.1 is quite flat for spacings less than 3/8 in., but it increases rapidly for greater distances. The optimum spacing is about 0.2 in. This corresponds to a 0.364-in. fuel-to-fuel spacing

Table 3.4.1. Critical Number of ORR Fuel Elements in Approximately Square Arrays in Water

Distance Between Locating Bosses (in.)		Approximate Critical Array	Approximate Critical Mass (g of U^{235})
Bosses Parallel to Fuel Plates	Bosses Perpendicular to Fuel Plates		
0	0	15 1/2 168-g elements	2575
1/8	1/8	15 168-g elements	2510
1/4	1/4	15 168-g elements	2515
3/8	3/8	15 1/2 168-g elements	2575
1/2	1/2	16 1/2 168-g elements	2775
3/4	3/4	20 1/2 168-g elements	3450
1	1	28 168-g elements 3 140-g elements[a]	5200
1 1/4	1 1/4	28 168-g elements 6 200-g elements[b] 27 140-g elements[a]	9575
1/8	3/16	15 168-g elements	2510
0	1/8	15 168-g elements	2510
0	1/4	15 168-g elements	2505
0	3/8	15 168-g elements	2520
0	1/2	15 1/4 168-g elements	2550
1/8	0	15 1/4 168-g elements	2540
1/4	0	15 1/4 168-g elements	2545
0	0	12 168-g elements 4 140-g elements[c]	2575
0	0	13 168-g elements 3 140-g elements[b]	2622
0	0	18 3/4 140-g elements	2615
0	0	13 200-g elements	2620

[a] On outside edge of array.
[b] In center of array.
[c] Dispersed throughout array.

along a perpendicular to the fuel plates and a 0.64-in. spacing along a parallel to the fuel plates. This agrees fairly well with data on the spacing of U^{235}-enriched uranium-aluminum slugs[1] for which the optimum spacing was found to be about 0.5 in.

The increase in the number of ORR elements required for criticality at spacings greater than 1 in. indicates that an infinite array one element high would probably be subcritical with a $1\frac{1}{2}$-in. spacing between the elements. Since the increase in the number of elements required for criticality at larger spacings in water is due to the absorption of neutrons that would otherwise interact between elements, it would appear that the separations required for the isolation of individual elements would not vary much with the element loading. However, no attempt was made to show this experimentally.

The experiments with approximately square arrays also included arrays of elements in contact. For uniform arrays, that is, arrays of elements having the same U^{235} loading, variations in the fuel loading per element between 140 and 200 g affected the critical mass very little, although the number of elements required for criticality differed. This can be shown by comparing the critical masses reported in Table 3.4.1 for arrays with no spacings between locating bosses. This insensitivity of the critical mass to a variation in the fuel element loading is not surprising since the $H:U^{235}$ atomic ratio for 168-g elements in contact in water is about 370, which is near the optimum moderation for minimum mass. Hence small changes in the U^{235} loading within the elements would have little effect on the critical mass. As mentioned above, small changes in the spacing, that is, less than $\frac{3}{8}$ in., between elements would also have little effect on the critical mass.

In addition to the experiments reported in Table 3.4.1 and Fig. 3.4.1, a number of individual experiments were performed to explore other parameters. In one of these the effect of placing 20-mil-thick cadmium sheets between rows of closely packed elements in water was determined. The elements, which had an average loading of 160 g per element, were stacked in an 11 by 12 array, with the heavier elements in the center to obtain maximum reactivity. The cadmium sheets between the rows were parallel to each other and perpendicular to the fuel plates within the elements. No appreciable multiplication of source neutrons was noted, nor was there any appreciable multiplication observed when both the cadmium sheets and water moderator and reflector were removed and the array was surrounded with a 12-in.-thick paraffin reflector.[2]

A study of slab-shaped arrays was also made with elements moderated and reflected by water at the optimum spacing of 0.2 in. between bosses. Step additions of elements were made to a two-row array which remained subcritical for all additions. The final two-row slab had twenty-four 200-g elements in the center and fourteen 168-g elements on each end. Increases in the source neutron multiplication were observed for all additions up to 17 elements per row; however, further additions to this 34-element array had no appreciable effect. The addition of three elements in a third row opposite the center of the 34-element array was sufficient to make the system critical. From these results it appears that two infinitely long rows of 168-g elements would be subcritical. There were insufficient data to determine the reactivity of two rows of 200-g elements.

This paper has been issued as a separate report.[3]

[1] D. Callihan *et al.*, Y-801 (1951) (classified).

[2] The experiment in which no water was used was performed by D. Scott and J. J. Lynn.

[3] J. K. Fox and L. W. Gilley, *Critical Experiments with Arrays of ORR and BSF Fuel Elements*, ORNL CF-58-9-40.

3.5. CRITICAL EXPERIMENTS WITH 2.09% U^{235}-ENRICHED URANIUM METAL PLATES IN WATER

J. K. Fox J. T. Mihalczo L. W. Gilley

Experiments were performed with 2.09% U^{235}-enriched uranium metal plates in a light-water-moderated and -reflected assembly. Each plate was 30 in. long, $3\frac{1}{8}$ in. wide, and $\frac{1}{4}$ in. thick and contained 7.09 kg of uranium metal. Some plates $1\frac{1}{2}$ in. wide were also available. All the plates were copper-plated and coated with varnish to prevent oxidation.

The plates were stacked horizontally on a Plexiglas table and separated with Plexiglas spacers, which resulted in a volume fraction of Plexiglas of about 0.20. In order to prevent trapping of air in the assembly, the lattice was tilted up on one end. This resulted in a nonuniform top reflector except in those cases where the water thickness above the assembly was effectively infinite. The spacing between rows of fuel plates was varied from $\frac{5}{8}$ in. to $1\frac{1}{8}$ in. In one assembly, which had a $\frac{7}{8}$-in. spacing between rows, the spacing between edges of fuel plates was varied from 0 to $\frac{5}{8}$ in.

The method of assembly resulted in an almost parallelepipedal geometry. Whenever the last row of fuel plates contained less than four plates, these plates were centered in the row if possible.

The results of the measurements are shown in Table 3.5.1. The minimum critical mass was 6.74 kg. If the total number of plates in each of these assemblies was reduced by a half plate in the top row, the resulting system was found to be subcritical with an infinite water reflector. For a zero edge-to-edge spacing of plates, the optimum spacing between rows of plates is about $\frac{7}{8}$ in. For the $\frac{7}{8}$-in. spacing between rows of plates the optimum edge-to-edge spacing is $\frac{5}{16}$ in.

These experiments have been reported in more detail elsewhere.[1]

[1] J. K. Fox, J. T. Mihalczo, and L. W. Gilley, *Critical Experiments with 2.09% U^{235}-Enriched Uranium Metal Plates in Water*, ORNL CF-58-8-3.

Table 3.5.1. Results of Measurements of Horizontal Assemblies

Spacing Between Rows (in.)	Spacing Between Plates in Row (in.)	Water:Metal Volume Ratio	Total Number of Plates	U^{235} Mass (kg)	Maximum[a] Fuel Height (cm)	Minimum[b] Fuel Height (cm)	Arrangement of Plates	Water Height at Criticality[c] (cm)
$\frac{5}{8}$	0	2.5	54	8.03	33.0	29.5	13 rows of 4 plates, 2 plates centered in next row	38.2
$\frac{3}{4}$	0	3.0	49	7.26	34.0	31.1	12 rows of 4 plates, 1 plate centered	40.5
$\frac{7}{8}$	0	3.5	47	6.97	35.0	32.0	11 rows of 4 plates, 3 plates centered	42.0
$\frac{7}{8}$	$\frac{1}{4}$	3.8	$45\frac{1}{2}$	6.74	35.0	32.0	11 rows of 4 plates, 1 plate centered, $\frac{1}{2}$ plate off center	39.8
$\frac{7}{8}$	$\frac{3}{8}$	3.9	$45\frac{1}{2}$	6.74	35.0	32.0	11 rows of 4 plates, 1 plate centered, $\frac{1}{2}$ plate off center	40.1
$\frac{7}{8}$	$\frac{5}{8}$	4.2	47	6.97	35.0	32.0	11 rows of 4 plates, 3 plates centered	41.0
1	0	4.0	48	7.12	39.8	35.6	12 rows of 4 plates	60.9
$1\frac{1}{8}$	0	4.5	51	7.57	45.8	42.6	12 rows of 4 plates, 3 plates centered	58.8

[a] Maximum distance from Plexiglas table to upper surface of fuel in top row.
[b] Minimum distance from Plexiglas table to upper surface of fuel in top row.
[c] Height above Plexiglas table.

3.6. SOME STUDIES OF WATER, STYROFOAM, AND PLEXIGLAS REFLECTORS

J. K. Fox L. W. Gilley

Two sets of critical experiments have been performed with slabs of uranium solutions in order to compare the reflecting properties of Styrofoam[1] and water and to determine the effect of placing various thicknesses of Plexiglas between two unreflected slabs. The fissile material used was an aqueous solution of UO_2F_2 which was enriched to 93.2% in U^{235} and had an $H:U^{235}$ atomic ratio of 293. The solution was contained in slab-shaped aluminum vessels having nominal dimensions of 6 × 48 × 48 in. and wall thicknesses of $\frac{1}{8}$ in.

The first group of experiments consisted in determining the critical height of a single 6-in.-thick slab under the following reflector conditions: (a) no reflector, (b) water reflector on the bottom and on all four sides of slab to the height of the solution, (c) a 3- or 6-in.-thick Styrofoam reflector on each face, that is, on each 48 by 48 in. side of the slab, and (d) a 3- or 6-in.-thick Styrofoam reflector on each face of the slab plus a water reflector on the bottom and all four sides of the slab-Styrofoam assembly to the height of the solution. The results are summarized in Table 3.6.1. It is noted that Styrofoam is significantly less effective as a neutron reflector than is water: a layer of the plastic 6 in. thick, which is nearly effectively infinite, reduced the critical height of the slab by only about 20%, while a water reflector reduced the height by more than a factor of 3. Replacing the first 3 in. of water on the two faces of the slab with Styrofoam increased the critical height about 33%; replacing the first 6 in. of water with Styrofoam increased the height about 53%. Using a 3-in.-thick Styrofoam reflector on each of the two faces of an otherwise unreflected slab is almost as effective as using a 6-in.-thick Styrofoam reflector on the faces.

In some of the experiments two 6-in.-thick parallel slabs were placed 6 and $12\frac{1}{6}$ in. apart, and the critical heights of the two-slab assemblies were determined for several reflector conditions. In one experiment the slabs were both reflected (except on top) and separated by water, and in another experiment they were reflected by water and separated by Styrofoam. In other experiments no water reflector was used, and the effect of placing Styrofoam between the slabs was determined. Comparison of the critical height of two water-reflected slabs separated by water with their critical height when they were separated by Styrofoam shows that replacing the water with the Styrofoam decreased the reactivity of the assembly, since the increased leakage more than compensated for the increased interaction. Placing 6 in. of Styrofoam between two unreflected slabs increased the critical height slightly; however, placing $12\frac{1}{6}$ in. of Styrofoam between two unreflected slabs decreased the critical height.

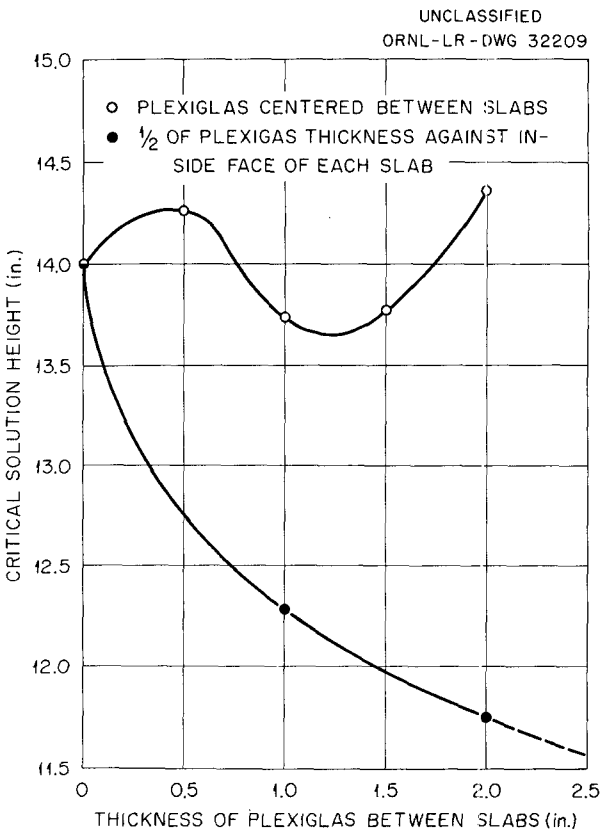

Fig. 3.6.1. Critical Height of Two Unreflected 6-in.-thick Slabs of 93% U^{235}-Enriched Uranium Solution 12 in. Apart as a Function of the Thickness of Plexiglas Moderator Between the Slabs.

[1]Styrofoam is the trade name for a foam-like form of polystyrene ($C_6H_5CH{:}CH_2$) in which small gas bubbles are homogeneously distributed throughout the plastic. The bubbles are apparently closed since Styrofoam does not absorb water.

Table 3.6.1. Critical Parameters of U^{235}-Enriched Uranium Solutions in Single and Interacting Slab Geometries Reflected with Styrofoam, Water, and Plexiglas

Density of Styrofoam:	0.028 g/cc
Concentration of solution:	0.0850 g of U per g of solution; 0.0878 g of U^{235} per cc of solution; H:U^{235} atomic ratio = 293
Isotopic analysis of uranium:	93.18% of U^{235}, 5.51% of U^{238}, 1.04% of U^{234}, and 0.27% of U^{236}
Specific gravity of solution:	1.108
Solution container:	Aluminum vessel 6 in. wide, 48 in. high, and 48 in. long with $\frac{1}{8}$-in.-thick walls

Reflector Conditions	Critical Solution Height (in.)
One 6-in.-thick Slab of Solution	
No reflector	27.25
Water reflector on bottom and on all four sides of slab to height of solution	8.09
3-in.-thick Styrofoam reflector on each face of slab	22.90
6-in.-thick Styrofoam reflector on each face of slab	21.83
3-in.-thick Styrofoam reflector on each face of slab plus a water reflector on bottom and on all four sides of slab-Styrofoam assembly to height of solution	10.84
6-in.-thick Styrofoam reflector on each face of slab plus a water reflector on bottom and on all four sides of slab-Styrofoam assembly to height of solution	12.35
Two 6-in.-thick Slabs of Solution 6 in. Apart	
No reflector	11.72
No water reflector: 6 in. of Styrofoam between slabs	12.14
Water reflector on bottom and on outside of assembly to height of solution: 6 in. of water between slabs	7.90
Water reflector on bottom and on outside of assembly to height of solution: 6 in. of Styrofoam between slabs	7.93
Two 6-in.-thick Slabs of Solution $12\frac{1}{6}$ in. Apart	
No reflector	14.58
No water reflector: $12\frac{1}{6}$ in. of Styrofoam between slabs	14.21
Water reflector on bottom and on outside of assembly to height of solution: $12\frac{1}{6}$ in. of water between slabs	8.09*
Water reflector on bottom and on outside of assembly to height of solution: $12\frac{1}{6}$ in. of Styrofoam between slabs	8.74
Two 6-in.-thick Slabs of Solution 12 in. Apart	
No reflector	14.01
No water reflector: 0.5 in. of Plexiglas centered between slabs	14.26
No water reflector: 1.0 in. of Plexiglas centered between slabs	13.74
No water reflector: 1.5 in. of Plexiglas centered between slabs	13.77
No water reflector: 2.0 in. of Plexiglas centered between slabs	14.36
No water reflector: One 0.5-in.-thick Plexiglas sheet positioned against inside face of each slab	12.28
No water reflector: One 1.0-in.-thick Plexiglas sheet positioned against inside face of each slab	11.75

*Value obtained with single 6-in.-thick slab in water. Previous experiments with interacting slabs in water have shown that 12 in. of water effectively isolates the individual slabs.

The effect of placing various thicknesses of Plexiglas between two 6-in.-thick slabs spaced 12 in. apart was also investigated. In one case successive thicknesses of 0.5, 1.0, 1.5, and 2.0 in. of Plexiglas were centered between the two slabs, and in other experiments 0.5- and 1.0-in. thicknesses were placed against each inside face of the two slabs. The data are plotted in Fig. 3.6.1. These curves should approach as asymptotes the critical heights corresponding to slabs one-half reflected with water or Plexiglas, since 12 in. of either material would effectively isolate the two slabs.

This paper has been issued as a separate report.[2]

[2] J. K. Fox and L. W. Gilley, *Some Studies of Water, Styrofoam and Plexiglas Reflectors*, ORNL CF-58-9-39.

3.7. HOMOGENEOUS HYDROGEN-MODERATED CRITICAL ASSEMBLIES WITH 2% U^{235} ENRICHED URANIUM

J. J. Lynn J. T. Mihalczo W. C. Connelly[1]

A knowledge of the nuclear properties of homogeneous hydrogen-moderated assemblies of slightly enriched uranium will allow the establishment of bases for nuclear safety specifications and will be of general interest in reactor analysis. This information is currently being obtained in a series of measurements with blocks of homogeneously mixed uranium tetrafluoride (UF_4) and paraffin ($C_{25}H_{52}$). The UF_4 particle size is less than 20 mils, and the U^{235} isotopic content of the uranium is 2.00%.

Thus far experiments have been performed with two mixtures, one containing 92.1 wt % UF_4 and the other containing 88.6 wt % UF_4, corresponding to $H:U^{235}$ atomic ratios of 195 and 294, respectively. The uranium concentrations in the two mixtures were 3.1 and 2.6 g/cc, respectively.

Both cylindrical and parallelepipedal geometries have been assembled, some of which were surrounded with an effectively infinite reflector of paraffin and Plexiglas. The base of each parallelepiped was square. The critical masses of both the reflected and the unreflected assemblies of blocks having an $H:U^{235}$ ratio of 294 are plotted in Fig. 3.7.1. The critical masses of the reflected assemblies of blocks having an $H:U^{235}$ ratio of 195 are plotted in Fig. 3.7.2. The critical heights for the two mixtures are given in Figs. 3.7.3 and 3.7.4.

Two additional experiments were performed. In one experiment blocks of the two fuel mixtures were alternated to give an effective $H:U^{235}$ atomic ratio of 245. In the other experiment the blocks having an $H:U^{235}$ ratio of 294 were separated with Plexiglas to give an effective ratio of 400. The validity of using this method to obtain the higher $H:U^{235}$ atomic ratio has been substantiated by previous experiments. The variation of the minimum critical masses with the $H:U^{235}$ ratio is shown in Fig. 3.7.5.

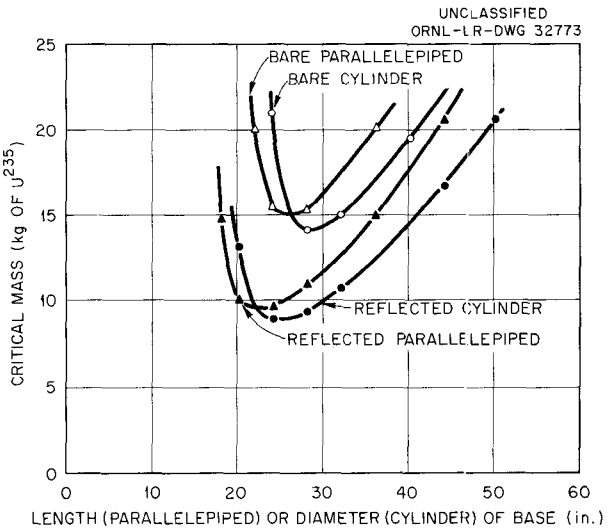

Fig. 3.7.1. Critical Masses as a Function of the Base Dimensions of Assemblies of a 2% U^{235}-Enriched UF_4-$C_{25}H_{52}$ Mixture with an $H:U^{235}$ Atomic Ratio of 294.

[1] Research participant, Alabama Polytechnic Institute, Auburn, Ala.

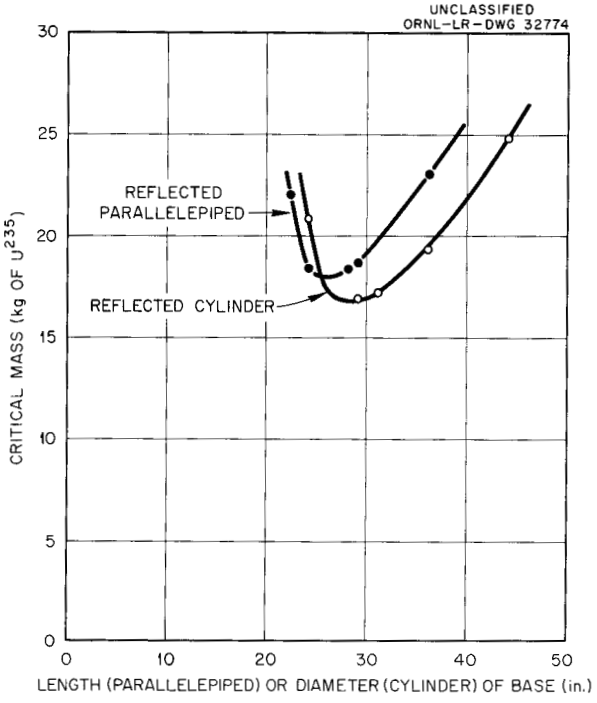

Fig. 3.7.2. Critical Masses as a Function of the Base Dimensions of Assemblies of a 2% U^{235}-Enriched UF_4-$C_{25}H_{52}$ Mixture with an $H:U^{235}$ Atomic Ratio of 195.

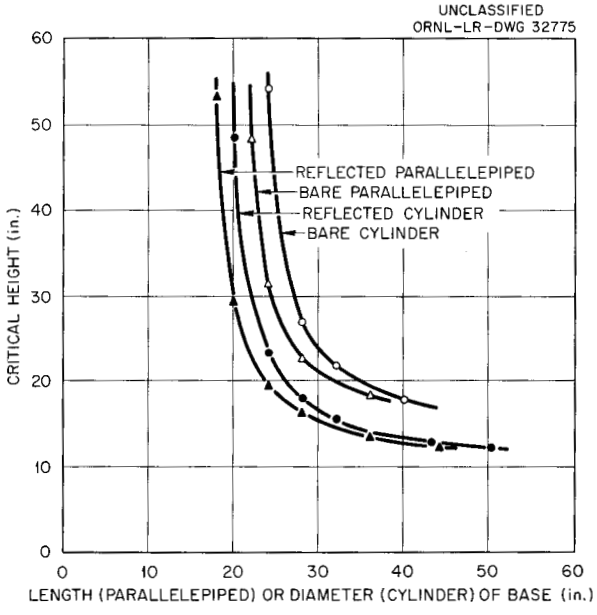

Fig. 3.7.3. Critical Heights as a Function of the Base Dimensions of Assemblies of a 2% U^{235}-Enriched UF_4-$C_{25}H_{52}$ Mixture with an $H:U^{235}$ Atomic Ratio of 294.

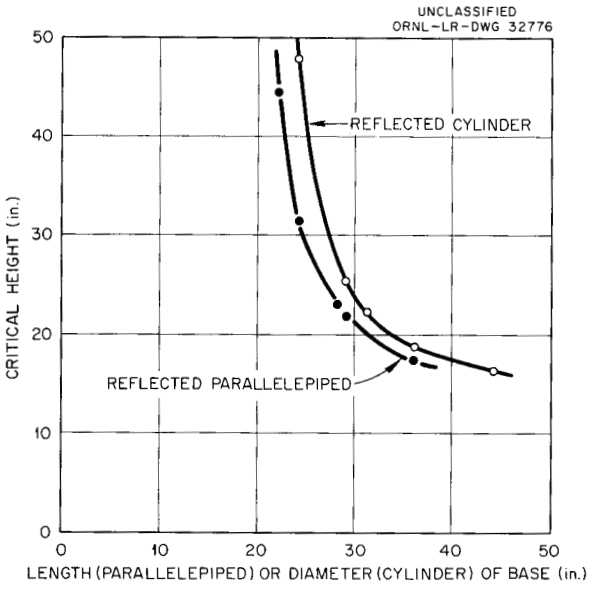

Fig. 3.7.4. Critical Masses as a Function of the Base Dimensions of Assemblies of a 2% U^{235}-Enriched UF_4-$C_{25}H_{52}$ Mixture with an $H:U^{235}$ Atomic Ratio of 195.

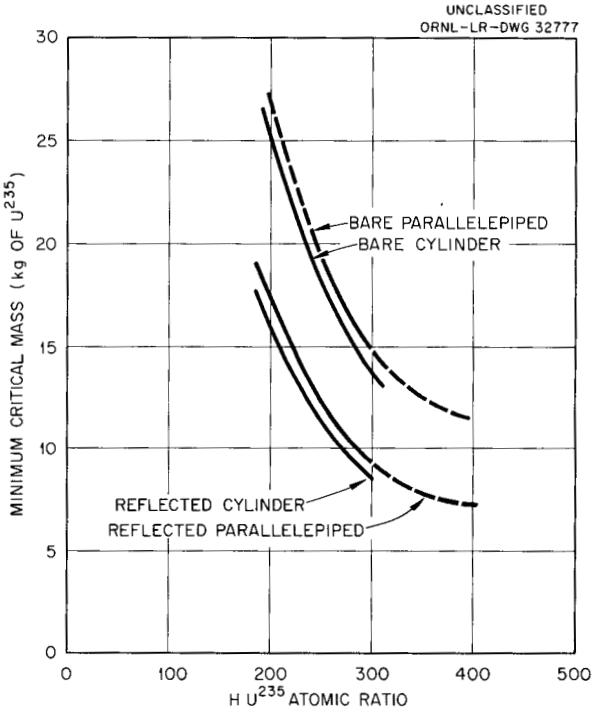

Fig. 3.7.5. Minimum Critical Masses of 2% U^{235}-Enriched UF_4-$C_{25}H_{52}$ Mixtures as a Function of the $H:U^{235}$ Atomic Ratio.

3.8. CRITICAL PARAMETERS OF URANIUM SOLUTIONS IN SIMPLE GEOMETRY

J. K. Fox L. W. Gilley R. Gwin J. T. Thomas

The measurement of the critical parameters of solutions of the fissionable uranium isotopes in simple geometry has been a continuing program for a number of years. Part of this program has been the establishment of values for the minimum critical volume and minimum critical mass both with and without an effectively infinite water reflector. The accuracy with which these limiting values are desired necessitates the evaluation of various experimental uncertainties such as the effect of the solution container itself. The correction described and applied in the past[1,2] to some of the data from aluminum cylinders is suspect and is to be reinvestigated. Further, the critical height (and, hence, volume and mass) reported[1] for a 10-in.-dia cylinder of solution having a chemical concentration near that yielding minimum volume now seems to be in additional error for reasons unknown. The reported volume of 5.78 liters appears to be too small by perhaps as much as 10%.

What are believed to be the best data describing some recent measurements with spheres of both U^{233} and U^{235} solutions are given in Table 3.8.1. The limit of accuracy of the volume is ±0.5% and of the concentration and mass is ±1%. These data have not been corrected for the effect of the type 1100 aluminum of which the containers were fabricated.

[1] J. K. Fox and L. W. Gilley, *Appl. Nuclear Phys. Ann. Prog. Rep. Sept. 1, 1957*, ORNL-2389, p 72.

[2] J. K. Fox, L. W. Gilley, and D. Callihan, *Critical Mass Studies. Part IX. Aqueous U^{235} Solutions*, ORNL-2367, p 22 (Feb. 5, 1958).

Table 3.8.1. Critical Parameters of Spheres of Uranium Solutions

Principal isotope	U^{235}	U^{235}	U^{235}	U^{233}	U^{235}	U^{235}	U^{235}
Sphere radius, cm	27.9	34.6	34.6*	34.6*	11.5	11.8	27.9
Sphere volume, liters	91.1	174	174	174	6.40	6.96	91.1
Sphere wall thickness, cm	0.20	0.32	0.32	0.32	0.16	0.16	0.20
Salt	UO_2F_2	UO_2F_2	$UO_2(NO_3)_2$	$UO_2(NO_3)_2$	UO_2F_2	UO_2F_2	UO_2F_2
Uranium isotopic composition, %							
U^{233}				97.65			
U^{234}	1.14	1.14	1.04	1.63	0.98	0.98	0.98
U^{235}	93.20	93.20	93.18	0.06	93.18	93.18	93.18
U^{236}			0.27		0.50	0.50	0.50
U^{238}	5.66	5.66	5.51	0.66	5.36	5.36	5.36
Specific gravity of solution	1.03	1.02	1.03	1.02	1.40	1.24	1.03
Uranium concentration in solution, mg/g	24.4	19.6	19.6	16.9	249	172	21.4
$H:U^{235}$ or $H:U^{233}$ ratio	1112	1393	1379	1521	76.1	126.5	1270
$N:U^{235}$ or $N:U^{233}$ ratio			3.64	2.69			
Uranium loading, kg of U^{235} or U^{233}	2.13	3.25	3.27	2.93	2.08	1.39	1.86
Reflector	None	None	None	None	Infinite water	Infinite water	Infinite water
k (at 25°C)	1.0004	1.0000	1.0001	1.0003	1.0000	1.0000	0.9999

*These experiments were performed by D. W. Magnuson and are also reported in Sec. 3.2.

Part 4

FISSION PHYSICS

4.1. THE ENERGY SPECTRUM OF PROMPT GAMMA RAYS ACCOMPANYING THE THERMAL FISSION OF U^{235}

R. W. Peelle F. C. Maienschein T. A. Love

The absolute energy spectrum of gamma rays emitted at the time of fission is of interest for at least two reasons. For fission physicists it has implications concerning the distributions of nuclear excitations of the fission fragments. For reactor physicists and engineers the spectrum is required for proper design of shielding and heat-removal systems for nuclear reactors, since prompt gamma rays are always present in all uranium fission reactors and release at least one-third of the total energy given off from fission in the form of penetrating radiations that require shielding.

Following a period in which extensive checks were made[1] to ensure credible results, many data have been obtained for a new determination of the spectrum of gamma rays emitted in time coincidence with the thermal-neutron fission of U^{235}. Multiple-crystal Compton and pair scintillation spectrometers were employed to provide a reasonably unique detector response. Backgrounds, caused by the detection of secondary gamma rays produced by prompt-neutron emission, were reduced to an unimportant (1 to 3%) level by using previously reported techniques.[1]

Additional experimental results will be required before a final evaluation can be made of these data, but a preliminary analysis of a portion of the data was performed. The results, which are shown in Fig. 4.1.1, are in fair agreement with a previously reported preliminary experiment,[2] and in general agreement with those of Gamble[3] in the energy region between 1 and 3.5 Mev. In the low-energy region the results are 20 to 30% higher than those of Gamble and in the high-energy region about a factor of 2 lower. There is a sudden drop in intensity for gamma rays with energies greater than 7.5 Mev. Nuclear excitations larger than this would usually lead to the emission of prompt neutrons. It is supposed that the observed continuous spectrum is caused by the decay of a statistical ensemble of many levels and by the finite detector resolution. In this connection, it may be noted that the spectrum shown in Fig. 4.1.1 is rather similar to a corresponding prompt gamma-ray spectrum from Cf^{252} spontaneous fission.[4]

Goldstein[5] has indicated that a reasonable fit (within ±40%) to the data of Fig. 4.1.1 may be obtained by the expression

$$I(E) = 8e^{-1.10E(\mathrm{Mev})}\ (\mathrm{photons \cdot fission^{-1} \cdot Mev^{-1}})$$

in the energy interval from 1 to 7 Mev.

The data shown in Fig. 4.1.1 may be summed to yield 7.2 ± 0.8 Mev per fission and 7.4 ± 0.8 photons per fission for the energy range between 0.3 and 10 Mev. This total is in agreement with the earlier work of Gamble.[3] Of the various theories of fission,[6] none predict the gamma-ray spectral distributions. The evaporation model of Leachman[7] leads to an expected energy of about 4 Mev for emission in the form of de-excitation radiation, rather less than that observed.

Unanalyzed data, not included in Fig. 4.1.1, have been obtained over the entire energy region above 1.5 Mev in order to improve the statistical accuracy. The region between 1.5 and 4 Mev has also been studied with increased resolution to allow possible identification of structure. Future experiments are planned to study the energy range between about 50 and 500 kev and to improve the accuracy to which experimental counting efficiencies are known as a function of energy. A final analysis of the entire body of data will be made available as soon as possible.

---

[1] F. C. Maienschein, T. A. Love, and R. W. Peelle, *Appl. Nuclear Phys. Ann. Prog. Rep. Sept. 1, 1957*, ORNL-2389, p 99–110.

[2] F. C. Maienschein *et al.*, *Phys. Semiann. Prog. Rep. March 20, 1955*, ORNL-1879, p 51.

[3] J. E. Francis and R. L. Gamble, *Phys. Semiann. Prog. Rep. March 20, 1955*, ORNL-1879, p 20.

[4] A. B. Smith, P. R. Fields, and A. M. Friedman, *Phys. Rev.* **104**, 699–702 (1956).

[5] H. Goldstein, *The Attenuation of Gamma Rays and Neutrons in Reactor Shields*, Section 3.6 (Revised), GPO, Washington, 1957.

[6] *Proc. Intern. Conf. Peaceful Uses Atomic Energy, Geneva, 1955* **2**, 151–220 (1956); and P. Fong, *Phys. Rev.* **102**, 434-448 (1956).

[7] R. B. Leachman, *Proc. Intern. Conf. Peaceful Uses Atomic Energy, Geneva, 1955* **2**, 193–200 (1956).

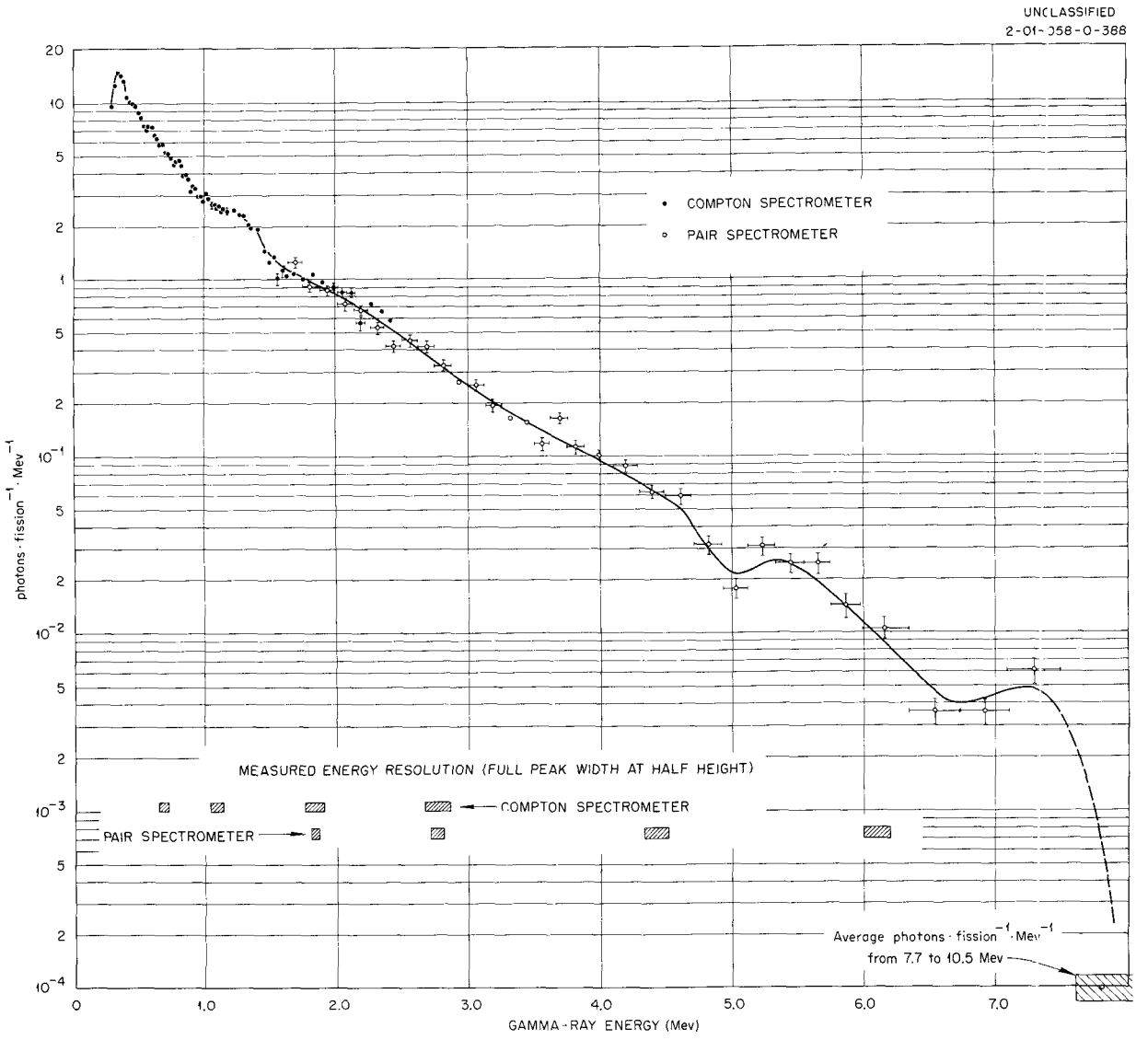

Fig. 4.1.1. Energy Spectrum of Gamma Rays Observed Within 10^{-7} sec After Fission. The ordinate errors shown were obtained from counting statistics, and the energy errors represent in each case the energy interval over which the results were averaged. The line is drawn only to connect the points. This plot represents a preliminary analysis of a fraction of the data, and systematic errors as large as 15% may occur in some energy regions. The nonunique response of the spectrometer to monoenergetic gamma radiation is approximately compensated for. The resolution functions of the spectrometers used are indicated by the horizontal bars. The data within smaller intervals of the 7.7- to 10.5-Mev region did not show statistically significant fluctuations.

4.2. CHARACTERISTICS OF FISSION-PRODUCT GAMMA RAYS EMITTED BETWEEN 5×10^{-8} AND 10^{-6} sec AFTER THERMAL FISSION OF U^{235}

F. C. Maienschein R. W. Peelle T. A. Love

During the preliminary experiments[1] designed to aid in the determination of the energy spectrum of gamma rays emitted in coincidence with fission, counts were observed in the time region between 5×10^{-8} and 10^{-6} sec after fission. These counts are now believed to have resulted from delayed gamma rays. More recently, a beam of thermal neutrons from the ORNL Graphite Reactor has been utilized to obtain rough measurements of the intensity and energy of these gamma rays. For experimental reasons involving low source strengths and/or high random backgrounds, it was impossible to use the multiple-crystal spectrometer for these measurements. Instead, a 1.0-in.-dia by 1.5-in.-long single-crystal sodium iodide detector was used; consequently, the results are presented in terms of pulse-height spectra rather than energy spectra.

Figure 4.2.1 shows some of the spectral data obtained by using standard delayed-coincidence techniques at various short times after fission. The source of the fission radiation was a 0.5-cm-dia by 1.0-cm-long spiral fission chamber. Figure 4.2.2 shows time-distribution data obtained, with the same fission source and the previously reported time analyzer,[2] for various energy groups. Gamma rays appearing after fission were compared with those before fission to avoid any effects from gamma rays coincident with fission. The intensities of the gamma radiation in these two experiments are known approximately in terms of the intensity of the prompt gamma radiation observed in the same geometry. Table 4.2.1 gives approximate values for the relative numbers of counts observed in a few pulse-height groups during the time interval after fission between 5×10^{-8} and 10^{-6} sec. Most of these groups correspond to peaks in the spectra of Fig. 4.2.1.

Although this contribution to the fission-associated gamma radiation does not appear to be negligible compared to the prompt radiation, such short-delayed gamma rays are not known to have been observed previously. In particular, experiments designed to observe prompt radiation may exclude these delayed radiations. For purposes of shield design these gamma rays follow fission by so short an interval that they may be considered prompt. As has been reported,[1] gamma rays emitted during

[1] F. C. Maienschein, R. W. Peelle, and T. A. Love, *Appl. Nuclear Phys. Ann. Prog. Rep. Sept. 1, 1957*, ORNL-2389, p 99.

[2] R. W. Peelle, F. C. Maienschein, and T. A. Love, *Appl. Nuclear Phys. Ann. Prog. Rep. Sept. 1, 1957*, ORNL-2389, p 263.

Table 4.2.1. Fission Gamma-Ray Delay Fraction as a Function of Energy*

Average Gamma-Ray Energy (Mev)	Gamma-Ray Energy Interval (Mev)	N_D/N_P**
0.19	0.15–0.22	0.20 ± 0.04
0.30	0.25–0.35	0.07 ± 0.03
0.70	0.48–0.92	0.038 ± 0.01
1.3	1.18–1.42	0.020 ± 0.004
	0.16–1.93	0.057 ± 0.003

*The data in this table were obtained from pulse-height measurements and apply to count-rate data as obtained with a small single crystal. Interpretation of these results as true photon intensities might lead to errors of a factor of 2.

**N_D = total number of counts per fission observed in the specified energy interval for delay times between 5×10^{-8} and 10^{-6} sec; N_P = number of counts per fission associated with prompt gamma rays in the same energy interval.

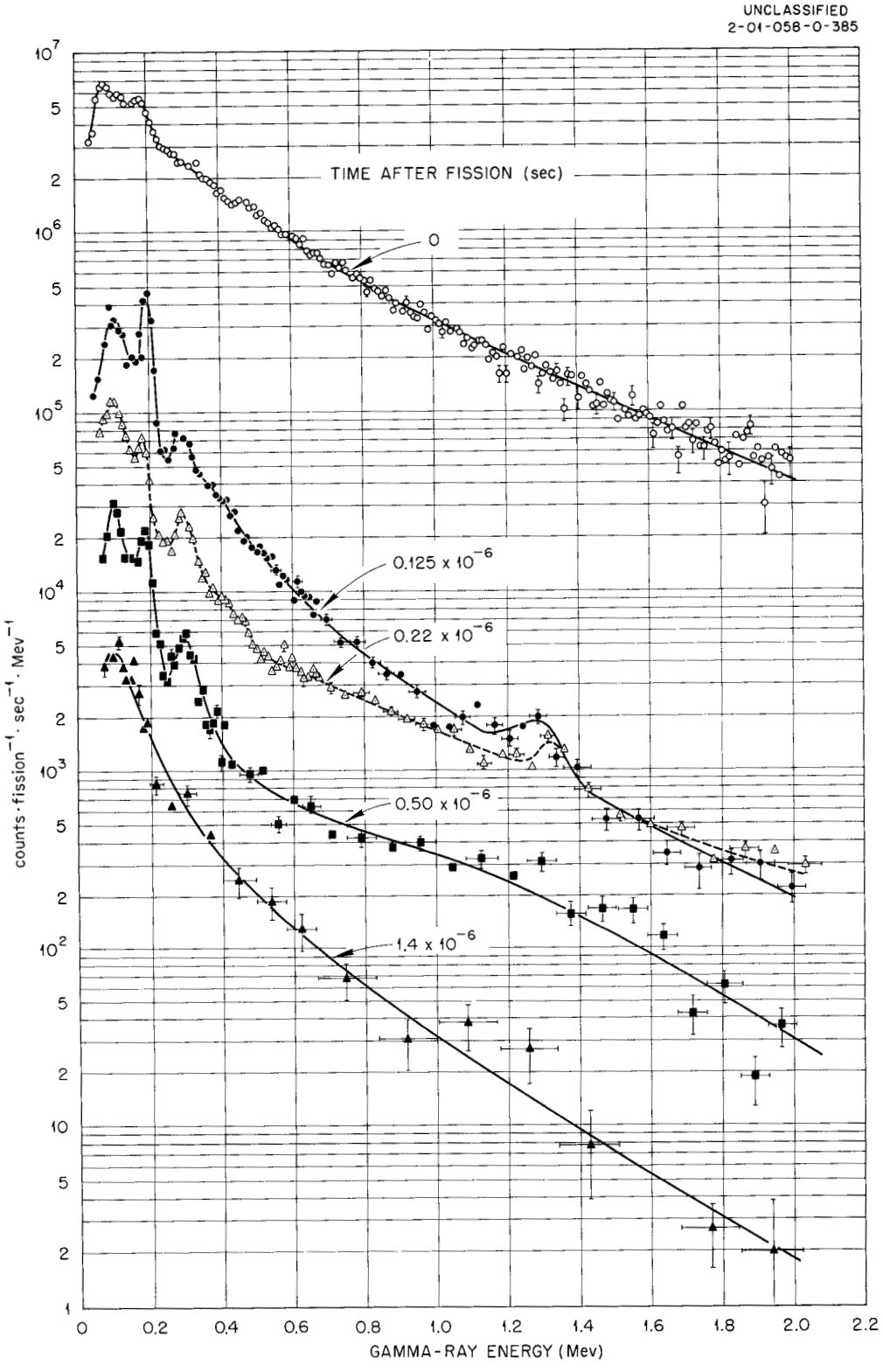

Fig. 4.2.1. Pulse-Height Spectra Observed at Short Times After Fission. The top curve represents the prompt radiation on an arbitrary scale. Random backgrounds have been subtracted, and lines are fitted to the points only to connect associated data.

 * See errata

this period may be important in consideration of the after-effects of nuclear explosions.[3]

If the observed gamma rays were to follow beta decay, the energy release would have to be very much larger than typical neutron binding energies. Therefore the short-period radiations described above are assumed to arise from primary fission products which are formed in isomeric states. While the above data extend only to 10^{-6} sec, the range to 10^{-5} sec has been surveyed. Random coincidence backgrounds were larger than the count rates which might have been present from any gamma radiation in this time region.

[3] S. Glasstone (ed.), *The Effects of Nuclear Weapons*, p 343, GPO, Washington, 1957.

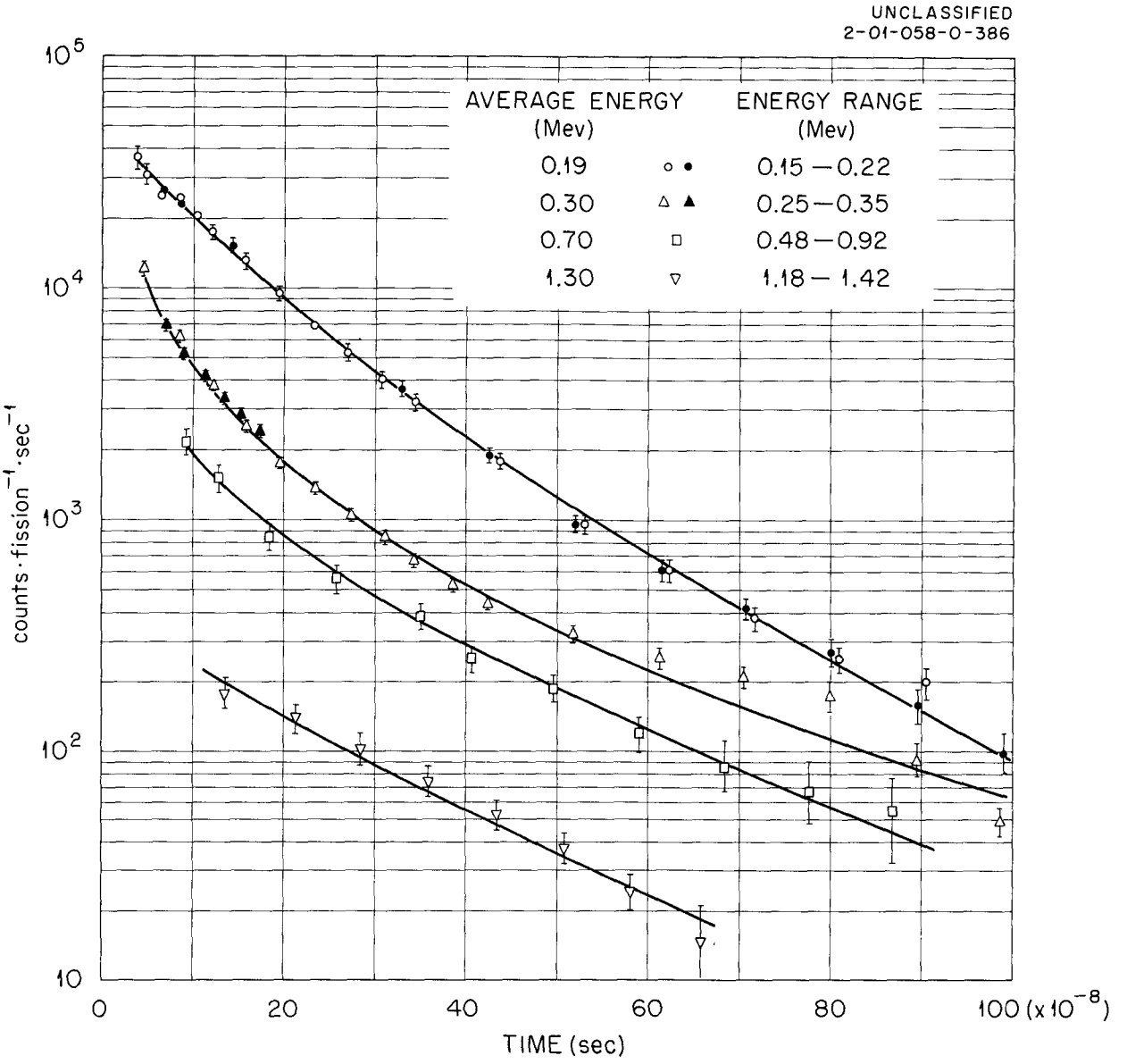

Fig. 4.2.2. Time Dependence of the Emission of Gamma Rays Within Selected Energy Groups for Times Less Than 10^{-6} sec After Fission. Corrections have been made for random backgrounds and the prompt gamma-ray contributions. Data have been combined for adjacent channels on the time analyzer. Before combination the time-channel width for most of the runs was $(9.3 \pm 0.2) \times 10^{-8}$ sec. The different symbols for a given energy group correspond to independent runs. The errors shown are determined from the number of recorded counts, and the lines are drawn only to connect related points. (Note that use of a small single sodium iodide crystal implies that these data correspond to pulse-height rather than energy groups.)

4.3. CHARACTERISTICS OF FISSION-PRODUCT GAMMA RAYS EMITTED FROM 1 TO 1800 sec AFTER THERMAL FISSION OF U^{235}

W. Zobel T. A. Love G. M. Estabrook R. W. Peelle

An experiment performed to measure the fission-product gamma-ray spectra from the thermal fission of U^{235} in the time range from approximately 1.7 to 1550 sec after fission was previously reported.[1] The importance of a knowledge of these spectra for certain shielding calculations was also discussed.[2] At that time it was pointed out that essentially no information was available from which such spectra could be determined, even though it appeared that about three-fourths of the total energy carried off by fission-product gamma rays might be emitted within the first hour (or less) after fission.

In a later report[3] a proposed method for the reduction of the data gathered during the fission-product gamma-ray experiment was described. Briefly, the difficulty involved the so-called "nonuniqueness" effect which is inherent in any spectrometer. It was proposed to remove the influence of this effect by inverting a matrix representing the spectrometer response and multiplying the experimental data by this inverse matrix. It was pointed out that, when this method was first tried, oscillations in the results were encountered, believed to be due to the peak (assumed Gaussian) of the response function. In order to confirm this assumption, a matrix was constructed in which the Gaussian peak of the response function was replaced by a rectangle one channel wide which had the same area as the peak. This matrix removes the influence of the "tail," which will affect results many channels away from a true gamma-ray line, but does not remove the influence on neighboring channels due to the broader "peak."

The results of the latest analysis, using this method, are shown in Figs. 4.3.1*a* and 4.3.1*b*. The new correction for the number of fissions, which was described previously,[3] is included in the calculations. For comparison, the results of the rotating belt experiment[2] are also shown.

Further calculations aimed at removing the influence of the peak are in progress.

---

[1] W. Zobel and T. A. Love, *Appl. Nuclear Phys. Ann. Rep. Sept. 10, 1956*, ORNL-2081, p 95.

[2] R. W. Peelle, W. Zobel, and T. A. Love, *Appl. Nuclear Phys. Ann. Rep. Sept. 10, 1956*, ORNL-2081, p 91.

[3] W. Zobel *et al.*, *Appl. Nuclear Phys. Ann. Prog. Rep. Sept. 1, 1957*, ORNL-2389, p 97.

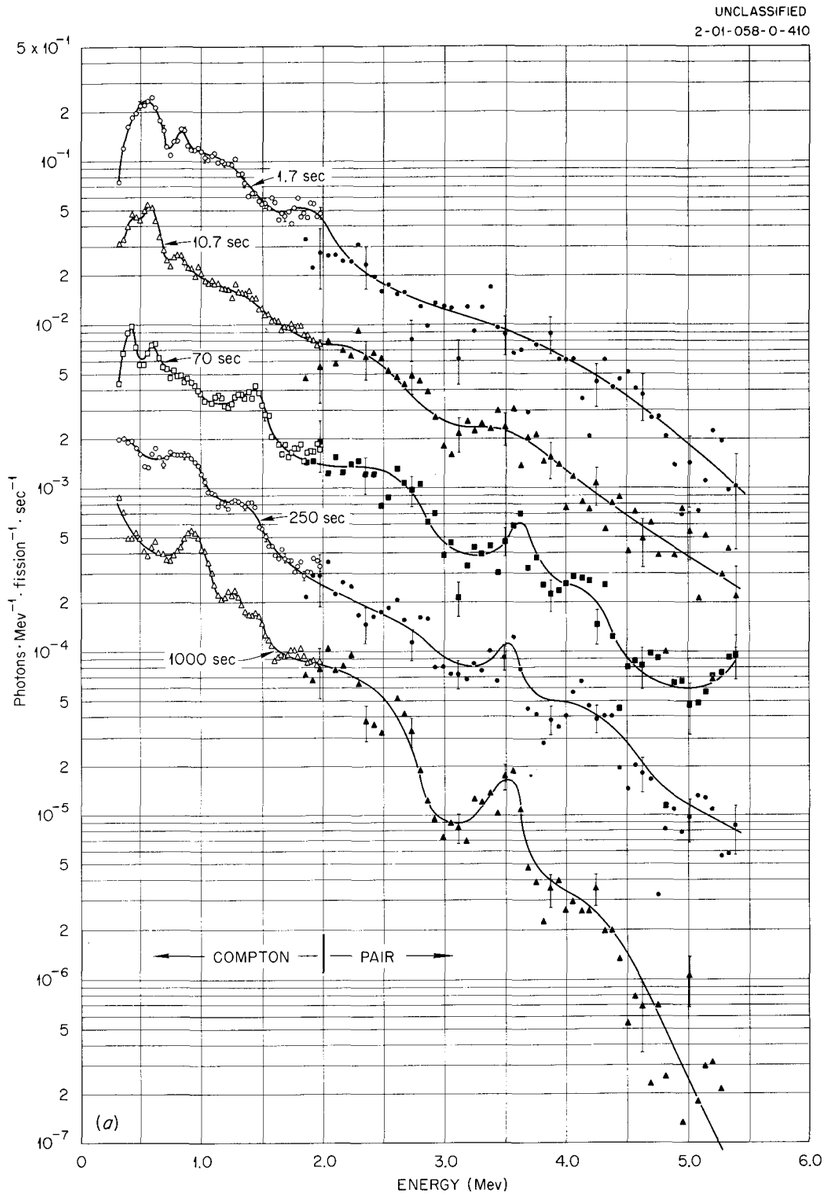

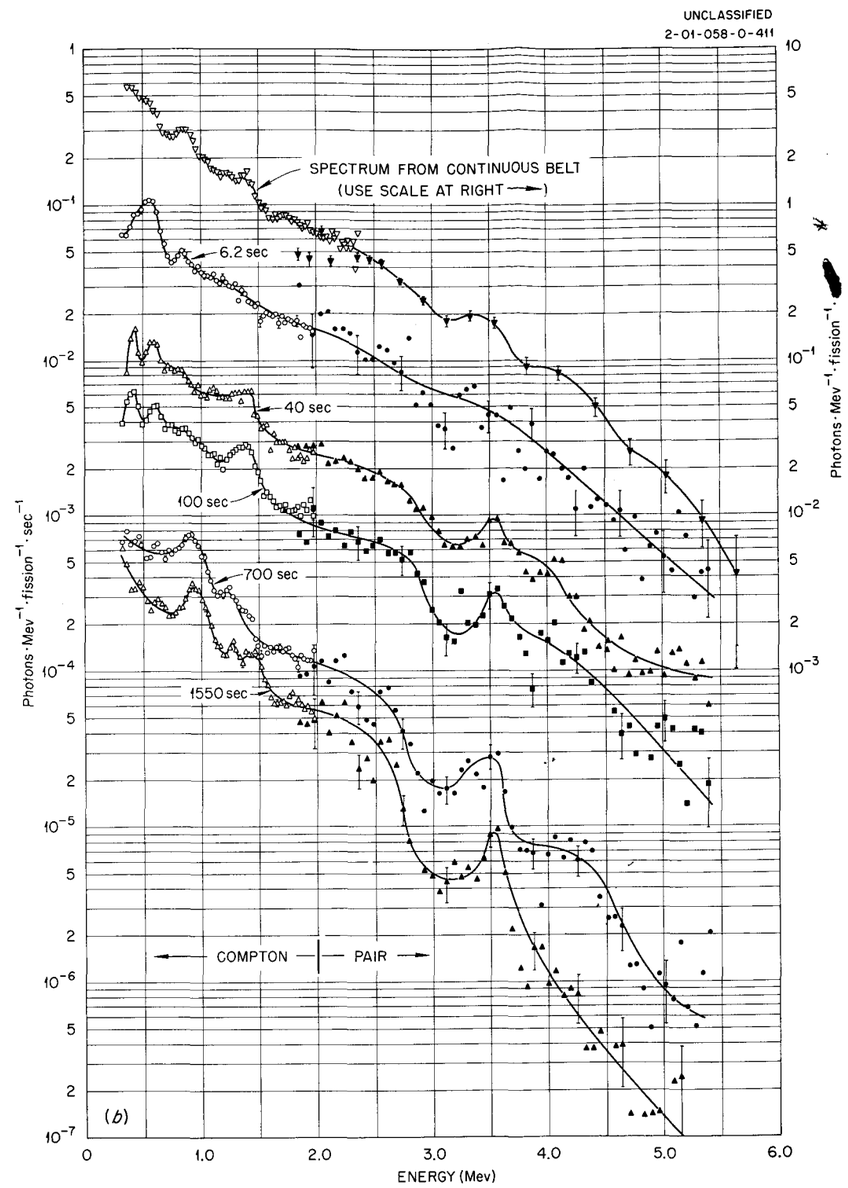

Fig. 4.3.1. Gamma-Ray Energy Spectra Observed at Long Times After Fission. The errors shown are a combination of counting statistics with other uncertainties. The lines were fitted to the points by eye. All data, except for the top curve in (*b*), were obtained at the stated times after fission. The top curve in (*b*) is the spectrum emitted from the continuous fuel belt about 8×10^3 sec after irradiation of the belt commenced (use right-hand scale). No response corrections were included in this top curve.

Part 5

EXPERIMENTAL REACTOR PHYSICS

5.1. AN INVESTIGATION OF THE SLOWING DOWN OF FISSION NEUTRONS IN WATER

T. V. Blosser D. K. Trubey E. P. Blizard

For several years a rather large discrepancy has existed between the experimentally determined age of fission neutrons to indium resonance energy (1.45 ev) in water and the computed age. Table 5.1.1 shows that attempts to measure this quantity have led to results that vary from 29.4 to 32.4 cm^2 (refs 1–4), all of which are considerably higher than the average computed value of 26.0 ± 0.5 cm^2 (ref 5). (Note added in proof: A recent unpublished experiment performed by F. H. Martens, R. C. Doerner, J. Haugsnes, and C. N. Kelber of Argonne National Laboratory yielded results which when corrected by W. E. Kinney of ORNL gave a value of 26.5 ± 0.5 cm^2 for the age in water.)

In an effort to explain why the computed results are consistently below those of the experiments, reviews of the calculations[5] have been made in which several possible sources of errors were examined. The effect of varying the oxygen cross section and the fission spectrum were especially investigated; however, none of the revisions produced differences of sufficient magnitude to resolve the discrepancy.

Table 5.1.1. Experimental and Computed Ages of Fission Neutrons Slowed to Indium Resonance Energy

Method	Age (cm^2)	Reference
Measured		
Hill, Roberts, and Fitch	30.8	*a*
Barkov and Mukhin	29.4 ± 1.5	*b*
Fermi, Anderson and Nagle	32.4	*c*
Wade	31 ± 1	*d*
Average	30 ± 1	*e*
Computed (average of eight calculations)	26.0 ± 0.5	*e*

[a]J. E. Hill, L. D. Roberts, and T. E. Fitch, *J. Appl. Phys.* 26, 1013 (1955).

[b]L. M. Barkov and K. N. Mukhin, *J. Nuclear Energy* 4, 91 (1957).

[c]E. Fermi, H. L. Anderson, and D. Nagle, *Nuclear Physics Research Report for Month Ending March 25, 1944*, CP-1531, p 6.

[d]J. W. Wade, *Nuclear Sci. and Eng.* 4, 12 (1958).

[e]Reported by H. Goldstein, P. F. Zweifel, and D. G. Foster, "The Slowing Down of Neutrons in Hydrogenous Media – Status of Theory and Experiment," *Proc. Intern. Conf. Peaceful Uses Atomic Energy, Geneva, 1958* (to be published).

Trubey *et al.*[6] made a comparison of the neutron distributions measured at large distances from fission sources in two independent experiments[1,7] and found them to be in reasonable agreement, which indicated that the disagreement in the age values may be due to differences in the distribution at small distances from the source. This prompted an experiment to further investigate the slowing down of fission neutrons to indium resonance energy, with emphasis on the measurements close to the source. The experiment, which is under way, largely consists in a study of various effects that may have been overlooked in the earlier experiments. The experiment is also designed to give information on the slowing down of fission neutrons to thermal energy and to gold energy (4.8 ev). In addition, the number of fission neutrons produced per thermal neutron absorbed in the fission source will be investigated.

It is the purpose of this paper to describe the experiment, to point out the effects which are being examined, and to explain the method for determining each of them. The method for performing the geometrical transformation to make the results apply for a point source and point detector is also described since it differs somewhat from the methods used in the earlier experiments.

[1]J. E. Hill, L. D. Roberts, and T. E. Fitch, *J. Appl. Phys.* 26, 1013–1017 (1955).

[2]L. M. Barkov and K. N. Mukhin, *J. Nuclear Energy* 4, 91–93 (1957).

[3]E. Fermi, H. L. Anderson, and D. Nagle, *Nuclear Physics Research Report for Month Ending March 25, 1944*, CP-1531, p 6.

[4]J. W. Wade, *Nuclear Sci. and Eng.* 4, 12 (1958).

[5]H. Goldstein, P. F. Zweifel and D. G. Foster, "The Slowing Down of Neutrons in Hydrogenous Media – Status of Theory and Experiment," *Proc. Intern. Conf. Peaceful Uses Atomic Energy, Geneva, 1958* (to be published).

[6]D. K. Trubey, H. S. Moran, and A. M. Weinberg, *Appl. Nuclear Phys. Ann. Prog. Rep. Sept. 1, 1957*, ORNL-2389, p 158.

[7]D. W. Cady and E. A. Warman, *Appl. Nuclear Phys. Ann. Prog. Rep. Sept. 1, 1957*, ORNL-2389, p 180.

Experimental Arrangement

Basically, the arrangement being used in this experiment is the same as that used in the earlier experiments.[1-4] A uranium source is placed in water, and neutrons are detected with cadmium-covered indium foils at various distances from the source. In this experiment the sources, which are of various sizes, consist of 93.15% U^{235}-enriched uranium metal foils which are placed near the bottom of a tank of water positioned over the thermal column on top of the ORNL Graphite Reactor. The fissions in the source are thus largely produced by thermal neutrons from the reactor, and measurements of the neutron distribution in the water are made at various distances above the source.

In order to investigate the various experimental effects, most of which concern the source and detector, it became necessary to fabricate a versatile source and detector holder which would make it possible not only to easily change the sources and detectors but also to know the source-detector separation distance within 0.1 cm at all times. Furthermore, it was necessary that the source-detector holder be made of a material that would affect the neutron distribution as little as possible.

The source-detector supports used by the earlier investigators were made of aluminum or stainless steel. Bothe,[8] Rush,[9] and Tittle[10] have pointed out that the presence of such materials in the medium perturbs the flux. The material chosen for the source-detector holder in this experiment is Lucite since it has been shown experimentally[10,11] that when measurements are made in water small amounts of Lucite in the vicinity of the source and detector do not cause a measurable change in the neutron flux distribution.

A sketch of the source-detector holder is shown in Fig. 5.1.1. The 2.5-in.-dia lead ring at the bottom of the holder rests on the bottom of the thermal column tank, and the source foil is embedded in the 0.040-in.-thick Lucite disk immediately above it. The other Lucite disks support the detector foils. The disks for the detector foils have indentures machined in them just large enough to accept the foils, which, like the source, vary in size. Lucite covers 0.040 in. thick are placed over the indentures, with thin films of petroleum jelly placed between the covers and the disks to make the unit watertight. All the disks can be moved to any position along the holder by the use of plastic set screws. A gold-foil power monitor is also shown in Fig. 5.1.1.

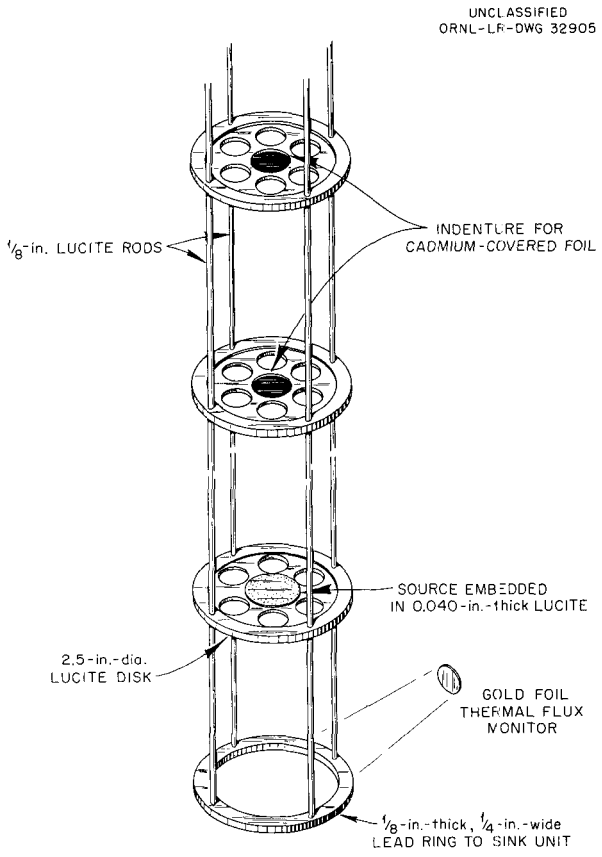

Fig. 5.1.1. Source-Detector Holder for Neutron Age Experiment.

Investigation of Experimental Effects

Four possible experimental effects are being investigated: (1) the effect of the water-graphite boundary on the flux within the noninfinite medium, (2) the effect of the detector on the flux detected, (3) the effect of the size of the source, and (4) the effect of the detector on the flux impinging on the source. The latter effect is observable only for short source-detector separation distances.

---

[8] W. Bothe, *Z. Physik* 120, 437 (1943); translated by S. R. Schram and issued as *The Use of Neutron Detectors*, CP-2964 (June 22, 1945).

[9] J. H. Rush, *Phys. Rev.* 73, 271 (1948).

[10] C. W. Tittle, *Nucleonics* 8(6), 5 (1951); also *Nucleonics* 9(1), 60 (1951).

[11] J. L. Meem and H. E. Hungerford, ORNL-1147 (April 30, 1952) (classified).

Effect of the Water-Graphite Boundary. – In order to determine the effect of the water-graphite boundary on the measured flux, a series of measurements is being made with the source positioned at various distances (0 to 15 cm) from the bottom of the water tank (that is, at various distances from the water-graphite boundary) while the source-detector separation distance is kept constant.

Effect of the Detector on the Detected Flux. – In order to establish that the same quantity is being measured by a foil at different source-detector distances, corrections must be applied to remove the effects of flux depression and self-shielding and the effect of suppressing the resonance neutrons by the cadmium covers. For water, these effects, which apparently were not all corrected for in the earlier measurements, are expected to be significant because of the anisotropy of the neutron flux and the small absorption mean free path. These are being determined experimentally by using indium detectors of different thicknesses (0.045 to 100 mg/cm^2) with cadmium covers of different thicknesses (0.015 to 0.060 in.).

The effect of varying the thickness of the cadmium cover on a 1.11-cm-dia indium foil 0.0127 cm thick is shown in Fig. 5.1.2. For these measurements the source was 1.9 cm in diameter and 0.1016 in. thick, and it was positioned 9.65 cm from the bottom of the water tank.

When logarithms of the saturated activities are plotted as a function of the cadmium thickness, the straight-line portion of the curve represents the attenuation of the epicadmium neutrons by the cadmium cover. The sharp rise in the curve for the 4.52-cm source-detector separation distance and thin cadmium cover thicknesses indicates that the cadmium did not filter out all of the thermal neutrons. An extrapolation of the straight-line portion of the curve to a zero cadmium thickness permits an evaluation of the correction factor. The fact that the curves in Fig. 5.1.2 have different slopes indicates that the effect of the cadmium cover varies with the source-detector separation distance. Values for the solid lines in the figure were computed by the method of least squares.

Effect of the Source Size. – In order to determine the flux perturbation by the source, sources of various sizes are being used. The foils will vary in thickness from 0.001 to 0.010 in. and in diameter from 0.5 to 12.35 cm. The larger sources will, of course, require a larger source holder than the one described above. The observed fluxes will be compared with computed values.

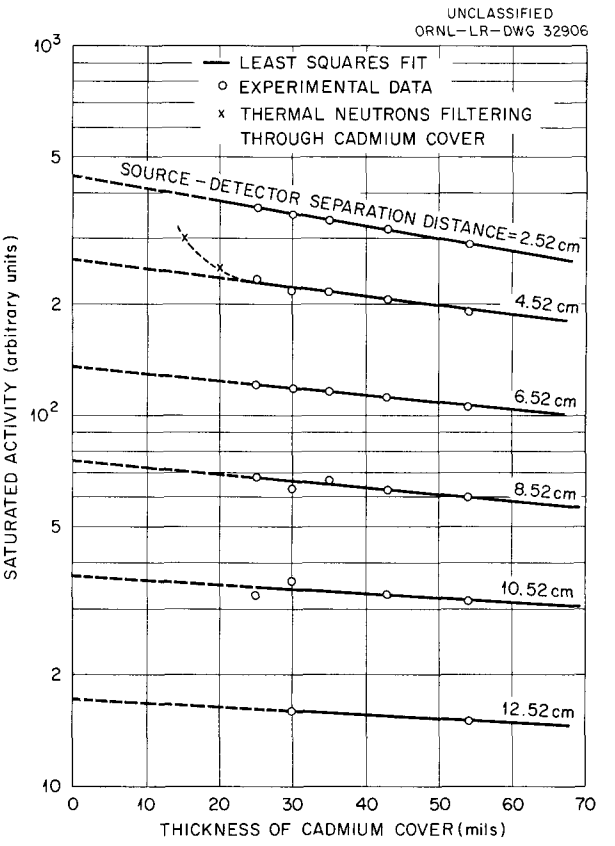

Fig. 5.1.2. Effect of Thickness of the Cadmium Covers on the Detector Response for Various Source-Detector Separation Distances.

Effect of the Detector on the Source. – When measurements are being made for small source-detector separation distances (2 to 3 diffusion lengths), the cadmium cover over the detector foil perturbs the thermal-neutron flux impinging on the upper side of the source. This reduction in the flux impinging on the source reduces the source strength and hence the indium foil activity. This effect is being investigated by measuring the gold-foil activity on each side of the source as the distance between the source and detector is varied. The effect for an indium foil with a 0.030-in.-thick cadmium cover is shown in Fig. 5.1.3. The curve at the top represents the activity on the side of the source nearest the thermal column, while the curve at the bottom represents the activity on the side of the source opposite the thermal column.

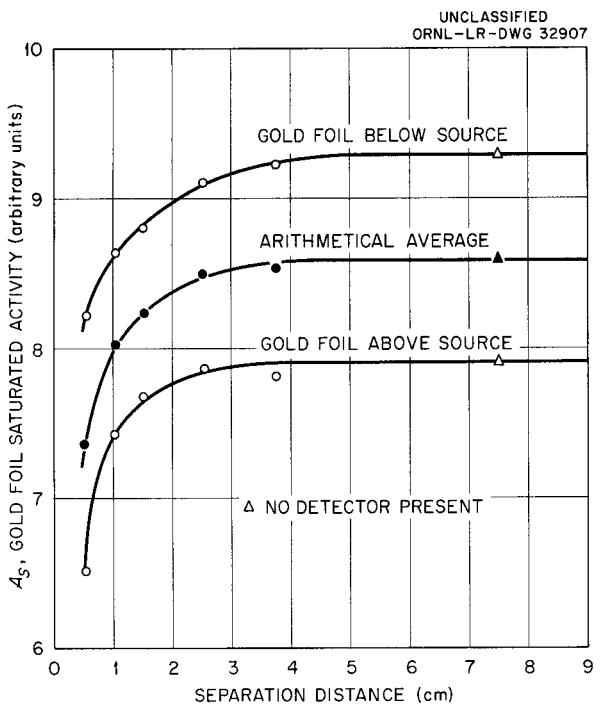

Fig. 5.1.3. Source Intensity as a Function of the Source-Detector Separation Distance.

The gold foils used for these measurements were 2 cm in diameter and 0.00254 cm thick.

The relative fission rate in the source was determined from the activation of these two thin gold foils. It was assumed that the attenuation of the outgoing fission neutrons in the foils was negligible, and the source strength was taken to be proportional to a simple arithmetic average of the gold foil activities.

Geometrical Corrections

Since a more intense source must be used for large source-detector separation distances, the size of the source or detector must be increased in either diameter or thickness. In order to reduce all the data obtained with the various source-detector configurations to a point source–point detector kernel, geometrical corrections must be applied. An Oracle program has been written to perform the geometrical transformation by numerically integrating a point-to-point kernel over the source and detector areas.

The transformation is performed by defining A as the ratio of the experimental detector response to the detector response in a point source–point detector geometry:

$$A(R_0) = \frac{\iint G(R)\, dS\, dS'}{G(R_0) \iint dS\, dS'},$$

where

R_0 = separation distance of foils,

$G(R)$ = point-to-point kernel,

dS, dS' = differential source and detector areas, respectively.

If values for the kernel $G(R)$ are assumed, a set of values for A may be computed. Dividing the measured data by the values of A yields a new kernel, which can be used to compute a better set of values of A. When the values of A have converged, the true point-to-point kernel is known. This is in contrast to previous work, in which the kernel $G(R)$ was approximated so that the transformation could be performed analytically.

5.2. TIME-DEPENDENT NEUTRON DIFFUSION MEASUREMENTS

G. deSaussure E. G. Silver

An experiment to measure the neutron diffusion properties of crystalline moderators at various temperatures by the pulsed-neutron technique is in progress. The theory of the method and a description of the experimental arrangement, as well as some preliminary measurements of diffusion constants in beryllium and graphite at room temperature, have been reported previously.[1]

Essentially, the method consists in irradiating a sample of the moderator under investigation with a short burst of neutrons and then observing the decay of the neutron population in the sample. After decay of higher modes, the neutron density at a point $\vec{r}$ and at a time t can be described as

$$n(\vec{r},t) = S(\vec{r})\, e^{-\lambda t} \quad , \tag{1}$$

where

$$\lambda = \lambda_a + DB^2(1 - CB^2) \tag{2}$$

and $S(\vec{r})$ and B^2 are respectively the fundamental eigenfunction and the eigenvalue of the equation

$$\Delta S = B^2 S \quad , \tag{3}$$

which satisfies the proper boundary conditions.

In Eq. 2, λ_a is the reciprocal of the mean lifetime τ_a, D is the diffusion coefficient, and C is the diffusion cooling constant. The significance of the three parameters τ_a, D, and C has been discussed elsewhere.[1-4]

The main purpose of the experiment now being performed is to determine the variation of the two diffusion parameters D and C with temperature in beryllium. (The mean lifetime of thermal neutrons in a $1/v$ absorber should not depend on temperature.) Equipment is now being built to facilitate these measurements; however, precise determinations of the three diffusion parameters in beryllium at room temperature have already been made with a 200-kv accelerator in the ORNL Van de Graaff building. These measurements are reported below, along with preliminary measurements of the diffusion parameters in beryllium at liquid-nitrogen temperature.

Diffusion Parameters of Beryllium at Room Temperature

The decay rate of the neutron population has been measured in 11 blocks of beryllium having bucklings ranging from 0.8×10^{-2} to 7.2×10^{-2} cm^{-2}. Figure 5.2.1 shows the decay constants for these blocks as a function of their bucklings. A parabola has been fitted to the experimental points by the method of least squares. The diffusion parameters

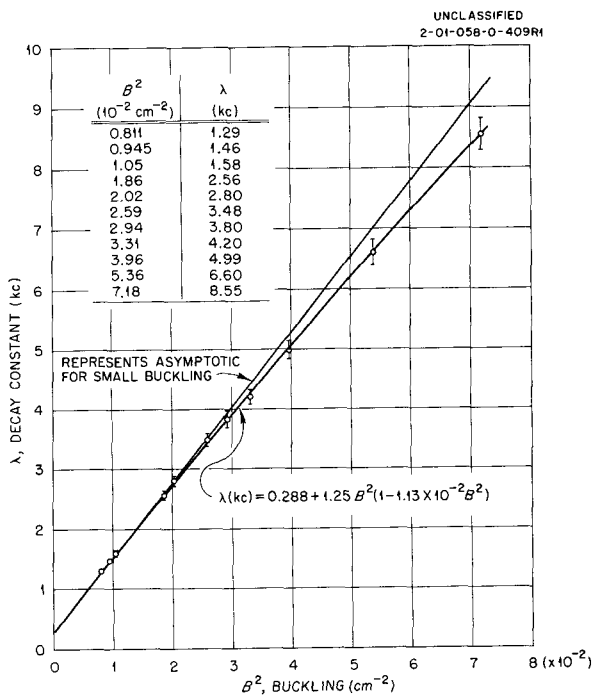

Fig. 5.2.1. Thermal-Neutron Decay Constant as a Function of Buckling for Beryllium at Room Temperature.

[1] G. deSaussure and E. G. Silver, *Appl. Nuclear Phys. Ann. Prog. Rep. Sept. 1, 1957*, ORNL-2389, p 119.

[2] A. M. Weinberg and E. P. Wigner, *Preliminary Draft, Theory of Neutron Chain Reactions*, ORNL CF-56-11-43, vol I, p 8.35 (1956).

[3] M. Nelkin, *The Diffusion Cooling of Neutrons in a Finite Moderator*, GA-248 (1958).

[4] G. von Dardel and N. G. Sjöstrand, p 183 in *Progress in Nuclear Energy, Series 1, Physics and Mathematics*, vol 2 (ed. by D. J. Hughes, J. E. Sanders, and J. Horowitz), Pergamon Press, New York, 1958.

corresponding to the coefficients of this parabola are presented in Table 5.2.1 with other values measured by the pulsed-neutron source method by various groups. In the last line of this table are also given calculated values of the three parameters. All the values of Table 5.2.1 were normalized to a beryllium density of 1.85 g/cc.

The values in Table 5.2.1 show that there is reasonable agreement among all the determinations of the diffusion coefficient D but that there are significant discrepancies among those of the diffusion cooling constant C. This constant can best be measured in small blocks (large bucklings), where the diffusion cooling effect is expected to be important. For this reason an attempt has been made in this experiment to measure the decay of very small blocks with bucklings larger than those used by the other groups.

Measurements with Beryllium at Liquid-Nitrogen Temperature

An attempt was made to determine the decay period of the neutron density in some blocks of beryllium at liquid-nitrogen temperature (100°K). Beryllium prisms, assembled in brass cans lined inside with 30-mil-thick cadmium foils, were cooled to the temperature of liquid nitrogen by immersion in a liquid-nitrogen bath. Measurements were started only after the assembly had been in the cold bath long enough for the liquid-nitrogen temperature to be attained throughout the block, as shown by inserted thermocouples. The measurements have thus far yielded inconclusive and somewhat nonreproducible results. Figure 5.2.2 shows a typical decay curve; on the same figure is also shown the decay curve of the same block, over the same time interval, at room temperature. From this figure it is apparent that at liquid-nitrogen temperature the neutron population does not decay exponentially and that it decays more slowly than at room temperature.

These results are perhaps not too surprising, considering that at liquid-nitrogen temperature the cross section for neutron inelastic scattering is much smaller than at room temperature, corresponding to an energy interchange transport mean free path of the order of 1 m or more.[5] Thus the neutron population in a block of beryllium of moderate size (14 in. on each edge, for instance) never reaches an equilibrium and therefore each energy group decays independently. Experiments with large blocks of beryllium at 100°K are being prepared.

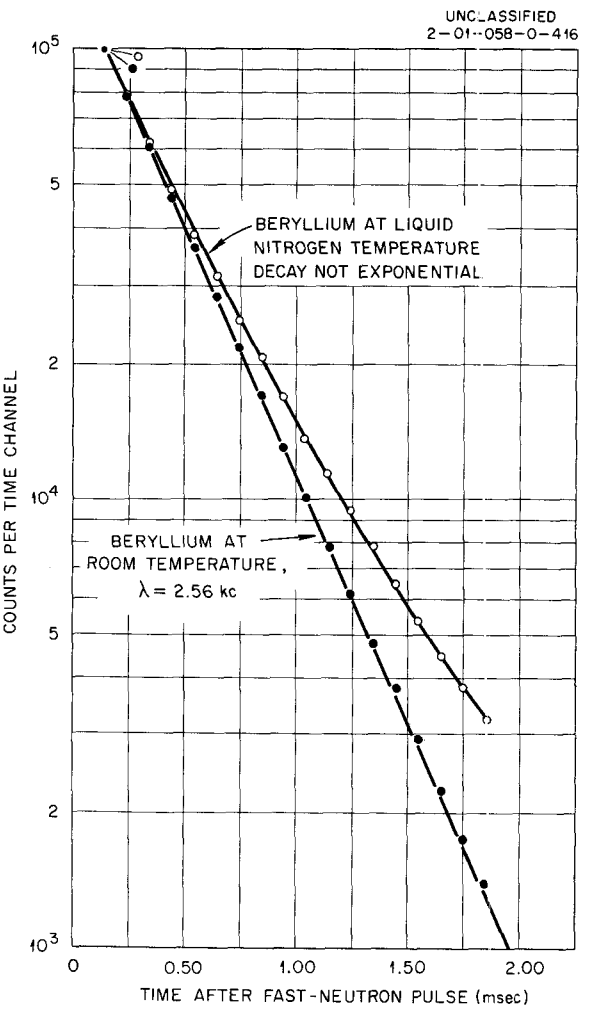

Fig. 5.2.2. Decay Curve of the Neutron Population in a Beryllium Block with Buckling $B^2 = 1.86 \times 10^{-2}$ cm^{-2}.

Construction of Equipment for Measurements at High Temperatures

No measurement of the neutron diffusion constants of beryllium at temperatures higher than room temperature has yet been made, but a particle accelerator has been assembled in Building 3010 (see Sec. 5.3) and a furnace has been designed and is being fabricated. The measurements at high temperatures will be started in the near future.

[5] D. J. Hughes, *Pile Neutron Research*, p 252, Addison-Wesley, Cambridge, Mass., 1953.

Table 5.2.1. Neutron Diffusion Parameters for Beryllium at Room Temperature

(Corrected to a density of 1.85 g/cc)

Authors	λ_a (sec^{-1})	D (cm^2/sec)	C (cm^2)	Range of B^2 Used (cm^{-2})	Reference
		$\times 10^5$			
Antonov *et al.*		1.17 ±0.05	2.5 ±0.9	0.008–0.061	*a*
Campbell and Stelson	150	1.25	0	0.005–0.036	*b*
Komoto and Kloverstrom	270 ± 19	1.24 ±0.04	3.15 ±0.65	0.003–0.041	*c*
deSaussure and Silver	288 ±60	1.25 ±0.06	1.1 ±0.9	0.008–0.072	
Calculated values	270 ±30	1.21	1.1		*d*

[a]A. V. Antonov *et al.*, *Proc. Intern. Conf. Peaceful Uses Atomic Energy, Geneva, 1955* 5, 3 (1956).

[b]E. C. Campbell and P. H. Stelson, *Phys. Semiann. Prog. Rep. March 10, 1956*, ORNL-2076, p 32.

[c]T. T. Komoto and F. Kloverstrom, *Diffusion Cooling in Beryllium and Graphite*, ~~1958 Annual Meeting~~ Transactions of the American ~~Physical Society~~ Nuclear Society, June ~~2~~, 1958, Session 11-1, vol. 1, p. 94.

[d]λ_a was calculated from the value $\sigma_a = 10 \pm 1$ mb given by D. J. Hughes and J. A. Harvey, *Neutron Cross Sections*, BNL-325 (July 1, 1955); D was calculated by R. C. Bhandari, *J. Nuclear Energy* 6, 104–112 (1957); and C was calculated by M. Nelkin, *The Diffusion Cooling of Neutrons in a Finite Moderator*, GA-248 (1958).

5.3. A 300-kv PARTICLE ACCELERATOR

J. D. Kington

A new particle accelerator has been designed[1] and constructed for the Bulk Shielding Facility. This accelerator, shown in Fig. 5.3.1, will make 300 kv available for accelerating charged particles, with major emphasis on protons and deuterons. Thus with the proper targets either neutrons or gamma rays of discrete energies may be produced.

The accelerator will be used to produce neutrons from the D-T reaction for the time-dependent neutron diffusion experiment (see Sec. 5.2). It will also be used to calibrate spectrometers. Neutron calibration will be provided by 2.5-Mev neutrons from the D-D reaction and 14-Mev neutrons from the D-T reaction. Gamma-ray calibrations will make use of the 4-, 12-, and 16-Mev gamma rays from the $B^{11}(p,\gamma)C^{12}$ reaction. It should also be possible to use the 6- and 7-Mev gamma rays from $F^{19}(p,\alpha\gamma)O^{16}$. Future neutron physics experiments in which the accelerator will be used may include studies of angular distributions and attenuation of monoenergetic neutrons in an infinite medium of water.

[1]By F. Duncan and F. Glass, Instrumentation and Controls Division.

The accelerator, which is horizontal, is portable and may be moved with little effort anywhere within a screened 12 × 30 ft area. Also, it is quite small, since a rotating cylinder instead of a belt is used as the charging device; otherwise the power supply of the accelerator is similar in principle to that of a Van de Graaff accelerator. This supply plus the auxiliary supply for equipment at the high voltage end of the accelerator is located on the floor above the accelerator. The power is fed to the head of the accelerator through the floor by carefully terminated cables. Electrical shielding is accomplished through the use of wire screening around the high potential portions of the accelerator, with interlocks at every entrance through this screen. Neutron shielding is accomplished with 34-in.-thick water tanks placed between the target and building personnel.

Initial operation proceeded smoothly and progressed rapidly to the rated 300 kv with no sparking or corona. Operations to date have employed beam currents to 200 μa, but larger currents are anticipated for future operations.

See errata

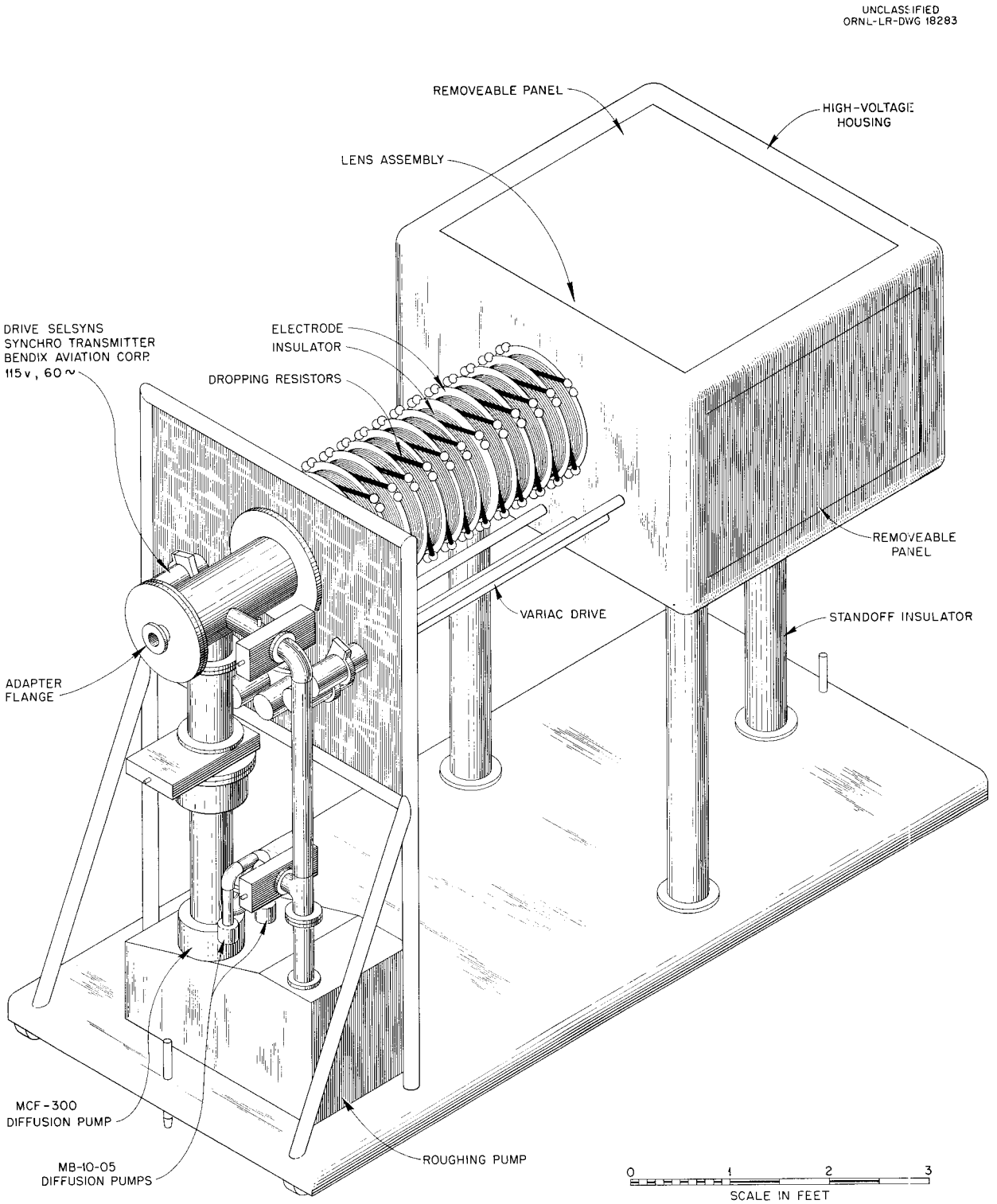

Fig. 5.3.1. 300-kv Proton Accelerator at the BSF.

Part 6

REACTOR THEORY

6.1. RESONANCE ABSORPTION OF NEUTRONS IN NUCLEAR REACTORS[1]

L. Dresner

A detailed theoretical study of resonance absorption of neutrons in nuclear reactors has been concluded. During this study formulas were determined for the effective resonance integral of single resonances for the narrow resonance approximation in homogeneous media and for both the narrow resonance and the "infinite mass absorber" approximations in heterogeneous media.

In homogeneous media it was found that the Doppler effect can be expressed through a certain function of two variables, $J(\xi,\beta)$, the properties of which were studied in detail. The effect of interference between resonance and potential scattering on the effective resonance integral for homogeneous media was also studied.

In heterogeneous media in the narrow resonance case it was found that the Doppler effect can again be expressed through the function $J(\xi,\beta)$ if Wigner's rational approximation for the average escape probabilities is introduced. Furthermore, it was shown that then a formal identity exists between the homogeneous and heterogeneous cases for narrow resonances. The error caused by Wigner's rational approximation was studied in detail, and in the case of no Doppler broadening and no interference scattering an improved formula was suggested.

In heterogeneous media in the infinite mass absorber case an approximate expression for the albedo of an absorber lump was suggested on the basis of heuristic arguments. Precise calculations of the albedo based on a variational method of solving the monoenergetic transport equation were compared with this approximation and showed it to be quite accurate. By using this approximate albedo, the Doppler effect for heterogeneous media for the infinite mass absorber case could also be expressed through the function $J(\xi,\beta)$. The effect of interference between potential and resonance scattering was also studied for the infinite mass absorber approximation in heterogeneous media.

The resulting formulas were used in a calculation of the absorption in low-energy resolved resonances for which the widths and energy were known. In the region beyond the experimental limit of resolution statistical considerations were employed. The formulas for single resonances were averaged over the probability distributions of the partial widths. The theory was then applied to the calculation of the effective resonance integrals of uranium and thorium rods, and good agreement was obtained for uranium and fair agreement for thorium.

At high energies resonance absorption cross sections fall sufficiently low to permit the flux depression effects to be neglected, and attention is focused on average reaction cross sections. A study of the effect of fluctuations in the partial widths on average reaction cross sections was made. Some general theorems were derived which are independent of the probability distributions of the widths. If the widths are distributed in member distributions of the chi-squared family, it can be shown that the multiple integrals over these distributions which express the averages $\langle \Gamma_s \Gamma_t / \Gamma \rangle$ can be reduced to a single infinite integral. This integral was evaluated in the 18 most simple cases of interest. A Monte Carlo code for the Oracle electronic computer for evaluating these averages was programed. It was shown that enough experimental data on neutron reactions in U^{238} exists below 500 kev to overdetermine the *s*-, *p*-, *d*-, and *f*-wave strength functions. Analysis of the data, including the important effects of fluctuations in the width, yielded consistent values for the strength functions, in support of the theory. Finally, the statistical formalism of Hauser and Feshbach[2] was transformed from the channel spin representation to one which is more convenient in the presence of spin-orbit coupling. The effect of small amounts of spin-orbit coupling in the analysis of the U^{238} reaction data was found to be unimportant. It was proved that the total cross section, the compound nucleus formation cross section, and, under certain circumstances, the radiative capture cross section are independent in first order of spin-orbit coupling in the neutron-nucleus interaction.

[1] This paper is an abstract of a doctoral thesis which has been submitted to the Graduate School of Princeton University. Because the entire study covered a period of several years, some of the work mentioned here has been reported in *Appl. Nuclear Phys. Ann. Rep. Sept. 10, 1956*, ORNL-2081, pp 116, 121, and 128, and in the *Appl. Nuclear Phys. Ann. Prog. Rep. Sept. 1, 1957*, ORNL-2389, pp 134, 138, and 143.

[2] W. Hauser and H. Feshbach, *Phys. Rev.* **87**, 366 (1952).

6.2. ON THE CONNECTION BETWEEN NEUTRON FLUX AND SLOWING-DOWN DENSITY

L. Dresner

In order to facilitate easy solution of the linear Boltzmann equation, three approximate expressions have been suggested for connecting the lethargy flux, $\phi(u)$, and slowing-down density, $q(u)$. These expressions are all of the form[1]

$$q(u) = (\xi\Sigma_s + \theta\Sigma_a)\,\phi(u) \quad , \tag{1}$$

where ξ is the average lethargy gain per collision and Σ_s and Σ_a are the macroscopic scattering and absorption cross sections, respectively. In the most elementary approximation $\theta = 0$, but the resulting expression is correct only for a non-absorbing medium, that is, for $\Sigma_a = 0$. If the ratio $\beta = \Sigma_a/\Sigma_s$ is both *small* and *slowly varying*, the effects of absorption may be included in first or second order in β by setting $\theta = \xi$ or γ, respectively, where $2\gamma\xi$ is the mean squared lethargy gain per collision. Equation 1 is a series of approximations to the case in which β is slowly varying but not small,[2] whence q and ϕ are connected by the equation

$$q(u) = \frac{\Sigma_a}{\lambda}\phi(u) \quad , \tag{2}$$

where λ is given by

$$1 + \beta = \frac{\Sigma_t}{\Sigma_s} = \frac{1 - \alpha^{1-\lambda}}{(1-\lambda)(1-\alpha)} \quad . \tag{3}$$

Here $\alpha = [(A-1)/(A+1)]^2$, where A is the mass of the moderating nucleus and Σ_t is the total cross section. Finally, since $dq/du = -\Sigma_a\phi$ in an infinite medium, it follows from Eq. 2 that the resonance escape probability is approximately given by

$$P(u) = \exp\left[-\int_0^u \lambda(u')du'\right] \quad . \tag{4}$$

In order to test the validity of these approximate formulas a particular class of problems has been solved exactly and comparisons have been made with the corresponding approximate results.

The resonance escape probability through a region of absorption which varies exponentially with lethargy has been calculated exactly.[3] The ratio β was taken to be zero up to a lethargy remote from the source lethargy and then to vary as $\beta_0 e^{-\kappa u}$. Numerical results were obtained for heavy moderators.

Exact calculations of P as a function of β for $\kappa = 1/\epsilon$ are plotted in Fig. 6.2.1, as well as four approximate calculations based on Eqs. 1 and 4. Here ϵ is the maximum lethargy gain per collision. The curves labeled "Fermi," "Wigner," and "Goertzel-Greuling" correspond to Eq. 1 with $\theta = 0$, ξ, and γ ($\sim\frac{2}{3}\xi$), respectively. The curve labeled "Hurwitz" corresponds to Eq. 4. For $P \geqq 0.20$ the Hurwitz and Goertzel-Greuling approximations are essentially exact and represent a substantial improvement over the Wigner or Fermi approximation. For $0.20 \geqq P \geqq 0.03$ all the approximations fail to some extent, although that of Hurwitz is best. For smaller values of κ and the same P as for $\kappa = 1/\epsilon$ better agreement would be expected with the Hurwitz approximation since the ratio Σ_a/Σ_s is smaller and more slowly varying. As κ increases, the curve labeled "exact" might be expected to approach Wigner's approximation since the latter is correct for a very thin absorbing spike. Figure 6.2.2, which is similar to Fig. 6.2.1 except that $\kappa = 2/\epsilon$, shows this effect clearly. Here the curve labeled "exact" lies above the Hurwitz approximation, whereas in Fig. 6.2.1 it lies below it.

The resonance escape probability P is a better index of the applicability of the Hurwitz approximation than the absorption-to-scattering parameter, A. For $\kappa \leqq 2/\epsilon$ and $P \geqq 0.20$ the Hurwitz approximation is probably adequate. For $\kappa \leqq 1/\epsilon$ and $P \geqq 0.20$ it gives essentially exact results. Considering that $\kappa = 2/\epsilon$ corresponds to a cross section which falls by a factor of e (= 2.718) in a lethargy interval ξ, the applicability of the Hurwitz approximation is very wide indeed.

[1] H. Soodak, F. Adler, and E. Greuling, *The Reactor Handbook*, vol 1, chap. 1.3, p 365, AECD-3645, (March 1955).

[2] H. Hurwitz, Jr., as quoted by G. M. Roe, *The Absorption of Neutrons in Doppler Broadened Resonances*, KAPL-1241, p 81 (Oct. 15, 1954).

[3] L. Dresner, *On the Connection Between Flux and Slowing-Down Density*, ORNL-2594.

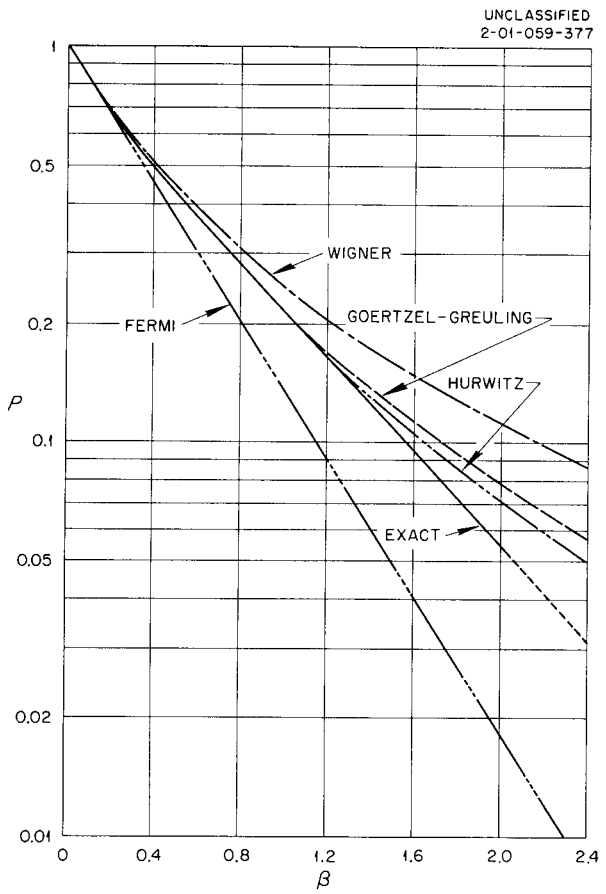

Fig. 6.2.1. Calculation of P as a Function of β for $\kappa = 1$.

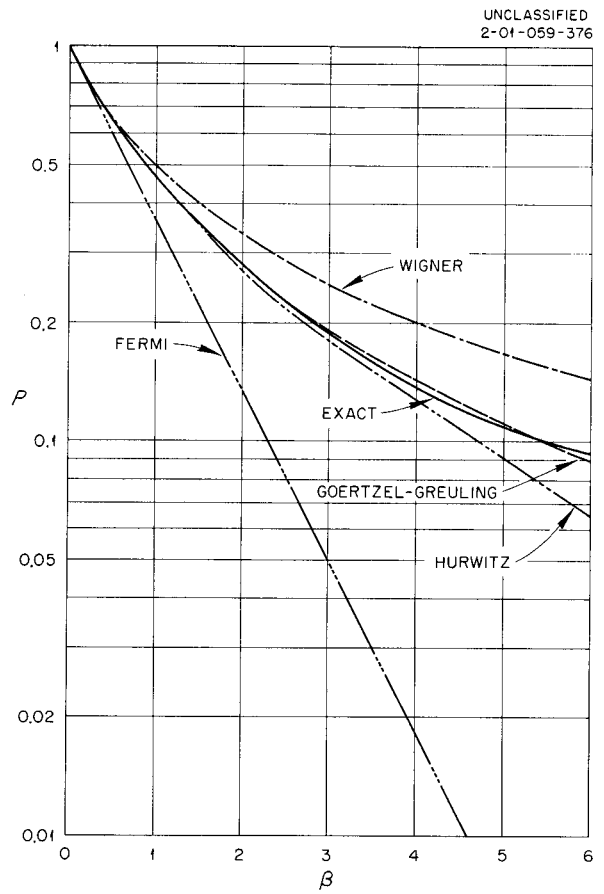

Fig. 6.2.2. Calculation of P as a Function of β for $\kappa = 2$.

6.3. COMPARISON OF THEORETICAL STUDIES OF UNREFLECTED AQUEOUS U^{235} CRITICAL ASSEMBLIES WITH EXPERIMENTS[1]

R. Gwin R. H. Lessig[2] D. K. Trubey A. M. Weinberg

An extensive program for investigating neutron chain-reacting assemblies of aqueous solutions of fissionable uranium isotopes has been in progress at ORNL for a number of years. The results of many of the experiments established the critical dimensions of the solutions, and these experiments have been analyzed by several well-known methods which differ in the manner of treating the energy degradation of neutrons by water.[3] Most of these works have been concerned with reflected systems. The present paper deals exclusively with unreflected uranyl fluoride solutions ($U^{235}O_2F_2$-H_2O), and the experimental data available for this analysis are better than most of the previously published data in that the effect of neutron reflection back into the system has been largely eliminated. In the theoretical analysis the empirical kernel method, rather than the more customary Goertzel-Selengut approximation, is employed.

The main purpose of this paper is to examine the limitations of the empirical kernel method when applied to unreflected reactors in which the extrapolation distance varies with neutron energy and in which there is appreciable resonance fission. The paper is divided into two parts: a review of the empirical kernel method as applied to unreflected systems and a comparison of the critical geometric buckling, as derived from experimental results, with the prediction of material buckling by the empirical kernel method.

Formulations of the critical conditions using a kernel are not new in the literature, but in most cases an approximate analytic model has been used when the energy distribution of fission was important. Several basic questions, however, still remain in the general application of the empirical kernel method:

1. Can the kernel method be applied even when there is appreciable resonance fission without making the assumption that either the age or the Goertzel-Selengut approximation is valid?

2. Does the so-called "Fundamental Theorem of Reactor Theory" apply to water-moderated systems? This theorem states that if the reactor is unreflected and uniform and if it is large enough to make the energy variation of the extrapolation distance unimportant, then the nonleakage probability is related to the kernel measured in an effectively infinite system.[4]

3. Can the kernel method be used to resolve the discrepancy[5] between the computed and the experimental age to indium resonance of U^{235} fission neutrons in water?

---

[1] A more extensive version of this paper will be published in the *Proc. Intern. Conf. Peaceful Uses Atomic Energy, Geneva, 1958.*

[2] On assignment from U.S. Air Force.

[3] See, for example, A. D. Callihan, J. W. Morfitt, and J. T. Thomas, *Proc. Intern. Conf. Peaceful Uses of Atomic Energy, Geneva, 1955* **5**, 145 (1956); N. C. Francis, H. Hurwitz, Jr., and P. F. Zweifel, *Nuclear Sci. and Eng.* **2**, 253 (1957); G. I. Bell, *A Simple Method of Calculating Masses of Proton Moderated Assemblies*, LA-1548 (1953).

[4] S. Glasstone and M. C. Edlund, *The Elements of Nuclear Reactor Theory*, chap. XII, p 345, Van Nostrand, New York, 1952; see also A. M. Weinberg and E. P. Wigner, *Physical Theory of Neutron Chain Reactors*, University of Chicago Press, Chicago, 1958.

[5] J. E. Wilkins, Jr., R. L. Hellens, and P. F. Zweifel, *Proc. Intern. Conf. Peaceful Uses of Atomic Energy, Geneva, 1955* **5**, 62 (1956).

Application of Empirical Kernel Method

Some of the basic relations of the kernel method formulation of the critical conditions are shown in Eqs. 1–4. Equation 1 is the general formulation of the critical conditions:

$$\Sigma_a(\vec{x},E)\,\phi(\vec{x},E) = \nu \iint P(\vec{x}' \longrightarrow \vec{x},E)\,\Sigma_f(\vec{x}',E')\,\phi(\vec{x}',E')\,d\vec{x}'dE' \;, \tag{1}$$

where

$\phi(\vec{x},E),\phi(\vec{x},E')$ = neutron fluxes at $\vec{x}$ for neutrons having energies E and E', respectively,

Σ_a,Σ_f = macroscopic absorption and fission cross sections, respectively,

ν = number of neutrons produced per fission,

P = kernel giving the probability that a fission neutron which originates at $\vec{x}'$, with an energy given by the normalized fission spectrum, will be absorbed with an energy E at $\vec{x}$.

By using the asymptotic theory for an unreflected uniform reactor, the first equation can be written as follows:

$$\Sigma_a(E)\,\phi(E) = \nu \iint P_\infty(|\vec{x}-\vec{x}'|,E')\,\Sigma_f(E')\,\phi(\vec{x}',E')\,dE'd\vec{x} \;. \tag{2}$$

Now the kernel, designated P_∞, is for an infinite medium and is therefore a displacement kernel. Since the kernel used in these calculations was measured in pure water, it must be modified to account for resonance absorption in the uranium. This can be done by making a fundamental assumption that in the presence of an absorbing material the kernel is the product of the kernel (K) in the pure moderator and the probability of absorption (p') averaged over the fission spectrum $f(E')$:

$$P_\infty(|\vec{x}-\vec{x}'|,E) = \int_E^\infty p'(E' \longrightarrow E)\,K(|\vec{x}-\vec{x}'|,E' \longrightarrow E)\,f(E')\,dE' \;. \tag{3}$$

Equation 4 gives the probability that a neutron starting at E' will be absorbed in the unit range around E':

$$p'(E' \longrightarrow E) = \frac{\Sigma_a(E)}{\xi\Sigma_t(E)E}\exp\left[-\int_E^{E'}\frac{\Sigma_a(E'')}{\xi\Sigma_t(E'')}\frac{dE''}{E''}\right] . \tag{4}$$

Equations 1–4 yield an energy distribution which is essentially $1/E$, but in order to obtain a more accurate neutron spectrum, the uncollided neutrons must be considered also. This was done by dividing the total flux into collided and uncollided components. The critical equation resulting from this modification and from applying the fundamental theorem that the nonleakage probability in a reactor of buckling B^2 is the Fourier transform of the kernel in the infinite system is then

$$\nu\int_0^\infty \frac{\Sigma_f(E)}{\xi\Sigma_t(E)}\,p(E)\,\bar{K}(B,E)\,\frac{dE}{E} + \nu\int \frac{\Sigma_f(E)}{\Sigma_t(E)}\,f(E)\,\frac{\Sigma_t(E)}{B}\tan^{-1}\frac{B}{\Sigma_t(E)}\,dE = 1 \;, \tag{5}$$

where

$$\bar{K}(B,E) = \int_E^{\infty} \frac{\Sigma_s(E')}{\Sigma_t(E')} \bar{K}(B,E' \longrightarrow E) \frac{\Sigma_t(E')}{B} \tan^{-1} \frac{B}{\Sigma_t(E')} f(E')\, dE' .$$

The term $[\Sigma_t(E)/B] \tan^{-1} [B/\Sigma_t(E)]$ is the Fourier transform of the transport kernel and thus is, by the asymptotic theory, the nonleakage probability for uncollided fission neutrons in an assembly having a buckling B^2; and $\bar{K}(B,E)$ is the Fourier transform of the slowing-down kernel for fission neutrons which have made at least one collision in reaching energy E.

Hill, Roberts, and Fitch[6] determined the distribution in water of neutrons having an energy of about 1.4 ev (indium resonance), and from these data the nonleakage probability for neutrons reaching 1.4 ev was computed; that is, the Fourier transform of the measured kernel was derived.[7] Since the nonleakage probability required in the critical equation is to an arbitrary energy E and since almost all the fissions occur in the low-energy resonance region, the assumption was made that the age theory is adequate to compute small increments in the nonleakage probability.

In order to solve the critical equation numerically, the neutron flux was separated into a number of energy groups. The epithermal groups in the collided component were chosen such that the resonance escape probability was essentially constant in a given group. The equation used in the calculations is as follows:

$$\bar{K}(B,1.4) \left(\frac{k_{th} e^{-B^2 \tau_t}}{1 + L^2 B^2} + \sum_i k_i e^{B^2 \tau_i} \right) + \sum_i k_{vi} \bar{T}_i = 1 , \tag{6}$$

where

$$k_{th} = \nu p_{th} \frac{\Sigma_f(E_{th})}{\Sigma_a(E_{th})} ,$$

$$k_{vi} = \nu \int_{E_{i-1}}^{E_i} \frac{\Sigma_f(E)}{\Sigma_t(E)} f(E)\, dE ,$$

$$\bar{T}_i = \frac{\Sigma_t(E)}{B} \tan^{-1} \frac{B}{\Sigma_t(E)} ,$$

where Σ_t is averaged over the energy group. The k's represent differential multiplication factors for the various groups. The term $e^{-B^2 \tau_t}$ is the nonleakage probability for neutrons slowing down from 1 ev to thermal, where τ_t, the age from 1.4 ev to thermal, is 1 cm^2 as measured by Barkov *et al.*[8] The product of the terms $\bar{K}(B,1.4)\, e^{B^2 \tau_i}$ gives the nonleakage probability to an energy E greater than 1.4 ev, where τ_i is

[6] J. E. Hill, L. D. Roberts, and T. E. Fitch, *J. Appl. Phys.* **26**, 1013 (1955).

[7] D. K. Trubey, H. S. Moran, and A. M. Weinberg, *Appl. Nuclear Phys. Ann. Prog. Rep. Sept. 1, 1957*, ORNL-2389, p 158.

[8] L. M. Barkov, V. K. Makarin, and K. N. Mukhin, *J. Nuclear Energy* **4**, 94 (1957).

the age from E to 1.4 ev. The term $\overline{T}_i$ is the Fourier transform of the transport kernel for the ith group of fission energy neutrons. The cross sections in this kernel were averaged over the group.

The thermal and fast infinite-medium multiplication factors calculated for these solutions as a function of the U^{235} concentration are shown in Fig. 6.4.3 in Sec. 6.4 of this report. The details of the calculation are also given in Sec. 6.4. It is seen that fast neutrons produce an appreciable fraction of the fissions over most of the concentration range and that, at 400 g of U^{235} per liter, they account for one-third of the total multiplication factor. Values of the calculated material buckling, B_M^2, as a function of concentration are shown in Fig. 6.3.1. Curve 1 was computed by using a nonleakage probability as derived by a numerical integration of the transport equation[9] and corresponds to an age of 26 cm^2. Curves 2 and 3 were computed by using the Fourier transform[7] of the Hill, Roberts, and Fitch kernel for two different assumptions of the effect of water displaced by the uranium salt. Curve 2 assumes the complete equivalence of the uranium salt and the displaced water, while curve 3 assumes that the uranium salt has no effect upon the nonleakage probability of the pure moderator. The points in the figure represent the geometric bucklings obtained from the experimental data and will be discussed later.

[9]H. Hurwitz, Jr., P. F. Zweifel, and C. D. Petrie, private communication.

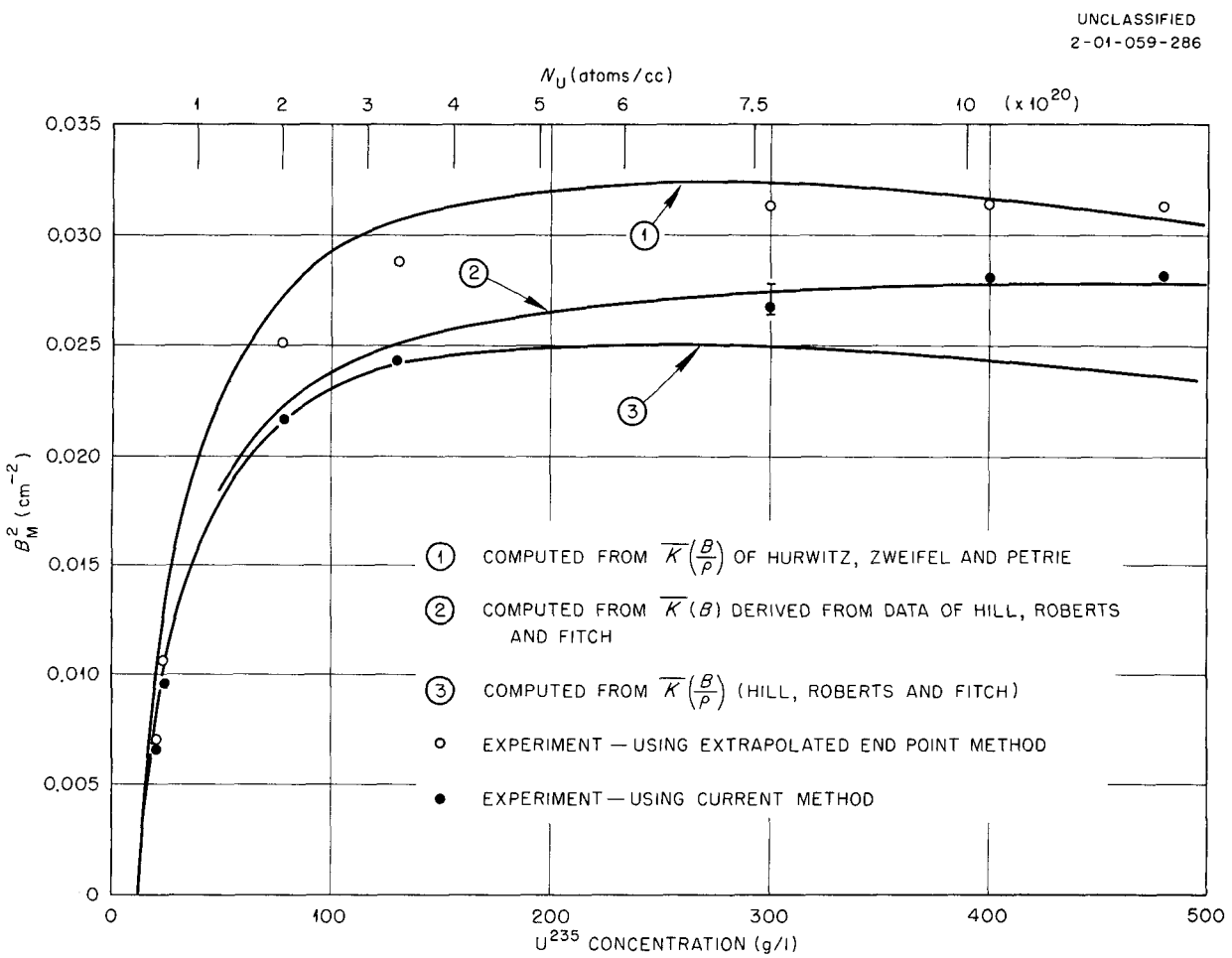

Fig. 6.3.1. Material Buckling of Aqueous Solutions of UO_2F_2 as a Function of U^{235} Concentration.

Comparison with Experiment

The comparison of the results of the calculations with experiments was made through the material buckling and the geometric buckling for two reasons. First, the geometric buckling must be shown to be an intensive parameter, and second, the calculation of an effective extrapolation length is quite difficult. Experimental measurements[10] have been made of the critical dimensions of unreflected right circular cylinders and parallelepipeds of aqueous solutions of uranyl fluoride enriched to 93.2% in U^{235}. A few critical experiments were also performed in unreflected spherical geometry.

Although the mean free path in water varies strongly with neutron energy, the deviations of the energy and spatial distributions from their asymptotic forms are confined to regions within about 1 mfp of the boundary. This region has low statistical weight, and it is therefore reasonable to consider an energy-independent extrapolation distance. Another point to consider is the ambiguity in the choice of boundary conditions. Two different treatments of these conditions were chosen: (1) the "end-point" method, which requires that the asymptotic solution for the flux distribution go to zero at a distance beyond the surface of the reactor, and (2) the "current" method, which simply requires that, in the P_1 approximation, there be no inwardly directed current, that is, that the logarithmic derivative of the flux at the boundary be the reciprocal of the linear extrapolation distances.

The two boundary conditions were used to analyze the experimental data by choosing the extrapolation distance that minimized the standard deviation of the values of the geometric bucklings from their mean. The end-point extrapolation length was found to be 2.5 cm over the range of concentrations investigated, while the linear extrapolation length varied from 3.2 to 3.7 cm.

The experimental values of the critical geometric bucklings are the points in Fig. 6.3.1. The open circles represent the results of the "end-point" method and the filled circles represent the results of the "current" method. Note that in both cases the geometric bucklings correspond to a curve shape which treats the uranium salt as equivalent in scattering properties to the water it displaces. This indicates that a scattering collision of a very energetic neutron with a nonhydrogen atom is nearly as important as a collision with a hydrogen atom.

It is gratifying that the value of the critical geometric buckling using a given extrapolation distance does seem to be quite constant for a particular concentration even with rather large changes in the geometry; that is, the material buckling is indeed an intensive parameter. However, it is puzzling that the two boundary-condition methods of solving for the buckling from the critical dimensions give values which differ by at least 10%.

In summary, the empirical kernel method as applied to unreflected water-moderated reactors, even those with large amounts of resonance fission, predicts material bucklings which are not inconsistent with the experimental values. It does not seem possible, however, to choose between the empirical and theoretical kernels in water on the basis of these critical experiments; that is, the long-standing discrepancy between the theoretical and experimental neutron age in water is not resolved by these experiments on unreflected water-moderated critical assemblies.

[10] J. K. Fox and L. W. Gilley, p 72, and R. Gwin, p 84 in *Appl. Nuclear Phys. Ann. Prog. Rep. Sept. 1, 1957*, ORNL-2389.

6.4. A CALCULATION[1] OF THE INFINITE-MEDIUM NEUTRON MULTIPLICATION FACTOR IN A U^{235}-H_2O SOLUTION

D. K. Trubey R. H. Lessig[2]

In order to compute the critical conditions for a reactor which has appreciable resonance fission, the infinite-medium neutron multiplication factor as a function of neutron energy must be known since the nonleakage probability is a function of energy. The multiplication factors for UO_2F_2-H_2O solutions have been calculated on the basis of a simple model for a number of concentrations, and the results are reported in this paper. These results have been combined with nonleakage probabilities reported previously[3] to yield an estimate of the critical buckling as a function of concentration. This work, along with a comparison with experiment, is being reported at the 1958 Geneva conference[4] and in Sec. 6.3.

The infinite-medium multiplication factor, k, may be defined as the number of neutrons produced per neutron absorbed:

$$k = \frac{\nu \int_0^\infty \phi(E)\, \Sigma_f(E)\, dE}{\int_0^\infty \phi(E)\, \Sigma_a(E)\, dE}, \tag{1}$$

where

ν = number of neutrons produced per fission,

$\phi(E)\, dE$ = neutron flux in dE about energy E,

$\Sigma_f(E)$ = macroscopic fission cross section,

$\Sigma_a(E)$ = macroscopic absorption cross section,

$\int_0^\infty \phi(E)\, \Sigma_a(E)\, dE = A$ = total number of absorptions.

The neutron flux, $\phi(E)$, was assumed to have a Maxwellian distribution in the thermal energy region and to be represented by a $1/E$ spectrum in the resonance region. In addition, there is an uncollided flux at the very high energies. Because of this behavior of the flux and so that the multiplication factor could be evaluated numerically for a small group of neutrons, the numerator of Eq. 1 was divided into a number of differential multiplication factors, beginning with the thermal multiplication and absorption and proceeding upward in energy.

Thermal Region. – The thermal multiplication factor may be defined as follows:

$$k_{th} = \frac{\nu \int_0^\infty M(E)\, \Sigma_f(E)\, dE}{A} = \frac{\nu \frac{\sqrt{\pi}}{2} \Sigma_f(0.025\text{ ev})\, g_f}{A}, \tag{2}$$

where

$M(E)$ = normalized Maxwellian distribution

$= (E/E_0^2)\, e^{-E/E_0}$.

The most probable energy, E_0, may be assumed to be given for water by

$$E_0 = E_m \left(1 + 0.92 \frac{\Sigma_a}{\Sigma_s}\right) \text{(ref 5)}, \tag{3}$$

where E_m = moderator energy and Σ_s = scattering cross section. Since the normalized Maxwellian distribution is used, the number of neutrons produced from thermal fissions is simply

$$\frac{\nu\sqrt{\pi}}{2} \Sigma_f(0.025\text{ ev})\, g_f ,$$

where g_f (ref 6) is a correction to the non-$1/v$

[1]The very helpful counsel of A. M. Weinberg during this calculation is gratefully acknowledged.

[2]On assignment from U.S. Air Force.

[3]D. K. Trubey, H. S. Moran, and A. M. Weinberg, *Appl. Nuclear Phys. Ann. Prog. Rep. Sept. 1, 1957*, ORNL-2389, p 158.

[4]R. Gwin, D. K. Trubey, and A. M. Weinberg, "Experimental and Theoretical Studies of Unreflected Aqueous U^{235} Critical Assemblies," *Proc. Intern. Conf. Peaceful Uses Atomic Energy, Geneva, 1958* (to be published).

[5]A. M. Weinberg and E. P. Wigner, *Physical Theory of Neutron Chain Reactors*, chap. 11, University of Chicago Press, Chicago, 1958.

[6]J. A. Harvey, *Thermal Neutron Cross Sections and Definition of the f-Factor in BNL-325*, ORNL CF-56-6-41 (June 7, 1956).

behavior of the uranium cross section:

$$(4)\quad g_f = \frac{\int M(E)\,\Sigma_x(E)\,dE}{\int \Sigma_x(0.025\text{ ev})\sqrt{\frac{0.025\text{ ev}}{E}}\,M(E)\,dE}\,.$$

The normalizing constant, A, may be broken down into a thermal term and a resonance term as follows:

$$(5)\quad A = \frac{\sqrt{\pi}}{2}\left[\Sigma_a^U(0.025\text{ ev})\,g_a + \Sigma_a^{H_2O}(0.025\text{ ev})\right] + \int_{E^*}^{\infty}\phi(E)\,\Sigma_a(E)\,dE\,,$$

where E^* is defined under the discussion of epithermal multiplication factor below. Since the normalizing constant, A, depends on the number of resonance absorptions, k_{th} is not known until the calculation is completed.

The thermal resonance escape probability, p, is the ratio of the number of neutrons absorbed at thermal energies to the total number of neutrons absorbed and is thus

$$(6)\quad p = \frac{\frac{\sqrt{\pi}}{2}\left[\Sigma_a^U(0.025\text{ ev})\,g_a + \Sigma_a^{H_2O}(0.025\text{ ev})\right]}{A}\,.$$

Then k_{th} may be written in the familiar fashion

$$(7)\quad k_{th} = \frac{\nu p\,\Sigma_f(0.025\text{ ev})\,g_f}{\Sigma_a^U(0.025\text{ ev})\,g_a + \Sigma_a^{H_2O}} = \eta f p\,,$$

where

η = number of neutrons produced per uranium absorption

$$= \frac{\nu\Sigma_f(0.025\text{ ev})\,g_f}{\Sigma_a^U(0.025\text{ ev})\,g_a}\,,$$

f = thermal utilization factor

$$= \frac{\Sigma_a^U(0.025\text{ ev})\,g_a}{\Sigma_a^U(0.025\text{ ev})\,g_a + \Sigma_a^{H_2O}(0.025\text{ ev})}\,.$$

Epithermal Region. – In the region just above thermal, η fluctuates strongly and so it is important to deal with this region accurately. Since there is no completely adequate thermalization theory which can be applied to the U^{235} system, especially since U^{235} absorption does not follow a $1/v$ behavior, a simple $1/E$ spectrum will be assumed but only the neutrons in excess of the Maxwellian distribution will be considered as resonance neutrons. These neutrons will be denoted by $\phi'(E)$. At energies above 0.7 ev, $\phi'(E)$ is indistinguishable from the total flux. Below about 0.05 ev, $\phi'(E)$ is zero since the distribution is Maxwellian. Thus the contribution to k of the thermalization or epithermal region is given by

$$(8a)\quad k_{epi} = \frac{\nu}{A}\int_0^{0.7\text{ ev}}\Sigma_f(E)\,\phi'(E)\,dE\,.$$

If it is assumed that

$$(9)\quad \phi(E) = \frac{q(E)}{\xi\Sigma_t(E)\,E}\,,$$

where

$q(E)$ = slowing-down density at E

= number of absorptions below E,

ξ = average logarithmic energy decrement,

$\Sigma_t(E)$ = macroscopic total cross section,

the normalization of $\phi(E)$ and E^*, the energy at which the Maxwellian intersects $\phi(E)$, may be determined from the solution of the following equations:

$$(10a)\quad \phi(E^*) = \frac{q(E^*)}{\xi\Sigma_t(E^*)\,E^*} = M(E^*)\,,$$

$$(10b)\quad q(E^*) = \int_0^{E^*} M(E)\,\Sigma_a(E)\,dE\,.$$

In all cases considered the value of E^* was between 0.1 and 0.2 ev, while $q(E^*)$ was nearly proportional to the U^{235} density.

Since $q(E^*)$ is known, k_{epi} can be computed from

$$(8b)\quad k_{epi} = \frac{\nu}{A}\int_{E^*}^{0.7\text{ ev}} q(E^*)\,\frac{\Sigma_f(E)}{\xi\Sigma_t(E)}\exp\left[\int_{E^*}^{E}\frac{\Sigma_a(E')}{\xi\Sigma_t(E')}\,\frac{dE'}{E'}\right]\frac{dE}{E} - \int_{E^*}^{0.7\text{ ev}} M(E)\,\Sigma_f(E)\,dE\,.$$

The cross sections for this region and for the region discussed below (0.7–1.7 ev) are given in detail in BNL-325, Supplement 1.[7]

Resonance Region. – Above 0.7 ev the number of absorptions is sufficiently small so that the slowing-down density may be taken to be a constant over a small interval. Thus the rest of the collided neutron multiplication factors were computed from

$$(11a) \qquad k_i = \frac{\nu q(E_i)}{A} \int_{E_{i-1}}^{E_i} \frac{\Sigma_f(E)}{\xi \Sigma_t(E)} \frac{dE}{E} ,$$

$$(12) \quad q(E_i) = \left[\frac{\sqrt{\pi}}{2} \left(\Sigma_a^U g_a + \Sigma_a^{H_2O} \right) + \right.$$

$$\left. + \sum_{j=1}^{i} q(E_j) \int_{E_{j-1}}^{E_j} \frac{\Sigma_a(E)}{\xi \Sigma_t(E)} \frac{dE}{E} \right] \int_{E_i}^{\infty} f(E)\, dE ,$$

where $f(E)$ is the normalized fission spectrum. The slowing-down density at E is equal to the number of absorptions below E times the fraction of neutrons born above E, since there is practically no absorption in the fission spectrum range.

Between 2 and 35 ev it is possible to compute many of the U^{235} resonance integrals by means of the Breit-Wigner resonance formula and the parameters listed in BNL-325, Supplement 1.[7] The contributions of each resonance are

$$(11b) \qquad k_i = \frac{\nu q(E_i)}{A} \frac{2\pi \hbar^2 N_U}{\xi \bar{p}_1^2 \Sigma_s} \frac{g_c}{g_1} \frac{\Gamma_n \Gamma_f}{\Gamma_{eff}} \text{(ref 5)} ,$$

where

$\bar{p}_1$ = momentum corresponding to E_i,

$\hbar = \pi/2 \times$ Planck's constant,

$g_c/g_1 = \frac{1}{2}$,

Γ_n = neutron width,

Γ_f = fission width,

N_U = uranium nuclear density,

$$\Gamma_{eff} = \left(\Gamma^2 + \frac{4\pi\hbar^2 N_U}{\bar{p}_1^2 \Sigma_s} \frac{g_c}{g_1} \Gamma \Gamma_n \right)^{1/2} ,$$

Γ = total width.

[7] D. J. Hughes and R. B. Schwartz, *Neutron Cross Sections*, BNL-325, Supplement 1 (Jan. 1, 1957).

Evaluation of the constants yields

$$(11c) \quad k_i = \frac{\nu q(E_i)}{A} \frac{N_U}{\xi \Sigma_s} \left[0.65 \times 10^6 \frac{\pi \Gamma_n \Gamma_f}{E_i^2 \Gamma_{eff}} \right] ,$$

if the widths and E_i are given in ev. The expression in brackets will be called the resonance integral and is given in barns. A similar expression may be used to estimate the resonance absorptions (for the evaluation of A) if Γ_f is replaced by Γ.

If the concentration is small (i.e., if N_U/Σ_s is small), $\Gamma_{eff} \sim \Gamma$. However, as the concentration increases Γ_{eff} tends to increase, being stronger for levels with large Γ_n. This means that the relative contribution to the resonance fission of the levels with large Γ_n is not as pronounced in the concentrated solutions as in the dilute solutions. The ratio Γ/Γ_{eff} was computed to be as low as 0.6 for some resonances with a high U^{235} concentration.

Unfortunately, not all the parameters of all the resonances are known. Where the ratio of Γ_f/Γ was unknown, it was assumed to have the same value as it had when averaged over the resonances where it was known [i.e., $\overline{(\Gamma_f/\Gamma)} = 0.567$]. By making the assumption that $\Gamma_\gamma = 30$ mv, all the resonances can be computed.

Above 35 ev the fission cross-section curves of BNL-325, Supplement 1,[7] were integrated numerically and the absorption was estimated from the values of α shown in Fig. 6.4.1. The Russian data shown is that quoted by Kurchatov *et al.*,[8]

[8] V. I. Kalashnikov *et al.*, *J. Nuclear Energy* **4**, 67 (1957).

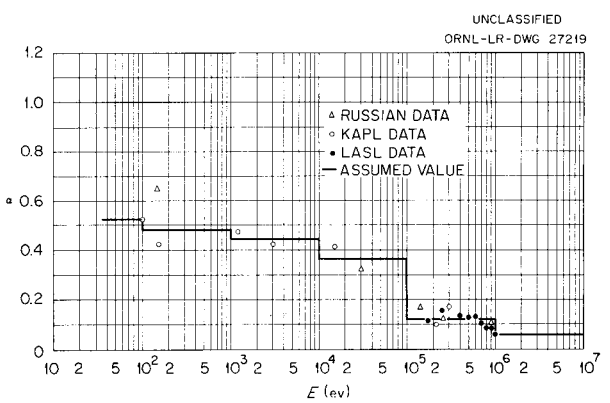

Fig. 6.4.1. Alpha as a Function of Energy for U^{235}.

the LASL data is that of Diven,[9] and the KAPL data is that quoted by Oleska.[10]

The resulting epicadmium resonance integrals as a function of concentration are shown in Fig. 6.4.2. The function $T(E)$, used to compute the epicadmium integral, is the transmission of a 20-mil-thick cadmium cover in an isotropic flux normalized so that it equals 1.0 at high energy.[11] Popovic[12] has estimated experimentally that the epicadmium integral is 20 ± 10 barns in excess of the $1/v$ fraction, which is 274 barns if the thermal cross section is taken to be 549 barns and the lower limit of the integral is 0.4 ev. Thus the calculated result (286 barns) is within the quoted uncertainty.

Uncollided Neutrons. – At the very high energies the uncollided neutrons contribute appreciably to the fission rate. The uncollided neutrons may be taken to be

$$\phi_v(E) = \frac{Af(E)}{\Sigma_t(E)} , \tag{13}$$

and the uncollided k to be

$$k_{vi} = \nu \int_{E_{i-1}}^{E_i} \frac{\Sigma_f(E)}{\Sigma_t(E)} f(E)\, dE . \tag{14}$$

[9] B. Diven, *Reports to the AEC Nuclear Cross Sections Advisory Group, Idaho Falls, Idaho, July 17–18, 1957*, WASH-194, p 41 (Feb. 14, 1958).

[10] S. Oleska, *J. Nuclear Energy* 5, 16 (1957).

[11] E. D. Clayton, HW-35729 (March 7, 1955) (classified).

[12] D. Popovic, *Physica* 20, 406–412 (1954).

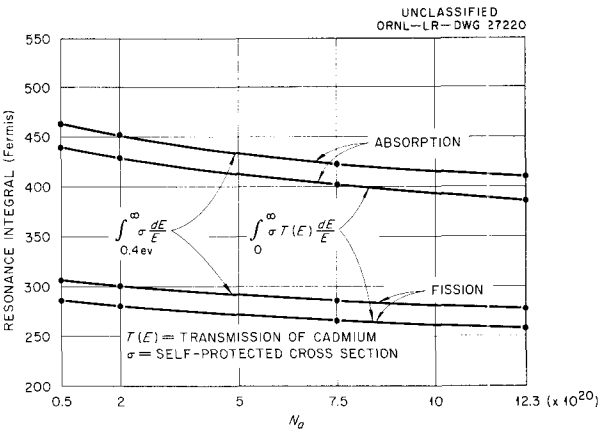

Fig. 6.4.2. Computed Resonance Integrals as a Function of U^{235} Concentration.

Results and Discussion

The resulting differential multiplication factors for a $U^{235}O_2F_2$-H_2O solution are shown in Table 6.4.1. The solution was assumed to have an H_2O specific gravity of $1 - 0.00642N_U \times 10^{-20}$, which is an empirical fit to experimental data.[13] The values shown in Table 6.4.1 verify strikingly that epithermal fission contributes importantly in all but the most dilute U^{235}-H_2O reactors. At the lowest concentration, 0.5×10^{20} atoms/cc, the nonthermal k amounts to about 0.04 and the thermal k to about 1.23. The relatively low thermal k in

[13] R. Gwin, private communication.

Table 6.4.1. Differential Multiplication Factors

Concentration			k (Collided)											k (Uncollided)		
			Energy Intervals (ev)											Energy Intervals (ev)		Total k
$N_{U^{235}}$ (atoms/cc)	U^{235} (g/liter)	$H:U^{235}$ Ratio	Th	E^*–0.7	0.7–1.7	1.7–15	15–35	35–100	10^2–10^3	10^3–10^4	10^4–10^5	10^5–10^6	10^6–10^7	10^5–10^6	10^6–10^7	
1.23×10^{21}	480	50	1.190	0.2228	0.0776	0.0938	0.0781	0.0685	0.0852	0.0323	0.0170	0.0153	0.00948	0.00223	0.01248	1.905
1.0×10^{21}	390	63	1.308	0.1956	0.0668	0.0823	0.0674	0.0559	0.0688	0.0258	0.0136	0.0123	0.00763	0.00177	0.01005	1.916
7.5×10^{20}	293	85	1.448	0.1600	0.0531	0.0664	0.0534	0.0419	0.0509	0.0190	0.01005	0.00914	0.00565	0.00129	0.00747	1.926
5×10^{20}	195	129	1.566	0.1127	0.0378	0.0487	0.0388	0.0282	0.0339	0.0125	0.00660	0.00602	0.00375	0.000850	0.00496	1.901
3×10^{20}	117	219	1.648	0.0675	0.0238	0.0315	0.0247	0.0170	0.0202	0.00744	0.00392	0.00360	0.00224	0.000508	0.00297	1.853
2×10^{20}	78	330	1.634	0.0457	0.0163	0.0218	0.0170	0.0113	0.0135	0.00495	0.00260	0.00239	0.00149	0.000337	0.00198	1.773
1.5×10^{20}	59	442	1.596	0.0340	0.0123	0.0166	0.0128	0.0085	0.0101	0.00373	0.00195	0.00179	0.00112	0.000253	0.00148	1.701
1.0×10^{20}	39	664	1.495	0.0223	0.0083	0.0113	0.0087	0.0056	0.0068	0.00250	0.00130	0.00119	0.00074	0.000168	0.00099	1.565
0.5×10^{20}	19	1333	1.228	0.01064	0.00427	0.00587	0.00449	0.00284	0.00335	0.00128	0.000654	0.000594	0.000370	0.000084	0.000491	1.263

this case arises from the parasitic thermal capture in water, that is, from the low thermal utilization in dilute solutions. At the highest concentration, $N_U = 1.23 \times 10^{21}$ atoms/cc, nearly one-half the multiplication is nonthermal. Again, the thermal k is very low, but this is the result of the very high fraction of neutrons which are captured (and cause fission) during moderation. The thermal utilization is very high in the concentrated solution; it is the resonance escape probability that is very small at high N_U.

The fast fission factors ϵ $(=k/k_{th})$, k_{th}, k_{fast} $(k - k_{th})$, f, and p are shown in Fig. 6.4.3 as a function of concentration. In Fig. 6.4.4, k is compared with ηf. It is seen that for the dilute concentrations $k \cong \eta f$, which means that $\epsilon p \cong 1$. For the concentrated cases the poor η in the resonances becomes important and k actually decreases. It should be pointed out, however, that the calculation becomes less reliable as more dependence is put on the assumed α at high energies.

UNCLASSIFIED
2-01-059-287

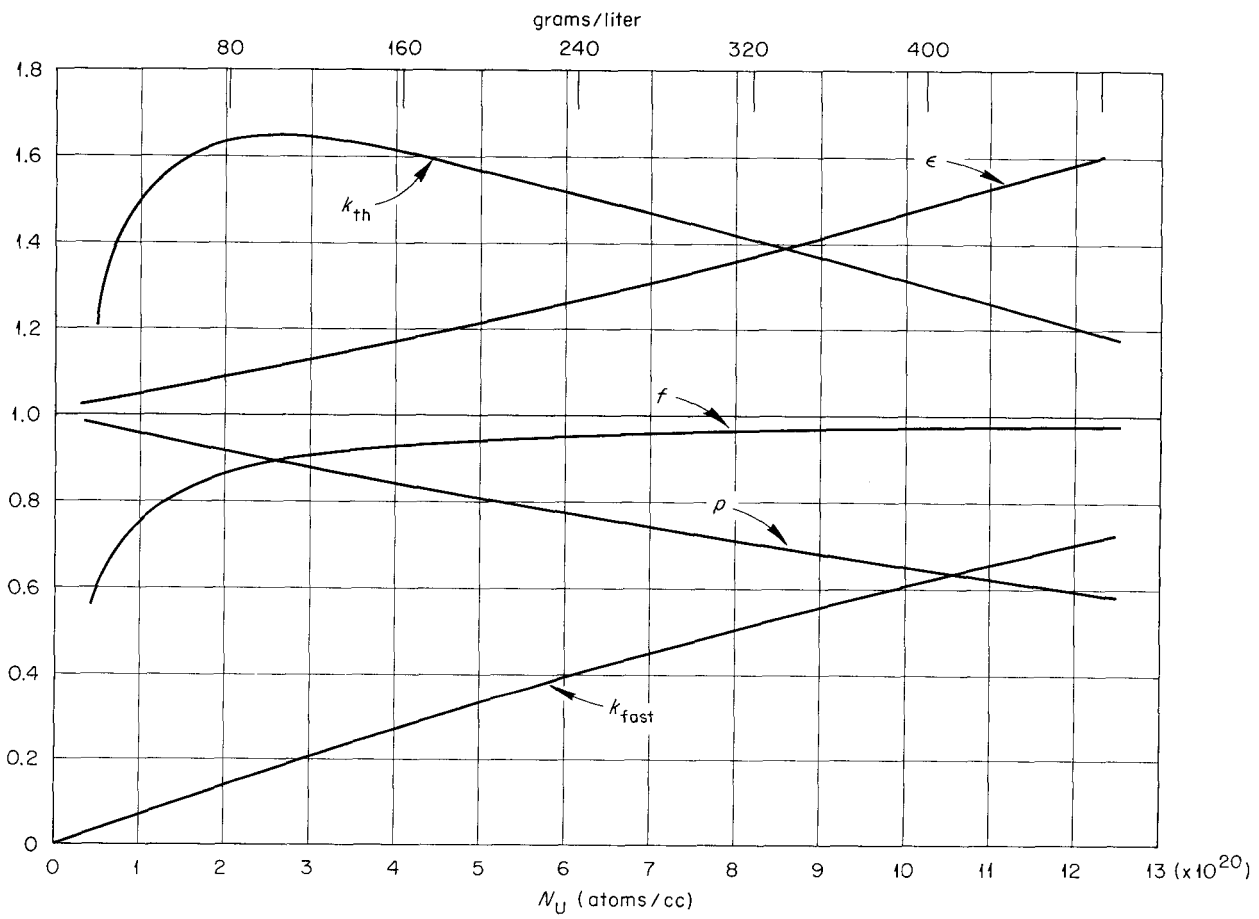

Fig. 6.4.3. Computed Infinite-Medium Multiplication Factors for a UO_2F_2-H_2O Solution as a Function of U^{235} Concentration.

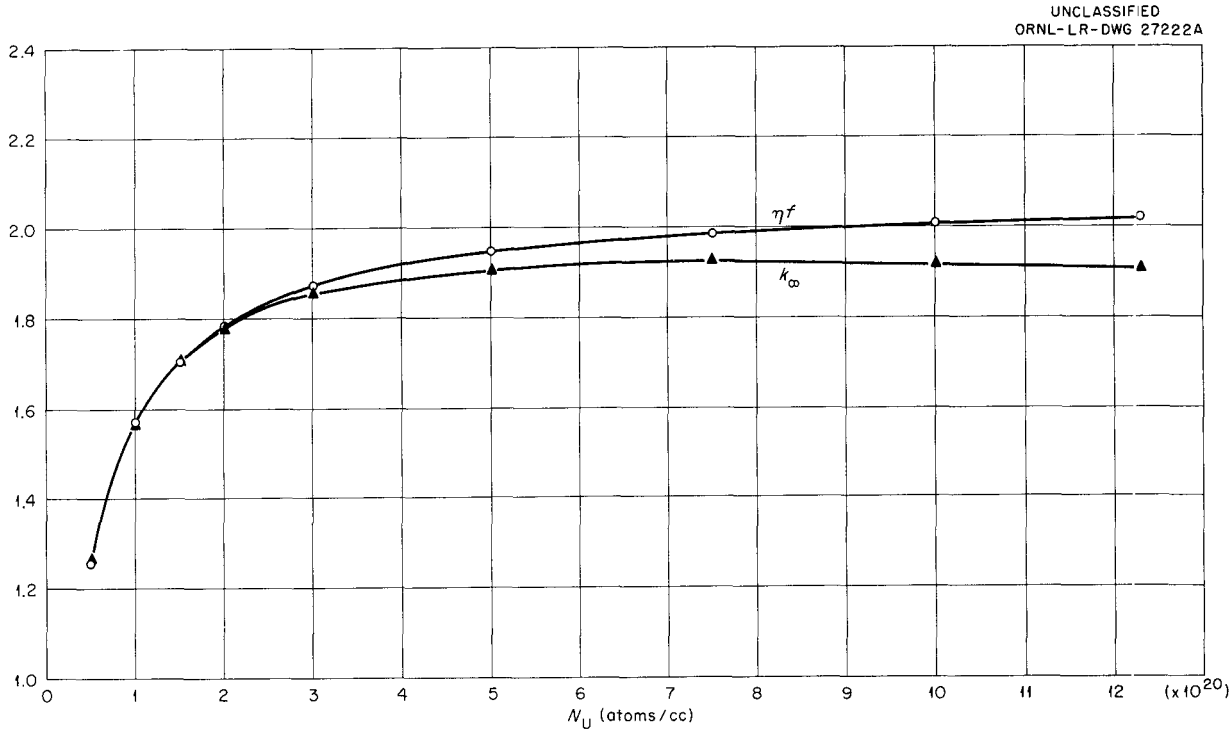

Fig. 6.4.4. Total Multiplication Factor as a Function of U^{235} Concentration.

6.5. THE EFFECT OF EPITHERMAL FISSION ON AQUEOUS HOMOGENEOUS REACTORS

S. Terasawa[1]

In light-water-moderated reactors epithermal fissions become important as the concentration of fissionable materials increases.[2] However, the multiplication factor, k_∞, for an infinite system, especially a dilute system, is approximated rather well by ηf, where η is the number of neutrons produced per neutron absorbed and f is the thermal utilization factor. In this case the epithermal fission factor ϵ in the usual formula $k = \eta\epsilon p f$ is almost canceled by the resonance escape probability p, even though ϵ itself becomes rather large. In this paper the magnitude of ϵp for U^{235} and U^{233} light-water-moderated reactors has been estimated by using a very simple model and values of numerical integrations of BNL-325 cross sections.[3] An attempt also has been made to reanalyze the experiment of Thomas *et al.*[4] in which the value of η of U^{233} was measured with respect to η of U^{235}. In the earlier analysis[4] the effect of epithermal fissions was neglected.

[1]On leave from Hitachi, Central Research Laboratory, Kokubunji, Tokyo, Japan.

[2]A. M. Weinberg and E. P. Wigner, *Physical Theory of Neutron Chain Reactors*, University of Chicago Press, Chicago, 1958.

[3]D. J. Hughes and R. B. Schwartz, *Neutron Cross Sections*, BNL-325, Supplement 1 (Jan. 1, 1957).

[4]J. T. Thomas, J. K. Fox, and D. Callihan, *A Direct Comparison of Some Nuclear Properties of U-233 and U-235*, ORNL-1992 (Nov. 28, 1955).

Theory

The multiplication factor k_∞ is given by

$$k_\infty = \frac{\nu \int_0^{E_c} \Sigma_f(E)\, M(E)\, dE + \nu \int_{E_c}^{\infty} \Sigma_f(E)\, \phi(E)\, dE}{\int_0^{E_c} \Sigma_a(E)\, M(E)\, dE + \int_{E_c}^{\infty} \Sigma_a(E)\, \phi(E)\, dE} \tag{1}$$

$$= \eta f \left[\frac{1 + \frac{\nu}{\eta f} \int_{E_c}^{\infty} \frac{\Sigma_f}{\xi \Sigma_s} \frac{dE}{E}}{1 + \int_{E_c}^{\infty} \frac{\Sigma_a}{\xi \Sigma_s} \frac{dE}{E}} \right] = \eta f (\epsilon p) \ ,$$

where

ν = number of neutrons per fission,

Σ_f = macroscopic fission cross section, cm^{-1},

Σ_a = total macroscopic absorption cross section, cm^{-1},

$M(E)$ = Maxwell-Boltzmann distribution of thermal-neutron flux, with an energy dependence proportional to $(E/E_0^2)\, e^{-E/E_0}$,

E_0 = most probable energy of thermal neutrons,

E_c = thermal cutoff energy,

$\phi(E)$ = neutron flux above thermal cutoff,

and where it is assumed that the neutron flux above the thermal cutoff energy is approximately

$$\phi(E) = \frac{C}{E} \ , \tag{2}$$

where C is constant.

The thermal cutoff energy E_c at which a $1/E$ spectrum joins the Maxwellian is given by

$$\phi(E_c) = M(E_c) \ , \tag{3}$$

$$q(E_c) = \xi \Sigma_s C = \int_0^{E_c} \Sigma_a(E)\, M(E)\, dE \ , \tag{4}$$

where

ξ = average logarithmic energy decrement per collision,

q = slowing-down density,

Σ_s = macroscopic scattering cross section.

Numerical integrations of the microscopic fission and total cross sections of U^{235} and U^{233} with a Fermi spectrum weighting $(1/E)$ were calculated from BNL-325 data[3] on the Oracle and are given in

Table 6.5.1. In order to obtain an integral of the microscopic absorption cross section, σ_a, the contribution of the scattering cross section of uranium, σ_s, must be subtracted from the total cross section, σ_t. For this calculation it is assumed that the scattering cross sections are those shown in Table 6.5.2.

Table 6.5.1. Resonance Integrals of Uranium

Isotope	Energy Interval (ev)	$\int \sigma_f \frac{dE}{E}$ (barns)	$\int \sigma_t \frac{dE}{E}$ (barns)
U^{235}	10^7–10^6	10	29
	10^6–0.4	330	570
	0.4–0.025	824	1010
U^{233}	10^8–10^6	11	31
	10^6–0.4	802	1106
	0.4–0.025	787	901

Table 6.5.2. Assumed Microscopic Scattering Cross Sections

Element	Energy Interval (ev)	σ_s (barns)
U^{235}	0.025–10^6	10
	$>10^6$	0
U^{233}	0.025–10^6	10 (lower limit)
		15.3 (upper limit)
	$>10^6$	0
H	$\geqq E_c$	20
O	$\geqq E_c$	4

The integrals of the cross sections from 0.025 ev to the thermal cutoff energy must be known in order to get the necessary integrals involved in Eq. 1 from Table 6.5.2. It is assumed that the energy dependence of the fission and absorption cross sections of U^{235} is given by

$$\sigma^{235}(E) = \sigma^{235}(E_0)\left(\frac{E_0}{E}\right)^{0.55} \quad \text{for } 0 \leqq E \leqq E_0 \tag{5}$$

$$= \sigma^{235}(E_0)\left(\frac{E_0}{E}\right)^{0.6} \quad \text{for } E_0 \leqq E \leqq E_c \ .$$

This assumption is consistent with the known deviation of the cross sections from a $1/v$ dependence. The fission and absorption cross sections of U^{233} and the absorption cross section of H_2O are assumed to obey a $1/v$ dependence. The variation of the effective resonance integral of uranium with concentration is neglected, and this may lead to a substantial error in this calculation.

Results

The calculated values of k_∞, ηf, ϵp, and

$$\frac{k_\infty}{k_{th}} = \frac{\int_0^{E_c} \Sigma_f(E)\, M(E)\, dE + \int_{E_c}^{\infty} \Sigma_f(E)\, \phi(E)\, dE}{\int_0^{\infty} \Sigma_f(E)\, M(E)\, dE} \tag{6}$$

which may correspond to ϵ, are shown in Figs. 6.5.1 and 6.5.2. The curve for k_∞/k_{th} shows that k_∞ becomes considerably larger than k_{th} with increasing uranium concentration per unit volume, N_U (atoms/cc), which means that the epithermal fission contribution becomes important. However, the product of ηf gives the tendency of k_∞ rather well within a few per cent error.

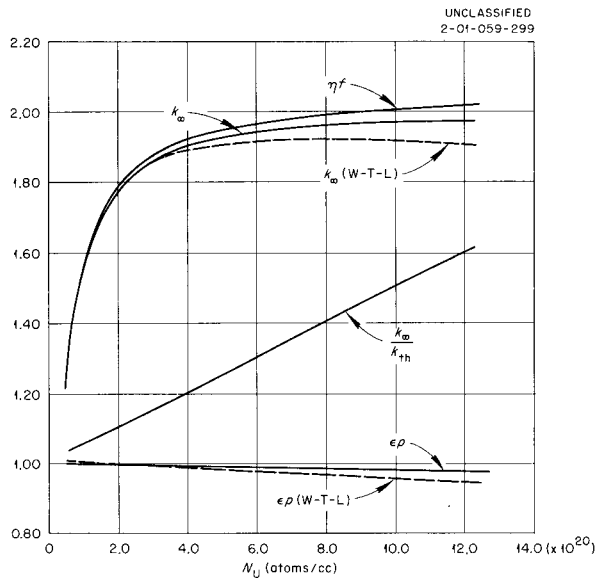

Fig. 6.5.1. Calculated Values of k_∞, ϵp, ηf, and k_∞/k_{th} of U^{235}.

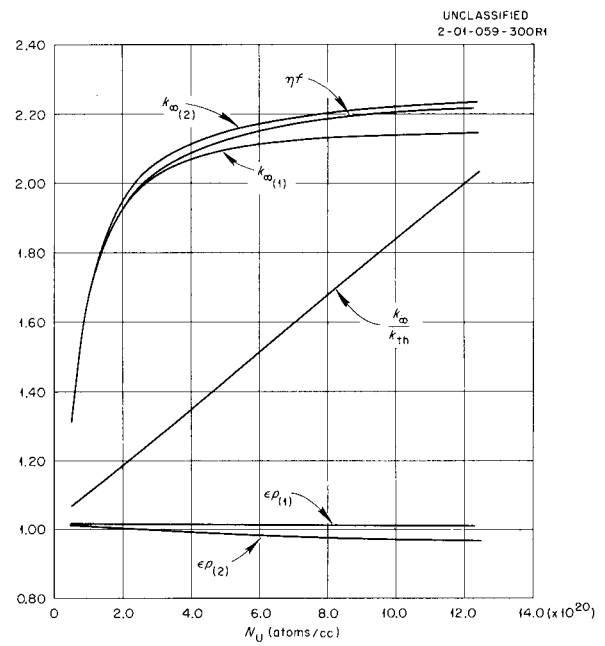

Fig. 6.5.2. Calculated Values of k_∞, ϵp, ηf, and k_∞/k_{th} of U^{233}.

Weinberg, Trubey, and Lessig (Sec. 6.4) have recently calculated k_∞ for U^{235}-H_2O reactors, using the ten-group theory and resonance parameters of U^{235} given in BNL-325.[3] Their results are shown in Fig. 6.5.1 by dotted lines. The discrepancy between their results and those computed by the method given here is about 1.5% when the concentration of uranium per unit volume becomes more than 7.5×10^{20} atoms/cc; this is mainly caused by the difference in effective resonance integrals.

Ordinary light-water-moderated reactors, such as a water-boiler reactor or a swimming pool reactor, have uranium concentrations less than 3.0×10^{20} atoms/cc; so this rather crude approximation seems to give a practical method for surveying the effect of epithermal fissions on the criticality conditions. Furthermore, since little information about the resonance parameters of U^{233} is available, it is not possible to calculate ϵp more rigorously for U^{233}-H_2O reactors at the present. This method of estimation apparently gives trustworthy results for this quantity.

Unfortunately, it was necessary in this calculation to assume the potential scattering cross section of U^{233}, which is rather obscure. Two values for σ_s^{233} were assumed: (1) $\sigma_s^{233} = 10$ barns for 0.025 ev $\leqq E \leqq 10^6$ ev, which seems a lower limit, and (2) $\sigma_s^{233} = 15.3$ barns for 0.025 ev $\leqq 10^6$ ev, which seems an

upper limit. These two different assumptions for the scattering cross section of U^{233} (50% different) lead to different estimates of ϵp and k_∞. They are shown in Fig. 6.5.2, each with an appropriate subscript; k_∞/k_{th} is the same for both cases.

Conclusions

This simple calculation gives an estimate of the epithermal fission effects on aqueous homogeneous reactors fairly well. The multiplication factor k_∞ of U^{235}-H_2O reactors is approximated by ηf, when the concentration of uranium is as dilute as that usually used in experimental reactors, even though epithermal fissions contribute up to about 10% to k_∞.

For U^{233}-H_2O reactors this calculation also gives a qualitative estimate of the effect of epithermal fissions. But the ambiguity of the scattering cross section makes the result quantitatively doubtful up to a few per cent in very highly concentrated cases. When this method was used for a reanalysis of the experiment of Thomas *et al.*,[4] and thereby the effect of epithermal fissions was taken into consideration, their results of $\eta^{233} = 2.35$ for bare reactors and $\eta^{233} = 2.31$ for reflected reactors were reduced by about 2%, but the difference in the values of η^{233} for the bare and reflected cases remains unexplained.

This paper has been published in more detail in another report.[5]

[5]S. Terasawa, *The Effect of Epithermal Fission on Aqueous Homogeneous Reactors*, ORNL-2553 (July 23, 1958).

6.6. CALCULATIONS OF NEUTRON AGES IN VARIOUS MEDIA

R. R. Coveyou J. G. Sullivan

At present two basic codes exist which are useful in calculations of neutron ages in various media. One of these is the Oracle Monte Carlo neutron age code, identified as "Chronos,"[1] which is essentially rigorous but is restricted to problems involving a point source in an infinite medium. This code has been used to compute the ages of neutrons from monoenergetic sources to indium resonance, as a function of source energy, in the following materials: Be, BeO, H, O, C, C + H_2O, CH_2 (oil), $C_{12}H_{10}$ (diphenyl), D_2O, and H_2O. A typical plot of the age in water is shown in Fig. 6.6.1. Also, the ages of neutrons from fission spectrum sources to indium resonance have been obtained in the above materials and in various H_2O-D_2O mixtures. The use of this code has been so arranged that the neutron age in almost any desired mixture can be obtained with but little labor.

The other code useful for age calculations is Corn Pone, a multigroup code employing the consistent P_1 approximation which can be used to calculate ages in heterogeneous media with very good accuracy although not with complete rigor. This code has been used to make estimates of the effect of source plate self-absorption on age measurements. The results of this application of Corn Pone are presented in Sec. 6.7.

A space-dependent Monte Carlo code, the Oak Ridge Random Research Reactor Routine (O5R), is being prepared for analyzing some problems not amenable to either of the existing codes. This third code is discussed in Sec. 6.8.

The results of all these calculations will be given later in a topical report.

[1]R. R. Coveyou, *Appl. Nuclear Phys. Ann. Rep. Sept. 10, 1956*, ORNL-2081, p 144; see also J. H. Marable, *Appl Nuclear Phys. Ann. Prog. Rep. Sept. 1, 1957*, ORNL-2389, p 176.

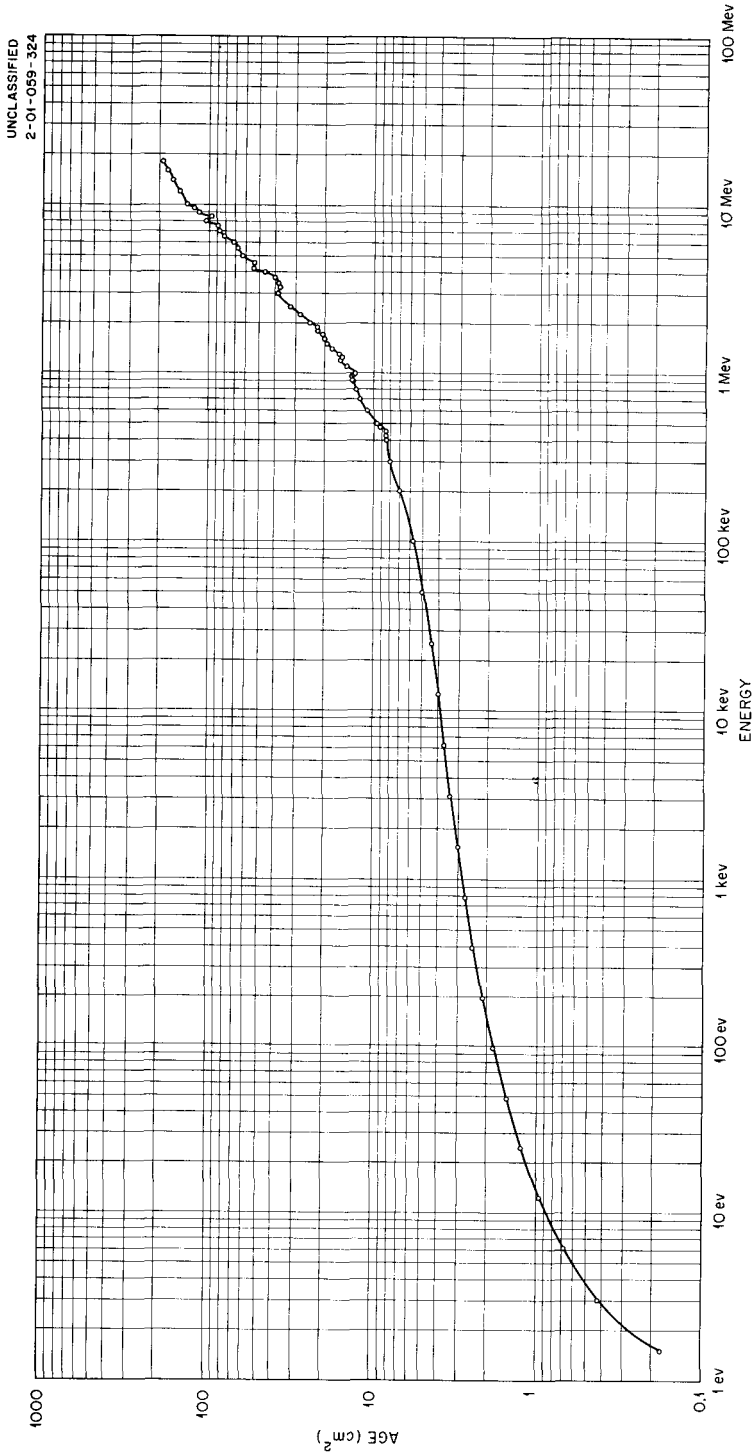

Fig. 6.6.1. Slowing-Down Age of Neutrons from Monoenergetic Sources to Indium Resonance in H_2O (1% Error).

6.7. CORN PONE: A MULTIGROUP, MULTIREGION REACTOR CODE

W. E. Kinney R. R. Coveyou J. G. Sullivan

The theory of Corn Pone, a multigroup, multiregion, one-dimensional reactor code for the Oracle, has been described previously.[1,2] With it the equations resulting from a P_1 approximation to the Boltzmann equation can be solved, as well as the Goertzel-Selengut and the age diffusion equations. It consists of four subcodes, the Group Constant Preparation Routine, the Reactor Constant Preparation Routine, the Integration Routine, and the Edit Routine. In the last report[3] of Corn Pone it was stated that the first three of these routines had been debugged but that coding of the Edit Routine had not yet begun. The Edit Routine is now nearly complete; however, a routine which computes and edits the events in specific materials is yet to be written.

The Edit Routine

The Edit Routine will print or plot the results of the calculations on the curve plotter. For each case the multiplication constant and the input data will be reported.

Any of the events, that is, absorptions, parallel leakages, transverse leakages, fissions, and neutron productions, may be edited in any or all regions for each group. The events may be reported as tables of group events vs group and/or as histograms of events per unit lethargy vs lethargy.

The sources and the source integral over space and lethargy may be edited. The sources may appear as tables of sources vs space point and/or as a curve of sources vs distance.

Any of the macroscopic absorption, fission, neutron producing, scattering, . or transverse leakage cross sections may be edited in any or all regions for each group. They may appear as tables of cross sections vs group and/or as histograms of cross sections vs lethargy.

Spatial integrals of the average and/or end-point fluxes may be edited in any or all regions for all groups. They may be reported as tables of flux integrals vs group and/or as histograms of flux integrals vs lethargy.

The average flux and/or the average current per unit lethargy over the reactor may be edited as tables of flux per unit lethargy vs space point, for example, and/or as curves of flux per unit lethargy vs distance. These quantities are edited in specified groups.

If any events or flux integrals are requested in the edit, a neutron balance is made and reported.

The routines to perform the edit are working and have been added to Corn Pone.

Reactor Calculations with Corn Pone

Corn Pone has been used in the Goertzel-Selengut approximation to compute the critical mass, the effectiveness of control shells, and the temperature coefficient of the TSR-II (see Sec. 2.2). The Goertzel-Selengut version has also been used for calculations in the Molten Salt Reactor Program.[4]

A calculation of the P_1 fluxes in the water tank of the Brookhaven National Laboratory Shielding Facility was made for M. Donnelly of the Bell Telephone Laboratories. A P_1 calculation and a Goertzel-Selengut calculation were made on a hydrogenous reactor for M. Butler of Argonne National Laboratory with cross sections and a group structure which she supplied.

Age Calculations with Corn Pone

Both the P_1 and the Goertzel-Selengut approximations were used to determine the effect of source plate absorption upon the fission neutron age in light water. Eyewash group structure and cross sections were used.[5] The flux in group 14 (4.564 to 1.375 ev) was used as the weighting function. The computations were performed in infinite-slab geometry. The calculation model

---

[1] B. J. Garrick, *Multigroup-Multiregion Theory for the Consistent* P_1 *Approximation to the Boltzmann Equation*, ORNL CF-55-8-189 (Aug. 1955).

[2] W. E. Kinney *et al.*, *Appl. Nuclear Phys. Ann. Rep. Sept. 10, 1956*, ORNL-2081, p 133.

[3] R. R. Coveyou, W. E. Kinney, and J. G. Sullivan, Jr., *Appl. Nuclear Phys. Ann. Prog. Rep. Sept. 1, 1957*, ORNL-2389, p 145.

[4] H. G. MacPherson *et al.*, *Status Report of the Molten Salt Reactor Program*, ORNL CF-58-5-3 (May 1, 1958).

[5] J. H. Alexander and N. D. Given, *A Machine Multigroup Calculation, The Eyewash Program for UNIVAC*, ORNL-1925 (Sept. 6, 1955).

was based on the age experiment of Hill, Roberts, and Fitch[6] and is shown in Fig. 6.7.1.

For a source plate thickness of 0.2032 cm and a uranium density of 1.478×10^{21} nuclei/cm^3, as used by Hill, Roberts, and Fitch, the P_1 group-14 flux age was 24.96 cm^2. The age with no source plate absorption was 24.84 cm^2.

A series of Goertzel-Selengut calculations were made on a 0.5-cm-thick pure uranium source plate. In this case of extreme source absorption, the group-14 flux age was 35.10 cm^2. The age was computed to be 29.36 cm^2 with no source absorption.

A calculation with graphite directly behind the Goertzel-Selengut source plate gave an age of 26.08 cm^2. A 5-cm-thick water layer between the source plate and the graphite gave nearly the same age as a 10-cm-thick layer.

UNCLASSIFIED
2-01-059-379

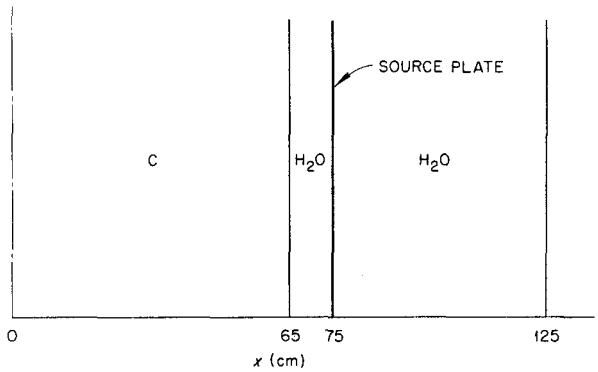

Fig. 6.7.1. Model for the Computation of Fission Neutron Age in Light Water with Corn Pone Code.

Cross-Section Integral Calculations

The Group Constant Preparation Routine was used to compute the lethargy integrals of U^{235} total, absorption, and fission cross sections over lethargy ranges. Such integrals can be computed rather easily and rapidly for any cross section on the master cross-section tape.

A Difficulty with the End-Point Fluxes

The P_1 difference equations which are good to the fourth order in the lattice spacing require the first, second, and third derivatives of source terms at each space point.[2] Two fictitious space points are introduced at region interfaces as shown in Fig. 6.7.2.

The group average fluxes at points $(I + 1)$ and $(I - 1)$ are used to compute the derivative of the flux at I and, from this, the group average current at I. The group average fluxes at points $(J + 1)$ and $(J - 1)$ are used similarly in the computation of the group average current at J. The fluxes at $(I + 1)$ and $(J - 1)$ are such that when used with the fluxes at $(I - 1)$, I, J, and $(J + 1)$, the currents at I and J are equal. The fictitious average fluxes are not analytic continuations of the fluxes within their respective regions.

The group upper end-point flux at space point k is computed from the relation

$$\phi_k(u_{i+1}) = 2\bar{\phi}_k - \phi_k(u_i) \ ,$$

where

$\bar{\phi}_k$ = group average flux at space point k,

$\phi_k(u_i)$ = lower end-point flux at space point k,

$\phi_k(u_{i+1})$ = upper end-point flux at space point k.

This formula had been applied at the fictitious points as well as at the real points, and so the end-point fluxes at $(I + 1)$ and $(J - 1)$ were not

UNCLASSIFIED
2-01-059-380

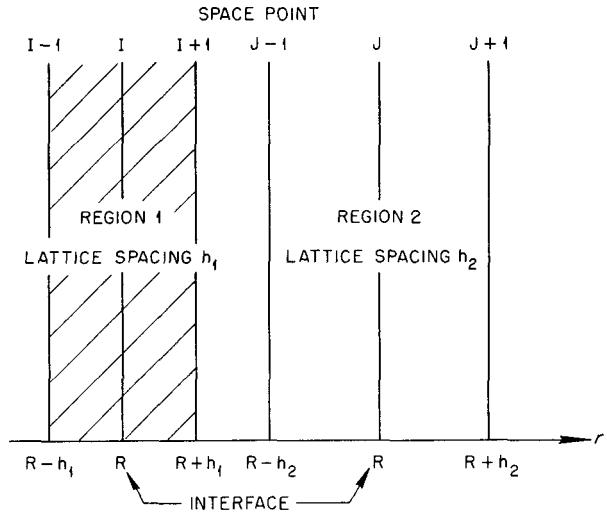

Fig. 6.7.2. Sequence of Space Points at Interface Showing Fictitious Points $(I + 1)$ and $(J - 1)$ (Corn Pone Code).

[6] J. E. Hill, L. D. Roberts, and T. E. Fitch, *J. Appl. Phys.* 26, 1013 (1955).

analytic continuations of the region end-point fluxes. The end-point fluxes at the fictitious points would, in fact, oscillate from group to group, the oscillations becoming more violent with increasing lethargy. The oscillations caused no difficulty when sources depended upon average fluxes only. However, when the sources depended upon end-point as well as average fluxes, the oscillations spread to the average fluxes and into real space points. In extreme cases the real fluxes were caused to go negative.

The present scheme treats the end-point fluxes at the fictitious points as continuations of the real fluxes and does not involve the average fluxes at $(I + 1)$ and $(J - 1)$ in their computation. This treatment removes the oscillations. The formulas for the fictitious end-point fluxes are:

$$\phi_{I+1}(u_{i+1}) = 4\phi_I(u_{i+1}) - 6\phi_{I-1}(u_{i+1}) + 4\phi_{I-2}(u_{i+1}) - \phi_{I-3}(u_{i+1}) \ ,$$

$$\phi_{J-1}(u_{i+1}) = 2(4\bar{\phi}_J - 6\bar{\phi}_{J+1} + 4\bar{\phi}_{J+2} - \bar{\phi}_{J+3}) - [4\phi_J(u_i) - 6\phi_{J+1}(u_i) + 4\phi_{J+2}(u_i) - \phi_{J+3}(u_i)] \ .$$

The Corn Pone Difference Equation Good to Second Order in the Lattice Spacing

The coefficients and the source term of the Corn Pone difference equation become relatively simple if numerical approximations to derivatives good to the second order in the lattice spacing rather than to the fourth order are used.

With the difference equation at space point k of the form

$$P_k\Omega_{k+1} - Q_k\Omega_k + R_k\Omega_{k-1} + S_k = 0 \ ,$$

the coefficients and source term are

$$P_k = \frac{1}{2} + \frac{1}{4}g\frac{h}{r} \ ,$$

$$Q_k = 1 + \frac{1}{2}\delta h^2 \ ,$$

$$R_k = \frac{1}{2} - \frac{1}{4}g\frac{h}{r} \ ,$$

$$S_k = \frac{1}{4}hB_{k+1} + \frac{1}{2}g\frac{h}{r}hB_k - \frac{1}{4}hB_{k-1} + \frac{1}{2}h^2AD_k \ ,$$

where

g = geometry factor = 0, 1, 2 for slabs, cylinders, and spheres, respectively,

h = lattice spacing,

r = distance from the origin of space point k,

and S, B, A, and D are as defined in ref 2. These expressions are to be compared with the fourth-order expressions in ref 2.

The expressions of the second-order approximation allow somewhat faster computation of the coefficients and the source term than those of the fourth-order approximation. More important, the lattice spacing may be as large as desired with no possibility of P_k or R_k becoming negative. This is not true of the fourth-order approximation. There can therefore be fewer space points in the second-order calculation than in the fourth-order calculation. For some cases this will allow a considerable saving in computing time.

The fourth-order approximations are always better than the second-order approximations, of course, but the second-order approximation may be sufficiently good in some cases, for example, for parameter studies.

A version of Corn Pone has been reduced for use of the second-order approximation equations and is now available.

6.8. THE OAK RIDGE RANDOM RESEARCH REACTOR ROUTINE (O5R): A GENERAL-PURPOSE MONTE CARLO CODE FOR THE IBM-704

R. R. Coveyou J. G. Sullivan H. P. Carter[1]

There are many problems in the mathematical analysis of the behavior of nuclear reactors which, for one reason or another, are not easily handled by analytical or conventional numerical calculations but which can be treated by the Monte Carlo method. Since considerable work has been done on the application of this method to reactor problems, it has been decided that a general-purpose Monte Carlo reactor code for the IBM-704 would furnish a useful additional tool for the analysis of reactors. The immediate purpose of the code, which will be identified as the Oak Ridge Random Research Reactor Routine (O5R), will be to facilitate the analysis of the problems which arise in the calculations and measurement of the age of neutrons in water, and the code will originally be somewhat specialized in this direction. It will be modified later to take care of more general situations.

The basic features of the code as presently programed may be summarized as follows:

1. The code can accommodate as many as six different material constituents in different reactor regions.
2. The number of available geometric regions is greater, since more than one region can show the same material constitutents.
3. Each region can contain up to seven different scatterers, and the number of absorbing elements in each region can be essentially unlimited.
4. Each relevant cross section is recorded in supergroups whose widths are a factor of 2 in energy. Within each supergroup, 64 cross sections equally spaced in energy are provided. This is considerably more cross-section detail than is usually considered practicable.
5. Because of the great bulk of cross-section information needed by item 4 above, the cross sections cannot all be stored in the fast memory but must be read in from magnetic tape. In order to use the cross-section storage efficiently, a large number of neutrons (about 300) are followed in parallel until all are removed from the energy group where cross sections are available before a new set of cross sections is read into the fast memory.
6. The original program will have the following limitations, which are to be removed after the age analyses are performed: (a) the geometry will be restricted to infinite slabs and (b) no provision will be made for thermal effects.
7. The code will use the 704 master cross-section tape and the 704 Monte Carlo cross-section tape as described in Sec. 6.9.

The programing is essentially complete; the coding for Model A is about 60% finished. It is anticipated that the code will be ready for use in analyzing projected measurements of the age of neutrons in water.

[1]Mathematics Panel.

6.9. CROSS-SECTION TAPES FOR IBM-704

J. G. Sullivan

The Oracle master cross-section tape which has been described previously[1] has now been transcribed for use on the IBM-704. Cross sections, or the logarithms of cross sections, are stored on the IBM-704 magnetic tape with the corresponding lethargy values. The lethargy points are so chosen that no substantial error is introduced by assuming linearity between recorded values. Pending decision as to liaison equipment between the Oracle and the IBM-704, cross sections are printed on the Oracle in forms convenient for the IBM-704 by punch operation.

The routines which produce the Oracle Monte Carlo cross-section tape from the master cross-section tape have been translated into the IBM-704 language. Hence the Monte Carlo tape for the IBM-704 may be prepared for use at any time.

[1]R. R. Bate, J. H. Marable, and J. W. Niestle, *Appl. Nuclear Phys. Ann. Rep. Sept. 10, 1956*, ORNL-2081, p 140.

Part 7

SHIELDING RESEARCH

7.1. MONTE CARLO CALCULATION OF GAMMA-RAY DOSE RATES RESULTING FROM NEUTRON CAPTURES IN AIR

F. L. Keller C. D. Zerby W. W. Dunn[1]

Very little quantitative work has been done on the problem of determining gamma-ray dose rates produced in air when low-energy neutrons are allowed to leave a source and are eventually captured in the air. The gamma rays which are produced by the radiative capture process in air are largely of rather high energy, ~5 to 10 Mev, and hence are quite penetrating. In the majority of the shielding problems which occur in connection with the shielding of fission sources, the gamma-ray dose rate resulting from these air captures is negligible when compared with the dose rate produced by gamma rays leaving the source shield surface directly. However, situations may arise in which the source itself is heavily gamma-ray shielded, at least in the directions which are favorable for air scattering to the detector, but in which a large neutron leakage is allowed and, perhaps, auxiliary neutron shielding material placed around the detector position. In many of these situations the fact that the air-capture gamma rays are quite penetrating and often produced at positions which are very favorable for allowing the gamma rays to penetrate the auxiliary shield makes it possible for the air-capture gamma rays to give a major contribution to the gamma-ray dose rate at the detector.

The problem may be idealized to that of determining the air-capture gamma-ray dose rate and angular distribution at a detector located an arbitrary distance from a point source of monoenergetic neutrons where both the source and the detector are considered to be embedded in an infinite volume of air. The calculation should include the contributions from captures which take place during the slowing-down process, as well as contributions from captures which occur during the diffusion at thermal energy. A portion of the results of a parameter study of this problem by the Monte Carlo technique for both point isotropic and line-beam sources is presented here. The complete results have been presented in a separate report.[2]

Calculational Method

The Monte Carlo machine code used for this problem was a modification of the Monte Carlo code which was used to calculate neutron scattering in air.[3] The total cross sections for oxygen and nitrogen were taken from BNL-325[4] and were considered to be identical with the scattering cross sections, except for the absorption cross section of nitrogen. The absorption cross section of oxygen is extremely small and was neglected. The absorption cross section of nitrogen is made up of the (n,p) and (n,γ) cross sections, which were taken to be 1.70 barns and 0.08 barn, respectively, at 0.025 ev and were assumed to have a $1/v$ dependence. The scattering probability was taken as isotropic in the center-of-mass system.

The source was taken to be either a point isotropic source of monoenergetic neutrons of energy E_n or a point source which emitted a monoenergetic line beam of neutrons of energy E_n at an angle θ_0 with respect to the source-detector axis. The space about the detector was divided into a number of solid-angle intervals, and estimates of the angular distribution of the dose rate at the detector were made.

The neutron histories were generated in exactly the same manner as described in the report on air scattering.[3] At each neutron collision the probability of capture was determined, and a statistical estimate was made of the capture gamma-ray dose-rate contribution at the detector from that collision. The neutron was then allowed to scatter randomly and to continue with a reduced weighting. The neutrons were degraded in energy at each scattering by the standard elastic-scattering relations until the neutron energy reached 0.025 ev. After the neutron energy was degraded to 0.025 ev, the neutron was permitted to scatter and diffuse without further energy loss. A neutron history was terminated if the neutron weight after the lth collision was less than about $1/600$ of its original weight or if the collision occurred at a distance

[1] On assignment from U.S. Air Force.

[2] W. W. Dunn, F. L. Keller, and C. D. Zerby, *A Calculation of Gamma-Ray Dose Rates from Neutron Capture in Air*, ORNL-2462.

[3] C. D. Zerby, *A Monte Carlo Calculation of Air-Scattered Neutrons*, ORNL-2277 (April 23, 1957).

[4] D. J. Hughes and J. A. Harvey, *Neutron Cross Sections*, BNL-325 (July 1, 1955).

greater than 32 mfp from the detector position. This enabled a 0.025-ev neutron to make approximately 45 collisions before its history was terminated. For higher source energies the average number of collisions was, of course, greater.

The capture gamma rays were assumed to be emitted isotropically from the collision point, and an exponential buildup factor was used in the dose-rate calculation. The spectrum of capture gamma rays used in the dose-rate determination was from the recent work of Bartholomew and Campion.[5] The dose-rate contributions were stored in appropriate solid-angle intervals at the detector under the assumption that all gamma rays from a given event entered the detector in the solid-angle interval which contained the radius vector from the detector to the collision point. All the results were normalized to 1 neutron/sec leaving the source, and all the results reported here were from calculations which used 500 neutron case histories. It is pointed out that because this method of statistical estimation was employed the results were relatively insensitive to the number of neutron histories used.

The result of the Monte Carlo calculation was checked against the result obtained from the neutron flux given by the direct solution to the transport equation for the case of a point isotropic source of 0.025-ev neutrons located a distance of 15 m from the detector. The assumptions involved in both calculations were the same except that the Monte Carlo calculation took the neutron-scattering probability to be isotropic in the center-of-mass system, whereas the transport equation treated the scattering as isotropic in the laboratory system. This would be expected to lead to a slightly lower value for the Monte Carlo result. The comparison showed that the Monte Carlo result was about 10% smaller than the result from the check calculation. Hence, the results reported here are believed to be good to about 10 to 20%. It is interesting to note that the dose-rate contribution from the flux given by the nonasymptotic part of the solution to the transport equation was about 30% of the total dose rate in the above case.

Results for Point Isotropic Sources

A series of calculations were performed for point isotropic neutron sources with energies of 0.025, 0.1, 1.0, 100, and 10,000 ev and a source-detector separation distance of about 50 ft. The air density was taken to be 0.001205 g/cm^3, which corresponds to approximately sea-level conditions. A plot of the total gamma-ray dose rate as a function of the neutron source energy (E_c) is shown in Fig. 7.1.1. It may be noted that the dose rate varies with the neutron source energy approximately as $E^{-1/3}$.

In these calculations each gamma-ray dose-rate contribution at the detector was also stored with respect to the energy, at capture, of the neutron which gave rise to the contribution. Figures 7.1.2, 7.1.3, and 7.1.4 show histograms of the dose rate

[5] G. A. Bartholomew and P. J. Campion, *Can. J. Phys.* 35, 1347 (1957).

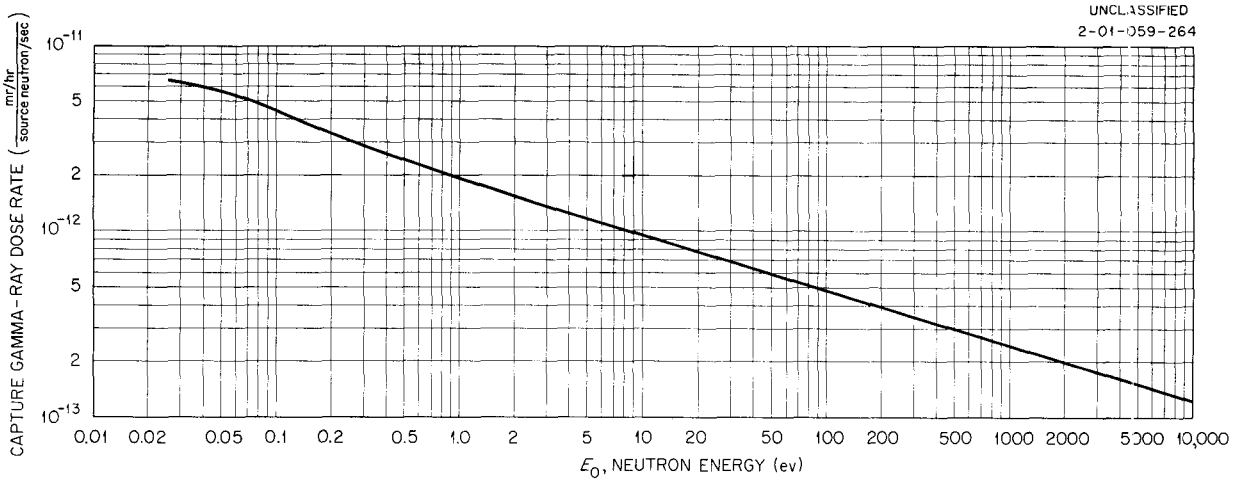

Fig. 7.1.1. Air-Capture Gamma-Ray Dose Rate at a Detector 50 ft from a Point Isotropic Monoenergetic Neutron Source.

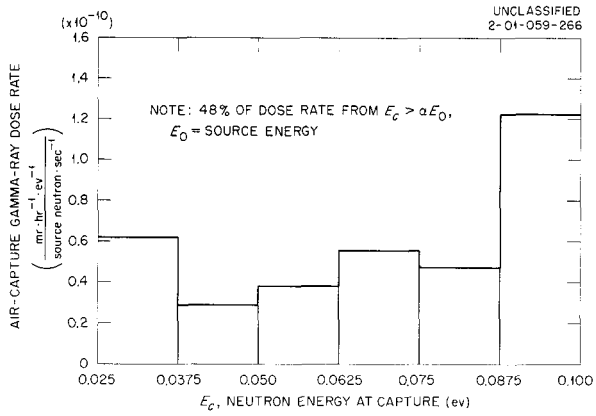

Fig. 7.1.2. Air-Capture Gamma-Ray Dose Rate 50 ft from a Point Isotropic Neutron Source as a Function of E_c for E_0 = 0.1 ev.

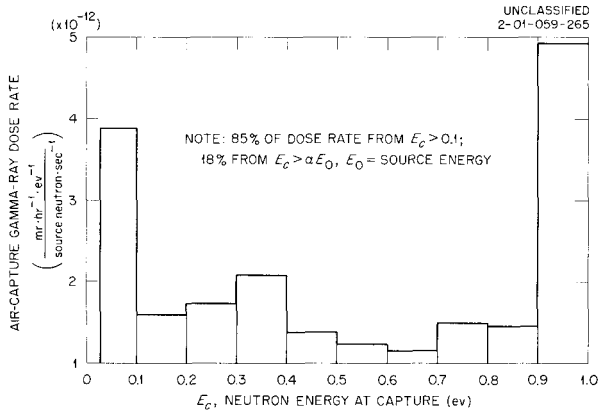

Fig. 7.1.3. Air-Capture Gamma-Ray Dose Rate 50 ft from a Point Isotropic Neutron Source as a Function of E_c for E_0 = 1.0 ev.

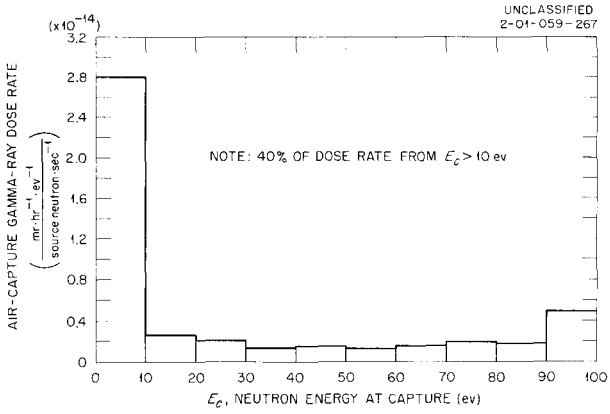

Fig. 7.1.4. Air-Capture Gamma-Ray Dose Rate 50 ft from a Point Isotropic Neutron Source as a Function of E_c for E_0 = 100 ev.

plotted as a function of neutron capture energy for several of the cases run in this study. It may be seen that, for relatively low neutron source energies, a large part of the gamma-ray dose rate at the detector comes from neutrons which are captured at energies that are within a factor of α of the source energy, where $\alpha = [(A - 1)/(A + 1)]^2$ and A is the average mass number for air. This fact throws considerable doubt on calculations of the air-capture gamma-ray dose rate which use the results of the standard age-diffusion equation for the neutron flux, since these results are known to break down for neutron energies which are within a factor of α of the source energy.

Results for Line-Beam Sources

Figure 7.1.5 shows the results for a series of problems performed for line-beam neutron sources.

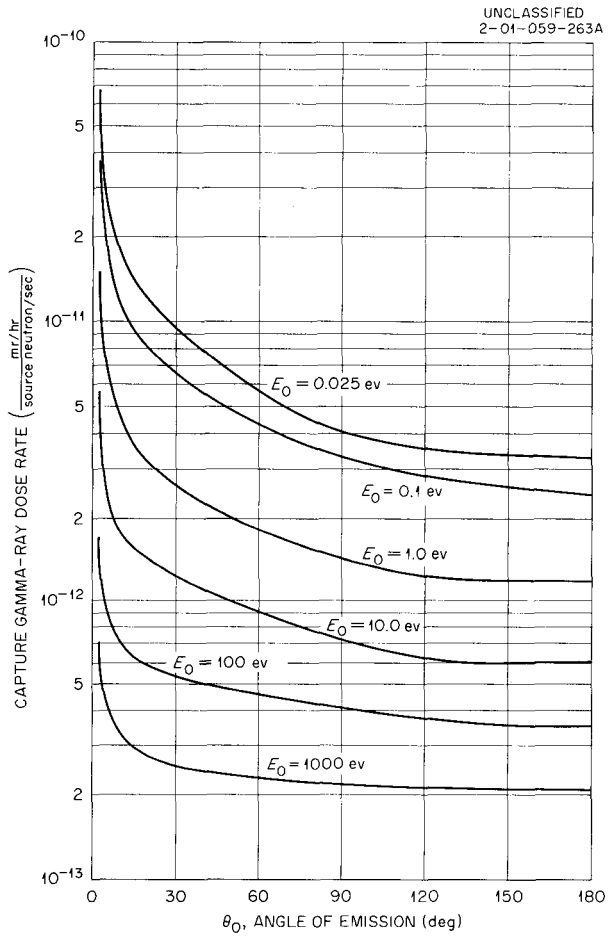

Fig. 7.1.5. Air-Capture Gamma-Ray Dose Rate at a Detector 65 ft from a Line-Beam Neutron Source Emitted at Various Angles from the Source-Detector Axis.

The gamma-ray dose rate at the detector is shown plotted as a function of the angle of emission of the beam for various monoenergetic sources. The source-detector separation distance was 65 ft, and the air density was again taken as 0.001205 g/cm^3. The curves are relatively flat over the region from 30 to 180 deg, and they become flatter as the source energy is increased, as would be expected.

7.2. STUDY OF GAMMA RAYS PRODUCED BY NEUTRON INTERACTIONS IN AIR

C. E. Clifford V. R. Cain F. J. Muckenthaler

The intensities of the gamma-ray dose rates measured in various experiments of the Tower Shielding Facility (TSF) have indicated that secondary gamma rays produced by neutron interactions in air are often important contributors. The neutron interactions which could result in gamma-ray production are inelastic scattering and thermal-neutron capture. Calculations of gamma-ray intensities from inelastically scattered neutrons are somewhat difficult because neither the scattering cross section nor the energy distribution of gamma rays for this interaction is well known. The fact that the neutron energy spectrum leaving the reactor tank is difficult to measure further complicates the problem. Measurements to determine the inelastic scattering cross section for neutrons in air at the TSF also would be very difficult; however, it was possible to perform an experiment in which gamma-ray spectral measurements were made, from which it is hoped that the order of magnitude of the dose rates to be expected from inelastic scattering and thermal-neutron capture can be deduced.

Experimental Configuration

In order to detect the high-energy gamma rays resulting from neutron interactions with air, it was necessary to eliminate, where possible, other sources of high-energy gamma rays. Since the number of gamma rays born in the Tower Shielding Reactor was larger by many orders of magnitude than the number born in the air, the reactor had to be well shielded from the detector. This was accomplished by submerging the reactor in the handling pool 8 ft below the surface of the ground, thus interposing approximately 40 ft of earth as shielding.

As shown in Fig. 7.2.1, the experimental configuration included an 8-in.-dia by 10-ft-long air-filled collimator attached to one face of the reactor so that a beam of radiation was emitted into the air at an angle of 60 deg from the horizontal. The axis of the collimator passed through the center of the face of the reactor. A partially shielded sodium iodide crystal (3 by 3 in.) mounted on a Dumont 6363 phototube was located approximately 1 ft above ground level at a horizontal distance of 52 ft from the reactor. The crystal was enclosed in a cavity surrounded by an 8-in. thickness of lead and at least 4 ft of concrete. On the side of the detector shield facing the reactor, a 4-in.-wide collimator slit extended through the shield to the detector position. The floor of the slit slanted 10 deg upward from the detector position so that no direct radiation from the ground would be admitted. The crystal and phototube were mounted so that the axis of the phototube was at an angle of 45 deg from the horizontal to ensure maximum sensitivity.

The collimator slit, which was 5 ft long and 5 ft deep at the deepest point (at the detector position), was filled with borated water contained in a 4 in. × 4 ft × 4 ft plastic bag. The borated water prevented neutrons from reaching the detector and also reduced the number of capture gamma rays produced in the concrete walls of the collimator. In addition, a $^3/_{16}$-in.-thick sheet of boron Plexiglas was placed over the outside of the collimator slit. (The boron Plexiglas used in this experiment was Plexiglas impregnated with boron carbide to a density of 0.55 g of boron per cubic centimeter.) The effectiveness of this neutron shielding was verified by a series of measurements with a BF_3 chamber and a fast-neutron dosimeter placed in the detector cavity. The measurements indicated that there was no detectable neutron flux in the cavity.

The intersection of the detector lines of sight with the cone of radiation from the reactor is

UNCLASSIFIED
2-01-056-22-D-594

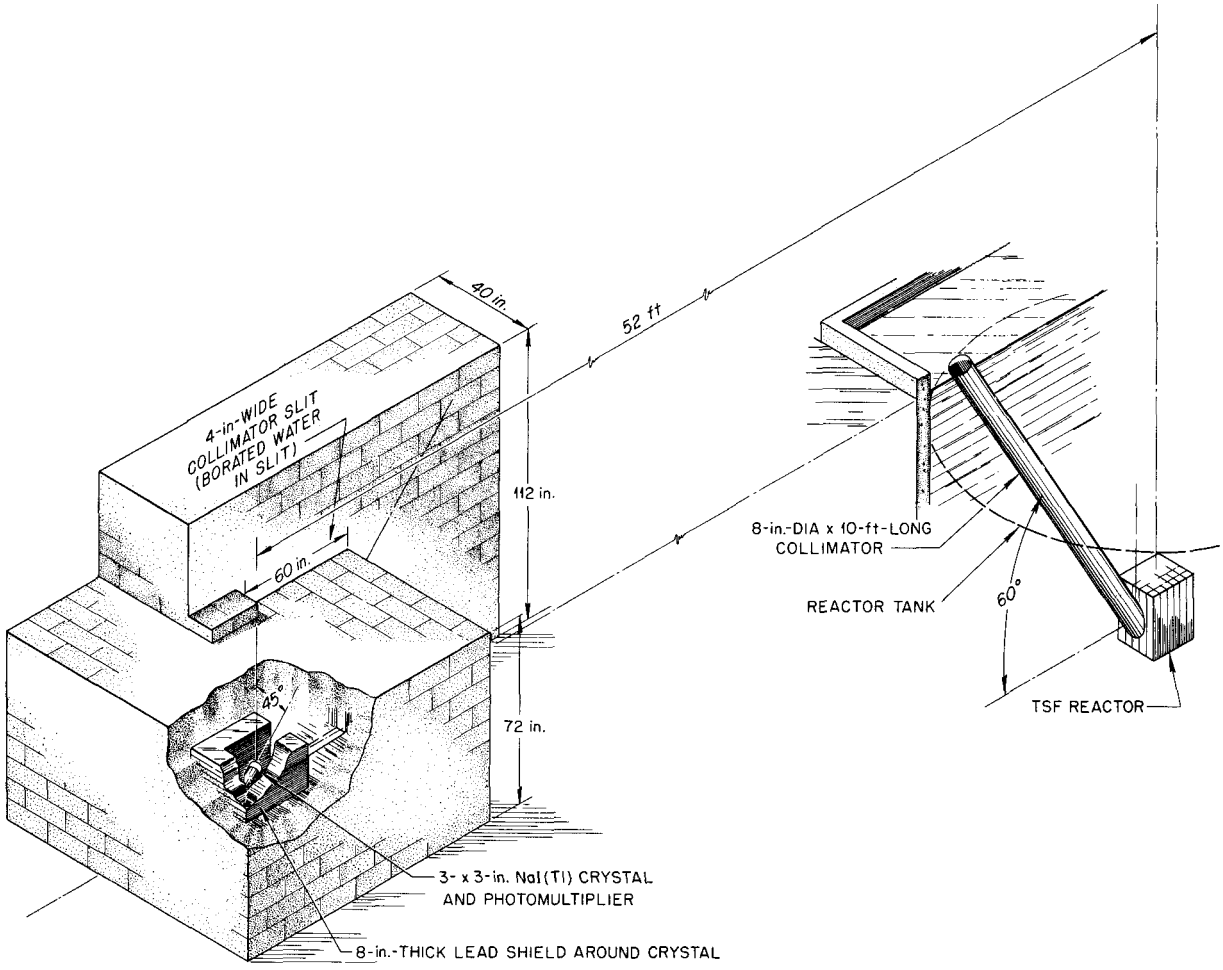

Fig. 7.2.1. Configuration for the TSF Measurement of the Spectra of Gamma Rays Resulting from Neutron Interactions in Air.

depicted in Fig. 7.2.2. It can be seen that the detector solid angle easily includes all of the radiation cone near the ground level, but the fraction of the cone included in the solid angle decreases as the distance from the reactor is increased.

Experimental Results and Discussion

The top curve in Fig. 7.2.3 represents the total gamma-ray pulse-height spectrum resulting from neutron interactions in air. This spectrum presumably consists of gamma rays resulting from the capture of thermal neutrons in the nitrogen of the air plus those from other sources. The highest energy gamma ray due to thermal-neutron capture by N^{14} which is known to have been observed[1] is at 10.8 Mev, and this can be identified in the curve at a pules-height setting of 1000. Unfortunately, it was not possible in the experiment to isolate the gamma-ray contribution from thermal-neutron captures from the contribution from inelastically scattered fast neutrons. It was possible, however, to reduce the effect of the capture gamma-ray contribution by blacking out most of the thermal neutrons so that a difference spectrum could be

[1] G. A. Bartholomew and P. J. Campion, *Can. J. Phys.* **35**, 1347 (1957).

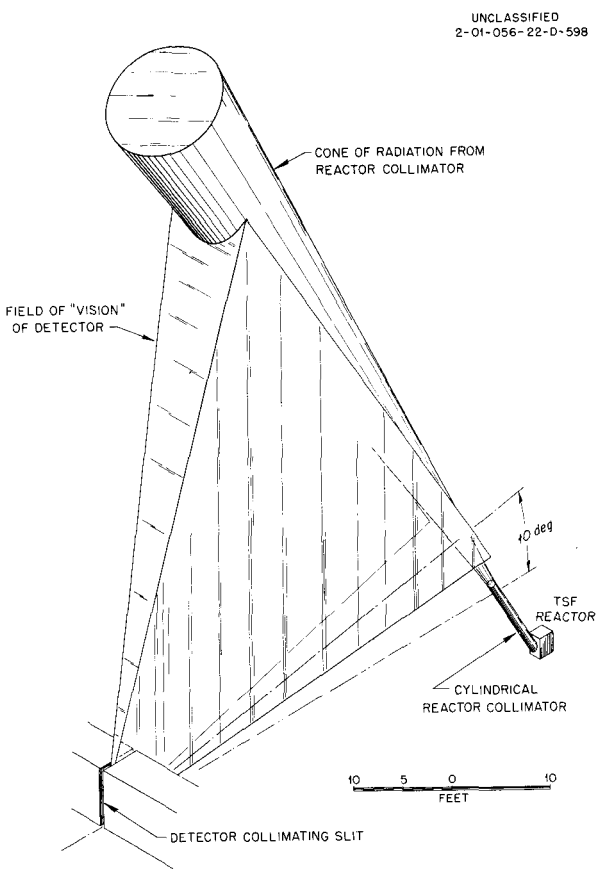

Fig. 7.2.2. Geometric Relationships of the Detector Lines of Sight and the Core of Radiation from the TSR.

obtained which could then be used to determine the approximate contribution from inelastically scattered neutrons. In order to obtain measurements with a reduced capture gamma-ray contribution, the upper end of the reactor collimator was covered with boron Plexiglas. The resulting gamma-ray spectrum is shown in the third curve from the top in Fig. 7.2.3. It can be seen that the 10.8-Mev capture gamma-ray peak was reduced in intensity by a factor of 40. However, the portion of the curve corresponding to lower pulse-height settings was not reduced by the same factor, which indicates that this portion of the spectrum does not merely represent gamma rays originating from thermal-neutron capture but also represents gamma rays from another source. This other source is presumably inelastically scattered fast neutrons that were unaffected by the boron Plexiglas on the reactor collimator. If this curve is subtracted from the top curve in the figure, which represents the total capture gamma-ray contribution plus the contribution from inelastically scattered neutrons, then the difference curve would represent the spectrum of capture gamma rays from low-energy neutrons which were eliminated by the boron Plexiglas on the reactor collimator. This difference curve, which is also plotted in Fig. 7.2.3, shows very little fine structure; however, the energy level distribution in N^{15} is such that it is possible for gamma rays of the order of 15 different energies ranging from 3.5 to 10.8 Mev to be emitted, and these would be smeared by scattering in air and in the borated water and by interactions in the crystal itself. Several energy levels from 5.2 to 5.6 Mev are responsible for about one-fourth of the gamma rays from thermal-neutron capture in nitrogen, and this difference curve does seem to indicate a prominent peak at about 4.5 to 5 Mev. The peak observed in this difference curve at a pulse-height setting of about 100 is due to a gain shift during the foreground and background runs which resulted in improper subtraction of the Zn^{65} gamma rays used as a calibration source.

If it is assumed that the 10.8-Mev peak obtained in the measurements in which boron Plexiglas was used on the reactor collimator is due only to thermal-neutron capture in nitrogen, then this peak can be normalized with the same peak in the capture gamma-ray difference curve. The difference between these two curves, shown in the lower curve in Fig. 7.2.4, was thought to be due to gamma rays resulting from inelastically scattered fast neutrons. The large number of high-energy gamma rays (>2.25 Mev), however, indicated the possibility that a significant contribution to this inelastic scattering spectrum might be resulting from neutron interactions in the concrete walls of the collimator. (For example, silicon capture gamma rays have very high energies.) In order to resolve this question, additional measurements were performed in which the neutron and gamma-ray intensities entering the collimator slit were changed through the use of lead and several thicknesses of paraffin placed over and in front of the slit. Throughout this series of measurements the gamma rays at the detector were greatly reduced when both lead and paraffin were used, but they were not reduced by the paraffin alone more than would be expected for gamma rays formed outside the collimator. It was

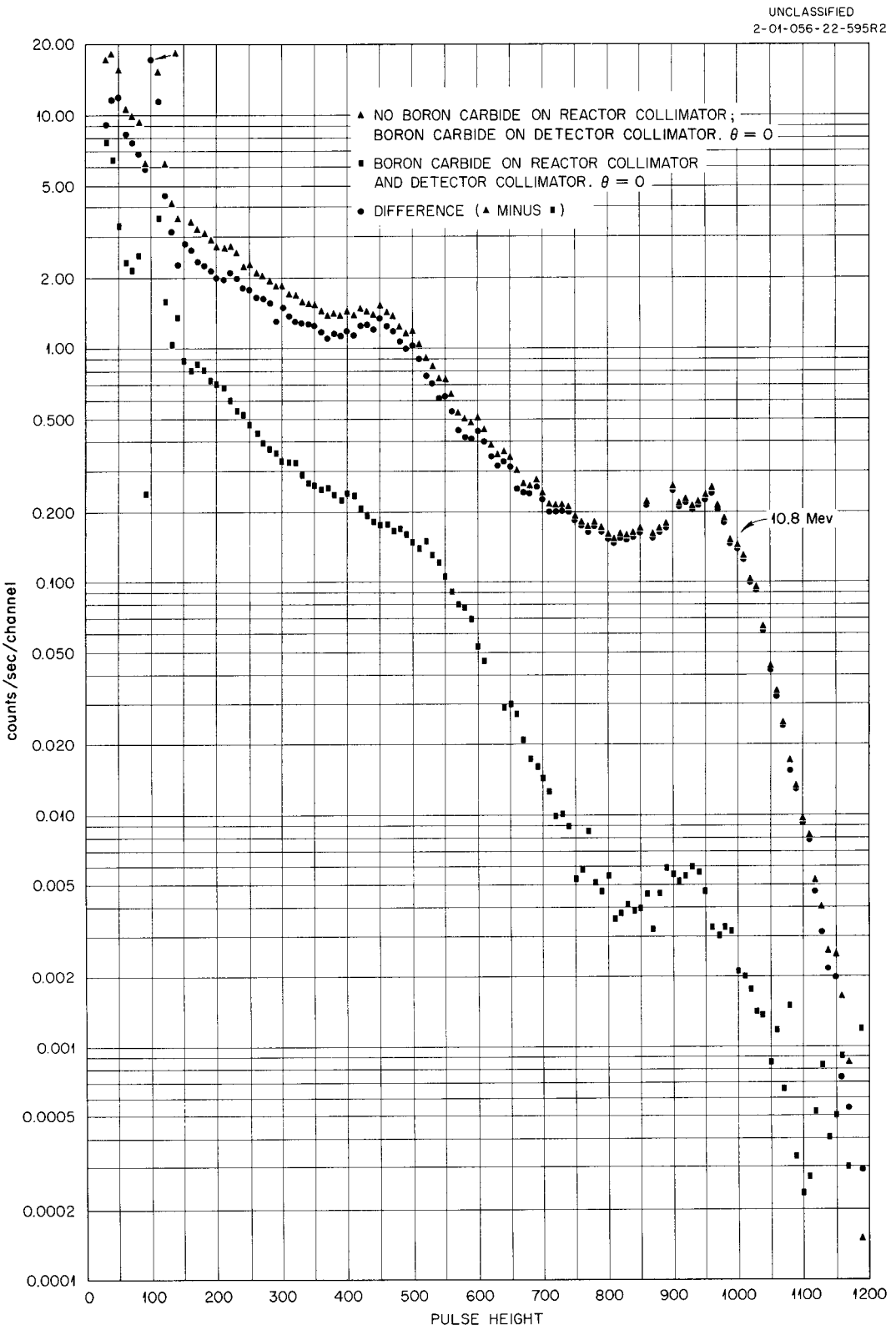

Fig. 7.2.3. Total Pulse-Height Spectra of Gamma Rays Resulting from Neutron Interactions in Air.

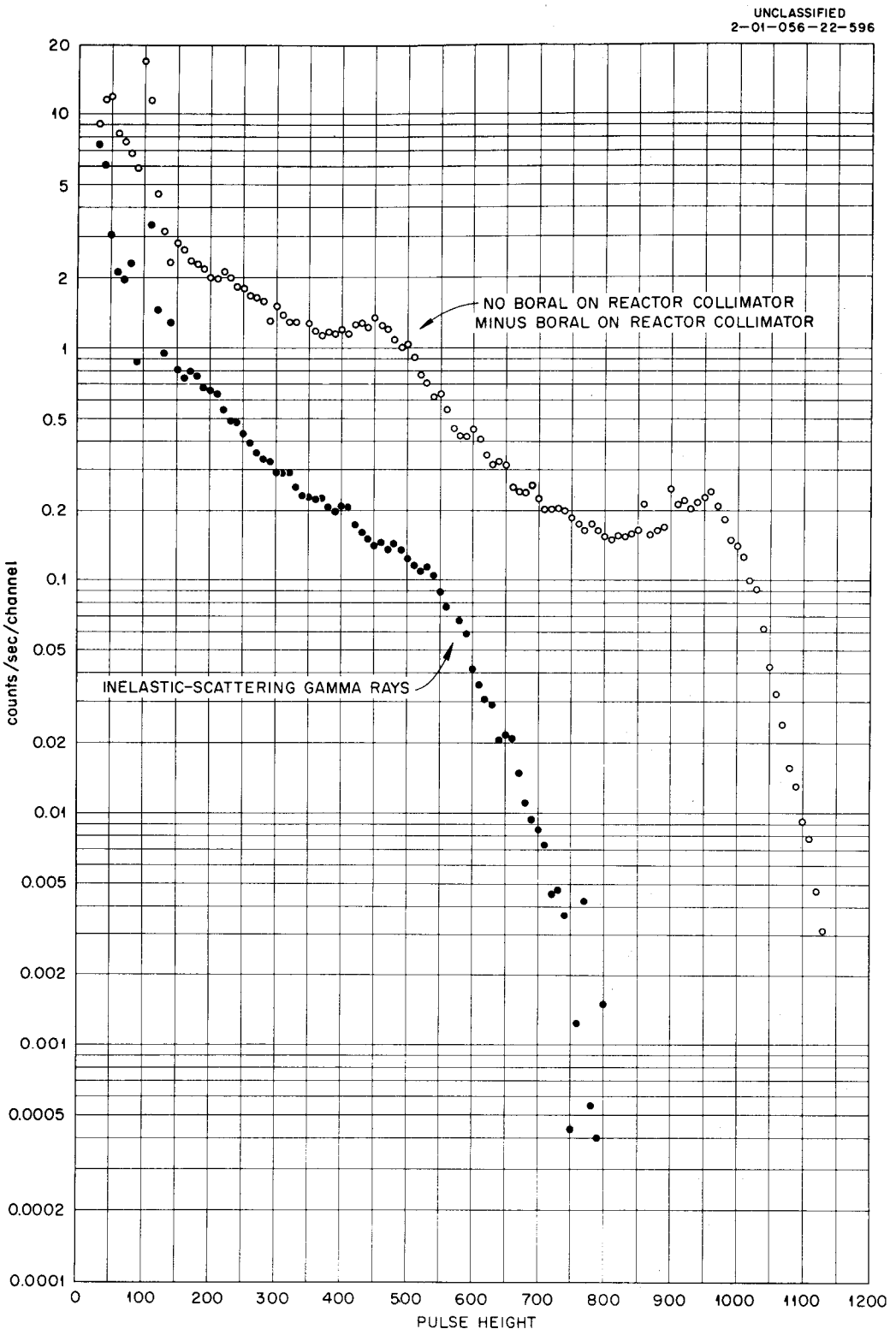

Fig. 7.2.4. Pulse-Height Spectra of Capture and Inelastic Scattering Gamma Rays Resulting from Neutron Interactions in Air.

therefore concluded that these gamma rays had resulted from interactions in air and not from thermal-neutron capture in the detector collimator. In this paper it is assumed that all the gamma rays observed by the detector were due either to the air capture of thermal neutrons or to the inelastic scattering of fast neutrons; however, contributions to the detector by other sources, such as multiply scattered gamma rays, may be included.

This investigation has been published in more detail in a separate report.[2]

[2]V. R. Cain, F. J. Muckenthaler, and C. E. Clifford, *Study of Gamma Rays Produced by Neutron Interactions in Air*, ORNL CF-58-4-77 (May 29, 1958).

7.3. ANALYSIS OF THE RECENT TSF SECONDARY GAMMA-RAY EXPERIMENT

F. L. Keller O. S. Merrill[1]

In the majority of reactor shielding problems the gamma-ray dose rate which results from secondary gamma rays produced by neutron interactions with the air is negligible compared with the dose rate which results from air-scattered source gamma rays. However, situations may arise in which it is desirable to allow a large neutron leakage from the reactor shield itself and then place part of the neutron shielding material around individual regions, which must be further shielded. In many of these situations the air-scattered gamma rays, which are generally of rather low energy ($\sim < 1$ Mev), are attenuated very rapidly by the shielding material around the individual regions, whereas the neutron-induced gamma rays, which are isotropically emitted with rather high energies (up to ~ 10.8 Mev), penetrate much more readily. Therefore, as the thickness of the shield around the individual regions is increased, the relative importance of the neutron-induced gamma rays is increased; and it is possible, in some instances, for these gamma rays to be the major contributor to the dose rate.

The two important methods of secondary gamma-ray production in air are neutron capture in N^{14} and inelastic neutron scattering with both nitrogen and oxygen. In order to accurately calculate the dose-rate contribution from these two processes, it is necessary to know the cross sections involved and the spectra of gamma rays produced. Experimental measurements of the thermal-neutron radiative capture cross section of N^{14} and the associated capture gamma-ray spectrum have been reported in the literature.[2] Very little experimental data is available on either the cross sections or the associated gamma-ray spectra for inelastic neutron scattering with nitrogen and oxygen. On the other hand, Lustig, Goldstein, and Kalos[3,4] have published theoretical values of the inelastic neutron scattering cross sections of nitrogen and oxygen from which it is possible to estimate the spectrum of inelastic scattering gamma rays produced from a given fast-neutron distribution. However, since these cross-section calculations are based on a model which assumes that a statistical model of the nucleus may be applied to the compound nucleus, the results are questionable for nuclei as light as oxygen and nitrogen. Thus, it was considered important to make a comparison between the shape of a measured inelastic scattering gamma-ray spectrum and one calculated by use of the above cross sections for at least one situation.

An experiment performed at the Tower Shielding Facility to separate out and measure as accurately as possible the spectra of gamma rays produced in air from neutron captures in N^{14} and inelastic neutron scattering is reported in Sec. 7.2. This experiment, which made use of a 3 by 3 in. sodium iodide crystal spectrometer, yielded two pulse-height distributions, one attributed to capture gamma rays and the other to inelastic scattering gamma rays. (These experimental pulse-height distribution curves are shown in Fig. 7.2.4 in Sec. 7.2.) However, in order to eliminate background counts from neutron interactions in the

[1]On assignment from Convair, San Diego, Calif.

[2]G. A. Bartholomew and P. J. Campion, *Can. J. Phys.* 35, 1347 (1957).

[3]H. Lustig, H. Goldstein, and M. H. Kalos, *The Neutron Cross Sections of Nitrogen*, NDA-86-1 (June 30, 1957).

[4]H. Lustig, H. Goldstein, and M. H. Kalos, *An Interim Report on the Neutron Cross Sections of Oxygen*, NDA-086-2 (1958).

crystal, it was necessary to make the gamma-ray measurements inside a thick shield through which a water-filled collimator was inserted. Hence, since the gamma rays which were detected had penetrated through the thick (~4-ft) water collimator, the measured pulse-height distributions were considerably altered from the desired ones by the water attenuation and buildup. It would be an almost impossible task to take the measured pulse-height distributions and attempt to work backwards to obtain the spectra of gamma rays incident on the outside of the collimator. Therefore it was considered more advisable to calculate pulse-height distributions by first determining the spectra incident on the outside of the water collimator from both capture and inelastic scattering gamma rays, then determining the attenuation and buildup associated with the passage of the radiation through the water collimator, and, finally, using detector response functions. The resulting calculated spectra could be compared directly with the experimental pulse-height spectra.

Spectra of Gamma Rays Incident on the Outside of the Collimator

A rather accurate estimate of the complete spectrum of gamma rays from neutron captures in N^{14} was obtained by making use of the direct experimental measurements of Bartholomew and Campion.[2]

The report by Lustig, Goldstein, and Kalos[3] on neutron cross sections of nitrogen gives theoretical values of the total inelastic scattering cross sections for neutrons with energies up to 18 Mev and the results of Hauser-Feshbach calculations of the cross sections for exciting the first four individual nuclear levels with various energy neutrons up to 6 Mev. Since these individual level cross sections are relatively flat in the region of 6 Mev, they may be extrapolated to somewhat higher neutron energies. For neutron energies above 6 Mev the difference between the total inelastic cross section and the sum of these individual level cross sections then represents the cross section for exciting some level whose energy is greater than ~6 Mev. Branching ratios obtained from a review article by Ajzenberg and Lauritsen[5] were used with the individual level cross-section curves to obtain cross-section curves for producing gamma rays with discrete energies less than 6 Mev from these levels. The branching ratios also indicate that most of the levels in the region from 6 to 9 Mev decay directly to the ground state. Hence, since these levels are rather closely spaced and since they decay predominantly to the ground state, it was assumed in calculating the gamma-ray spectrum that the difference cross section mentioned above could be treated as a cross section for producing an inelastic scattering gamma ray with an energy approximately equal to the initial energy of the neutron. In the case of oxygen the first, and most important, level is at 6.09 Mev, and it was assumed that the entire inelastic oxygen cross sections could be taken as the cross section for producing a 6.09-Mev gamma ray. With these cross sections and an assumed neutron distribution it was then possible to estimate the spectrum of inelastic scattering gamma rays produced. The spectrum of fast neutrons above 3 to 4 Mev (which are the only neutrons of importance for inelastic scattering in air) was assumed to have a fission shape in these calculations. The spectrum of inelastic scattering gamma rays obtained in this manner is shown in Fig. 7.3.1, where the discrete energy gamma rays have been represented in histogram form with an energy width of 0.2 Mev. The fact that the calculated distribution above 6 Mev is continuous rather than discrete is, of course, due to the lack of detailed knowledge concerning the excitation of individual levels in this region. Fortunately, the number of gamma rays in the continuous portion of the curve is small compared with the number of gamma rays in the discrete lines, and hence the approximate treatment of these gamma rays is probably adequate.

Spectrum After Attenuation and Buildup in the Water Collimator

Since all gamma rays which reached the detector without making a collision in the water collimator traveled through approximately the same water thickness (~4 ft), the uncollided spectra at the detector were determined by simply multiplying the incident spectra by $e^{-u(E)T}$ at each energy point, where $u(E)$ is the total linear absorption coefficient of water at energy E and T is the water thickness (~4 ft). Next, it was necessary to determine the distribution of scattered, or buildup, gamma rays at the detector for each case. Since all the uncollided gamma rays which reached the detector

[5] F. Ajzenberg and T. Lauritsen, *Revs. Modern Phys.* 27, 77 (1955).

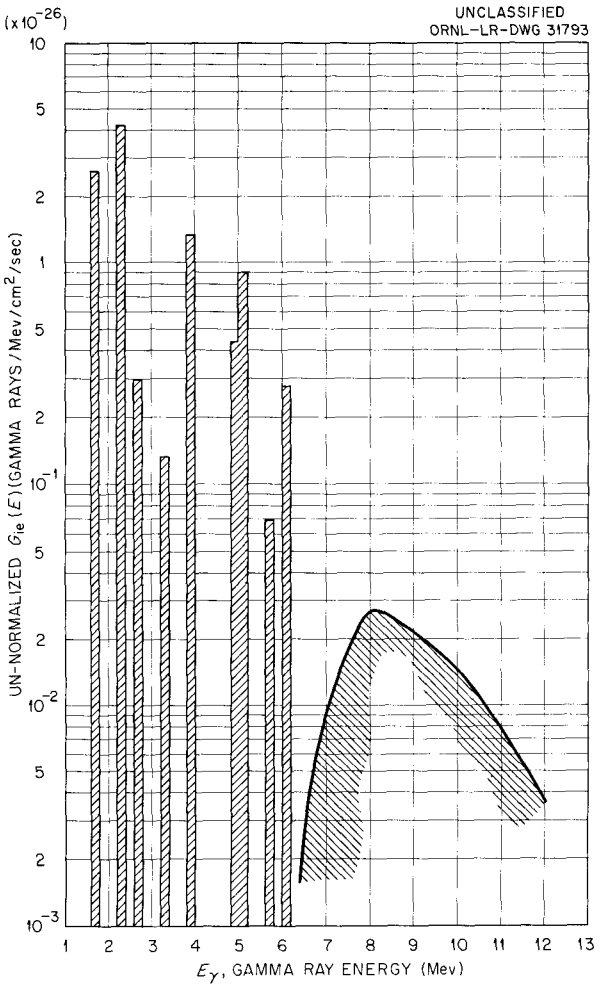

Fig. 7.3.1. Calculated Inelastic Scattering Gamma-Ray Number Flux Spectrum at the Detector (No Water in Collimator).

penetrated essentially the same water thickness, it was assumed that the distribution at the outside of the water collimator could be artificially represented by a single point isotropic source whose strength was normalized so as to give the same uncollided flux at the detector as was calculated above. In the case of gamma rays it appears that even for point isotropic sources in infinite media most of the scattered gamma rays which reach a detector are gamma rays which leave the source in almost the right direction to reach the detector without scattering. Goldstein and Wilkins[6] have calculated the spectra of buildup gamma rays at a detector for cases of point isotropic sources in infinite media. Hence, since the artificial point source introduced above was normalized so that the correct number of gamma rays left the source in the direction toward the detector (although an incorrect number left at large angles to the source-detector axis), it was assumed that the Goldstein-Wilkins results could be applied directly to this artificial point source to determine the buildup spectrum at the detector in the actual problems.

Plots of the total unnormalized gamma-ray number-flux distributions at the detector (i.e., collided, or buildup, plus uncollided) which were obtained in the above manner for capture and inelastic scattering gamma rays are shown in Figs. 7.3.2 and 7.3.3, respectively. In these

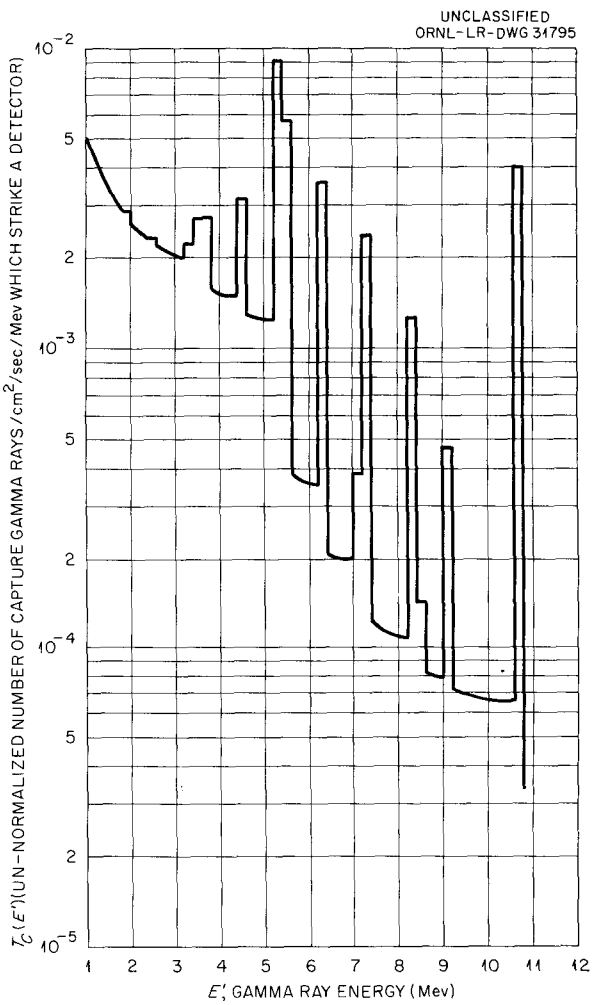

Fig. 7.3.2. Calculated Total Gamma-Ray Number Flux Spectrum at the Detector (Water in Collimator).

[6]H. Goldstein and J. E. Wilkins, Jr., *Calculations of the Penetrations of Gamma Rays. Final Report*, NYO-3075 (June 30, 1954).

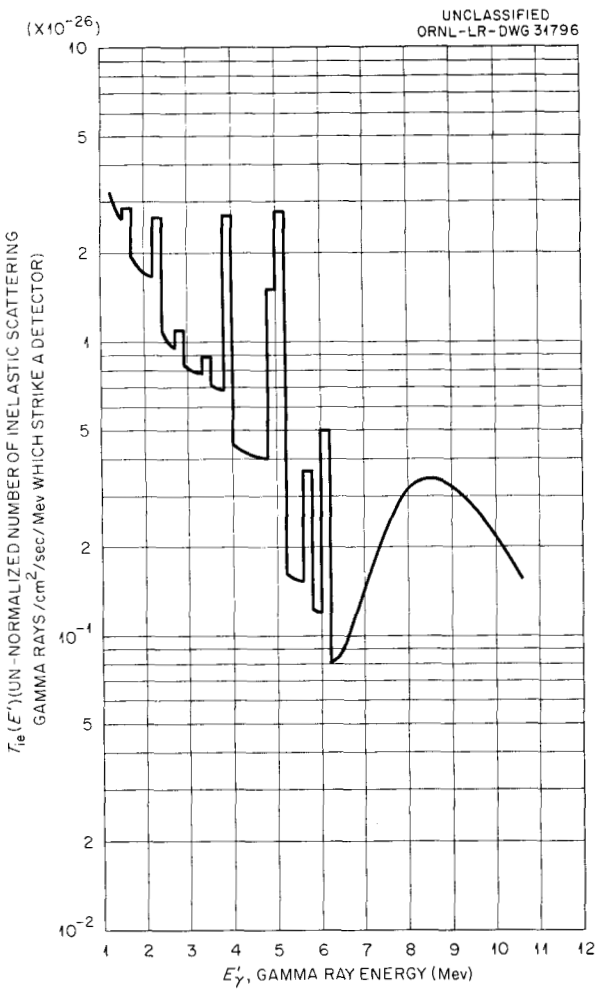

Fig. 7.3.3. Calculated Total Inelastic Scattering Gamma-Ray Number Flux Spectrum at the Detector (Water in Collimator).

figures the histograms representing the uncollided discrete energy gamma rays are superimposed on continuous distributions which are almost entirely due to scattered, or buildup, gamma rays.

Calculation of Pulse-Height Distributions from the Detector

It was necessary to include the detector response so as to obtain pulse-height distribution curves whose shapes could then be compared directly with the experimental results. Experimental measurements of response functions of a 3 by 3 in. sodium iodide crystal are available for various monoenergetic gamma-ray sources. These response functions were replotted in histogram form, where the averaging was performed over 1-Mev intervals, and interpolations were then performed to obtain estimates of the response functions at 0.2-Mev intervals over the entire energy range of interest. These response functions were then applied to the calculated number-flux distributions at the detector to give calculated pulse-height distributions from the detector for both capture and inelastic scattering gamma rays. A comparison of the shapes of the experimental and calculated pulse-height distributions from both capture and inelastic scattering gamma rays is shown in Fig. 7.3.4.

The shapes of the measured and calculated curves are in excellent agreement. Hence, since the spectrum of capture gamma rays which was taken to be incident on the outside of the water collimator was known to be good (i.e., since most of this spectrum was obtained from the results of direct experimental measurements), the excellent agreement between the shapes of the calculated and measured pulse-height distributions from capture gamma rays caused a considerable amount of reliance to be placed in the methods which were used to determine the effects of water buildup and detector response. In view of this, the excellent agreement also obtained between the shapes of the calculated and measured pulse-height distributions from inelastic scattering gamma rays allows a considerable amount of confidence to be placed in the results of calculations based on a spectrum of inelastic scattering gamma rays obtained in the manner outlined.

This analysis has been published in more detail in a recent report.[7]

---

[7] F. L. Keller and O. S. Merrill, *Analysis of the Recent TSF Secondary Gamma-Ray Experiment*, ORNL-2586 (Aug. 25, 1958).

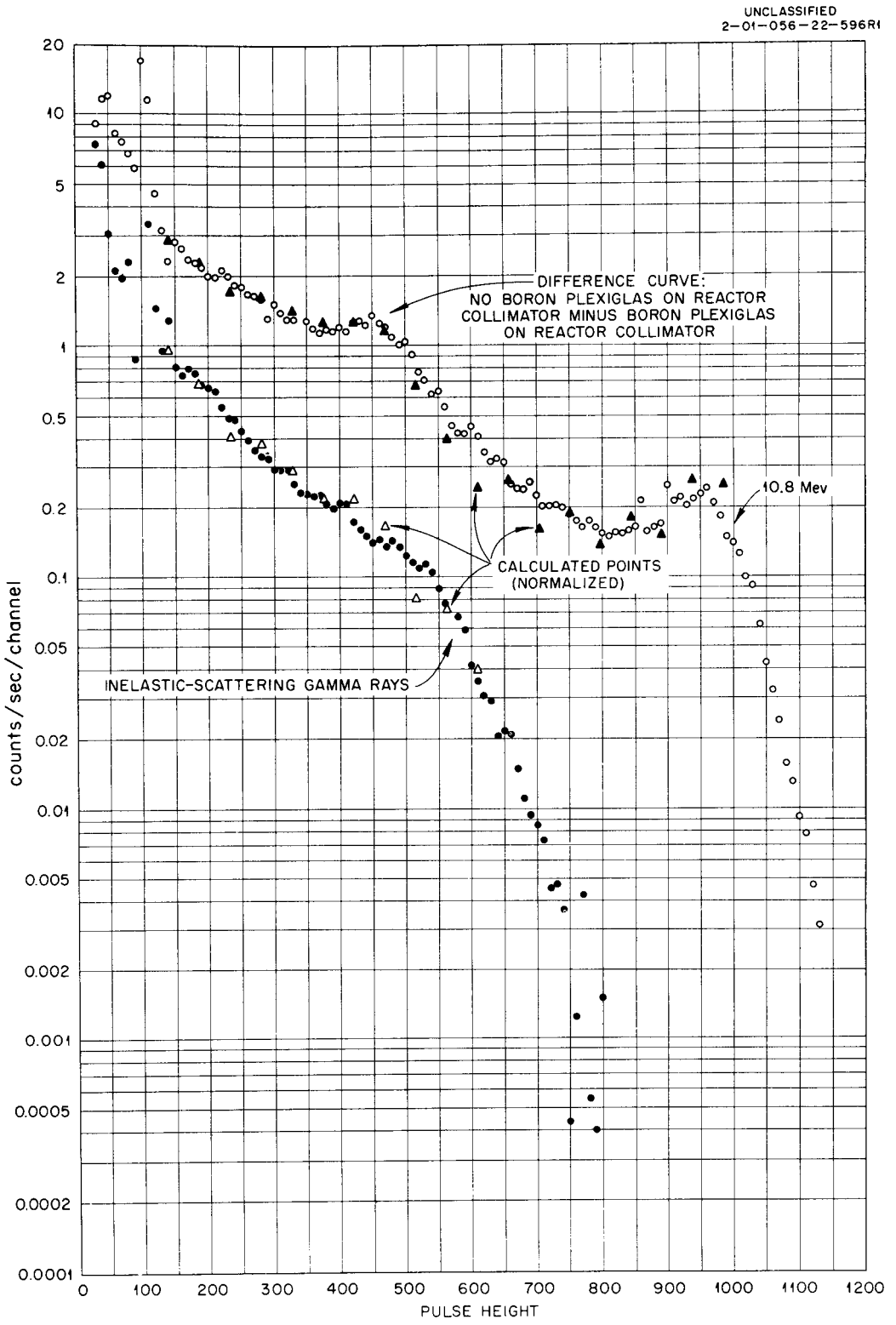

Fig. 7.3.4. Comparison of Experimental and Calculated Pulse-Height Spectra of Capture and Inelastic Scattering Gamma Rays Resulting from Neutron Interactions in Air.

7.4. LTSF STUDY OF SECONDARY GAMMA-RAY PRODUCTION IN LEAD

J. M. Miller

A study of the production of secondary gamma rays in lead was performed at the Lid Tank Shielding Facility. The tests utilized different thicknesses of lead in ½-in. steps from 1 to 6 in. and additional thicknesses of 7½ and 9 in. In each case the lead was kept dry by placing it in a steel tank (⅝-in.-thick walls) positioned against the source plate. An aluminum tank (⅛-in.-thick walls) filled with either oil or borated water was always placed immediately behind the lead. The steel tank, which held the entire configuration, has a 30 × 30 × ⅜ in. aluminum window on the source side, and the recession in the tank wall between the window and the first slab of lead introduced a 1-cm-thick air gap at this point in each of the configurations. Gamma-ray tissue dose-rate measurements were made in both the oil and borated water, and in some cases fast-neutron tissue dose-rate and thermal-neutron flux measurements were made in the oil.

The gamma-ray dose-rate measurements in oil and borated water beyond the various thicknesses of lead are plotted in Fig. 7.4.1 as a function of the distance from the source plate. The measurements in the borated water were made primarily to determine the effect on the secondary production of suppressing the thermal-neutron flux beyond the lead. The gamma-ray dose rates in the borated water were a factor of 3 lower than the dose rates in the oil in the region close to the lead and a factor of 13 lower approximately 120 cm beyond the lead.

Cross-plots of the data from Fig. 7.4.1 are shown in Figs. 7.4.2 and 7.4.3. The plots in Fig. 7.4.2 represent the gamma-ray dose rates at points 100 cm beyond the configurations, corrected for the inverse r^2 attenuation, and show that most of the primary gamma rays are attenuated by the first 3 in. of lead. The gamma rays observed beyond greater thicknesses of lead are practically all secondary gamma rays. The plots in Fig. 7.4.3 represent the gamma-ray dose rates beyond the various configurations at distances of 80 and 100 cm from the source. This figure illustrates that a lead thickness of 3 in. gives the maximum effectiveness in reducing the gamma-ray dose rate at a fixed distance from the source and that increasing the thickness beyond 3 in. does not result in a further reduction.

The thermal- and fast-neutron measurements in oil beyond various configurations are plotted in Figs. 7.4.4 and 7.4.5, respectively, as a function of the distance from the source.

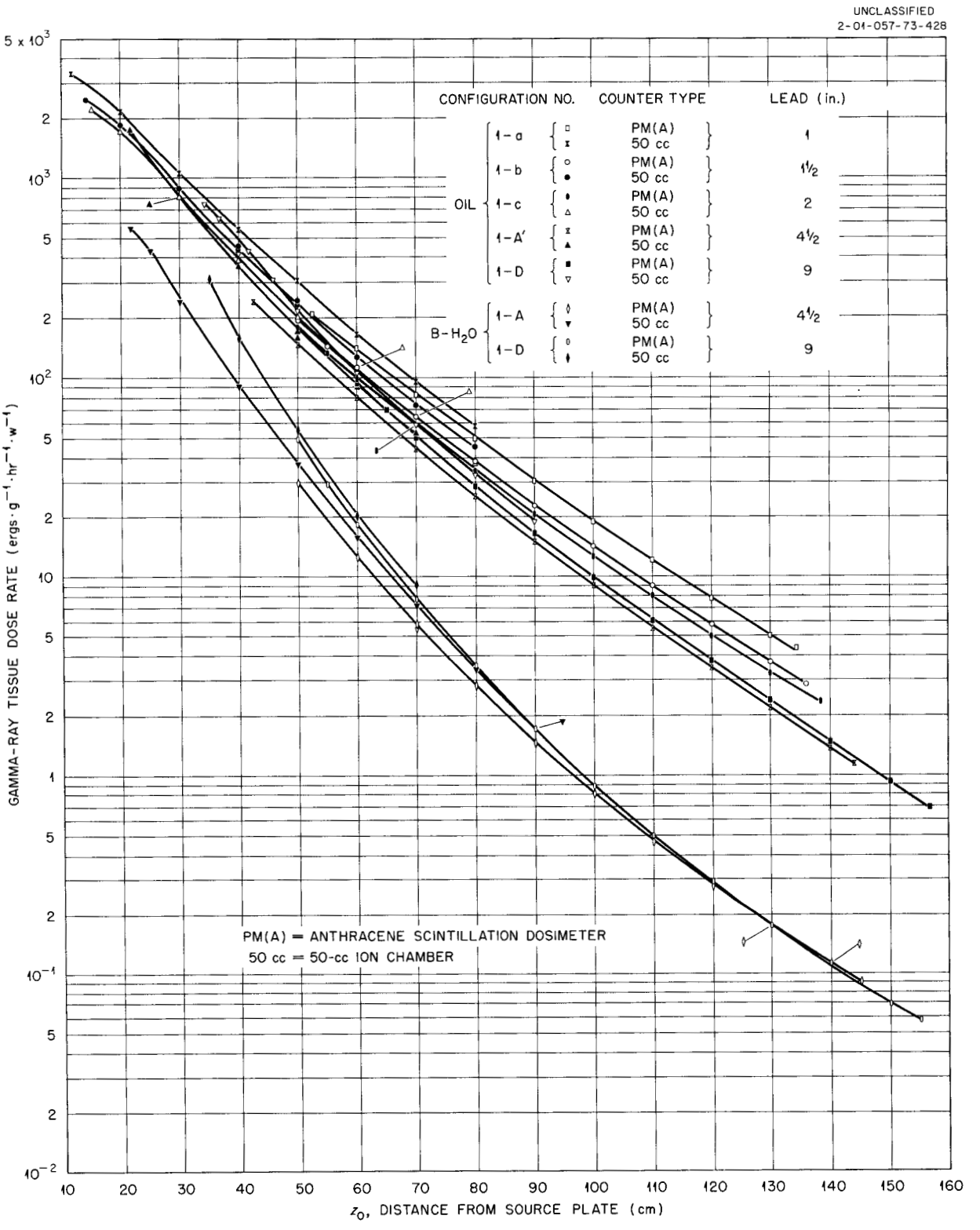

Fig. 7.4.1. Gamma-Ray Dose Rates in Oil and Borated Water Beyond Various Thicknesses of Lead as a Function of the Distance from the Source Plate.

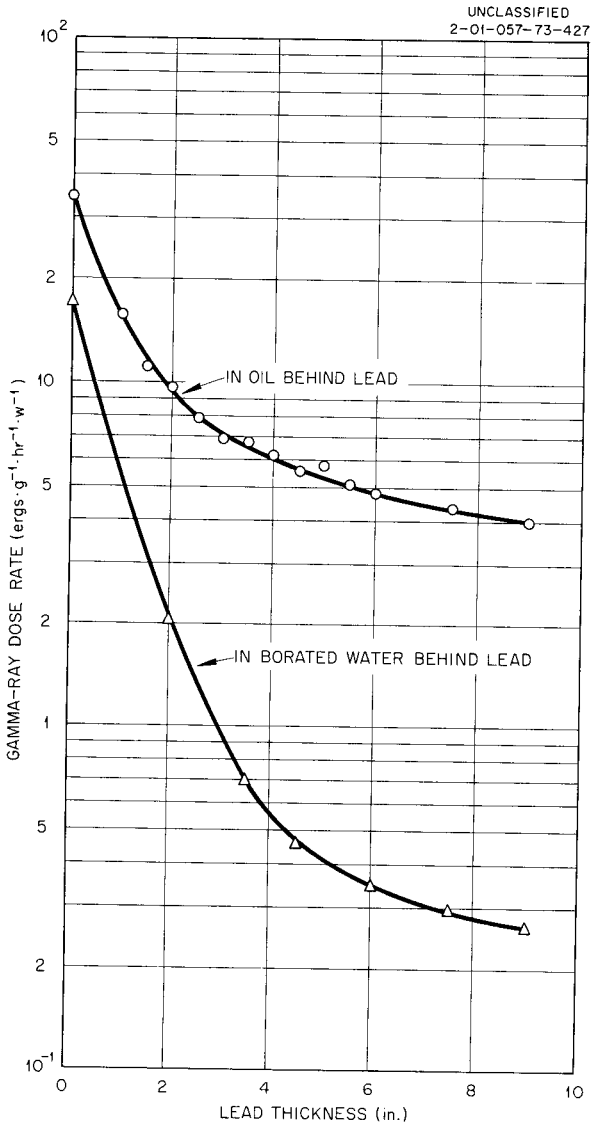

Fig. 7.4.2. Gamma-Ray Dose Rates in Oil and Borated Water 100 cm Beyond Various Thicknesses of Lead (Measurements Corrected for Inverse r^2 Attenuation).

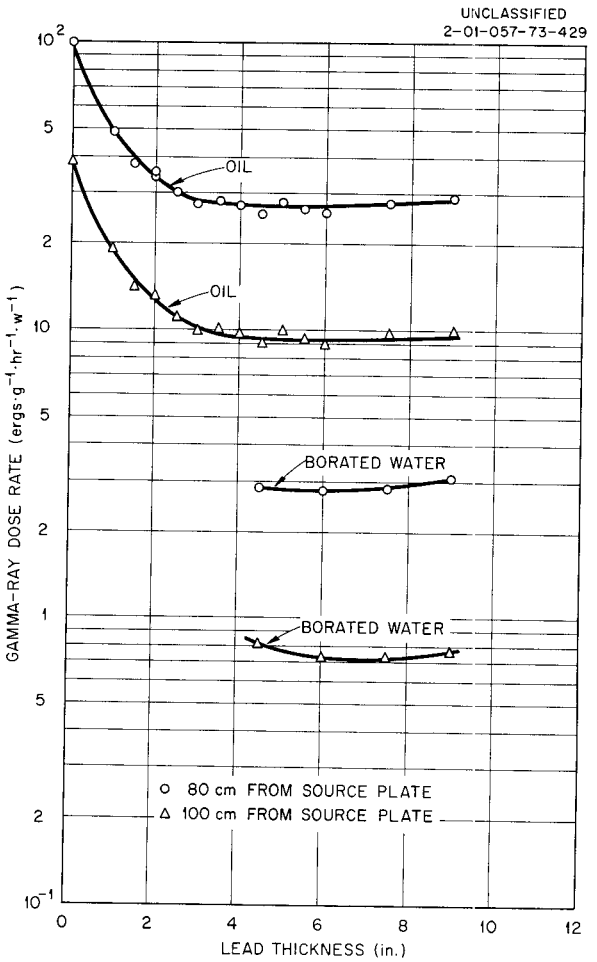

Fig. 7.4.3. Gamma-Ray Dose Rates in Oil and Borated Water at Points 80 and 100 cm from the Source Plate as a Function of the Thickness of Lead Adjacent to the Source.

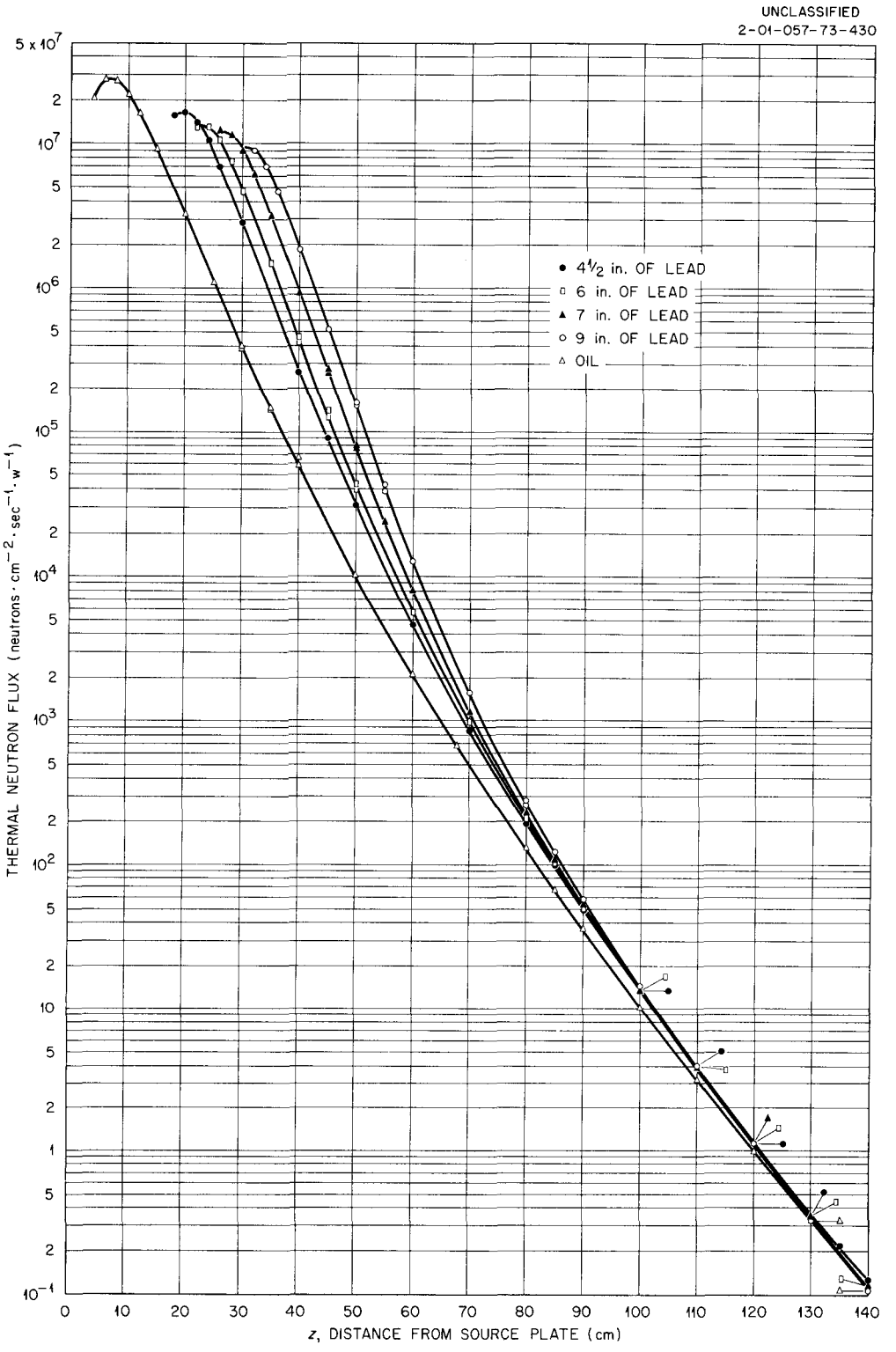

Fig. 7.4.4. Thermal-Neutron Fluxes in Oil Beyond Various Thicknesses of Lead as a Function of Distance from the Source Plate.

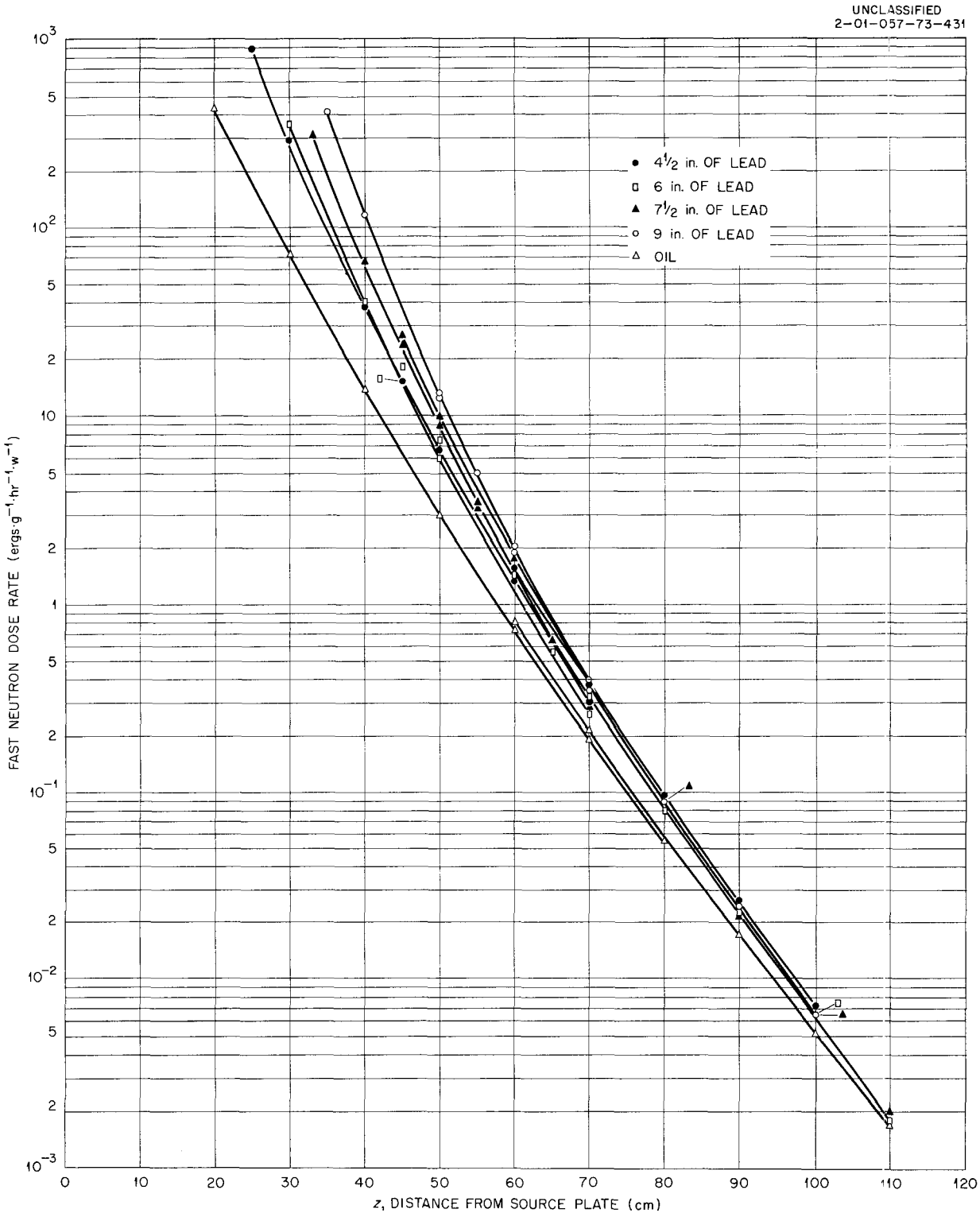

Fig. 7.4.5. Fast-Neutron Dose Rates in Oil Beyond Various Thicknesses of Lead as a Function of the Distance from the Source Plate.

7.5. THERMAL-NEUTRON FLUXES MEASURED IN OIL AT THE LTSF: AN ERRATUM

L. Jung

In the previous progress report[1] measurements of the thermal-neutron fluxes in oil in the usual LTSF configuration tank (a steel tank with an aluminum window on the source side) were presented. During a periodic check of the measurements a computational error was discovered which had caused the reported curve to be 16% too low. Figure 7.5.1 shows the corrected curve.

[1] D. W. Cady and E. A. Warman, *Appl. Nuclear Phys. Ann. Prog. Rep. Sept. 1, 1957*, ORNL-2389, p 180.

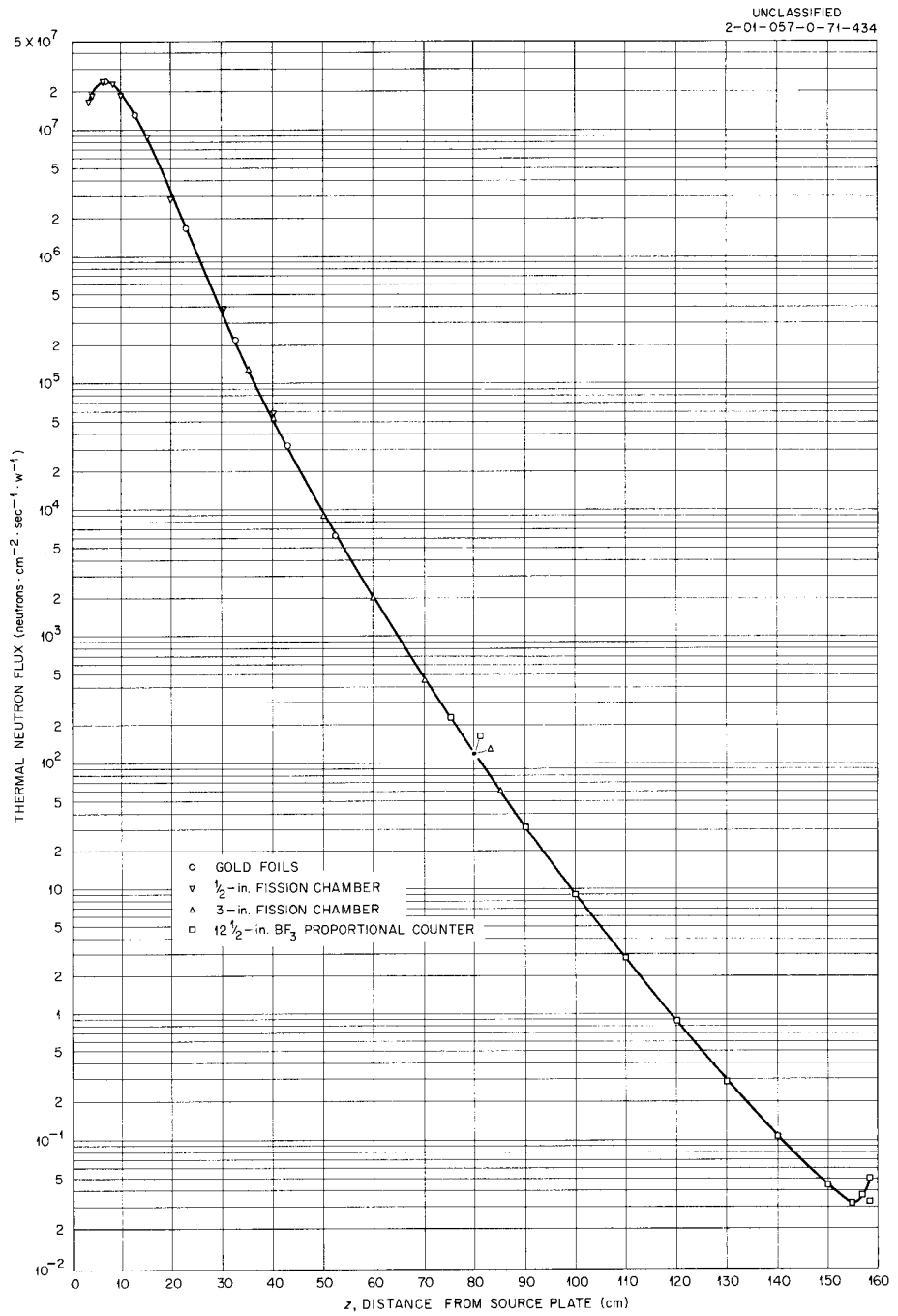

Fig. 7.5.1. Thermal-Neutron Flux in Oil in the LTSF Configuration Tank.

7.6. MONTE CARLO CALCULATION OF GAMMA-RAY DOSE-RATE BUILDUP FACTORS FOR LEAD AND WATER SHIELDS

L. A. Bowman[1] D. K. Trubey

It was previously reported[2] that the Oracle Monte Carlo code[3] for the calculation of the penetration of gamma rays through stratified slabs had been used to calculate a total of 512 problems for the eight different lead and water configurations shown in Fig. 7.6.1 but that the data had not yet been analyzed. The energy of the incident radiation, the angle of incidence, the thickness of the shield, and the percentage of lead preceding or following water were the parameters varied. The source was assumed to be a monoenergetic, monodirectional beam with energies, E_0, of 1, 3, 6, and 10 Mev. The incident angles, θ, at which the beam was incident on the slab were chosen so that they would give slant thicknesses of 1, 2, 3, and 4 times the normal thickness; these angles were 0, 60, 70.5, and 75.5 deg. The slabs, which were infinite in two directions, had finite thicknesses of 1, 2, 4, and 6 mfp. The results obtained included the dose rate and energy flux throughout the slab and at the rear of the slab, the dose-rate buildup factors, the heat deposited throughout the slab, and the energy and angular distribution of the gamma rays reflected from and transmitted through the slab. The analysis of this data has proceeded to the extent that the dose-rate buildup factors for normal incidence and the heat deposition throughout the slabs can be compared with empirical formulas. This section considers the dose-rate buildup factors. The heat deposition is presented in Sec. 7.7.

The buildup factors resulting from this calculation for $\theta = 0$ are shown in Figs. 7.6.2 through

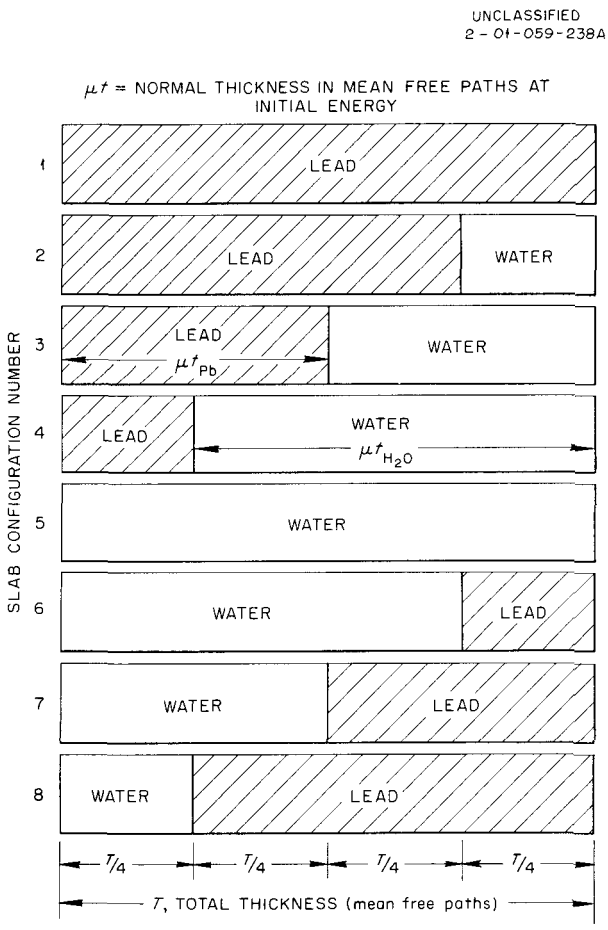

Fig. 7.6.1. Lead and Water Slab Configurations Used in Monte Carlo Calculations.

[1]On assignment from U.S. Air Force.

[2]L. A. Bowman and D. K. Trubey, *Appl. Nuclear Phys. Ann. Prog. Rep. Sept. 1, 1957*, ORNL-2389, p 218.

[3]S. Auslender, *Compilations of Monte Carlo Calculations of Gamma-Ray Penetration in Multiregion Shields with Slab Geometry*, ORNL-2310 (to be published).

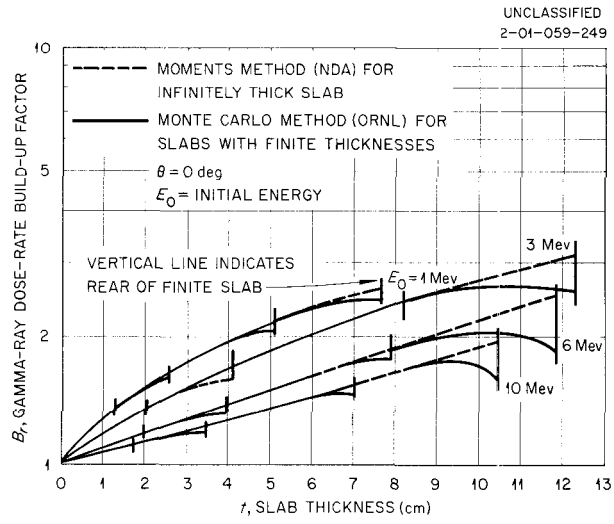

Fig. 7.6.2. Comparison of Dose-Rate Buildup Factors for Lead Slabs Computed by Monte Carlo Method with Those Computed by Moments Method. Normally incident gamma rays.

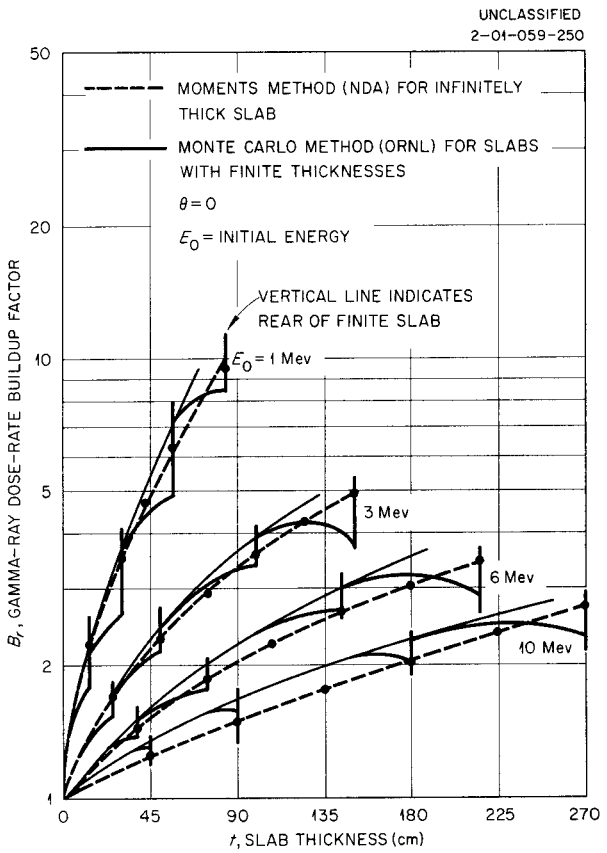

Fig. 7.6.3. Comparison of Dose-Rate Buildup Factors for Water Slabs Computed by Monte Carlo Method with Those Computed by Moments Method. Normally incident gamma rays.

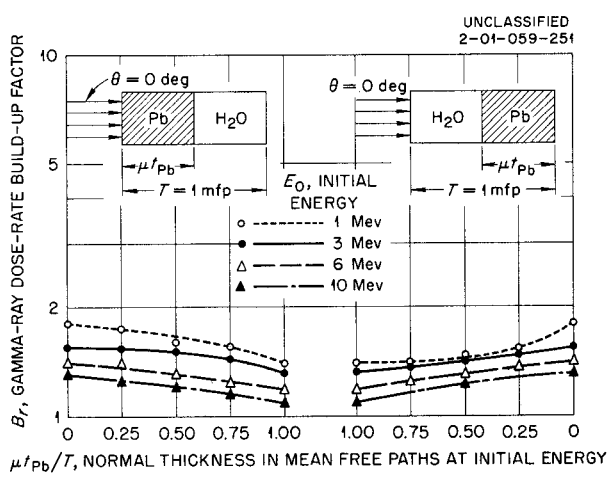

Fig. 7.6.4. Monte Carlo Dose-Rate Buildup Factors at the Rear of Composite Lead-Water Slab Shields 1 mfp Thick. Normally incident gamma rays.

7.6.7. Figures 7.6.2 and 7.6.3 show the buildup factors for pure lead and water, respectively, and these are compared with the NDA buildup factors[4] for infinitely thick slabs of the materials. Figures 7.6.4 through 7.6.7 show the buildup factors for the various slabs in which the water and lead were combined.

[4]H. Goldstein and J. E. Wilkins, Jr., *Calculations of the Penetrations of Gamma Rays. Final Report.* NYO-3075 (June 30, 1954).

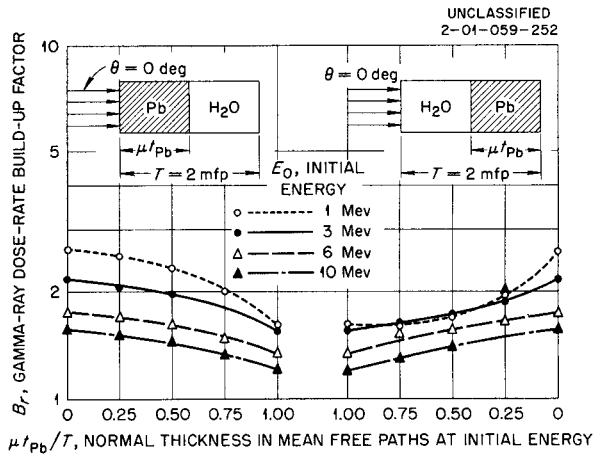

Fig. 7.6.5. Monte Carlo Dose-Rate Buildup Factors at the Rear of Composite Lead-Water Slab Shields 2 mfp Thick. Normally incident gamma rays.

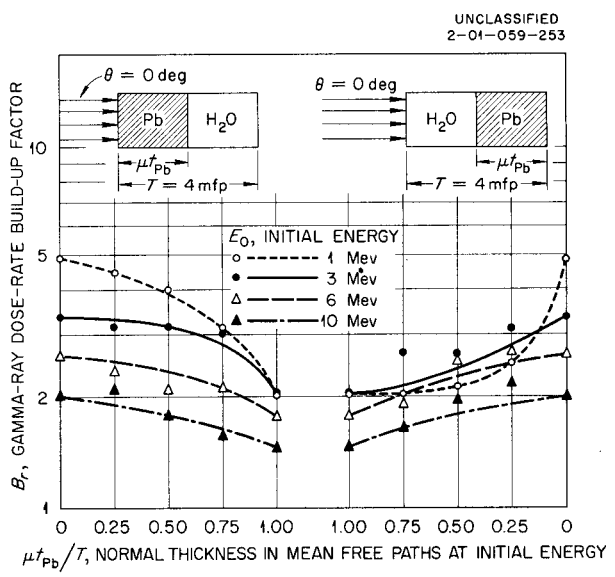

Fig. 7.6.6. Monte Carlo Dose-Rate Buildup Factors at the Rear of Composite Lead-Water Slab Shields 4 mfp Thick. Normally incident gamma rays.

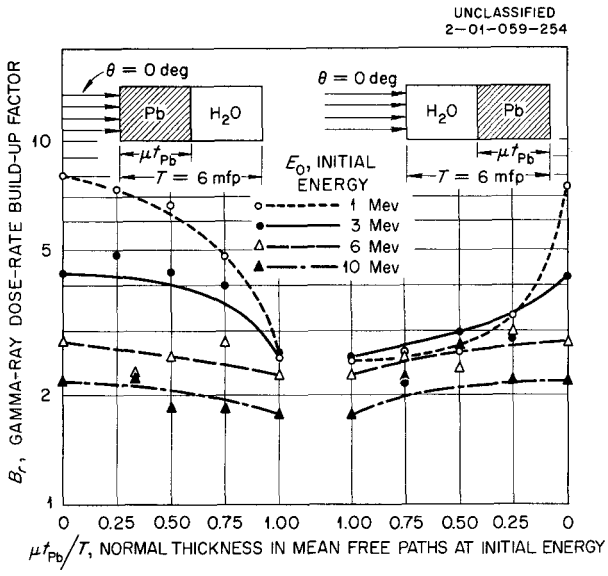

Fig. 7.6.7. Monte Carlo Dose-Rate Buildup Factors at the Rear of Composite Lead-Water Slab Shields 6 mfp Thick. Normally incident gamma rays.

All the buildup factors determined for composite slabs in this series have been compared with values obtained by use of a formula proposed by M. H. Kalos (quoted by Goldstein[5]) in which the buildup factors computed independently for lead and water are combined to determine the buildup factor for a composite slab consisting of two materials. For a lead-water slab (that is, lead followed by water) the formula is written as follows:

$$B(X_1,X_2) = B_2(X_2) + \frac{B_1(X_1) - 1}{B_2(X_1) - 1}[B_2(X_1 + X_2) - B_2(X_2)] ,$$

where

B_1,B_2 = gamma-ray dose-rate buildup factors for the first and second materials, respectively,

X_1,X_2 = thickness, in mfp, of the first and second materials, respectively.

For a water-lead shield the formula is

$$B(X_1,X_2) = B_2(X_2) + \left[\frac{B_1(X_1) - 1}{B_2(X_1) - 1} e^{-1.7X_2} + \frac{(\mu_{cs}/\mu_t)_1}{(\mu_{cs}/\mu_t)_2}(1 - e^{-X_2})\right] \times [B_2(X_1 + X_2) - B_2(X_2)] ,$$

where μ_{cs} = Compton scattering cross section and μ_t = total cross section. Tables 7.6.1 and 7.6.2 give the buildup factors determined both by Oracle calculations and by the Kalos formula.

This paper has been published previously.[6]

[5] H. Goldstein, *The Attenuation of Gamma Rays and Neutrons in Reactor Shields*, p 192–193, GPO, Washington, 1957.

[6] L. A. Bowman and D. K. Trubey, *Stratified Slab Gamma-Ray Dose-Rate Buildup Factors for Lead and Water Shields*, ORNL CF-58-1-41 (Jan. 16, 1958).

Table 7.6.1. Monte Carlo Gamma-Ray Dose-Rate Buildup Factors (B_r) at Rear of Lead-Water Slab Shields: Comparison of Oracle Calculations with Values Obtained with Kalos Formula

Incident Gamma-Ray Energy (Mev)	Shield (mfp)		B_r		Ratio of B_r (calc) to B_r (Kalos)
	Lead	Water	Oracle Calculations	Kalos Formula	
1	1	1	2.33	2.18	1.069
		2	3.30	3.13	1.054
		3	4.48	4.27	1.049
		4	5.81	5.60	1.038
		5	7.51	7.14	1.052
	2	1	2.72	2.51	1.084
		2	3.90	3.47	1.124
		3	5.33	4.73	1.127
		4	6.95	6.06	1.147
	3	1	3.10	3.00	1.033
		2	4.50	4.05	1.111
		3	6.22	5.36	1.160
3	1	1	1.95	1.90	1.026
		2	2.58	2.54	1.016
		3	3.30	3.10	1.065
		4	3.80	3.60	1.056
		5	4.21	4.07	1.034
	2	1	2.47	2.46	1.004
		2	3.15	3.00	1.050
		3	3.69	3.52	1.048
		4	4.18	4.03	1.037
	3	1	2.80	2.85	0.982
		2	3.44	2.89	1.190
		3	4.00	3.47	1.153
6	1	1	1.60	1.55	1.032
		2	2.03	1.98	1.025
		3	2.50	2.43	1.029
		4	2.66	2.67	0.996
		5	2.71	2.74	0.989
	2	1	1.98	1.80	1.100
		2	2.34	2.14	1.093
		3	2.55	2.50	1.020
		4	2.62	2.70	0.970
	3	1	2.11	1.96	1.077
		2	2.31	2.18	1.060
		3	2.41	2.52	0.956
10	1	1	1.41	1.38	1.022
		2	1.68	1.64	1.024
		3	1.90	1.88	1.011
		4	2.04	2.03	1.005
		5	2.14	2.12	1.009
	2	1	1.55	1.50	1.033
		2	1.78	1.72	1.035
		3	1.97	1.93	1.021
		4	2.10	2.07	1.014
	3	1	1.65	1.65	1.000
		2	1.81	1.84	0.984
		3	1.94	2.02	0.960

Table 7.6.2. Monte Carlo Gamma-Ray Dose-Rate Buildup Factors (B_r) at Rear of Water-Lead Slab Shields: Comparison of Oracle Calculations with Values Obtained with Kalos Formula

Incident Gamma-Ray Energy (Mev)	Shield (mfp)		B_r		Ratio of B_r (calc) to B_r (Kalos)
	Water	Lead	Oracle Calculations	Kalos Formula	
1	1	1	1.70	1.66	1.024
		2	1.86	1.92	0.969
		3	2.05	2.12	0.967
		4	2.22	2.35	0.945
		5	2.42	2.55	0.949
	2	1	2.20	1.96	1.122
		2	2.18	2.17	1.005
		3	2.31	2.45	0.943
		4	2.52	2.63	0.958
	3	1	2.50	2.27	1.101
		2	2.46	2.50	0.984
		3	2.72	2.73	0.996
3	1	1	1.74	1.62	1.074
		2	1.92	1.88	1.021
		3	2.15	2.16	0.995
		4	2.39	2.44	0.980
		5	2.66	2.68	0.993
	2	1	2.28	1.96	1.163
		2	2.39	2.24	1.067
		3	2.51	2.54	0.988
		4	2.70	2.78	0.971
	3	1	2.80	2.33	1.202
		2	2.88	2.60	1.108
		3	2.97	2.88	1.031
6	1	1	1.55	1.50	1.033
		2	1.75	1.79	0.978
		3	2.01	2.04	0.985
		4	2.20	2.27	0.969
		5	2.40	2.56	0.938
	2	1	2.09	1.89	1.106
		2	2.24	2.23	1.004
		3	2.38	2.50	0.952
		4	2.48	2.82	0.879
	3	1	2.48	2.31	1.074
		2	2.58	2.68	0.963
		3	2.61	3.04	0.859
10	1	1	1.39	1.41	0.986
		2	1.52	1.55	0.981
		3	1.65	1.70	0.971
		4	1.77	1.92	0.922
		5	1.90	2.07	0.918
	2	1	1.70	1.72	0.988
		2	1.79	1.92	0.932
		3	1.88	2.16	0.870
		4	1.96	2.39	0.820
	3	1	1.95	2.00	0.975
		2	1.99	2.34	0.850
		3	2.08	2.61	0.797

7.7. MONTE CARLO CALCULATION OF THE DEPOSITION OF GAMMA-RAY HEATING IN STRATIFIED LEAD AND WATER SLABS

L. A. Bowman[1] D. K. Trubey

The heating results from the calculations discussed in Sec. 7.6 are given as the per cent of the total energy incident upon the slab absorbed in a specified region in the slab. Some typical plots of these results are shown in Figs. 7.7.1 through 7.7.4, which compare the Monte Carlo results averaged over a region of four intervals to the values obtained by using the following empirical formula:

$$J_x(E_0,\theta,x,\mathrm{Mat}_x) = \left[\sec\theta \frac{\mu_a(E_0,\mathrm{Mat}_x)}{\mu_t(E_0,\mathrm{Mat}_x)} e^{-(x_1+x_2/\cos\theta)}\right] \times$$

$$\times \left[B_{a_1}\left(\frac{x_1}{\cos\theta},E_0\right) B_{a_2}\left(\frac{x_2}{\cos\theta},E_0\right) e^{-x_2/\cos\theta} + B_{a_2}\left(\frac{x_1+x_2}{\cos\theta},E_0\right)\left(1-e^{-x_2/\cos\theta}\right)\right] \times$$

$$\times \exp - \left\{4\cos\theta(1-\cos\theta)\left[1-\frac{\mu_a(E_0,\mathrm{Mat}_1)}{\mu_t(E_0,\mathrm{Mat}_1)}\right]\left[\frac{x_1+x_2}{(x_1+x_2)^4+1}\right]\frac{2}{\sqrt{E_0}}\right\},$$

where

$J_x(E_0,\theta,x,\mathrm{Mat}_x)$ = per cent of total energy incident upon the slab absorbed in the slab at point x per mean free path,

x_1 = number of mean free paths of the first material,

x_2 = number of mean free paths of the second material,

E_0 = energy of the incident gamma ray,

θ = angle between the direction of the incident gamma ray and the normal to the slab,

$$\frac{\mu_a(E_0,\mathrm{Mat}_x)}{\mu_t(E_0,\mathrm{Mat}_x)} = \frac{\text{energy absorption coefficient}}{\text{total absorption coefficient}},$$

$B_{a_1}\left(\frac{x_1}{\cos\theta},E_0\right)$ = NDA point isotropic energy absorption buildup factor for the first material (see Sec. 7.6),

$B_{a_2}\left(\frac{x_2}{\cos\theta},E_0\right)$ = NDA point isotropic energy absorption buildup factor for the second material,

$e^{-(x_1+x_2/\cos\theta)}$ = exponential attenuation to point that heating is calculated,

and

$$\exp - \left\{4\cos\theta(1-\cos\theta)\left[1-\frac{\mu_a(E_0,\mathrm{Mat}_1)}{\mu_t(E_0,\mathrm{Mat}_1)}\right]\left[\frac{x_1+x_2}{(x_1+x_2)^4+1}\right]\frac{2}{\sqrt{E_0}}\right\}$$

is the empirical short-circuiting correction.

[1]On assignment from Wright Air Development Center.

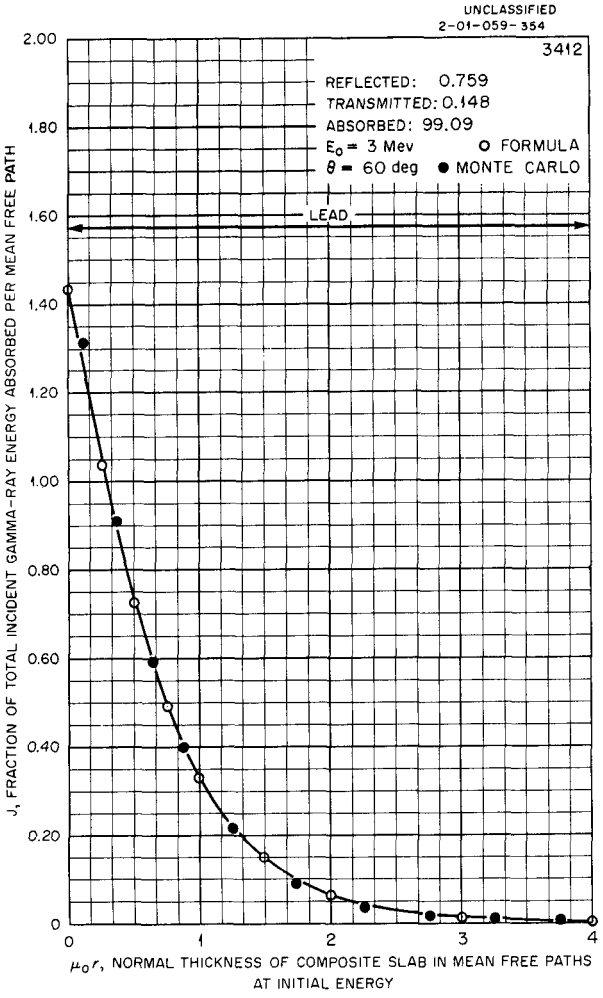

Fig. 7.7.1. Gamma-Ray Energy Absorption in a Lead Shield as a Function of the Shield Thickness.

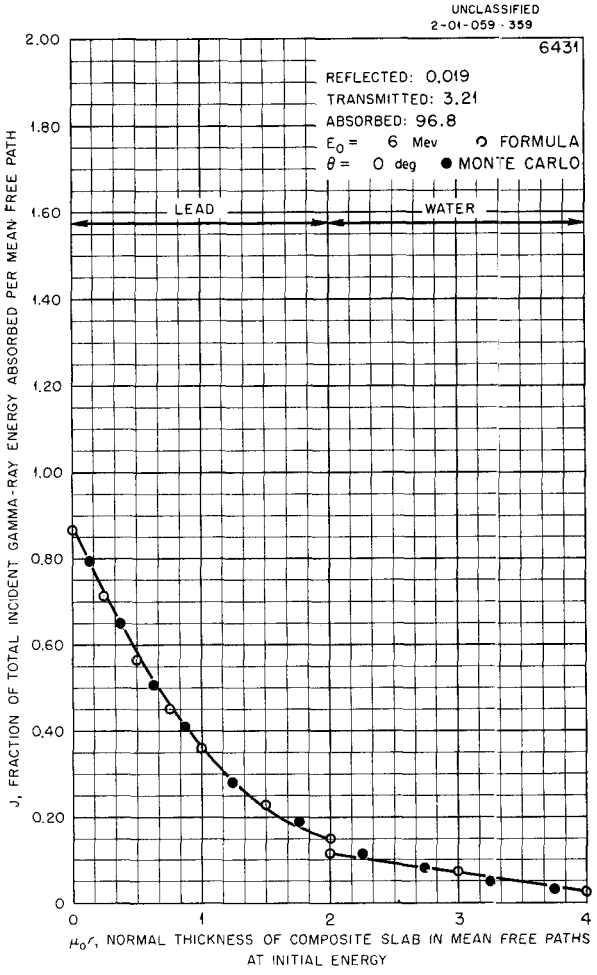

Fig. 7.7.2. Gamma-Ray Energy Absorption in a Lead-Water Shield as a Function of the Shield Thickness.

The first bracketed factor represents the expected fraction of incident energy to be deposited per mean free path if the scattered gamma rays are neglected. The next bracketed term is the buildup factor. Near the boundary (x_2 small), where the spectrum is largely determined by the first material, the buildup is given by the first term. This term damps out as x_2 becomes large, and the buildup factor is characteristic of the second material. The buildup factors used in the formula were the results of the well-known NDA moments method calculation.[2] The energy absorption buildup factors used were for a point isotropic source, since these were the only buildup factors presented by Goldstein and Wilkins.[2] The last, exponential, factor is the "short-circuiting" factor. An attempt was made to separate the effects of the various parameters in the exponent.

The factors which depend on the angle peak at 60 deg. It seems reasonable that a peak might occur about there, owing to the combination of a decreasing path length and a decreasing cross section and

[2]H. Goldstein and J. E. Wilkins, Jr., *Calculations of the Penetrations of Gamma Rays. Final Report*, NYO-3075 (June 30, 1954).

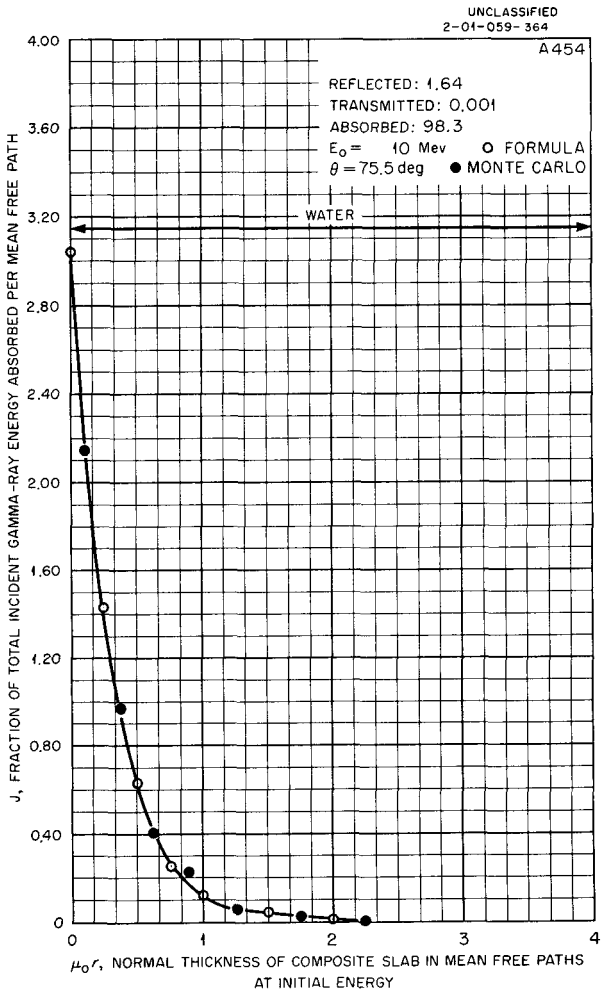

Fig. 7.7.3. Gamma-Ray Energy Absorption in a Water Shield as a Function of the Shield Thickness.

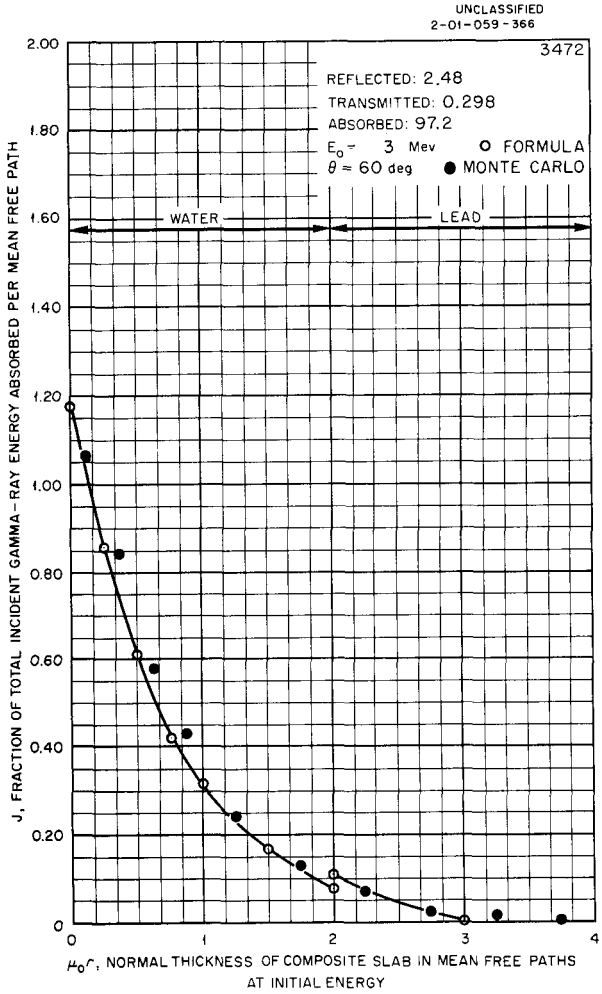

Fig. 7.7.4. Gamma-Ray Energy Absorption in a Water-Lead Shield as a Function of the Shield Thickness.

final energy of a scattered gamma ray as the angle of scattering increases. The effect of distance from the initial boundary also shows a peak (near 1 mfp). There is little short-circuiting at short distances since the heating is due largely to first collisions. The short-circuiting damps out at large distances since the buildup factor adequately accounts for the scattered gamma rays far from boundaries. The factor $1 - [\mu_a(E_0, \mathrm{Mat}_1)/\mu_t(E_0, \mathrm{Mat}_1)]$ is generally taken to be that of the first material since, in general, the short-circuiting effect is due to scattering near the initial boundary. This procedure seems to be adequate only if the first material is no less than 0.25 mfp thick. The variation with energy seems to break down with low energy, and as a result the formula can be low by as much as 20% for the 1-Mev case.

It should be emphasized that this formula has been compared only with data from this calculation which had a very limited number of parameters (as listed in the first paragraph of Sec. 7.6), and therefore it is possible that the fit is not so good for other parameters, particularly outside the energy range

examined. The worst fits were obtained for low energies, especially with lead following water, but even in these cases the error was less than 20%. In nearly all the cases examined, the error was less than 5%.

This paper has been presented in more detail in another report.[3]

[3]L. A. Bowman and D. K. Trubey, *Deposition of Gamma-Ray Heating in Stratified Lead and Water Slabs*, ORNL CF-58-7-99 (July 28, 1958).

7.8. A MONTE CARLO CODE FOR THE CALCULATION OF DEEP PENETRATIONS OF GAMMA RAYS

S. K. Penny

A Monte Carlo code is being developed to calculate the angular and energy distributions of gamma rays at a point detector emitted from a monoenergetic point isotropic or point monodirectional source embedded in an infinite, homogeneous isotropic medium with constant density. The word "monodirectional" is used here in a loose sense; the emission directions are actually in a half-cone specified by a polar angle, where the source-detector axis is the polar axis, and they are uniformly distributed in the azimuthal angle. The code is now in the debugging stage on the IBM-704 electronic data processing machine. It is hoped that by using special techniques it will be useful for penetrations as deep as 20 mfp. In its final form the code can be used for neutron penetration also, provided that a differential cross section for scattering is given.

The purpose of this code is twofold. First, it is hoped that it will shed some light on the discrepancy between calculated[1-4] and experimental[5] energy distributions from a Co^{60} source in water, the chief difficulty being the magnitude of the distributions. (The calculational method used was the moments method.) Second, there is merit in experimenting with these special Monte Carlo techniques in order to see when and where they can be applied.

The special techniques mentioned above are (1) importance sampling on the first-collision distribution, coupled with double systematic sampling, statistical estimation, splitting and "Russian Roulette" and (2) a special form of output, which will be estimated coefficients in an expansion of the flux in Legendre polynomials rather than in histogram form. Other features in the code are an energy cutoff, a weight cutoff, and a cutoff for distance from the detector.

The code will be tested against three standards: (1) problems with no energy degradation and isotropic scattering will be checked against the exact solutions given by Case *et al.*;[6] (2) problems with a medium other than water will be checked against the energy distributions of energy flux furnished by the moments method;[1-4] (3) problems with water as a medium will be checked against the experimental work of Peelle *et al.*[5] and the moments method calculations.[1-4]

[1]L. V. Spencer and U. Fano, *Phys. Rev.* 81, 464 (1951); see also *J. Research Natl. Bur. Standards* 46, 446 (1951).

[2]L. V. Spencer and F. Stinson, *Phys. Rev.* 85, 662 (1952).

[3]U. Fano, *J. Research Natl. Bur. Standards* 51, 95 (1953).

[4]H. Goldstein and J. E. Wilkins, Jr., *Calculations of the Penetrations of Gamma Rays. Final Report*, NDA-15C-41 or NYO-3075 (June 30, 1954).

[5]R. W. Peelle, F. C. Maienschein, and T. A. Love, *Energy and Angular Distribution of Gamma Radiation from a Co^{60} Source After Diffusion Through Many Mean Free Paths of Water*, ORNL-2196 (Aug. 12, 1957).

[6]K. M. Case, F. de Hoffman, G. Placzek, *Introduction to the Theory of Neutron Diffusion*, Los Alamos Scientific Laboratory, Los Alamos, 1953.

7.9. THE EFFECT OF ANISOTROPIC SCATTERING ON THE NEUTRON FLUX IN AIR

C. D. Zerby

For many calculations[1] of fluxes and dose rates resulting from air-scattered neutrons, isotropic scattering in the center-of-mass system is assumed. The question naturally arises as to the validity of this assumption. In order to obtain some insight into the problem, the Monte Carlo code for calculating the fluxes and dose rates of multiply scattered neutrons used previously[1] was altered to use an anisotropic scattering cross section proportional to $1 + a \cos \theta$ in the center-of-mass system. Thus, the differential cross section is given by

$$\frac{d\sigma}{d\Omega} = K(1 + a \cos \theta) \ . \tag{1}$$

The value of the constant K was chosen to make the integral of the differential cross section equal to the total cross section. The constant a is arbitrary and constant over the whole energy range.

The cases investigated were for a point monodirectional beam of neutrons in an infinite volume of air. The beam angle with respect to the source-detector axis θ and the constant a were the only variables. The constants of the problem were: source energy, E_0 = 5 Mev; separation distance, g = 50 ft; air density, ρ = 0.00125 g/cm^3. Three problems were calculated for each value of θ corresponding to the values of the constant a of 0, 0.3, and 0.7. By expressing the value obtained from the calculation as a function of a, that is, $\Phi(a)$, the ratio of $\Phi(a)$ to $\Phi(0)$ was obtained. This ratio then represents the fractional change that would be expected in the results of a calculation in which isotropic scattering was assumed if anisotropy were to be introduced.

The resulting ratios of the total number flux, energy flux, and dose rate are presented as a function of beam angle of emission in Figs. 7.9.1, 7.9.2, and 7.9.3. It will be observed that in each case the ratio is less than 1 for beam angles greater than 10 deg, which indicates that the results based on isotropic scattering in the center-of-mass system are generally conservative.

[1]For example, see C. D. Zerby, *A Monte Carlo Calculation of Air-Scattered Neutrons*, ORNL-2277 (April 23 (1957).

It was found from the calculations based on isotropic scattering in the center-of-mass system[2] that the equation which fits the neutron flux data best was

$$\Phi_N(0) = \frac{\Sigma_s(E_0)}{4\pi g} \frac{\pi - \theta}{\sin \theta} \ , \tag{2}$$

where

$\Phi_N(0)$ = neutron flux per source neutron,

$\Sigma_s(E_0)$ = macroscopic scattering cross section at the source energy E_0,

g = separation distance.

This same equation was found to fit the neutron flux calculated for singly scattered neutrons in

[2]J. Hilgeman, F. L. Keller, and C. D. Zerby, *Monte Carlo Calculations of Fluxes and Dose Rates Resulting from Neutrons Multiply Scattered in Air*, ORNL-2375.

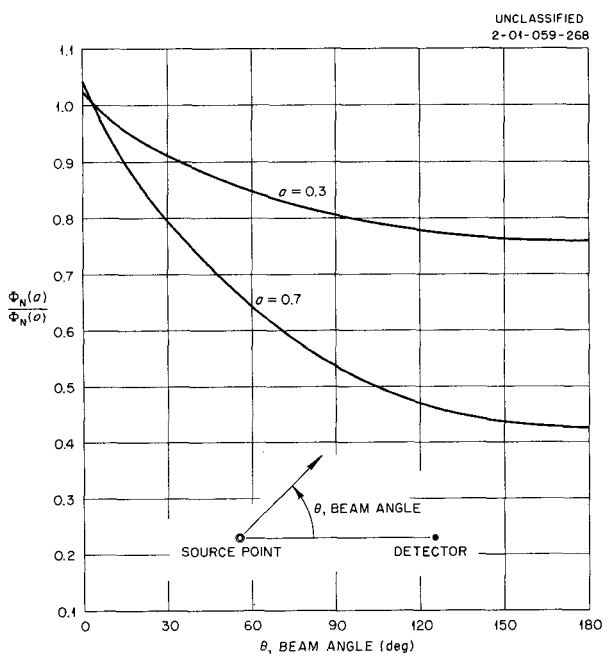

Fig. 7.9.1. Ratio of the Total Neutron Flux in Air with Anisotropic Scattering to That Obtained with Isotropic Scattering. Detector 50 ft from a monodirectional beam of 5-Mev neutrons. Air density = 0.00125 g/cm^3.

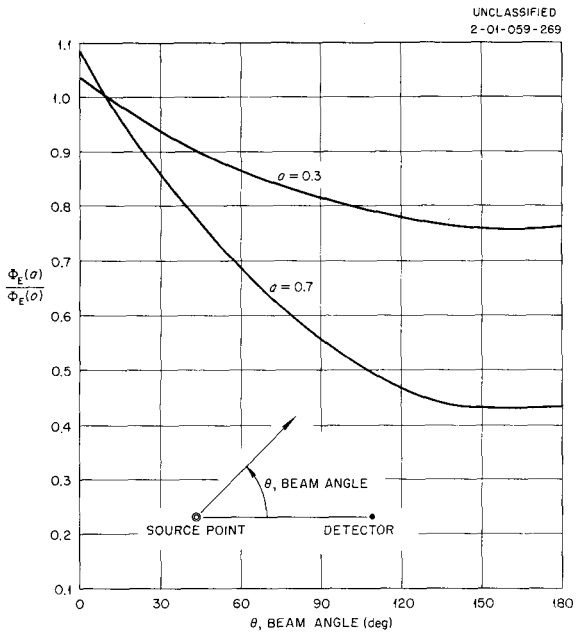

Fig. 7.9.2. Ratio of the Total Neutron Energy Flux in Air with Anisotropic Scattering to That Obtained with Isotropic Scattering. Detector 50 ft from a monodirectional beam of 5-Mev neutrons. Air density = 0.00125 g/cm^3.

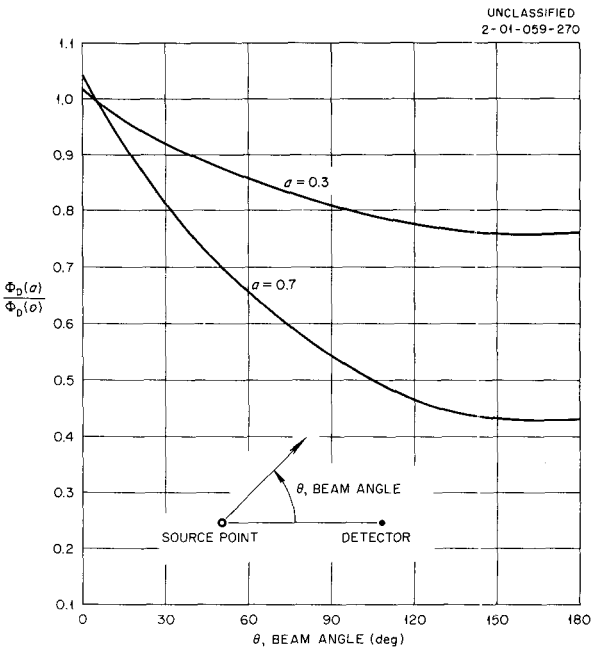

Fig. 7.9.3. Ratio of the Total Neutron Dose Rate in Air with Anisotropic Scattering to That Obtained with Isotropic Scattering. Detector 50 ft from a monodirectional beam of 5-Mev neutrons. Air density = 0.00125 g/cm^3.

which isotropic scattering in the laboratory system and no attenuation on either leg were assumed.

A similar expression fits the calculated total dose rate, $\Phi_D(0)$, per source neutron:

$$\Phi_D(0) = \frac{C(E_0)}{1.2} \frac{\Sigma_s(E_0)}{4\pi g} \frac{\pi - \theta}{\sin\theta} , \tag{3}$$

where $C(E_0)$ is the flux-to-dose-rate conversion factor at the source energy E_0.

Since such a simple approach worked so nicely in fitting the data for isotropic scattering in the center-of-mass system, a similar set of equations for the cases of anisotropic scattering was investigated. Assuming the differential scattering cross section given in Eq. 1 to be effective in the laboratory system and calculating the singly scattered flux where attenuation on both legs was neglected yields

$$\Phi_N(a) = \Phi_N(0)\left(1 - a\frac{\sin\theta}{\pi - \theta}\right) , \tag{4}$$

where $\Phi_N(0)$ is given in Eq. 2. From Eq. 4 and a similar equation for $\Phi_D(a)$, it is seen that

$$\frac{\Phi_N(a)}{\Phi_N(0)} = \frac{\Phi_D(a)}{\Phi_D(0)} = \left(1 - a\frac{\sin\theta}{\pi - \theta}\right) . \tag{5}$$

Results of the values of these ratios calculated with the use of Eq. 5 are compared in Tables 7.9.1 and 7.9.2 with results obtained in Monte Carlo calculations. It will be observed that Eq. 5 does not fit the results of the calculation based on anisotropic scattering as closely as would be desired. In fact, it is obvious from a qualitative analysis that Eq. 4 should become less accurate the more anisotropic the scattering. This is borne out in Tables 7.9.1 and 7.9.2.

Table 7.9.1. Ratio of the Total Neutron Flux in Air with Anisotropic Scattering to That Obtained with Isotropic Scattering

θ (deg)	Formula	Monte Carlo	Error of Formula (%)
		$a = 0.3$	
2	0.997	1.008	−1.1
30	0.943	0.911	+3.5
90	0.809	0.806	+0.3
130	0.737	0.769	−4.2
180	0.700	0.760	−7.9
		$a = 0.7$	
2	0.992	1.020	−2.7
30	0.866	0.796	+8.8
90	0.554	0.537	+3.2
130	0.386	0.453	−14.8
180	0.300	0.425	−29.4

Table 7.9.2. Ratio of the Total Dose Rate in Air with Anisotropic Scattering to That Obtained with Isotropic Scattering

θ (deg)	Formula	Monte Carlo	Error of Formula (%)
		$a = 0.3$	
2	0.997	1.011	−1.4
30	0.943	0.920	+2.5
90	0.809	0.810	−0.2
130	0.737	0.768	−4.0
180	0.700	0.761	−8.0
		$a = 0.7$	
2	0.992	1.026	−3.3
30	0.866	0.815	+6.1
90	0.554	0.545	+1.7
130	0.386	0.449	−14.0
180	0.300	0.430	−30.2

7.10. BREMSSTRAHLUNG SPECTRA IN SODIUM IODIDE AND IN AIR

C. D. Zerby H. S. Moran

In order to provide some information on the production of secondary electromagnetic radiation in materials, a calculation was set up on the Oracle to determine the spectra of bremsstrahlung radiation resulting from the degradation of electrons. The results of calculations for two materials, sodium iodide and air, are shown in Figs. 7.10.1 and 7.10.2.

In the calculation the degradation of the electrons was assumed to occur only by inelastic collisions with the bound electrons of the medium and by radiative collisions with nuclei. It was also assumed that the initial electron energy was sufficiently low for the energy degradation by inelastic collisions to predominate. For the cases presented in Figs. 7.10.1 and 7.10.2 the last assumption is certainly true.[1]

The energy loss per centimeter of path length (stopping power) for an electron making inelastic collisions is given by the equation[2]

$$(1) \quad -\frac{dE}{dx} = \frac{2\pi r_0^2 NZ}{\beta^2}\left[\ln\frac{\beta^2(E-1)}{2I^2(1-\beta^2)} - \left(2\sqrt{1-\beta^2} - 1 + \beta^2\right)\ln 2 + 1 - \beta^2 + \frac{1}{8}\left(1-\sqrt{1-\beta^2}\right)^2\right],$$

[1] W. Heitler, *The Quantum Theory of Radiation*, 3rd ed., p 252, Clarendon Press, Oxford, 1954.

[2] H. A. Bethe and J. Ashkin, *Experimental Nuclear Physics* (ed. by E. Segrè), p 254, Wiley, New York, 1953.

where

E = total relativistic electron energy $(m_0 c^2)$,

I = mean excitation potential $(m_0 c^2)$,

$\beta^2 = (v/c)^2 = (E^2 - 1)/E^2$,

r_0 = classical electron radius, cm,

N = atomic density, cm^{-3},

Z = charge number.

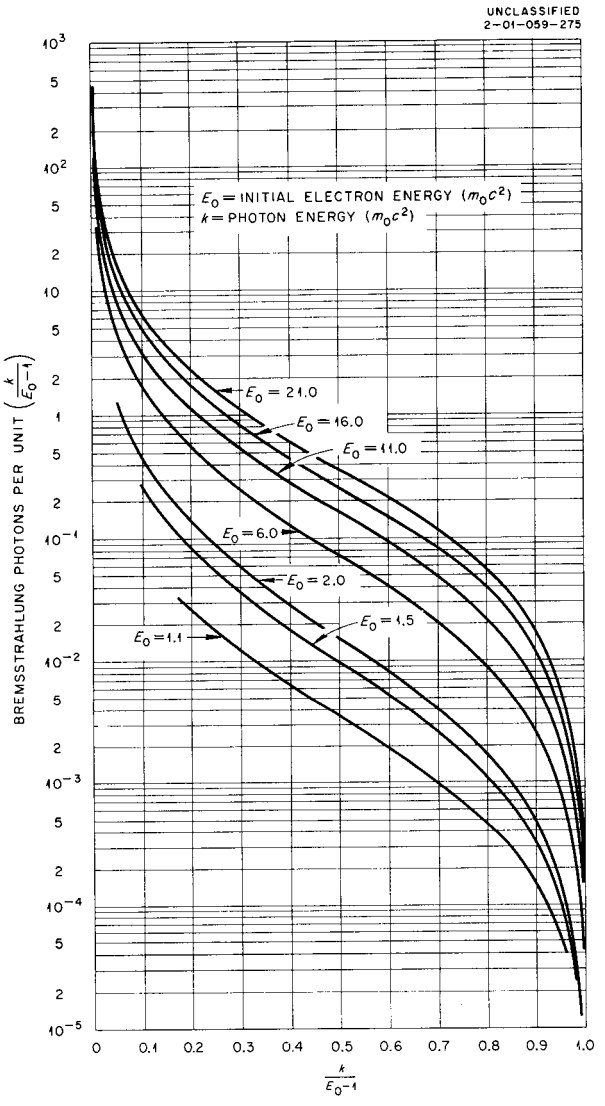

Fig. 7.10.1. Bremsstrahlung Spectrum in Sodium Iodide.

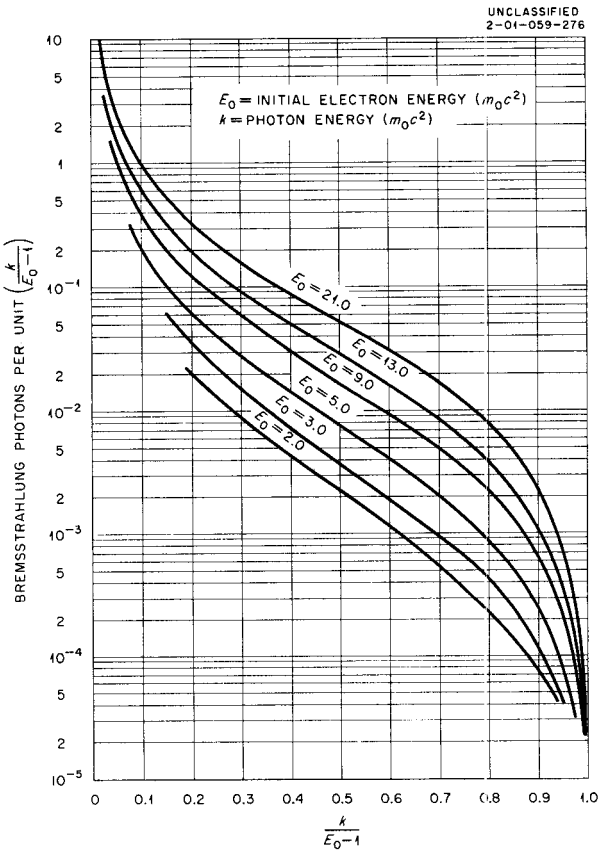

Fig. 7.10.2. Bremsstrahlung Spectrum in Air.

The Born-approximation cross section for the production of light (bremsstrahlung radiation) by an electron in the field of a nucleus without screening is given by[3]

$$(2)\quad \phi^a(E,k) = \frac{r_0^2 Z^2}{137}\frac{N}{k}\frac{p_1}{p}\left\{\frac{4}{3} - 2EE_1\frac{p_1^2+p^2}{p_1^2 p^2} + \left(\frac{\epsilon E_1}{p^3} + \frac{\epsilon_1 E}{p_1^3} - \frac{\epsilon_1 \epsilon}{p p_1}\right) + \right.$$

$$\left. + L\left[\frac{8}{3}\frac{EE_1}{pp_1} + \frac{k^2}{p^3 p_1^3}\; E^2E_1^2 + p^2p_1^2 \;+ \frac{k}{2pp_1}\left(\frac{EE_1+p^2}{p^3}\,\epsilon - \frac{EE_1+p_1^2}{p_1^3}\,\epsilon_1 + \frac{2kEE_1}{p_1^2p^2}\right)\right]\right\} ,$$

where the following relations are used:

$$(3)\quad \begin{aligned} L &= 2\ln\left(\frac{EE_1+pp_1-1}{k}\right) , \\ \epsilon &= 2\ln(E+p) , \\ \epsilon_1 &= 2\ln(E_1+p_1) , \\ E_1 &= E-k , \\ p^2 &= E^2-1 , \\ p_1^2 &= E_1^2-1 . \end{aligned}$$

As may be seen from Eqs. 3, Eq. 2 is simply a function of E and k, where E has the same definition as in Eq. 1 and k is the photon energy expressed in units of m_0c^2. The expression $\phi^a(E,k)\,dk$ is the electron cross section (cm^{-1}) for producing a photon in the interval k to $k+dk$.

When the electron screening of the nucleus is taken into account and Eq. 2 is reduced to the relativistic case, $E \gg m_0c^2$, the following equation[4] is obtained:

$$(4)\quad \phi^b(E,k) = \frac{r_0^2 Z^2 N}{137}\frac{4}{k}\left\{\left[1+\left(\frac{E-k}{E}\right)^2\right]\left[\frac{\phi_1(\gamma)}{4} - \frac{1}{3}\ln Z\right] - \frac{2}{3}\left(\frac{E-k}{E}\right)\left[\frac{\phi_2(\gamma)}{4} - \frac{1}{3}\ln Z\right]\right\} ,$$

where γ is given by[5]

$$(5)\quad \gamma = 100\,\frac{k}{E(E-k)\,Z^{1/3}} .$$

The functions $\phi_1(\gamma)$ and $\phi_2(\gamma)$ are presented graphically by Bethe and Ashkin;[6] however, they are well

[3] W. Heitler, *The Quantum Theory of Radiation*, 3rd ed., p 245, Clarendon Press, Oxford, 1954.

[4] H. A. Bethe and J. Ashkin, *Experimental Nuclear Physics* (ed. by E. Segrè), p 260, Wiley, New York, 1953.

[5] *Ibid.*, p 259.

[6] *Ibid.*, p 262.

represented with less than 0.3% error by the empirical relations

$$\phi_1(\gamma) = 5.089\, e^{-0.6587\gamma} + 15.661\, e^{-0.0481\gamma} \quad , \tag{6}$$

$$\phi_2(\gamma) = \phi_1(\gamma) - 0.595\, e^{-3.04\gamma} \quad . \tag{7}$$

The quantity γ measures the effect of screening. For $\gamma >> 1$ the screening can be neglected; however, for $\gamma = 0$ the screening is complete. Although Bethe and Ashkin give a series of equations similar to Eq. 4 that are valid for various ranges of γ, the use of Eqs. 6 and 7 in Eq. 4 makes Eq. 4 valid for all values of γ.

With the use of Eqs. 1, 2, and 4, the total bremsstrahlung spectra from an electron slowing down in a compound are given by

$$K(E_0,k_0)\, dk_0 = \int_{k+1}^{E_0} \frac{\sum_j \phi_j(E,k)\, dE}{\sum_j (-dE/dx)_j}\, dk_0 \quad , \tag{8}$$

where $K(E_0,k_0)\, dk_0$ is the number of photons produced by an electron slowing down from energy E_0 in the interval k_0 to $k_0 + dk_0$. The subscript j refers to the jth element of the compound. The quantity $\phi(E,k)$ is obtained from Eq. 2 or Eq. 4, depending on which is appropriate in the course of integration.

Equation 8 was solved on the Oracle to provide the data presented in Figs. 7.10.1 and 7.10.2. For convenience, the results are presented as the number of photons per unit $(k/E_0) - 1$ as a function of $(k/E_0) - 1$. The integral under the curve represents the total number of photons released.

This calculation is presented in more detail in a separate report.[7]

---

[7]C. D. Zerby and H. S. Moran, *Bremsstrahlung Spectra in NaI and Air*, ORNL-2454 (Feb. 25, 1958).

7.11. RADIATION TRANSMISSION THROUGH BORAL AND SIMILAR HETEROGENEOUS MATERIALS CONSISTING OF RANDOMLY DISTRIBUTED ABSORBING CHUNKS

W. R. Burrus[1]

One material commonly used as a thermal-neutron suppressor is boral, a heterogeneous mixture of commercial-grade boron carbide and aluminum sandwiched between aluminum sheets. The sandwich is usually rolled to a thickness of $\frac{1}{4}$ or $\frac{1}{8}$ in. Since the mixture is nonuniform, considerable space exists between the chunks of boron carbide attenuating material, and consequently radiation can penetrate the shield by passing unattenuated between the chunks. Because of this "channeling effect," which is a statistical effect caused by the increased transmission along paths which pass through less than the average material thickness, the masses of boral and similar heterogeneous shields must be from a few per cent to several hundred per cent greater than the masses of homogeneous shields which give the same amount of attenuation.

R. R. Coveyou[2] has suggested a model to calculate the approximate transmission of radiation through materials that consist of randomly distributed chunks. The material is considered to be divided into layers which have a thickness characteristic of the size of the chunks. The holes in the layers are assumed to be located in a manner statistically independent of the holes in adjacent layers, so that the over-all transmission is the product of the transmissions of all the layers. As the chunks are made more attenuating, the radiation passing through the holes between the chunks becomes more important.

A method which is based on the Coveyou model and has been extended to include a distribution of various chunk sizes and shapes has been developed for calculating the transmission of radiation through heterogeneous shields. The method has been used to compute the transmission of neutrons through boral. For the calculation it was assumed that the boral sandwich was rolled to a thickness of $\frac{1}{8}$ in. and that the thickness of the B_4C-Al mixture was 0.085 in. with 40 vol % boron carbide. This resulted in an over-all volume fraction of approximately 25% for the absorbing chunks, which were assumed to be spherical in shape. The chunks were first considered to be of 11 different sizes between 20 and 100 mesh; however, it was found that assuming only four sizes gave approximately the same results, and only four groups were used thereafter.

The transmission calculated by this method for normally incident 2200-m/sec (0.0253-ev) neutrons through $\frac{1}{8}$-in.-thick boral was 0.076. This is to be compared with a transmission of 0.0015 calculated for normally incident 2200-m/sec neutrons by the homogeneous approximation. However, the homogeneous approximation is an inappropriate first approximation for this type of shield.

The transmission of normally incident neutrons through a $\frac{1}{8}$-in.-thick boral shield as a function of energy is shown in Fig. 7.11.1, along with the limit as the chunks become opaque (low energies). The average transmission over the neutron distribution shown (Maxwell-Boltzmann distribution at room temperature) is 0.096 for a constant efficiency detector and 0.084 for a $1/v$ detector.

The transmission of isotropically incident neutrons through $\frac{1}{8}$-in.-thick boral as a function of energy is shown in Fig. 7.11.2. For this case the average transmissions are 0.024 for a constant efficiency flux detector, 0.021 for a $1/v$ flux detector, 0.041 for a constant efficiency current detector, and 0.034 for a $1/v$ current detector.

The calculated results can be compared with the results of two experiments which have been performed at ORNL to determine the transmission through $\frac{1}{8}$-in. thicknesses of boral as measured by $1/v$ detectors. In the first experiment[3] the radiation consisted of thermal neutrons escaping from a thermal column on top of the ORNL Graphite Reactor with an angular distribution of the $(1 + \sqrt{3} \cos \theta)$ type,[4] which is more forwardly peaked than an isotropic flux. Consequently, the experimental values should be between the computed values for

[1]Now at Ohio State University, Dept. of Physics, Columbus, Ohio.

[2]Private communication.

[3]R. O. Maak, B. E. Prince, and P. C. Rekemeyer, *Boral Radiation Attenuation Characteristics*, MIT Engineering Practice School, KT-251 (Nov. 27, 1956).

[4]R. F. Christy *et al.*, *Lecture Series in Nuclear Physics*, MDDC-1175 (Dec. 1947).

normal incidence and those for isotropic incidence. The transmission obtained for a Brooks and Perkins boral sample was 0.070, while the transmission for a Carbide sample was 0.094. In the second experiment[5] the radiation was a collimated beam of normally incident neutrons from a beam hole at the ORNL Graphite Reactor. The transmissions obtained for two different Alcoa samples were 0.065 and 0.070, respectively.

This method will be described in detail in a separate report.[6]

[5] G. deSaussure, private communication.

[6] W. R. Burrus, *Neutron Transmission Through Boral and Similar Heterogeneous Materials Consisting of Randomly Distributed Absorbing Chunks*, ORNL-2528 (to be published).

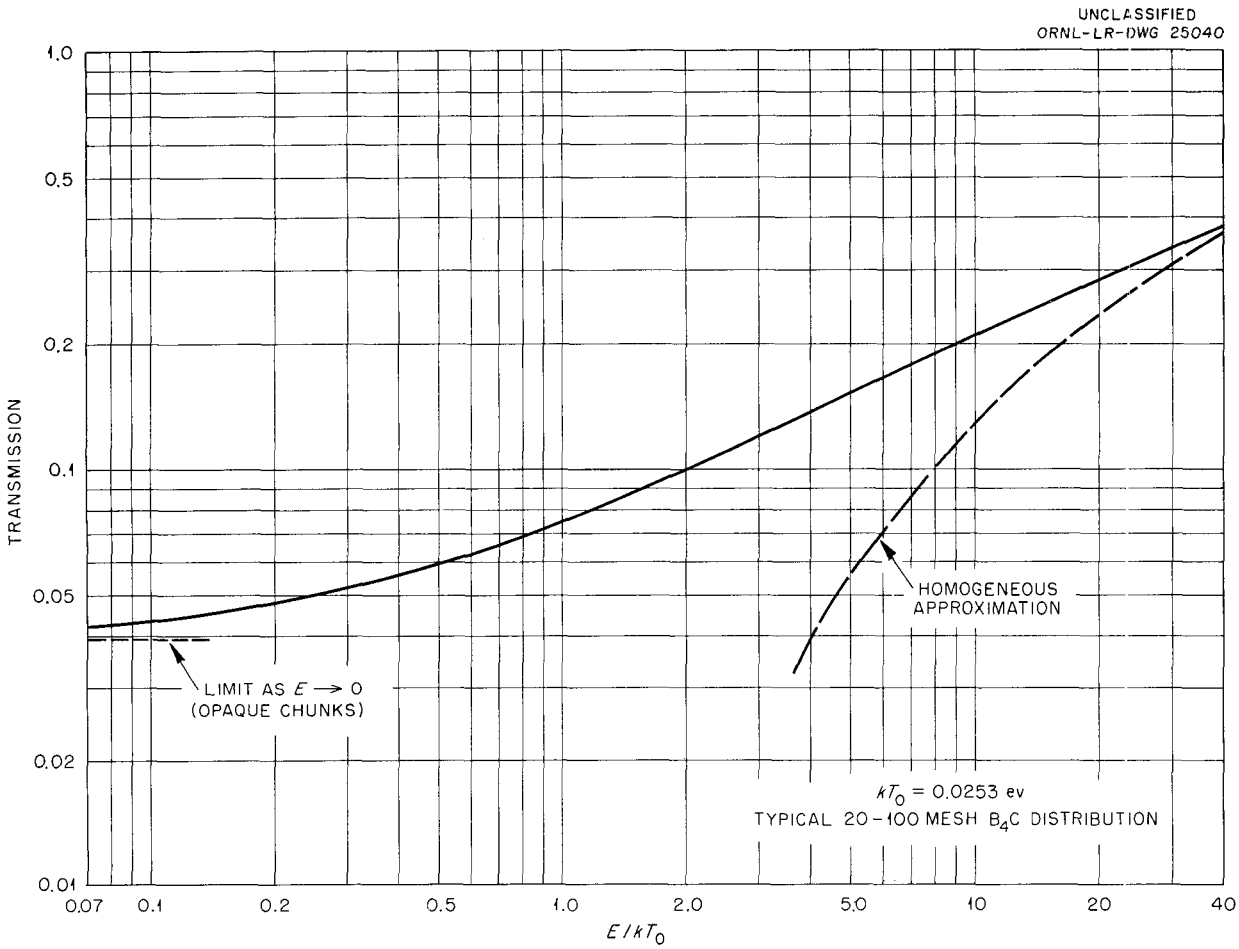

Fig. 7.11.1. Neutron Transmission Through $\frac{1}{8}$-in.-thick Boral as a Function of Energy; Normally Incident Flux.

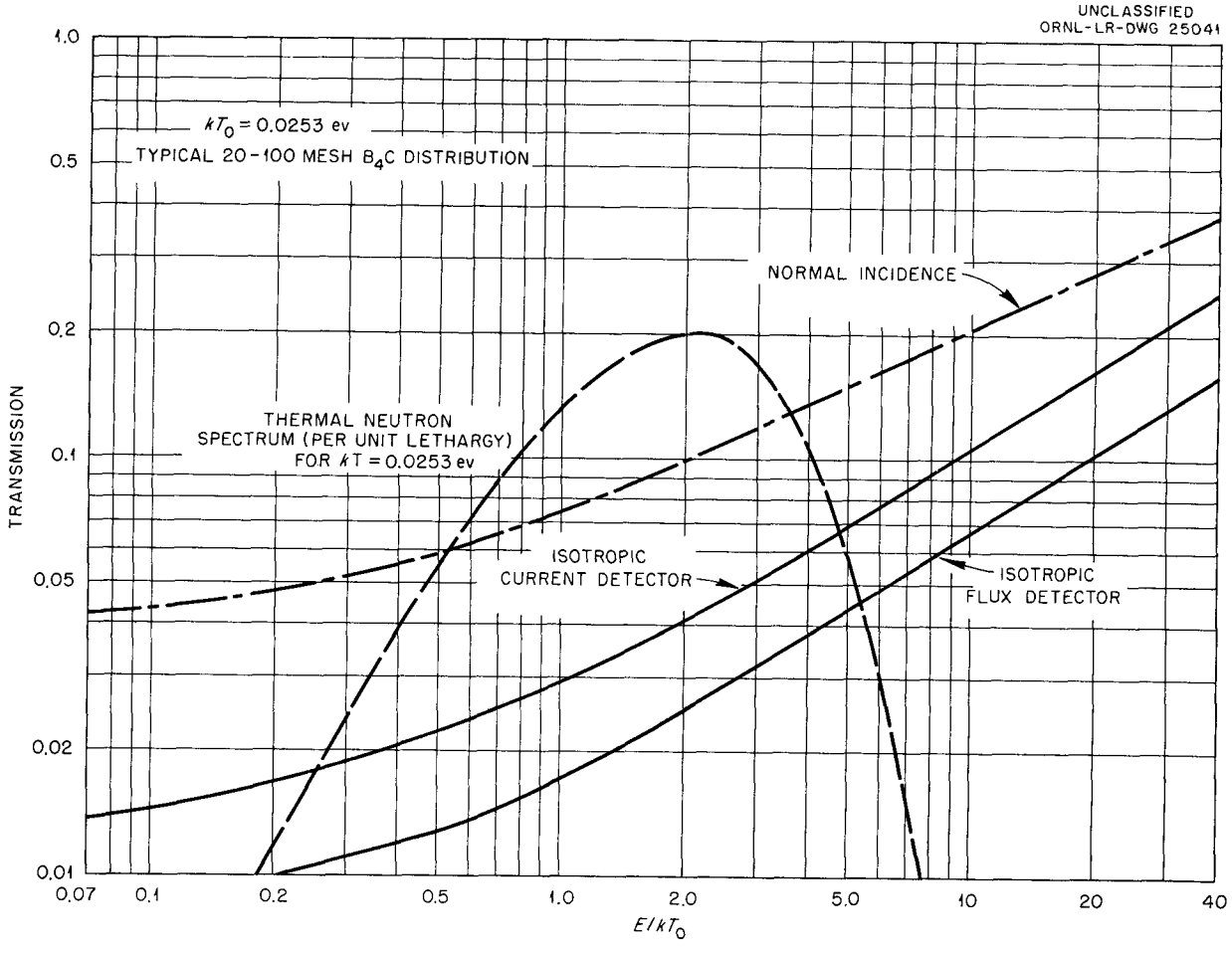

Fig. 7.11.2. Neutron Transmission Through ⅛-in.-thick Boral as a Function of Energy; Isotropically Incident Flux.

7.12. A MONTE CARLO CALCULATION OF THE NEUTRON PENETRATION OF FINITE WATER SLABS

J. B. Hilgeman[1] F. L. Keller C. D. Zerby

Monte Carlo calculations[2] of the neutron dose-rate distribution beyond finite water slabs have been performed for various parameter combinations. In the idealized problem a plane monodirectional, monoenergetic beam of neutrons was assumed to be incident on a water slab of infinite area and finite thickness. The angle between the incident neutron direction and the normal to the slab was denoted as θ_0, and the number of neutrons which penetrated the slab was assumed to be recorded by a spherical detector. The space around the detector was divided into a number of solid angle intervals with the apex at the detector point, and the number of neutrons which entered into each of these solid angle intervals was recorded. The energy spectrum of the radiation which entered each of the solid angle intervals was determined by dividing the energy range from

[1]On assignment from U.S. Air Force.

[2]The Monte Carlo machine program which was used in this study is a revision of the neutron air-scattering program which has been described by C. D. Zerby, *A Monte Carlo Calculation of Air-Scattered Neutrons*, ORNL-2277 (April 23, 1957). This program employs the method of statistical estimation.

some cutoff energy, E_c, to the source energy, E_0, into an arbitrary number of equal intervals and recording each contribution in its appropriate energy interval. This energy spectrum was then used to determine the tissue dose-rate contribution from each energy and solid angle interval.

The scattering probability was assumed to be isotropic in the center-of-mass system. This is essentially exact for the scattering by hydrogen (the major scatterer) and is fairly satisfactory for the scattering by oxygen over most of the energy range of interest in these calculations. The density of water was taken to be 1 g/cm^3. All the results are normalized to 1 incident neutron per second per square centimeter of slab surface.

A parameter study was carried out in which plane monodirectional beams of neutrons with energies, E_0, of 0.55, 1.2, 2, 4, 6, and 8 Mev were incident on the water slabs at angles, θ_0, of 0, 30, 60, and 75 deg. The thicknesses of the slabs ranged from 1 to 8 mfp. The number of case histories used for a particular problem varied from 5000 to 10,000, depending upon the slab thickness and the angle of incidence. The solid angle intervals at the detector were defined by 90-deg azimuthal angle intervals and 15-deg polar angle intervals with respect to a polar axis which was normal to the slab surface. A cutoff energy, E_c, of 0.1 Mev was used. This value was chosen to approximate the low-energy cutoff of most of the present dosimeters. Fifteen equal energy intervals were used to determine the spectrum.

Figure 7.12.1 shows a set of representative curves which were generated from data obtained from this study. In this figure dose-rate buildup factors, B_r, have been plotted as a function of the finite slab thicknesses for 2-Mev neutrons incident at θ_0 = 0, 30, 60, and 75 deg. The dose-rate buildup factor may be defined as the ratio of the total dose rate at the detector to the dose rate which would result if every collision were equivalent to an absorption. It should be noted that the results are plotted as a function of the *normal* thickness of the slab in mean free paths. When plotted in this manner, it is obvious that the buildup factor for a given energy and slab thickness should increase with increasing values of

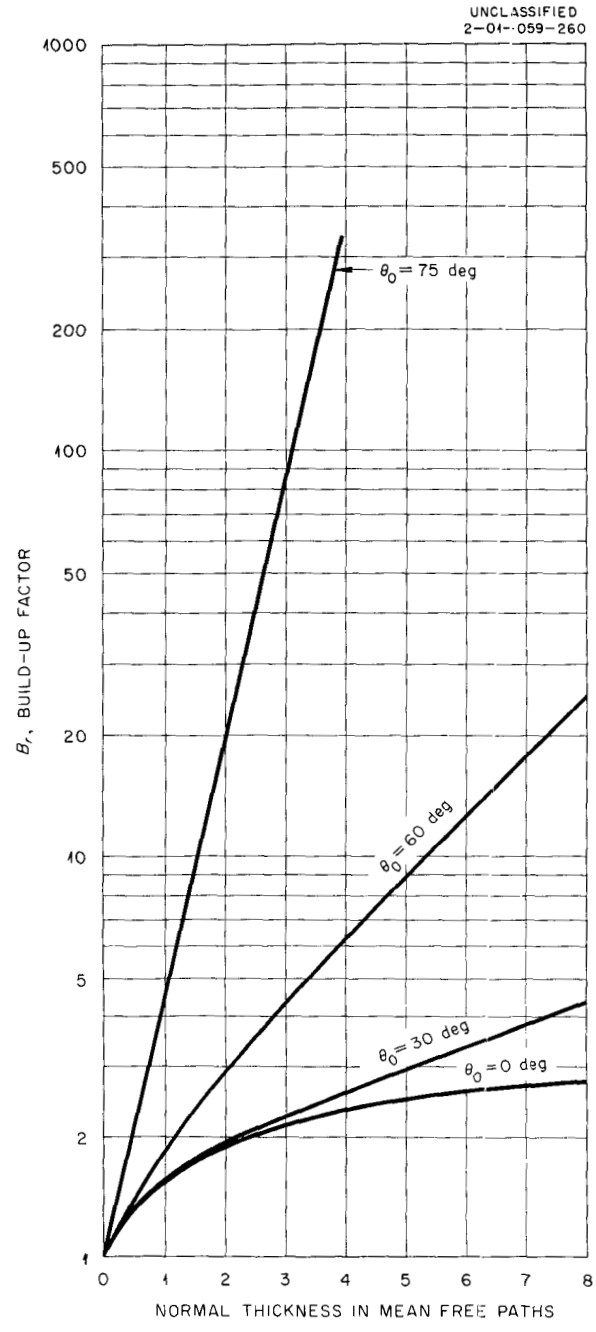

Fig. 7.12.1. Dose-Rate Buildup Factors for 2-Mev Neutrons Incident at Various Angles on Finite Water Slabs.

θ_0 because of the "short-circuiting" effect. These results have been compared with the results of a similar calculation performed by Obenshain, Eddy, and Kuehn,[3] and the buildup factors from the present calculation have been found to be considerably smaller, in general, than their values. The cause of this apparent discrepancy is not yet known.

Figure 7.12.2 shows the angular distribution of the scattered neutron dose rate at the detector for a 2-Mev neutron beam normally incident ($\theta_0 = 0$) on water slabs of various thicknesses. Since there is azimuthal symmetry at the detector for these cases, the curves are plotted as dose rate per steradian vs cos α, where α is the polar angle at the detector. These plots were generated by drawing smooth curves through the histogram output of the machine calculations.

For cases of normal incidence ($\theta_0 = 0$), a very large fraction of the total scattered dose rate at the detector is contributed by neutrons which have undergone only one scattering event in the slab. The fraction of the total scattered dose rate which was contributed by singly scattered neutrons for each of these cases is given in Table 7.12.1. From this table it is seen that single scattering calculations may be expected to yield fairly accurate results for dose rates from neutrons which are normally incident on thick water slabs. The higher orders of scattering become more important, however, as the angle of incidence, θ_0, is increased.

A detailed description of all the results of this parameter study will be given in a separate report.[4]

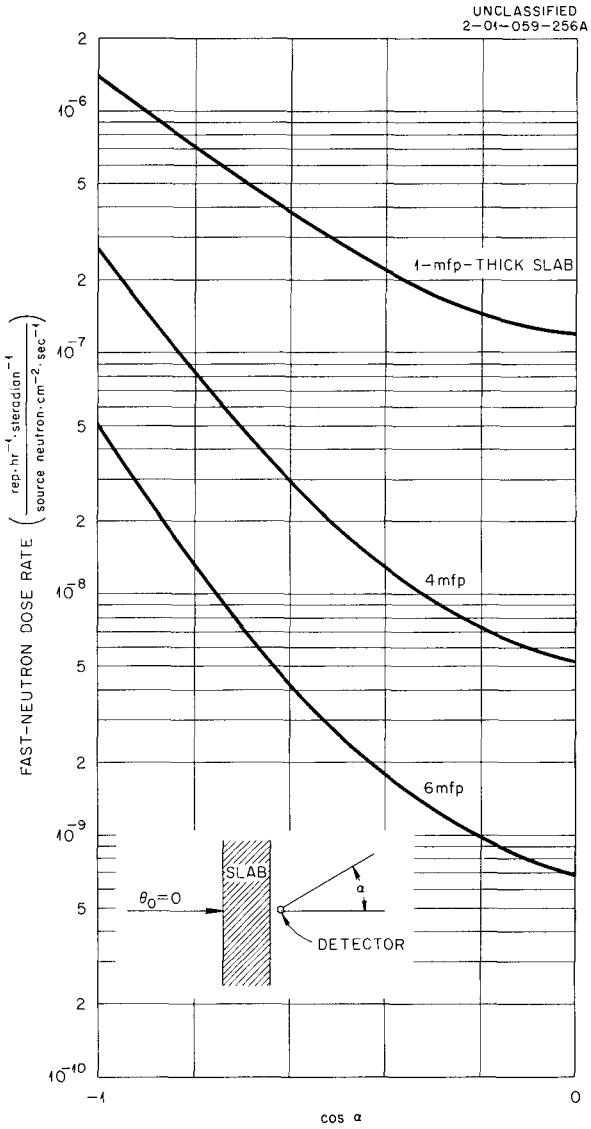

Fig. 7.12.2. Fast-Neutron Dose Rates at Rear of Finite Water Slabs Resulting from Multiply Scattered Neutrons (E_0 = 2 Mev).

[3] F. Obenshain, A. Eddy, and H. Kuehn, *Polyphemus. A Monte Carlo Study of Neutron Penetrations Through Finite Water Slabs*, WAPD-TM-54 (1957).

[4] J. B. Hilgeman, F. L. Keller, and C. D. Zerby, *Neutron Penetration of Finite Water Slabs*, ORNL-2463 (unpublished).

Table 7.12.1. Fraction of Total Scattered Dose Rate at the Detector Contributed by Neutrons Which Have Undergone Only One Scattering Event ($\theta_0 = 0$)

E_0 (Mev)	Fraction of Dose Contributed by Singly Scattered Neutrons			
	At 1 mfp	At 3 mfp	At 4 mfp	At 6 mfp
0.55		0.827	0.864	0.902
2.0	0.727		0.86	0.846
4.0		0.791	0.832	0.877
8.0	0.707		0.829	0.762

7.13. A HIGH-ENERGY ACCELERATOR SHIELDING PROGRAM

C. D. Zerby

The Neutron Physics Division has initiated a high-energy accelerator shielding program which is essentially divided into two parts. One part is the development of an IBM-704 machine code to calculate the spatial and energy distributions of high-energy particles penetrating an idealized shield. Initially only the transmission of pions and nucleons will be considered until such time as more physical data become available. The Monte Carlo method of calculation will be used for solving this problem. The techniques to be used in the process of calculation have been decided upon, and a rough flow diagram of the calculation has been made.

The second part of the program is the determination of the best differential cross-section data to be used in the shielding calculation. For this purpose a nuclear cascade code is being developed and is in the flow diagram stage at the present time.

Part 8

RADIATION DETECTOR STUDIES

8.1. THE MODEL IV GAMMA-RAY SPECTROMETER

G. T. Chapman T. A. Love

A new gamma-ray spectrometer system is currently being fabricated for use at the Bulk Shielding Facility. This spectrometer, which will be referred to as the model IV gamma-ray spectrometer, will consist of a total absorption NaI(Tl) crystal, housing for the crystal, a positioning device, and the associated electronics. These major components are discussed below.

Total Absorption NaI(Tl) Crystal

The possibility of using a $9\frac{3}{8}$-in.-dia sodium iodide thallium-activated crystal for gamma-ray spectral measurements at the Bulk Shielding Facility (BSF) has been discussed previously.[1] In recent work an attempt was made to improve the response of the crystal to monoenergetic gamma rays by using an array of seven DuMont 6363 3-in.-dia photomultiplier tubes on the crystal. The voltages for the tubes are received from a common supply through a voltage divider consisting of seven 10-turn potentiometers, each of which is in series with one of the photomultiplier tubes.

The crystal was exposed to monoenergetic gamma rays from different sources. The gamma rays were collimated into the well of the crystal and also into its side. Similar investigations were made previously[1] by using a single 5-in.-dia photomultiplier tube with a truncated cone light piper and by using an array of three 5-in.-dia photomultiplier tubes mounted directly onto the $\frac{1}{2}$-in.-thick glass window. Figure 8.1.1 indicates the response of the crystal for the various conditions in terms of energy resolution, that is, the ratio of the Gaussian full width at half maximum to the energy of the incident photons. It will be noted that the array of seven photomultiplier tubes shows some improvement over the other arrangements throughout the range of gamma-ray energies investigated.

The crystal has consistently exhibited a better resolution when the gamma rays were collimated into the side of the cylindrical section. This implies that the conical section is detrimental to the response by virtue of the geometry or because of a nonuniformity in the crystal material in this region. A study of the effect of the cone on the response is being made by the vendor.[2]

A further improvement in the resolution may be obtained by improving the reflecting surface between the photomultiplier tubes. Experiments are being initiated to study this possibility.

Crystal Housing

Basically, the housing for the spectrometer will consist of a neutron and gamma-ray shield surrounding a cavity large enough to hold the crystal detector and associated photomultiplier tubes. The over-all dimensions will be 58 in. long by 42 in. in diameter, and it will weigh about 15 tons. The shield surrounding the detector will be fabricated

[1]G. T. Chapman and T. A. Love, *Appl. Nuclear Phys. Ann. Prog. Rep. Sept. 1, 1957*, ORNL-2389, p 233.

[2]Harshaw Chemical Co., Cleveland, Ohio.

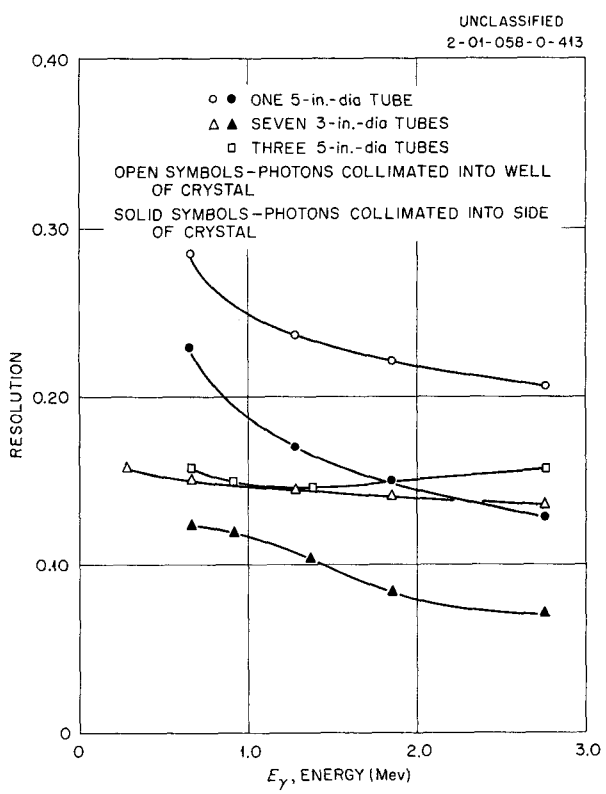

Fig. 8.1.1. Resolution as a Function of Photon Energy for Various Photomultiplier Tube Arrangements.

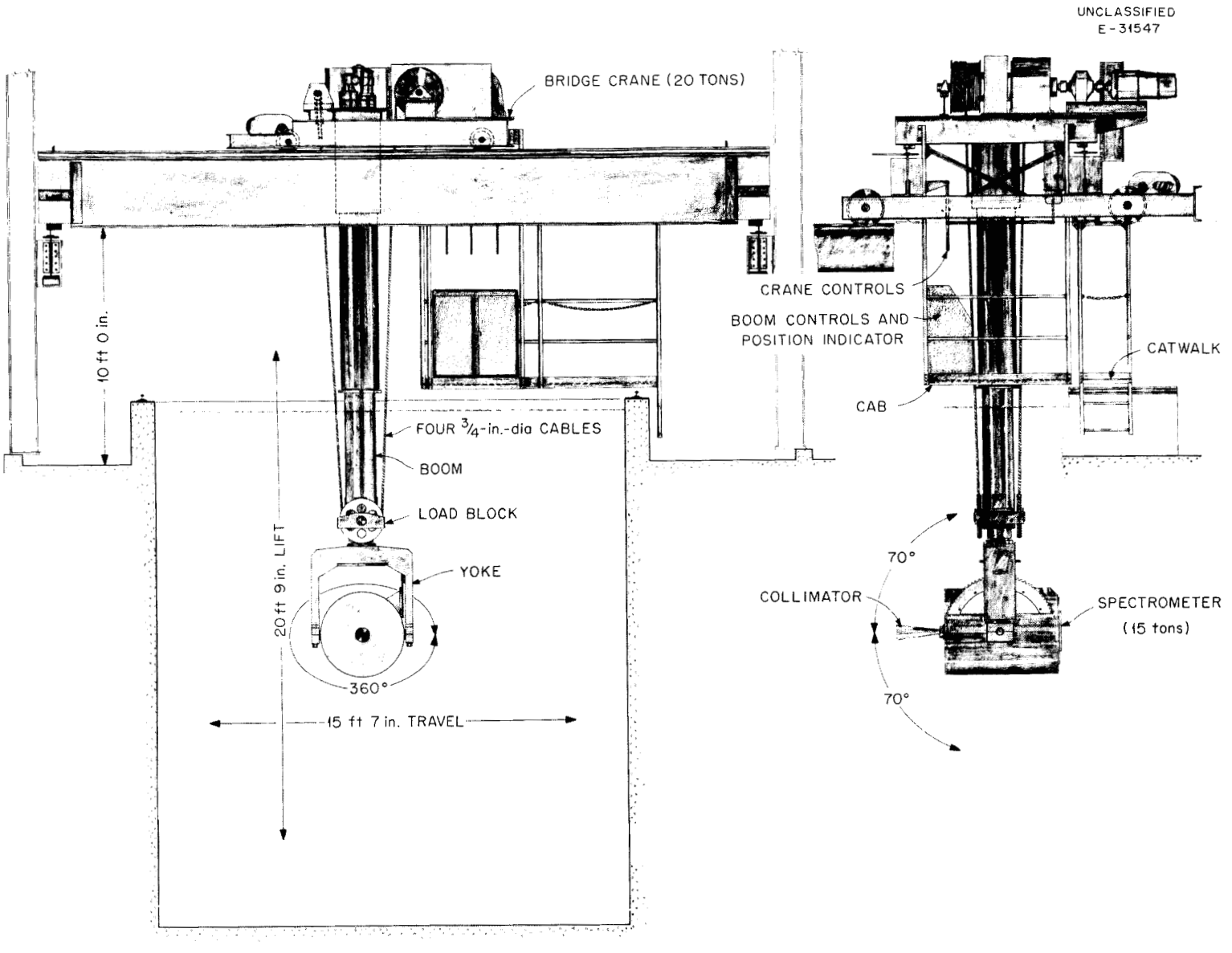

Fig. 8.1.2. Positioning Device for the BSF Spectrometer.

from a eutectic alloy of lead and lithium to reduce the gamma-ray background. The lithium will reduce the probability of neutrons reaching the crystal, and the lead, of course, will attenuate those gamma rays which enter the shield from the outside or originate within the shield from neutron interactions.

Positioning Device

The spectrometer will be positioned in the BSF pool relative to the reactor with the device shown in Fig. 8.1.2. This device will consist of a 20-ton bridge-type crane with a telescoping boom to support the spectrometer housing and a simple analog computer[3] for position readout and control purposes. The spectrometer will have a vertical travel of 20 ft 9 in. and a horizontal travel 15 ft 7 in. across the width of the pool. It will be possible at any point in the pool to rotate the spectrometer in a horizontal plane through 360 deg and in a vertical plane through ±70 deg from the horizontal position. The accuracy of the position-indicating system will be such that an indicated point at the entrance of the collimator may be located within ±0.25 in. in any direction.

[3]D. J. Knowles, *A Computer for a Position Indicating System*, ORNL-2534 (July 18, 1958).

Status

With the exception of the crystal shield, all major components of the model IV gamma-ray spectrometer are available and ready for assembly at ORNL. It is anticipated that the system will have been tested and will be ready for operation by January 1959.

8.2. A PULSE PREAMPLIFIER WITH CASCODE INPUT

T. A. Love W. R. Burrus[1]
R. W. Peelle

A linear pulse preamplifier which incorporates twin-triode "cascode"[2,3] input and "bootstrap"[4] output stages has been designed to amplify pulses from low-output nuclear detectors to a voltage level sufficient for the input of a standard linear pulse amplifier. In the circuit for this preamplifier attempts are made to overcome two deficiencies common among units in use for similar purposes: (1) unnecessarily high random noise and (2) output circuits incapable of driving a 100-Ω transmission line in a linear and gain-stable fashion.

The cascode input stage, which replaces the usual pentode, consists of a grounded-grid triode amplifier serving as the plate load of an input triode. The lower "shot" noise of a triode may thus be obtained without the usual gain disadvantages induced by the Miller effect. Since plate-current shot noise is likely to be the most important noise source for the type of preamplifier required, noise reduction by a factor of 2 or 3 is obtainable with the cascode combination.[2,3]

Figure 8.2.1 shows the circuit which has been used to amplify pulses from a spiral-wound fission chamber. It has, as drawn, a gain of about 33 and a loop gain of about 480. Rise time at the output (10 to 90% of the pulse height for a step-function input) is about 4.0×10^{-8} sec.

The input circuit has been designed with a 2×10^{-5} sec decay constant for application to a high-capacity detector. If the input time constant were lengthened significantly, longer clipping time constants would be needed within the feedback loop.

The output for single pulses observed at the end of a long transmission line tends to saturate at +3.5 or −4.5 v. Since the pulse amplifier which typically follows has a gain greater than 2000 with an overload at 100 v, overload in the preamplifier is not usually serious, and no particular precautions have been taken. Also, overload pulses are uncommon from fission chambers.

The noise voltage from this circuit is less than one-half that observed when a 5654(6AK5) pentode input stage was used in an otherwise identical circuit having just the same gain. For this comparison, the noise voltage was determined by the

[1]Now at Ohio State University, Dept. of Physics, Columbus, Ohio.

[2]F. Langford-Smith, *Radiotron Designer's Handbook*, pp 914, 513, Radio Corporation of America, Harrison, N. J., 1953.

[3]A. B. Gillespie, *Signal, Noise, and Resolution in Nuclear Counter Amplifiers*, p 55–57, McGraw-Hill, New York, 1953.

[4]E. Fairstein, *Rev. Sci. Instr.* 27, 475 (1956).

UNCLASSIFIED
2-01-058-0-417

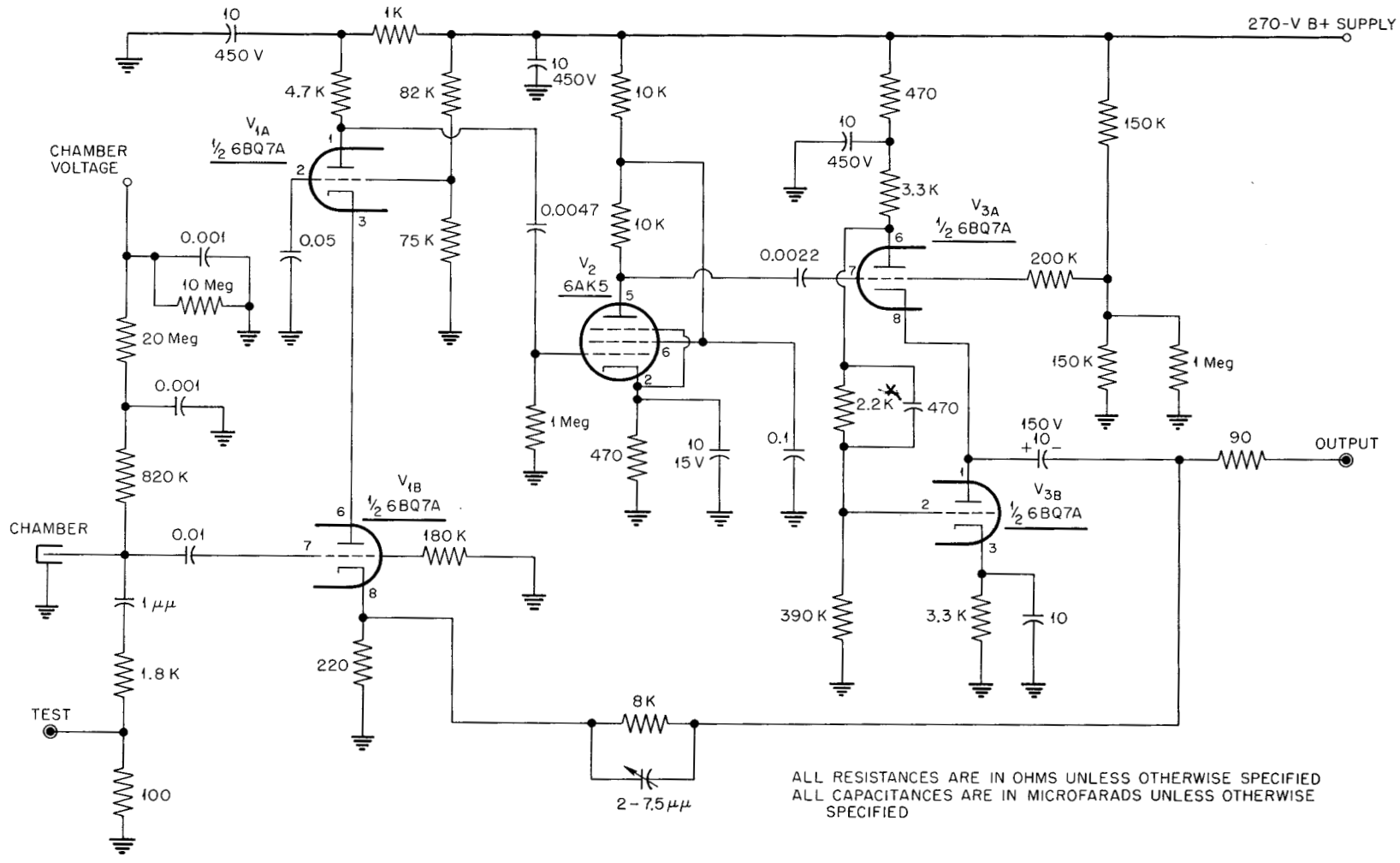

Fig. 8.2.1. Circuit Diagram for Linear Pulse Preamplifier with Cascode Input.

* 2.2 Meg. See Erratum

pulse-height distribution of noise crests measured by a standard discriminator circuit at the output of of a DD2 linear amplifier[4] having 0.7-μsec clipping lines and an $\sim$0.2-μsec rise time. Comparison of circuit parameters with standard noise formulas[5] leads to estimated noise voltage in good relative agreement with the results above.

[5]A. B. Gillespie, *op. cit.*, chap. 3.

The circuit described in this paper has been used continuously for about one year. No unusual gain shifts have been observed, and only a normal amount of maintenance has been required. The success of the present design in reducing observed noise supports the premise that cascode input stages should always be at least considered for pulse preamplifiers.

8.3. ENERGY RESPONSE OF THE HORNYAK SCINTILLATION NEUTRON DETECTOR

W. J. Fader[1]

Two difficulties often encountered in the measurement of the spatial distributions of Mev neutrons in the vicinity of nuclear chain-reacting systems are the high gamma-ray backgrounds to which the detectors are invariably sensitive and the low counting efficiencies of the detectors. One detector which appears to be promising in overcoming these difficulties is the Hornyak scintillator; a detailed description of its design and fabrication has been published.[2] The Hornyak scintillator has several advantages: its gamma-ray sensitivity is low, its neutron counting efficiency is as high as 1%, and its small physical size allows measurements with high spatial resolution. In order that reactor fast-neutron measurements made with this detector might be intelligently interpreted, an investigation of its neutron energy response was undertaken. The investigation included an attempt to predict the pulse-height distributions and energy response of the detector from a few assumptions about the mechanism of production of the scintillations by neutrons. In addition, measurements of the pulse-height distribution observed for monoenergetic neutrons and of the counting efficiency dependence on neutron energy were made with monoenergetic neutrons from the ORNL 5-Mev electrostatic generator. The results of the investigation will be published in a separate report.[3]

[1]On assignment from Pratt & Whitney Aircraft.

[2]W. F. Hornyak, *Rev. Sci. Instr.* 23, 264 (1952).

[3]W. J. Fader, *Energy Response of the Hornyak Scintillation Neutron Detector*, ORNL-2527 (to be published).

8.4. LUMINESCENCE EMISSION SPECTRA OF LITHIUM IODIDE SCINTILLATION CRYSTALS

H. G. Hanson[1] J. J. Manning R. B. Murray

The scintillation response of $Li^6I(Eu)$ crystals to fast neutrons has been the subject of previous investigations at this Laboratory.[2] The width of the fast-neutron peak in a pulse-height spectrum is attributed to a difference in the scintillation response of the crystal to the reaction products resulting from the $Li^6(n,\alpha)T$ reaction. The scintillation light output per Mev from an alpha particle is about one-half that from the triton.[2,3] Any further attempts to improve the fast-neutron resolution must be based on an understanding of the fundamentals of the scintillation process in lithium iodide. Unfortunately, rather little information of a basic nature is available on this subject. Therefore a program has been initiated in an attempt to determine the factors influencing the scintillation response of lithium iodide to various charged particles. As a first step, the luminescence emission spectra of both unactivated and activated lithium iodide crystals upon being excited by alpha particles, gamma rays, and the alpha-triton pair resulting from slow-neutron capture have been determined as a function of temperature in the region between room temperature and liquid-nitrogen temperature.

Experimental Method

Emission spectra were measured with a Bausch & Lomb 500-mm focal length plane grating monochromator, blazed in the ultraviolet, which has an aperture of $f/5$ and a nominal dispersion of 16 Å/mm. The slit widths used varied from 1 to 5 mm, corresponding to bands from 16 to 80 Å. The luminescent light passed out the exit slit to an RCA 6903 photomultiplier tube (quartz envelope) operated at 930 v. The photomultiplier anode current was measured by a Leeds & Northrup micromicroammeter whose output was attached to the Y axis of a Moseley X-Y recorder. A synchronous motor turned the wavelength control drum of the monochromator, as well as a potentiometer whose output was attached to the X axis of the recorder. Scanning speeds of 5 to 10 Å/sec were used.

Three crystals of $Li^6I(Eu)$ and one crystal of "pure" Li^6I, all of which were grown at this Laboratory, were used in the experiment. The crystals were each approximately 24 mm in diameter and varied in thickness from 1 to 5 mm. They were polished with fine sandpaper in a dry box and placed in a luminescence chamber (shown in Fig. 8.4.1), which was promptly evacuated through a vacuum line containing a liquid-nitrogen trap. The luminescence chamber was attached to the monochromator at the position of the entrance slit. All the data reported here were taken on freshly mounted crystals. Some attenuation of the luminescence intensity on the short wavelength side of the maximum was noted after the crystals had been in the chamber for several days.

The temperature of each scintillation crystal was continuously variable from room temperature to liquid-nitrogen temperature. Cooling was accomplished by a flow of nitrogen gas which had been cooled in a liquid-nitrogen heat exchanger. The lowest temperature, about −192°C, was achieved by pouring liquid nitrogen into the Dewar vessel. The crystal temperature was always taken to be that indicated by a copper-constantan thermocouple soldered to a thin brass ring which was inserted into the hole at the bottom of the Dewar flask. In this position the ring was adjacent to the crystal. Care was taken to ensure that the crystal was in thermal equilibrium with its surroundings prior to the recording of each spectrum. In every case data were taken only after the thermocouple had indicated a constant temperature for a period of 1 hr. Repeated measurements demonstrated no change in the emission spectrum after thermal equilibrium had been established.

The crystals could be excited by any one of three sources: a 50-mc Hg^{203} gamma-ray source, a U^{233} alpha-particle source (total activity $= 4 \times 10^7$ alpha particles/min), and a beam of thermal neutrons collimated by a graphite channel from the hole 59 of the ORNL Graphite Reactor. The experiment was arranged so that the spectra resulting from excitation by all three sources could be taken in quick succession while the crystal was at the same temperature. The alpha-particle source could

[1]Summer research participant from University of Minnesota, Duluth Branch.

[2]R. B. Murray, *Nuclear Instr.* 2, 237 (1958); see also R. B. Murray and J. J. Manning, *Appl. Nuclear Phys. Ann. Prog. Rep. Sept. 1, 1957*, ORNL-2389, p 240.

[3]T. R. Ophel, *Nuclear Instr.* 3, 45 (1958).

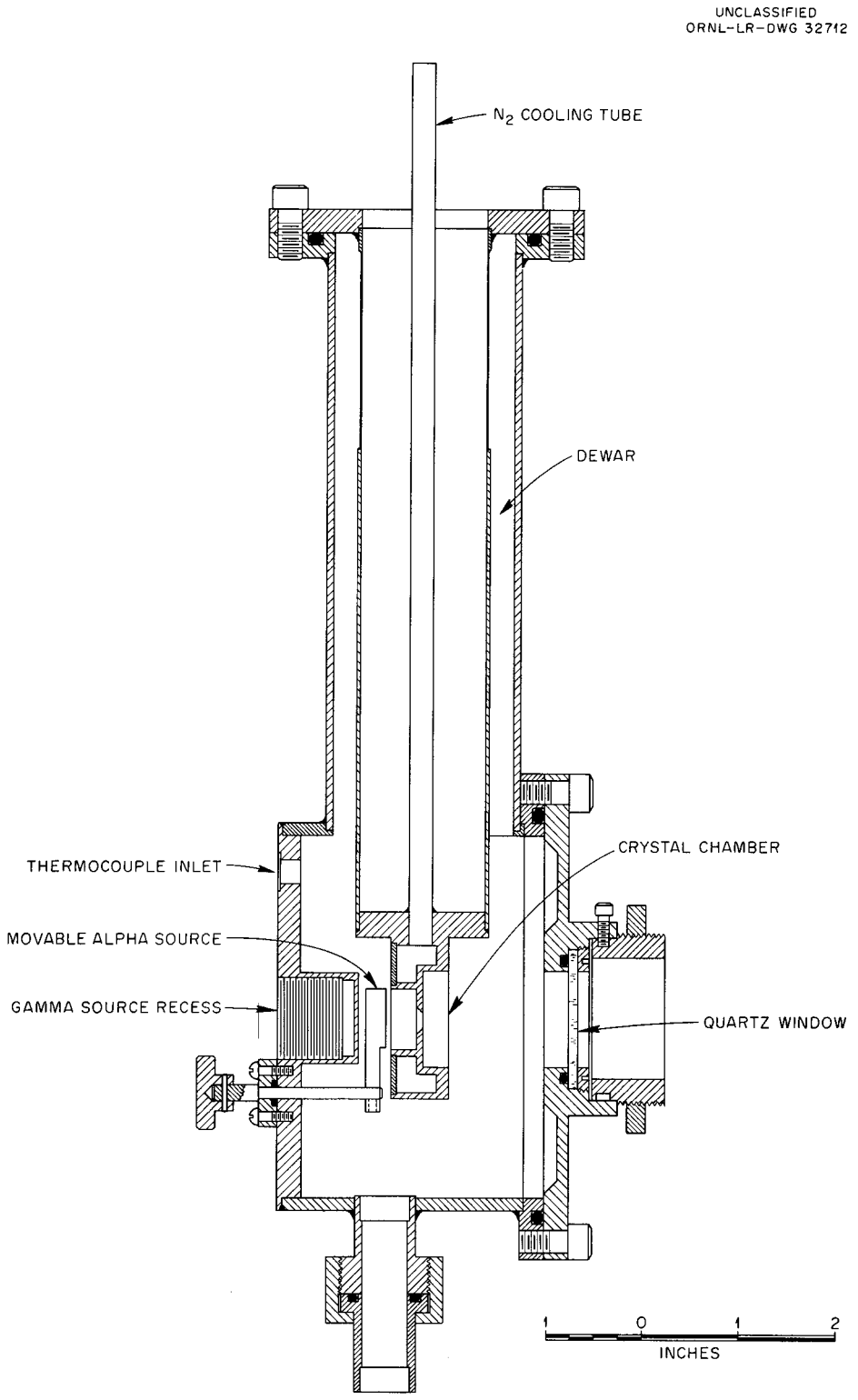

Fig. 8.4.1. Luminescence Chamber for Lithium Iodide Crystals.

be moved into position, directly behind the crystal, by an external lever (Fig. 8.4.1). For gamma-ray excitation, the Hg^{203} source, which was contained in a sealed thimble, was inserted in the recess of the luminescence chamber. During alpha-particle or gamma-ray excitation the slow-neutron beam was stopped by an opaque shield.

All curves were double-traced, and, with the exception of the alpha-particle data, the responses seldom varied by more than a pen-line width on the recorder. The alpha-particle data showed somewhat larger irregularities, owing to the low signal, and therefore dark current fluctuations became apparent. The wavelength axis of the recorder was frequently checked against a mercury arc source. The accuracy of the wavelengths taken from the recordings is estimated to be ±7 Å. Wavelength shifts between successive tracings due to instrumental effects were negligible, and so the observed slight shifts of band maxima due to different modes of excitation, or due to different temperatures, are dependable.

Results

Tracings of the recorded emission spectra from the four crystals studied are shown in Figs. 8.4.2 through 8.4.5. In the case of crystal 1 no data were recorded for excitation by slow-neutron capture. The maxima shown in Fig. 8.4.2 for alpha-particle and gamma-ray excitation at room temperature (22°C) are located near 4700 Å; there is some evidence that the alpha-particle peak is at a slightly shorter wavelength. At a temperature of −192°C, the intensity of the light output increases significantly, the relative increase being greater for alpha-particle excitation than for gamma-ray excitation. Examination of the spectra obtained with a narrower slit while the crystal was at −192°C (Fig. 8.4.2) indicates the existence of two bands with maxima at *about* 4700 and 4875 Å.

Crystals 2 and 3 were activated with less than one-half the europium concentration of crystal 1. At room temperature both crystals demonstrate a spectral maximum near 4650 Å, as shown in Figs. 8.4.3 and 8.4.4. The maximum is at a slightly shorter wavelength for neutron and alpha-particle excitation than it is for gamma-ray excitation. There is also a somewhat higher luminescence intensity on the short wavelength side of the maximum for neutron and alpha-particle excitation. At reduced temperatures the single maximum observed at room temperature shifts 30 or 40 Å to shorter wavelengths for all types of excitation. The band width also narrows with decreasing temperature, while the magnitude of the maximum increases. Both crystals 2 and 3 show a band with a maximum at approximately 4875 Å, which appears at reduced temperatures. The magnitude of this band appears to depend on the europium content of the crystal.

The relative increase in the luminescence intensity of crystals 2 and 3 as their temperatures decrease from room temperature to liquid-nitrogen temperature is greatest for alpha-particle excitation, intermediate for neutron excitation, and least for gamma-ray excitation. This is in qualitative agreement with previous measurements of pulse height as a function of temperature.[2]

Crystal 4 was the "pure" Li^6I crystal, "pure" in the sense that it was not deliberately activated. Care was taken in the preparation of the material and during crystal growth to avoid any contact with vessels or apparatus which had previously contained europium. A semiquantitative spectrographic analysis showed the presence of Ca, Mo, Pb, and Si (10^{-2} to 10^{-3}%), Cu, Fe, and Mg (10^{-3} to 10^{-4}%). Similar impurities are usually observed in the activated crystals grown at this Laboratory.

The emission spectra for crystal 4 are shown in Fig. 8.2.5. The band maxima near 3700 and 4000 Å show a marked increase in magnitude with decrease in temperature. A similar increase in intensity with decreasing temperature for the unresolved spectrum of pure LiI was previously reported by Bonanomi and Rossel.[4] The maximum at 3700 Å shifts slightly to shorter wavelengths with decreasing temperature. The maximum at 4050 Å shifts approximately 125 Å to shorter wavelengths as the temperature decreases from room temperature to liquid-nitrogen temperature.

For all the crystals studied no bands other than those shown in the figures were found in the spectral region to which the RCA 6903 tube would respond. Any significant luminescence should have been detected in the range from 2100 to 6000 Å.

Thermoluminescence curves for both Li^6I(Eu) and pure Li^6I were recorded by attaching the output of the thermocouple to the *X* axis of the recorder

[4] J. Bonanomi and J. Rossel, *Helv. Phys. Acta* **25**, 725 (1952).

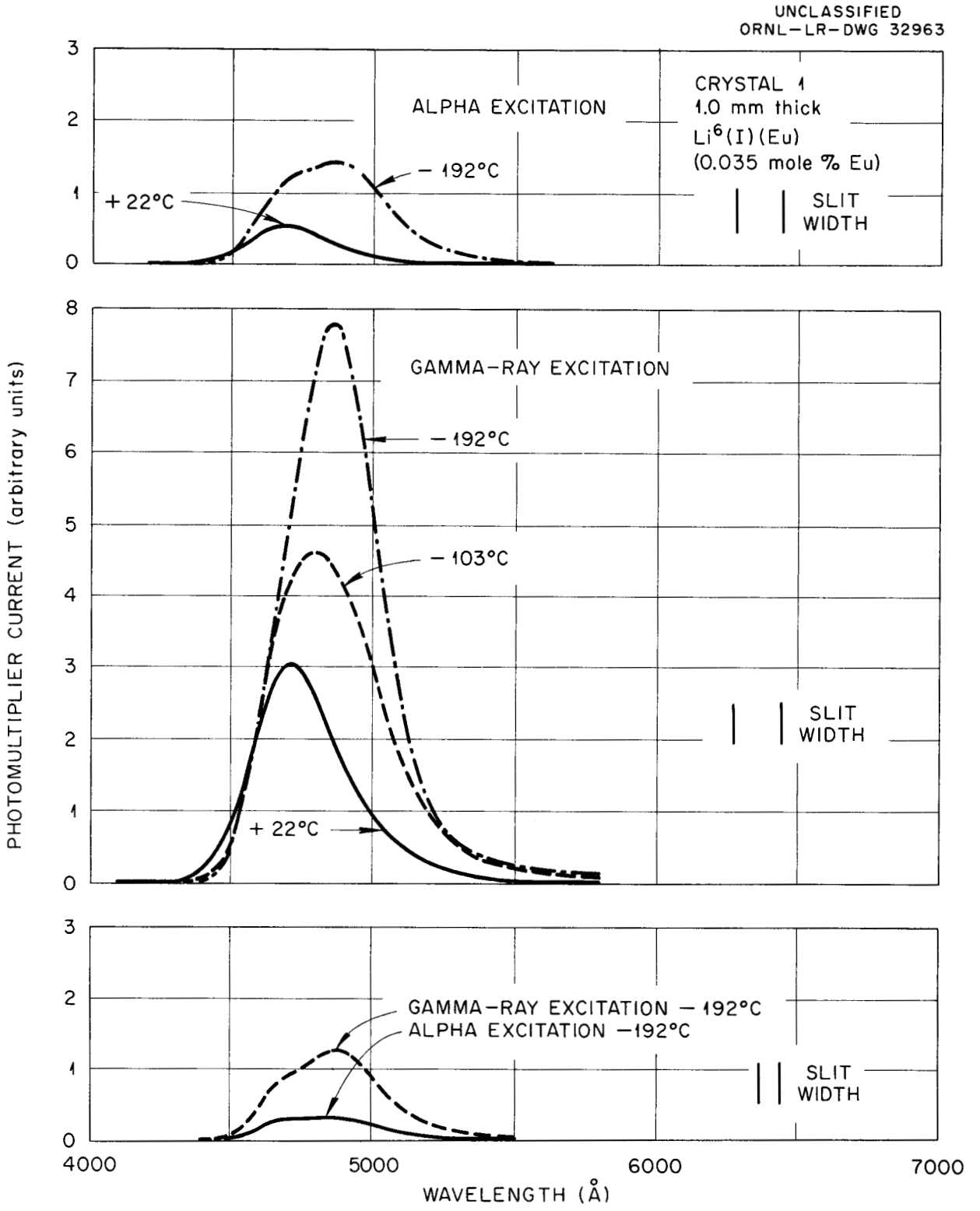

Fig. 8.4.2. Luminescence Spectra of $Li^6I(Eu)$, Crystal 1.

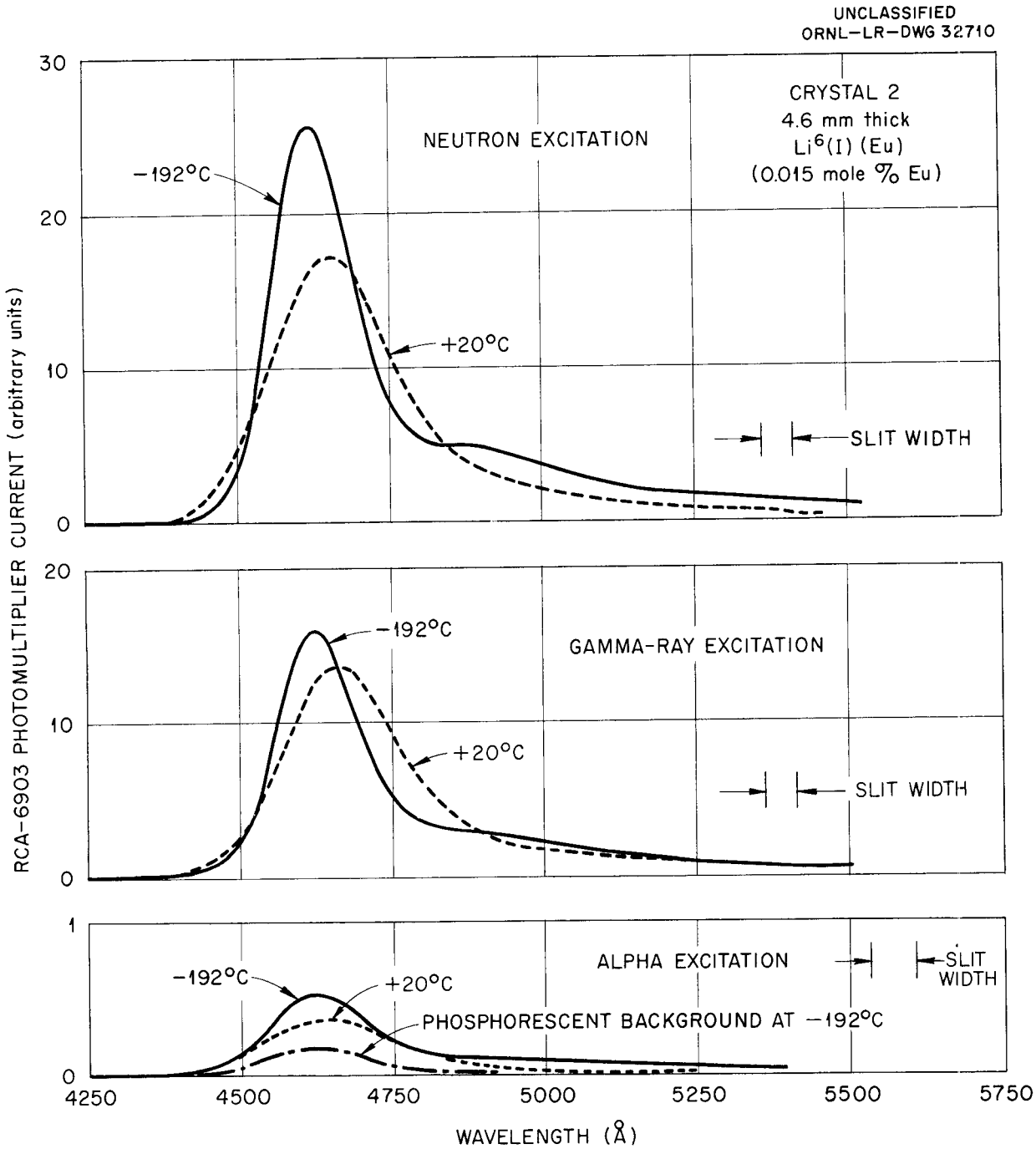

Fig. 8.4.3. Luminescence Spectra of $Li^6I(Eu)$, Crystal 2.

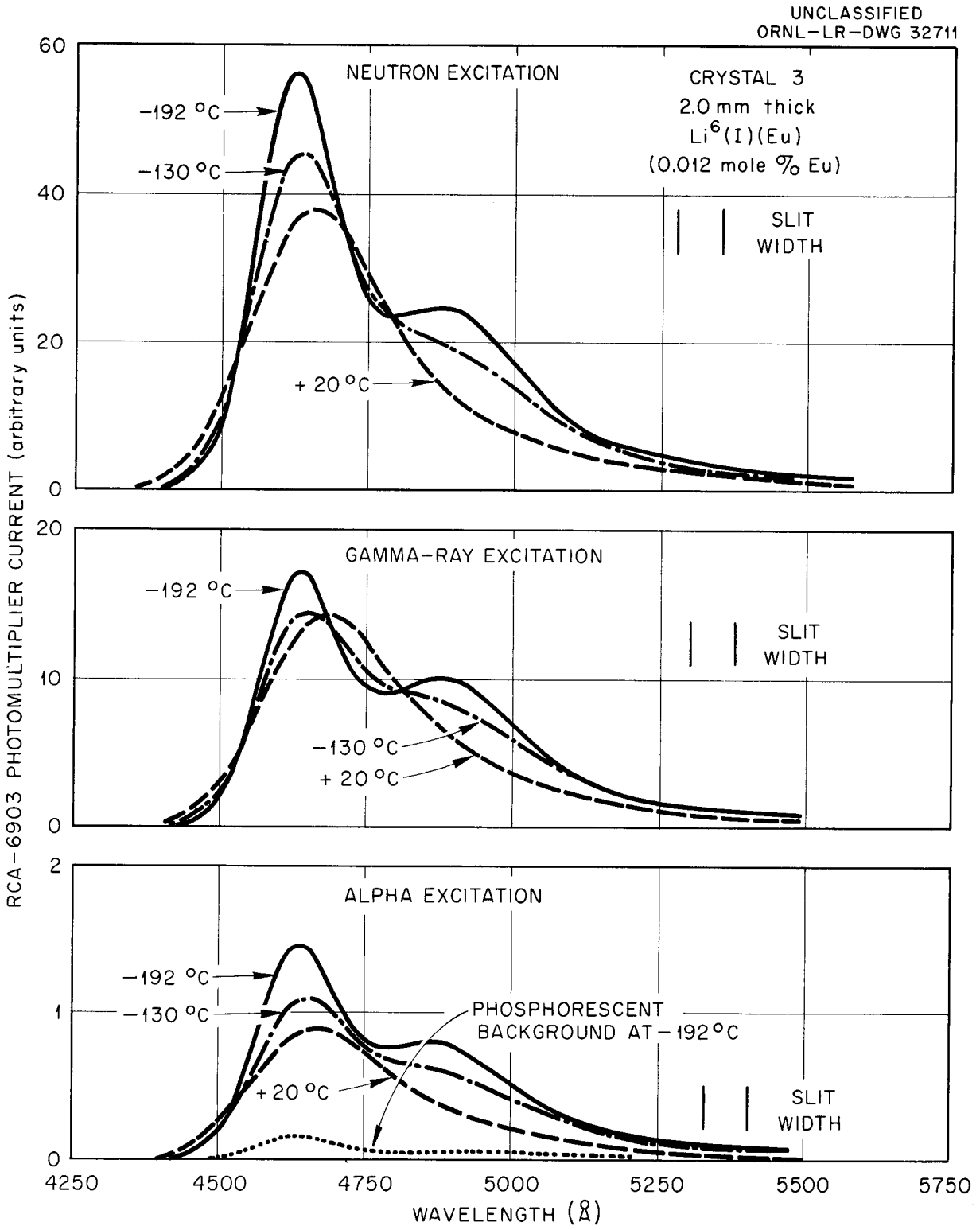

Fig. 8.4.4. Luminescence Spectra of $Li^6I(Eu)$, Crystal 3.

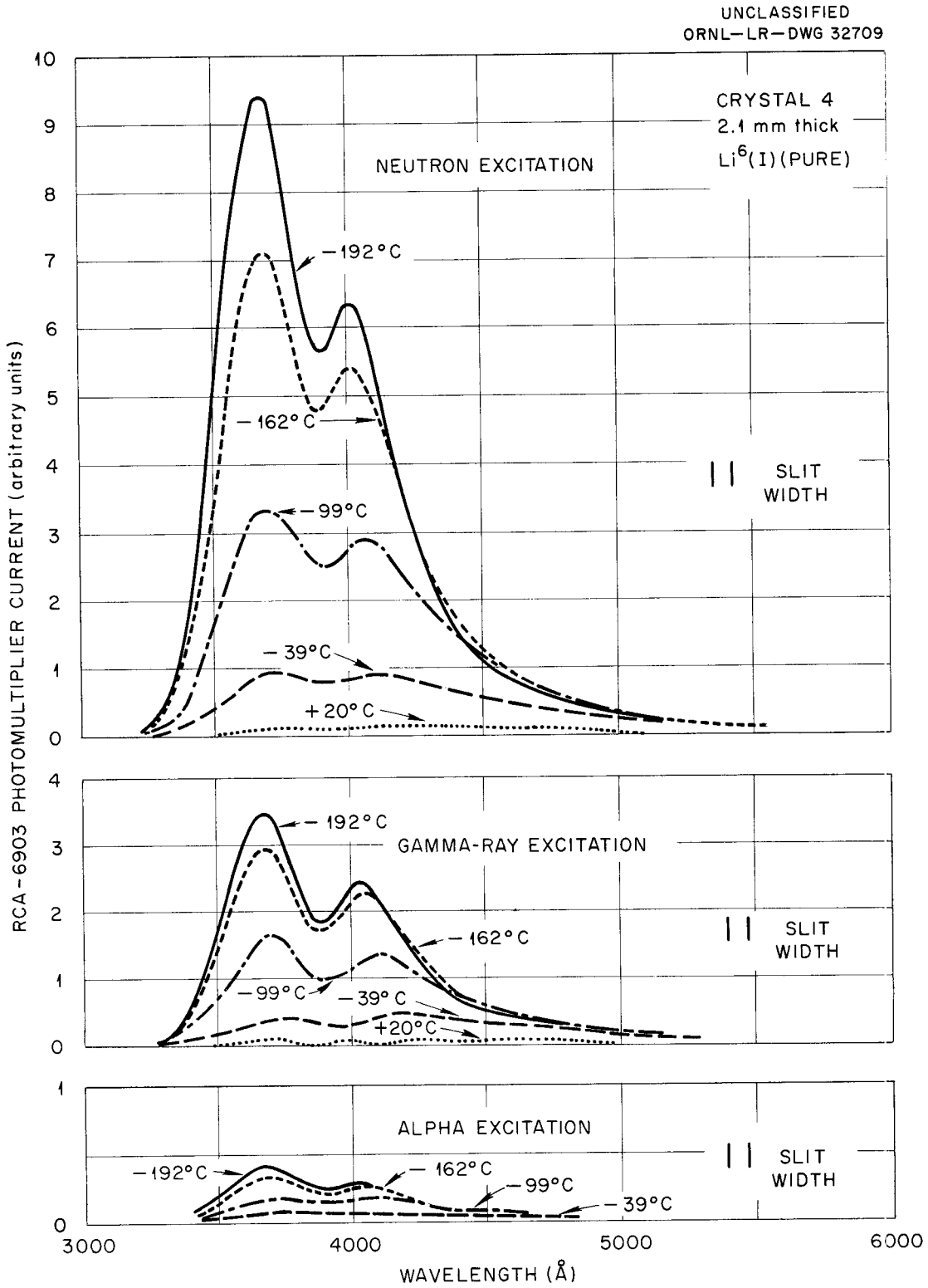

Fig. 8.4.5. Luminescence Spectra of "Pure" Li^6I, Crystal 4.

while the photomultiplier output was attached to the Y axis. A record of the thermoluminescence intensity at the band maxima was recorded as the crystals warmed slowly to room temperature. For warming rates of approximately 1 to 2°C/min a major thermoluminescence peak was recorded at −83°C, with smaller peaks recorded at −43, −33, and −23°C for crystal 2. Thermoluminescence from both the 4650 and 4875 Å bands varied in the same general fashion with increasing temperature. The thermoluminescence of pure Li^6I shows maxima at −180°C and smaller, broader peaks between −155 and −120°C at a warming rate of approximately 12°C/min.

At reduced temperatures crystals 2 and 3 showed a phosphorescence which continued for several minutes after removal of the source. The phosphorescence was nearly 4% of the intensity observed when the crystal was excited by neutrons and gamma rays. The spectrum of the phosphorescence is similar to the luminescence spectra and is shown in Figs. 8.2.3 and 8.2.4 as it was recorded after the alpha-particle spectrum had been recorded at −192°C. The pure crystal exhibited no phosphorescence. The work on crystal 1 was done with sources which were considerably weaker than those used in later experiments; as a result it is not known whether phosphorescence occurred in this crystal.

Summary

The luminescence emission spectra of lithium iodide scintillation crystals are observed to depend on activator content, temperature, and, to a lesser extent, on the type of exciting charged particle. The data given here are presented in the form of a progress report. It is hoped that further experiments of this type will provide information leading to a better understanding of the scintillation process in lithium iodide.

8.5. THE $Li^6(n,\alpha)T$ CROSS SECTION AS A FUNCTION OF NEUTRON ENERGY FROM 1.2 TO 8 Mev

R. B. Murray H. W. Schmitt[1] J. J. Manning

The use of $Li^6I(Eu)$ scintillation crystals for purposes of fast-neutron detection and spectroscopy has been described previously.[2] The neutron detection efficiency of such a crystal depends upon the probability of interaction of an incident neutron with a Li^6 nucleus to give a $Li^6(n,\alpha)T$ event. The interpretation of the data obtained from a $Li^6I(Eu)$ detector thus depends upon knowledge of the $Li^6(n,\alpha)T$ cross section as a function of neutron energy. The energy interval in which the $Li^6I(Eu)$ technique is applicable extends from about 1 to 20 Mev. The data available on the (n,α) cross section in this region, prior to this time, have been summarized in BNL-325. The cross section given there is taken largely from the work of Ribe[3] and extends from below 1 Mev to 6.5 Mev, with a single point at 14 Mev. The uncertainty in the cross section in the work of Ribe ranges from 11 to 18%. In view of the numerous possible uses of $Li^6I(Eu)$, both as an absolute monitor and as a spectrometer for fast neutrons, it was felt that more detailed and accurate information on the (n,α) cross section would be of considerable value. As a result, a new measurement of the $Li^6(n,\alpha)T$ cross section, in the energy interval from 1.2 to 8 Mev, was performed and is described below.

Description of the Method

Monoenergetic neutrons were obtained from the $T(p,n)He^3$ and $D(d,n)He^3$ reactions, the ORNL 5.5-Mev Van de Graaff generator being used to accelerate the incident charged particle. Those neutrons emitted in a small cone about 0 deg with respect to the incident beam were used in the cross-section determination, as described below. The neutron energy was varied by changing the energy of the charged particle. Neutron energies were calculated from published tables,[4] taking

[1] ORNL Physics Division.

[2] R. B. Murray, *Nuclear Instr.* 2, 237 (1958); R. B. Murray and J. J. Manning, *Appl. Nuclear Phys. Ann. Prog. Rep. Sept. 1, 1957*, ORNL-2389, p 240.

[3] F. L. Ribe, *Phys. Rev.* 103, 741 (1956).

[4] J. L. Fowler and J. E. Brolley, Jr., *Revs. Modern Phys.* 28, 103 (1956).

into account the loss of charged-particle energy upon penetration of target foils and target gas.

The $Li^6(n,\alpha)T$ events were detected in a $Li^6I(Eu)$ scintillation crystal. Pulse-height analysis of the counts from the crystal permitted a determination of those (n,α) events arising from primary target neutrons. The fast-neutron flux was determined by counting fission events occurring in a thin-walled ionization chamber containing a deposit of either U^{238} or Np^{237}. Three separate runs were carried out in the course of the experiment; different geometries, $Li^6I(Eu)$ crystals, and fission detectors were employed in the various runs. A description of the principal features in each case is given below.

Run No. 1. – The $Li^6I(Eu)$ scintillation crystal (3 mm thick) was contained in a low-temperature cell in the apparatus shown in Fig. 8.5.1 and was operated at the liquid-nitrogen point to take advantage of the improved fast-neutron resolution obtained at low temperatures. This device was designed to eliminate the Lucite or glass light piper usually needed in a scintillation spectrometer and to provide a reliable scheme for maintaining the crystal near −196°C. Elimination of the light piper provided a considerable reduction in the slow-neutron background usually encountered.[2] The resolutions of both the slow-neutron and fast-neutron peaks obtained with this device, however, are generally somewhat broader than in the case of a conventional spectrometer with a light piper. A typical pulse-height spectrum, resulting from 2.52-Mev neutrons, is shown in Fig. 8.5.2.

In the cross-section measurement, the apparatus of Fig. 8.5.1 was placed so that the crystal was located at an accurately known distance from the neutron source (4.343 in.). A solid target of ZrT evaporated onto a platinum backing was used. The neutron spectrum was recorded on a 20-channel analyzer; at the same time, the neutron flux was carefully monitored by auxiliary neutron counters and a beam-current integrator. The scintillation crystal was then replaced by the fission chamber in such a manner that the fission foil (U^{238}) was exactly the same distance from the target as the $Li^6I(Eu)$ crystal. The number of fission events per monitor count, or per beam-current integrator count, was then determined to establish the absolute neutron flux which had been incident on the $Li^6I(Eu)$ crystal.

Run No. 2. – A 10-mm-thick by 38-mm-dia $Li^6I(Eu)$ crystal was mounted directly behind, and concentric with, the fission foil (U^{238}) in the ionization chamber (Fig. 8.5.3). The crystal was operated

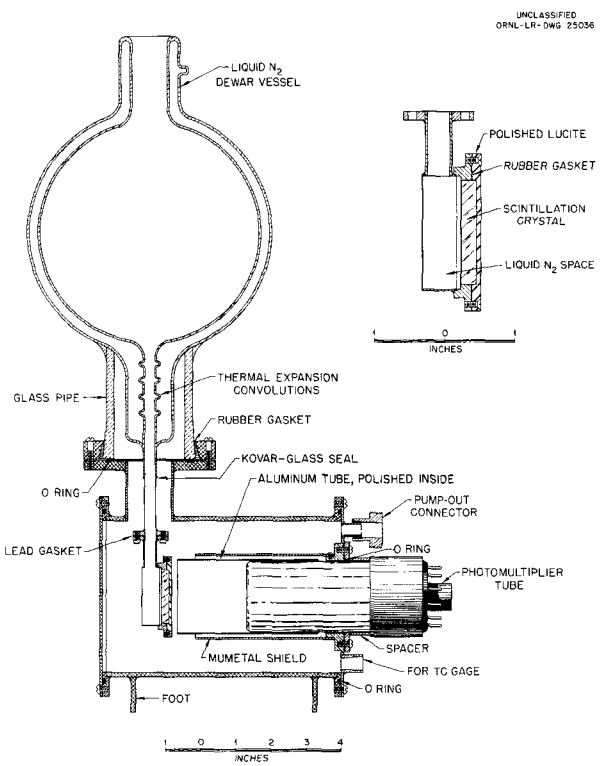

Fig. 8.5.1. Low-Temperature Scintillation Spectrometer.

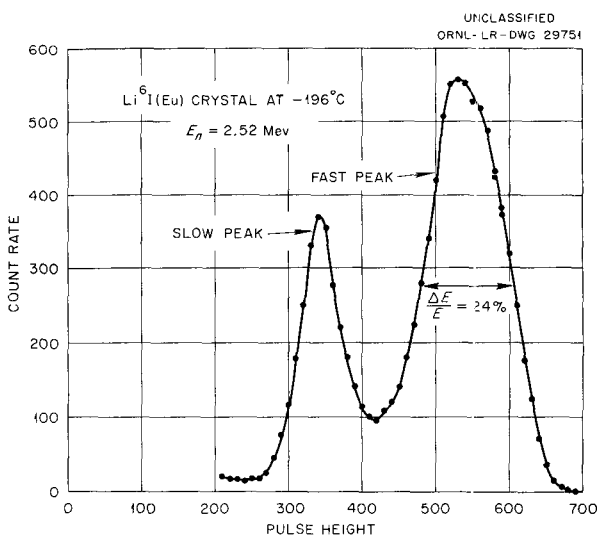

Fig. 8.5.2. Typical Pulse-Height Spectrum from Monoenergetic Fast Neutrons Obtained with Low-Temperature Spectrometer.

UNCLASSIFIED
ORNL-LR-DWG 32111

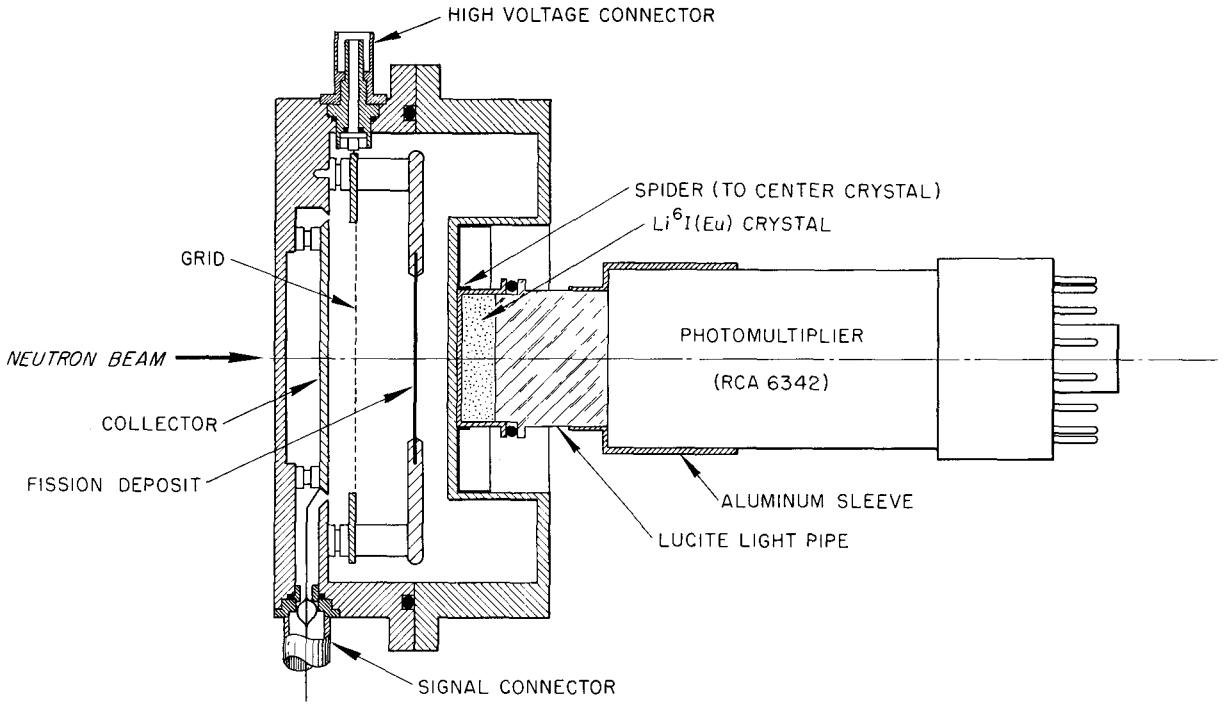

Fig. 8.5.3. Schematic Diagram of Fission Chamber and Scintillation Crystal Apparatus.

at room temperature. The apparatus was placed at a known distance from the neutron source, which was, in this case, a 3-cm-long gas cell containing tritium at a pressure of about 1 atm. Because of the vastly different counting rates in the fission counter and crystal, it was necessary to take the scintillation counter data at a low beam current ($\sim$0.1 μa) and the fission data at a high current (10 μa). The correlation between the fission data and $Li^6I(Eu)$ crystal data was again determined by careful monitoring of the neutron flux with the auxiliary counters and beam-current integrator. It was, of course, necessary to make a geometrical correction to take account of the separation in distance between the fission deposit and the crystal. This correction, amounting to about 22%, was calculated from the published angular distributions of $T(p,n)He^3$ neutrons[4] and was verified by an experimental determination of neutron flux versus distance.

Run No. 3. – Exactly the same geometry was used as in the preceding run. In this case, however, a much smaller scintillation crystal was used (2.5 mm thick by 19 mm in diameter) and the fission deposit was made of Np^{237}. As a result, the counting rates in the crystal and ionization chamber were more compatible than in run No. 2, permitting the simultaneous recording of data from the two detectors. Neutrons were generated in a gas target containing either tritium or deuterium. Typical pulse-height spectra obtained in this run are given in Figs. 8.5.4 and 8.5.5. In an auxiliary experiment, the fission counting rate from the Np^{237} deposit was determined relative to that of the previously used U^{238} foil by simultaneous counting of fission events in a back-to-back geometry. This comparison permitted analysis of all data in terms of the absolute value of the U^{238} fission cross section only, as will be discussed below.

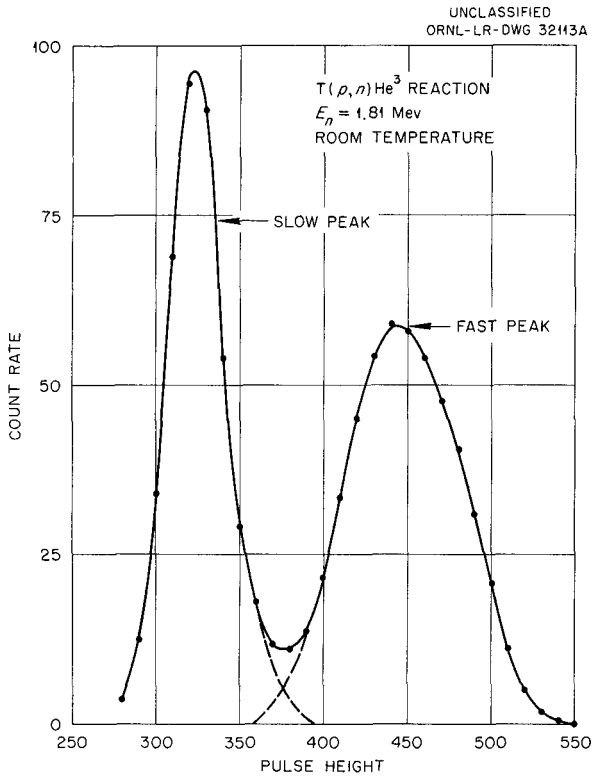

Fig. 8.5.4. Typical Pulse-Height Spectrum from $T(p,n)He^3$ Neutrons.

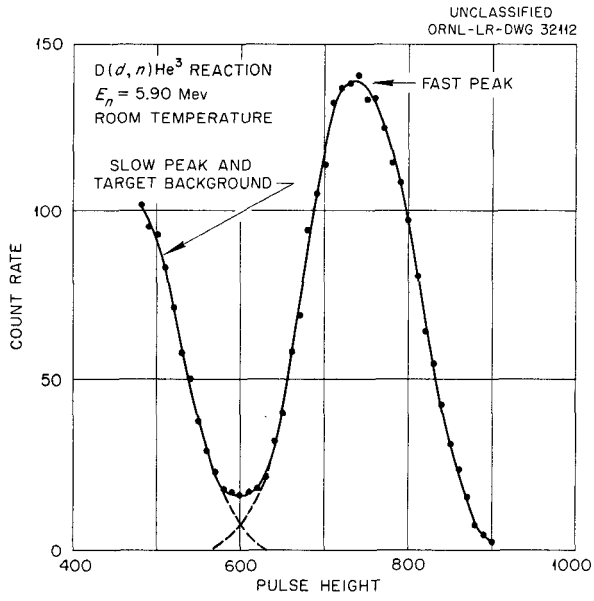

Fig. 8.5.5. Typical Pulse-Height Spectrum from $D(d,n)He^3$ Neutrons.

Analysis of Data

The calculation of the $Li^6(n,\alpha)T$ cross section from the experimental data of the first two runs was performed according to the following equation:

$$(1)\quad \frac{\sigma_{n,\alpha}(E_n)}{\sigma_{fiss}(E_n)} = \frac{(n,\alpha)\text{ counts}}{\text{fission counts}} \times \frac{\text{mass of } U^{238}}{\text{mass of } Li^6} \times \frac{\text{at. wt of } Li^6}{\text{at. wt of } U^{238}} \times \frac{\bar{\phi}(U^{238})}{\bar{\phi}(Li^6)} .$$

The ratio $\bar{\phi}(U^{238})/\bar{\phi}(Li^6)$ represents the ratio of the neutron flux (averaged over the detector) at the position of the fission deposit to that at the scintillation crystal. This ratio was determined by calculation and experiment as indicated above. The number of (n,α) counts was determined from the observed pulse-height spectrum, as in Figs. 8.5.2, 8.5.4, and 8.5.5. It is, of course, necessary to include counts contained in the extrapolated tail on the low-energy side of the fast-neutron peak. The fraction of the total (n,α) counts contained in the extrapolated tail was usually quite small, of the order of a few per cent. The U^{238} mass was determined by alpha-counting the U^{238} deposit in the 2π geometry of the ionization chamber. The mass was calculated from the alpha count rate using a half life of 4.51×10^9 years and a counting geometry factor of 0.52. The mass of Li^6 was determined by careful weighing of the crystals before and after each run, combined with an isotopic analysis for Li^6 content (96% enrichment). The fission cross section for U^{238} was taken from Los Alamos report LA-2114.[5]

For run No. 3, in which the Np^{237} deposit was used, the calculation of $\sigma_{n,\alpha}$ goes according to the above equation with the U^{238} terms replaced by Np^{237} terms. In this case, it can be noted that

$$(2)\quad \sigma_{n,\alpha}(E_n) \sim (\text{mass of Np}) \times \sigma_{fiss}^{Np}(E_n) .$$

The mass of Np^{237} was determined by comparison fission counting with U^{238} at a neutron energy of 5 Mev. In this comparison experiment, the Np^{237}

[5] R. L. Henkel, *Summary of Neutron-Induced Fission Cross Sections*, LA-2114 (Feb. 25, 1957).

mass is obtained from

(3) mass of Np = (mass of U) ×

$$\times \frac{\text{Np fission counts}}{\text{U fission counts}} \times \frac{\sigma^{U}_{fiss}\,(5\text{ Mev})}{\sigma^{Np}_{fiss}\,(5\text{ Mev})}.$$

Combining Eqs. 3 and 2 gives

(4) $\sigma_{n,\alpha}(E_n) \sim$ (mass of U) ×

$$\times\, \sigma^{U}_{fiss}\,(5\text{ Mev}) \times \frac{\sigma^{Np}_{fiss}\,(E_n)}{\sigma^{Np}_{fiss}\,(5\text{ Mev})}.$$

Thus, $\sigma_{n,\alpha}(E_n)$ as determined from Eq. 4 is proportional to (1) the previously determined mass of the U^{238} deposit, (2) the absolute value of σ^{U}_{fiss} at 5 Mev, and (3) the *shape* of the Np^{237} fission cross section curve (taken from BNL-325).

The probable errors associated with the determination of $\sigma_{n,\alpha}$ have been separated into two types: (1) statistical errors in counting and other uncertainties which vary from point to point and (2) those uncertainties which are energy independent, e.g., the mass of U^{238} and the absolute magnitude of the U^{238} fission cross section. The probable errors of type 1 are shown on the individual data points, while the over-all uncertainty in the absolute value of $\sigma_{n,\alpha}$ is estimated to be ±7%.

Results and Discussion

The results of the three runs discussed above are shown in Fig. 8.5.6. These data are in very good agreement with the previous work of Ribe.[3]

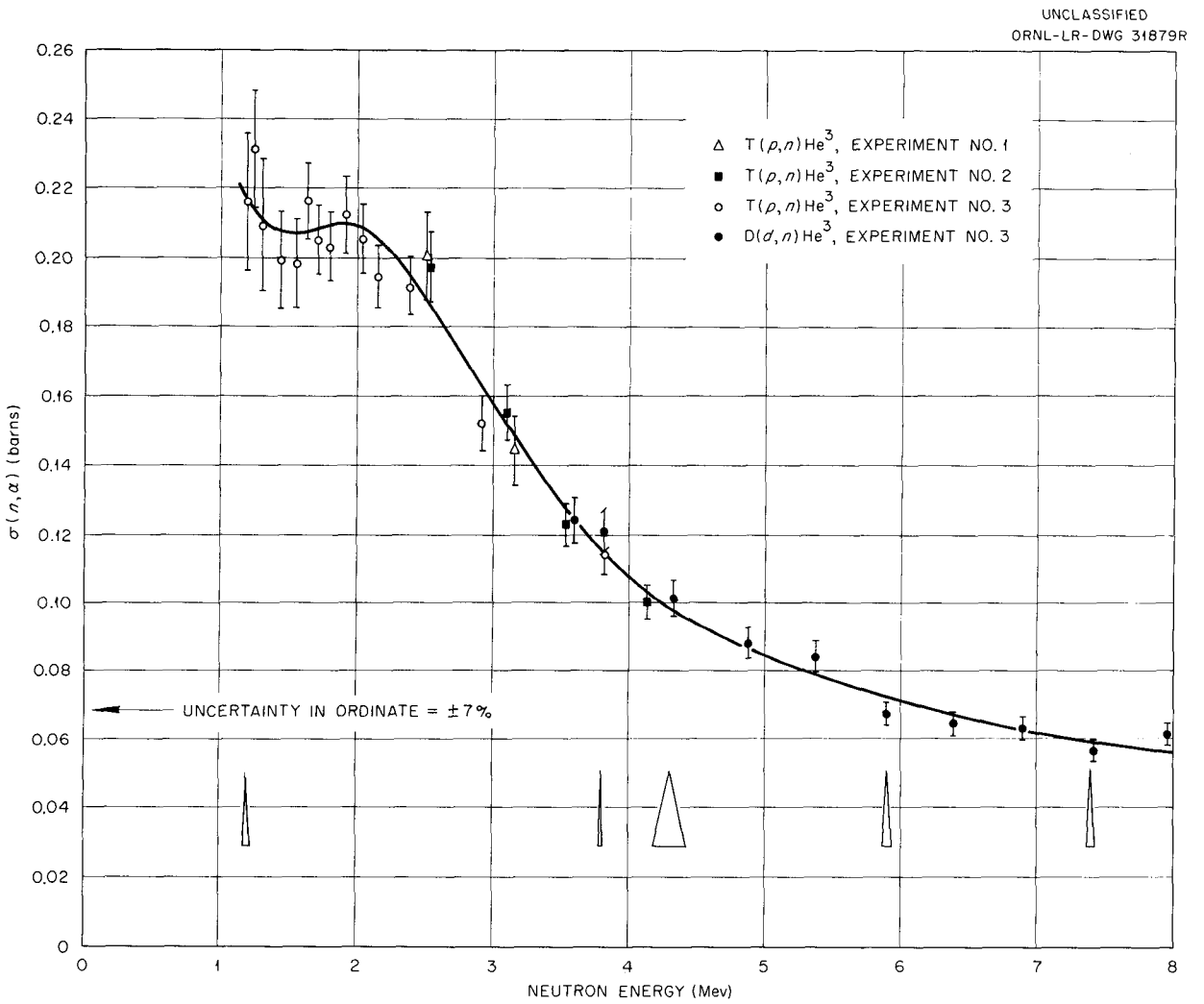

Fig. 8.5.6. Measured Values of $Li^6(n,\alpha)T$ Cross Section as a Function of Neutron Energy. The base of the triangles represents typical target thickness, i.e., full neutron energy spread.

One feature noted in Fig. 8.5.6 which has not been explicitly observed previously is the broad hump (or plateau) at 2 Mev. A possible explanation for this effect may be sought in the formation of the Li^7 compound nucleus in a (previously observed) state at about 9.6 Mev. An analysis of the data in terms of this mechanism has not yet been carried out.

In conclusion, it may be noted that a measurement of the $Li^6(n,\alpha)T$ cross section from 12.5 to 18.3 Mev has recently been reported by Kern and Kreger.[6] A plot of a smooth curve through their data, together with a smooth curve through the data reported here, is given in Fig. 8.5.7. It is seen that the two sets of data may be smoothly joined by a straight line on a semilogarithmic plot.

[6] B. D. Kern and W. E. Kreger, *Bull. Am. Phys. Soc.* 3, 187 (1958); also private communication.

Summary

The cross section for the reaction $Li^6(n,\alpha)T$ has been measured as a function of neutron energy in the region $1.2 \leq E_n \leq 8$ Mev. The magnitude of $\sigma_{n,\alpha}$, as measured in this experiment, depends on the absolute value of σ_{fiss} (U^{238}), while the shape of the cross section vs energy curve depends on the known energy dependence of σ_{fiss} (U^{238} or Np^{237}). Statistical and other point-to-point uncertainties range from ±5% to ±9%, while the over-all uncertainty in absolute value of the cross section is ±7%. The cross section obtained from these measurements is consistent with that determined at other laboratories. The data presented here can be smoothly joined to the measured cross section above 12.5 Mev.

A more detailed description of this experiment will be presented elsewhere.

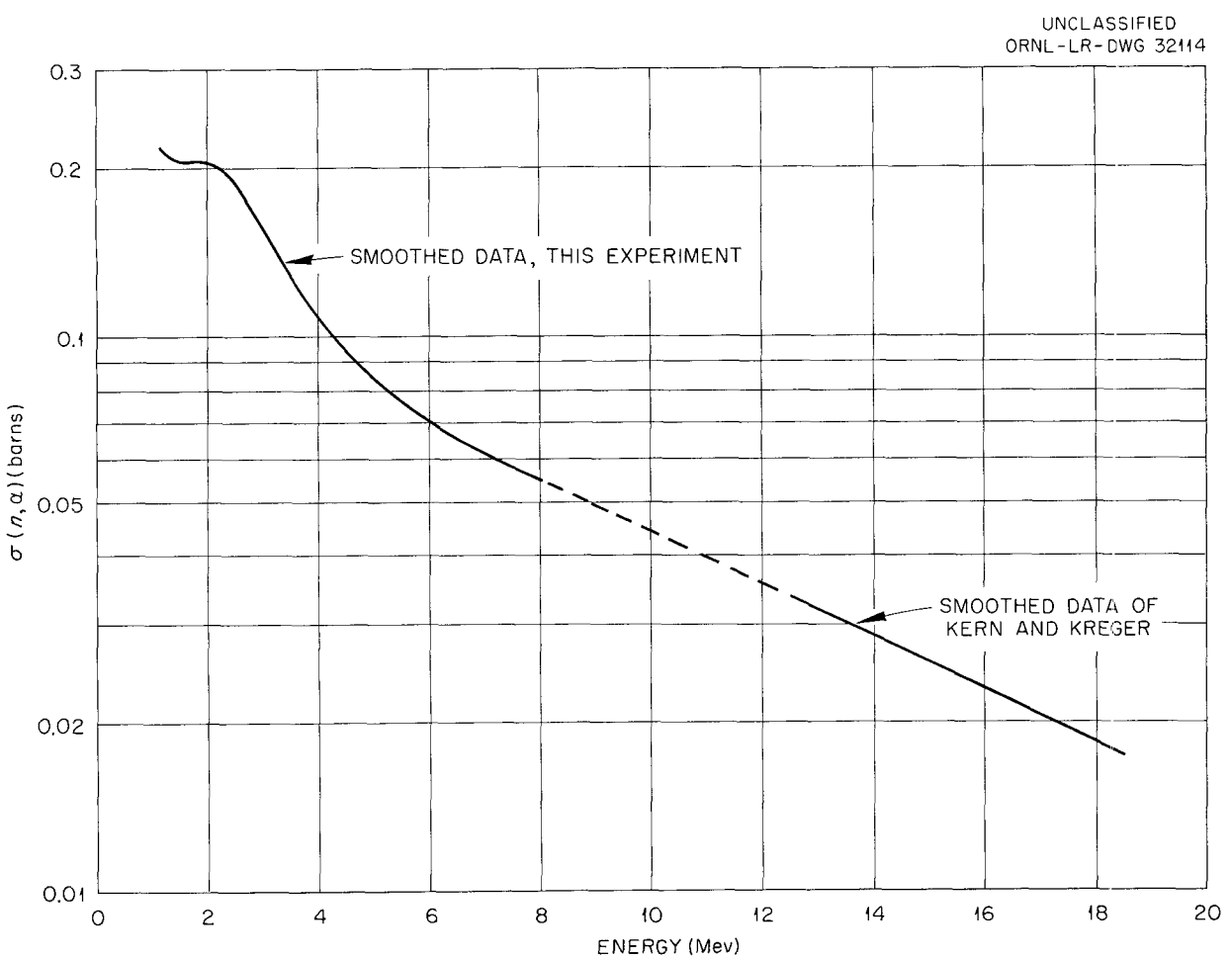

Fig. 8.5.7. Smoothed Curves Through the $Li^6(n,\alpha)T$ Cross-Section Data Reported Here and Those of Kern and Kreger.

ORNL-2609
Physics and Mathematics
TID-4500 (14th ed.)
February 15, 1958

INTERNAL DISTRIBUTION

1. C. E. Center
2. Biology Library
3. Health Physics Library
4–6. Central Research Library
7. Reactor Experimental Engineering Library
8–42. Laboratory Records Department
43. Laboratory Records, ORNL R.C.
44. A. M. Weinberg
45. L. B. Emlet (K-25)
46. J. P. Murray (Y-12)
47. J. A. Swartout
48. E. H. Taylor
49. E. D. Shipley
50. A. H. Snell
51. W. H. Jordan
52. M. L. Nelson
53. G. E. Boyd
54. R. A. Charpie
55. S. C. Lind
56. F. L. Culler
57. A. Hollaender
58. J. H. Frye, Jr.
59. M. T. Kelley
60. R. S. Livingston
61. K. Z. Morgan
62. E. J. Murphy
63. A. S. Householder
64. C. P. Keim
65. C. S. Harrill
66. C. E. Winters
67. D. S. Billington
68. H. E. Seagren
69. D. Phillips
70. A. J. Miller
71. M. J. Skinner
72. R. R. Dickison
73. P. M. Reyling
74. G. C. Williams
75. L. S. Abbott
76. R. G. Alsmiller
77. J. L. Fowler
78–102. E. P. Blizard
103. A. D. Callihan
104. G. T. Chapman
105. C. E. Clifford
106. R. R. Coveyou
107. G. deSaussure
108. L. Dresner
109. J. K. Fox
110. L. W. Gilley
111. E. Guth
112. R. Gwin
113. K. M. Henry
114. L. B. Holland
115. E. B. Johnson
116. F. L. Keller
117. W. E. Kinney
118. M. E. LaVerne
119. T. A. Love
120–122. F. C. Maienschein
123. H. Bertini
124. J. M. Miller
125. F. J. Muckenthaler
126. R. B. Murray
127. R. W. Peelle
128. A. B. Reynolds
129. E. G. Silver
130. A. Simon
131. J. G. Sullivan
132. D. K. Trubey
133. T. A. Welton
134. C. D. Zerby
135. W. Zobel
136. V. R. Cain
137. G. M. Estabrook
138. T. K. Fowler
139. H. P. Carter
140. N. H. Ethridge
141. J. L. Hull
142. J. D. Kington
143. D. Magnuson
144. J. J. Manning
145. H. S. Moran
146. J. Lewin
147. T. V. Blosser
148. T. J. Mihalczo
149. D. F. Cronin
150. J. F. Ellis
151. R. M. Freestone

152. V. G. Harness
153. L. Jung
154. R. J. Kerr
155. J. J. Lynn
156. R. J. Mackin
157. S. K. Penny
158. E. R. Rohrer
159. F. S. Alsmiller
160. W. L. Riggle
161. S. Terasawa
162. D. R. Ward
163. J. T. Thomas
164. W. C. Tunnell
165. Francis L. Friedman (consultant)
166. Herbert Goldstein (consultant)
167. Henry Hurwitz, Jr. (consultant)
168. L. W. Nordheim (consultant)
169. Robert R. Wilson (consultant)

EXTERNAL DISTRIBUTION

170. R. V. Meghreblian, Jet Propulsion Laboratory, Pasadena, California
171. H. G. Hanson, University of Minnesota
172. E. Kuhn, Reactor Design Development Division, Combustion Engineering, Windsor, Connecticut
173. Division of Research and Development, AEC, ORO
174–781. Given distribution as shown in TID-4500 (14th ed.) under Physics and Mathematics Category (75 copies – OTS)